THERMAL SPRAY AND LASER CLADDING OF NICKEL-CHROMIUM COATINGS FOR HIGH TEMPERATURE APPLICATIONS

Bo Song, BEng,MSc

Thesis submitted to the University of Nottingham for the degree of Doctor of Philosophy

October 2018

Abstract

To reduce the environmental impact, there is a trend for the thermal power generation industry to increase the usage of the biomass fuel. However, the severe corrosion of boiler materials that is brought about by the high chlorine and alkaline content in the biomass limits the application of biomass fuel and the operation temperature of the biomass boiler. NiCr based alloys that have high Cr content are an ideal solution to combat this problem; they can protect the boiler steel substrate from the chlorine-induced corrosion. There are quite a lot of coating deposition techniques, but the most suitable one for the deposition of Ni50Cr alloy on the boiler material and thereby provides satisfactory protection is still in debate.

The major aims of this research included: determining the most suitable coating deposition technique for high temperature oxidation/corrosion applications of NiCr alloys in four candidates (high velocity oxygen liquid/gas fuel (HVOLF/HVOGF) thermal, cold spray and laser cladding); describing and explaining the high temperature oxidation/corrosion performance of coatings deposited using shortlisted deposition routine. The key objectives of this research were: a literature review that can identify the knowledge gap existing in the current research of high temperature oxidation/corrosion NiCr-based coatings; successful deposition of NiCr-based coatings using techniques include in this study, and the deposition product should be of satisfactory quality; high temperature oxidation/corrosion exposure of deposited coatings in test rigs; comprehensive summary of the oxidation/corrosion behaviours of coatings and identification of possible mechanism to explain these behaviours;

direction for the future development of high temperature NiCr-based corrosion resistance coatings.

To achieve abovementioned objectives, following work were conducted. Short-term air thermogravimetric analysis (TGA) results of as-sprayed HVOF coatings were used to determine the air oxidation resistance of the five HVOF thermal sprayed coatings. The HVOLF and HVOGF coatings that had better air oxidation resistance were hypothesized to have better steam oxidation and fireside corrosion performance and shortlisted for the subsequent high temperature test in various atmospheres.

There was no recommended process parameter sets for the laser cladding of the Ni50Cr powder. Therefore, a process window was built to help decide the most suitable parameter set. Laser cladded coating that had satisfactory metallurgical quality, acceptable thickness, maximum width and minimum dilution was selected as the candidate for subsequent high temperature exposure. The optimization process of the laser cladding parameter had been published and was not included in this thesis.

The cold sprayed coating was deposited by using the Xi'an Jiaotong University's custom-made cold spray set-up. The microstructure of the deposited cold sprayed coating was acceptable after grinding several top layers of the coating (~ 500 μm), and the coating was placed into the high temperature test rigs for the further investigation of the high temperature oxidation/performance of cold sprayed coating.

Longer-term air oxidation (compared with the TGA dwell time), steam oxidation and chlorine-induced fireside corrosion tests of four coatings were conducted in the simulation test rigs built in our laboratory. Following procedures were adopted to investigate the oxidation/corrosion behaviour. In the case of the air oxidation test, three

samples of each coating were placed into the high temperature box furnace and was removed from the furnace after 1 h, 10 h and 100 h of exposure time, in succession. In the case of the steam oxidation test, four samples of each coating were sent into the test rig and collected after 250 h, 500 h, 750 h and 1000 h of exposure time one after another. While in the case of the chlorine-induced fireside corrosion test, two samples, with KCl and without KCl deposit on the surface of coating, were the candidates of the 250 h high temperature corrosion exposure. Adopting a relative short exposure time in the chlorine-induced corrosion test was owing to the severe attack ability of chlorine and alkali metal on material.

Specimens, after the high temperature oxidation/corrosion and collected at the specific time points, can provide valuable information about the evolution of the air oxidation, steam oxidation and fireside corrosion behaviour of four coatings. Several material characterisation methods such as X-ray diffraction (XRD), scanning electron microscopy (SEM) and energy-dispersive X-ray spectroscopy (EDX) were used to obtain the said information.

By conducting the abovementioned experiments and analysing the obtained results, the rank of the oxidation/ corrosion resistance of four coatings in various atmospheres at high temperature can be asserted. The mechanism behind the different oxidation/corrosion behaviour for various coatings can be investigated and several possible mechanisms that can explain the observed results are adopted. Finally, a promising Ni50Cr coating deposition method – HOVLF and laser cladding is recommended.

List of journal publications

- Song, B., Voisey, K. T., & Hussain, T. (2018). High temperature chlorine-induced corrosion of Ni50Cr coating: HVOLF, HVOGF, cold spray and laser cladding. **Surface and Coatings Technology**, 337, 357-369.
- Song, B., Bai, M., Voisey, K. T., & Hussain, T. (2017). Role of Oxides and Porosity on High-Temperature Oxidation of Liquid-Fueled HVOF Thermal-Sprayed Ni50Cr Coatings. **Journal of Thermal Spray Technology**, 26(3), 554-568.
- Song, B., Pala, Z., Voisey, K. T., & Hussain, T. (2017). Gas and liquid-fuelled HVOF spraying of Ni50Cr coating: Microstructure and high temperature oxidation. **Surface and Coatings Technology**, 318, 224-232.
- Song, B., Hussain, T., & Voisey, K. T. (2016). Laser cladding of Ni50Cr: a parametric and dilution study. **Physics Procedia,** 83, 706-715.

Oral/poster presentation or papers in conferences

- Song, B., Hussain, T., & Voisey, K. T. Steam Oxidation of HVOF Thermal Sprayed NI50Cr Coating at 700 °C: Microstructure and Scale Morphology. Proceedings: EPRI **International Conference on Corrosion in Power Plants**, Electric Power Research Institute Inc, CD-ROM, p. 7-188-197
- Song, B., Hussain, T & Voisey, K. T. Laser cladding of Ni50Cr: a parametric and dilution study. **9th International Conference on Photonic Technologies**, 19-22 Sep 2016, (Furth, Germany), Bayerisches Laserzentrum GmbH & Institute of Photonic Technologies (Poster presentation)
- Song, B., Pala, Z., Voisey, K. T., & Hussain, T. (2017). Gas and liquid-fuelled HVOF spraying of Ni50Cr coating: Microstructure and high temperature oxidation. **7th Rencontres Internationales sur la Projection Thermique**, 9-11 Dec 2015, (Limoges, France), SPCTS, Centre Européen de la Céramique (Oral presentation)
- Song, B., Hussain T. HVOF sprayed Ni50Cr coatings for power plants: Microstructure, Porosity and Oxidation. **International Thermal Spray Conference 2015**, 11-14 May 2015, (Long beach, California, USA), ASM (Poster presentation)

Acknowledgement

I would first like to thank my supervisor Dr Tanvir Hussain and Dr Katy Voisey for their invaluable support, advice and mentoring during my three years of doctoral research. I learnt to be critical to ideas, progress logically through the course of an investigation and think rationally from working with them. It has been a life changing experience for me. I would also like to thank Mr. Keith Dinsdale, Mr. Rory Screaton and Dr Deen Zhang for all the equipment training, technical solutions and invaluable discussion.

I am also very grateful to all my colleagues and friends at Wolfson building who made my four-year study at the university a pleasant one.

Last, but not least I would like to dedicate this thesis to my wife, my father and mother, who I will always love and try to make them proud of who I am.

Contents

List of figures

List of tables

Chapter 1 Introduction

1.1 Background

The high temperature chlorine-induced corrosion of boiler steels usually occurs in thermal power plants using biomass fuel, and not only limits the thermal efficiency of the biomass boiler but also results in higher costs because of the frequent maintenance and replacement of the heat exchanger components [1-9]. Therefore currently, biomass thermal power plants as well as waste to energy (WTE) thermal power plants operate with mixed fuels, i.e. a minor amount of biomass/waste fuel and a major amount of traditional fossil fuel (coal/oil) [10-13]. This co-firing operation is a precaution to prevent the intense high temperature chlorine-induced corrosion of the boiler material, as it will bring about a rapid failure of the heat exchanger components in the biomass boilers. Therefore, it is necessary to provide solutions that can combat the high temperature chlorine-induced corrosion problems of boiler materials satisfactorily so that the application of biomass boilers can be promoted by increasing the operating temperature and the biomass fuel usage ratio.

The deposition of a protective and sacrificial coating on the fireside surface of the biomass boiler material is a promising approach to solve the abovementioned problem of the high temperature chlorine-induced corrosion of the substrate. The requirement of a coating material for boiler applications usually includes two aspects: high temperature oxidation/corrosion resistance and high temperature creep resistance. The high temperature oxidation/corrosion resistance of a certain material is determined by the oxidation rate of the constituents of such material and the integrity of the formed oxidation scale [14-19]. Hence, a desired high temperature

oxidation/corrosion resistance coating material should at least have one constituent which can form an oxidation barrier layer of the required microstructure [20]. The creep rate of a coating material increases significantly at high temperature, and finally, the coating may spall from the substrate because of the creep effect. This will lead to the subsequent failure of the substrate material, as it will immediately come into contact with the corrosive atmosphere/environment under this condition [21]. Therefore, an ideal coating material for the biomass boiler should also have a small high temperature creep rate.

On the basis of two abovementioned criteria, NiCr alloys were selected among the commercially available coating materials for this study. A large number of previous publications and research works have indicated that NiCr alloys are widely used in various areas to provide corrosion resistance at elevated temperatures, since the selective oxidation of Cr can form a slowly growing and protective layer, which is the basis for the corrosion protection of NiCr coatings used at high temperature [14, 20, 22, 23]. Moreover, Ni can act as an excellent matrix for NiCr alloys, as the solubility of Cr in Ni can reach 35 wt.% [24]. According to Zhang *et al.* [25], thermally sprayed NiCr coating can increase the creep resistance of the substrate. This is, the creep resistance of the substrate in a biomass boiler will at least not be reduced after coating deposition using the feedstock material NiCr alloys.

Several techniques, such as cold spray, high velocity oxygen–fuel (HVOF) thermal spray and laser cladding, can be used to deposit protective coatings onto substrates. Cold spray as well as HVOF thermal spray has been used to spray protective coatings on water-wall tubes and heat exchangers in a boiler [26-32]. Cold spray is a process where feedstock particles do not undergo any bulk melting or phase changes as the

deposition occurs in the solid state. The particles are accelerated to supersonic velocities using an accelerating gas such as helium (He) or heated nitrogen (N_2) [33]. Cold sprayed coatings retain the microstructural features from the original feedstock powder, but the coatings may suffer from porosity because of the insufficient plastic deformation of feedstock powder [32, 34, 35]. In the HVOF thermal spray process, the hypersonic velocity of the flame shortens the time of interaction between the powder and the flame and the low temperature of the flame (as compared to plasma spray) limits the coarse grains and the decomposition of the coating [36].Because of the high impact velocity of the particles, the coating has high adhesive strength, high cohesive strength, high density and low porosity. As Bluni *et al.* [37] suggested, interconnected porosity, oxide-containing splat boundaries, voids formed at splat boundaries and compositional inhomogeneity in the HVOF thermal sprayed coatings can lead to limited corrosion resistance. These features vary in coatings manufactured using the same powder but different types of fuels that combust in the HVOF spray gun. For instance, in general, gas fuelled HVOF (HVOGF) thermal sprayed coating contain considerably more oxides and has less porosity than the liquid fuelled HVOF (HVOLF) thermal sprayed coating, as the flame temperature during the HVOGF process is considerably higher than that during the HOVLF process, which promotes the oxidation process of feedstock powder and increases the plasticity of the splats [37]. Hence, an obvious difference in the corrosion resistance between coatings deposited with the same feedstock powder but using the HVOLF and HVOGF thermal spray technique is observed. Laser cladding is material deposition method in which a powdered or wire feedstock material is melted and consolidated with the use of a laser to coat the substrate [38]. Compared with coatings deposited using the thermal spray process, laser cladded coatings have better a microstructure (almost no defects and

porosity if deposited with suitable parameters) and can be manufactured to a larger thickness (~2000 µm) [39]. Defects and porosity are the main transport path for oxidising ions in the coating surface during the oxidation process [20]. Therefore, performance at high temperature in a chlorine-containing atmosphere is different from that of thermal sprayed coatings. Laser cladding is a welding-based technique that results in superior bonding with the substrate, but the clad suffers from dilution because of the substrate melting [39-42]. The dilution may bring element of the substrate (usually Fe) to the coating, which could undermine the oxidation/corrosion resistance of the coatings. However, this concern does not exist in the application of thermal spray processes, as the bonding between the coating and the substrate is based on mechanical interlocking [36]. Thus, these four different material processing routes from the powder of a single composition can result in considerably different microstructures, which could result in various levels of performance in case of high temperature chlorine-induced corrosion. Moreover, laser cladded coatings have a different composition from coatings manufactured using the other three techniques. This is also an important factor that can influence the oxidation/corrosion of the deposited coatings.

The determination of the most suitable technique for the deposition of NiCr alloys on the surface of biomass boiler tubes is a complex issue for both industrial and academic researchers. Furthermore, the application of coatings in the industry depends on the manufacturing cost of the technique. Thermal power plant operators prefer techniques that are cheaper and can provide acceptable (not the best) results because of the limited resources. For instance, laser cladding is the second choice if thermal spray

can solve the problem due to the higher cost of laser and a series of derivative issues involving laser usage such as laser safety and the potential danger of laser [43, 44].

In the research area, no consensus has been reached on the best technique to deposit NiCr coatings for achieving high temperature chlorine-induced corrosion resistance, as there are few studies focused on this topic. Uusitalo *et al.* conducted a series of corrosion tests in a chlorine-containing atmosphere on boiler steels, HVOF thermal sprayed NiCr alloy coatings and laser melted HVOF NiCr alloy coating, for 100, 400, and 1000 h [45-47]. The coatings were prepared from two powder compositions, namely Ni50Cr and Ni57Cr. The corrosion resistance of nickel-based, high Cr coating materials was satisfactory under test conditions. The interconnected porosity, oxide-containing splat boundaries, and compositional inhomogeneity created by the HVOF thermal spray reduced the corrosion resistance of the coatings [37]. Nevertheless, laser melting remarkably increased the corrosion resistance of the HVOF coatings by homogenising the structure of the coatings [45-47]. On the basis of this argument, a laser cladded nickel-based high Cr layer may provide a better solution to chlorine-induced corrosion, as laser cladding will bring about a protective layer of no oxides, minor porosity, refined crystals and altered microstructure [48]. Yet, detrimental impurities from the substrate steel (mainly Fe) during laser cladding will come into the melt pool and thereby be retained in the coating material and the amount of those detrimental s cannot be neglected (> 10 wt.%) [49]. Therefore, laser cladded NiCr coatings are NiCrFe coatings. Several researchers [9, 50-52] have reported the disastrous effects of Fe within alloys/coatings on the high temperature chlorine-induced corrosion resistance. Hence, whether the NiCr coatings directly deposited

using the laser cladding technique can provide satisfactory protection for corrosion is still in doubt and requires more investigation.

Besides the deposition routes, the composition of the NiCr alloy coatings may influence their corrosion resistance. With respect to the concentration of Cr on the corrosion resistance of NiCr alloys, it is generally accepted that the corrosion resistance of nickel-based coating materials increases with an increase in the Cr content [14, 20, 22, 23]. However, after comparing the chlorine-associated corrosion performance of both HVOF spray Ni50Cr and Ni57Cr coatings, Uusitalo *et al.* [45] found that although the HVOF sprayed Ni57Cr coating has a higher Cr level than the HVOF sprayed Ni50Cr coating, the latter provided better corrosion resistance than the former. The Ni57Cr coating is infiltrated by corrosive species. In contrast, the Ni50Cr coating is covered with oxide and sulphide scales and thereby is not penetrated by corrosive species. Many other previous publications have mostly focused on the oxidation/corrosion performance of Ni20Cr alloys [53-56]. Hence, because of the limited literature on the various corrosion resistances of coatings with different Cr concentrations, it is difficult to determine the alloys/coatings whose Cr content has the best high temperature chlorine corrosion resistance. Therefore, the Ni50Cr powder was selected in this study to simplify the problem, as its Cr content is in the midrange of the commercially available NiCr alloys (usually Ni25Cr, Ni50Cr and Ni75Cr) [57].

1.2 Aims and objectives

The major aims of this study are to determine the most suitable NiCr-based alloy powder deposition technique for the high temperature oxidation/corrosion application in four candidates (HVOLF, HVOGF, cold spray and laser cladding) and to describe

the high temperature oxidation/corrosion performance of coatings deposited using shortlisted deposition routine. To achieve these aims, several objectives are listed as follows:

- Identify the knowledge gap that exists in the current area of high temperature oxidation/corrosion of NiCr-based coatings from the literature.
- Deposit the NiCr-based coatings using various technique routines and optimize the process parameters to make sure the best coatings in this study can be manufactured with the supplied source.
- Conduct a series of high temperature oxidation/corrosion exposure of deposited coatings in various atmospheres to help examine their oxidation/corrosion behavi55our in harsh environment.
- Summarise the oxidation/corrosion performance of objective coatings and draw the possible mechanisms that could be used to explain the difference of oxidation/corrosion performance of various coatings.
- Fill the knowledge gap to some extent by using the results, discussions and conclusions that obtained in this study.
- Provide potential solutions for the applications of NiCr-based coatings in high temperature oxidation/corrosion resistance area.

1.3 Structure of the thesis

In the first part of this thesis, background information obtained from the literature is summarised and the knowledge gap that we hope to fill in by this study is identified. Then, all the experimental methods and equipment used in this study are presented.

The principles of the experimental techniques are also included so that readers get a better understanding of the experimental activities carried out in this study.

The main body of this thesis contains two sections:

- Deposition of Ni50Cr coatings using various surface engineering techniques such as HVOLF and HVOGF thermal spray, cold spray and laser cladding. The HVOLF and HVOGF coatings were deposited using the equipment from the Advance Material Research Group (AMRG) of the University of Nottingham. The process parameter window was developed by depositing a coating using various parameter combinations and the subsequent characterisation of the coating specimens by using X-ray diffraction (XRD), scanning electron microscopy (SEM) and energy-dispersive X-ray spectroscopy (EDX). Short time air oxidation (TGA) of thermal sprayed coatings was also conducted to investigate the air oxidation behaviour of HVOF thermal sprayed Ni50Cr coatings to select the coating with the best air oxidation performance. The two shortlisted coatings (one HVOLF coating and one HVOGF coating) with the best oxidation resistance were selected as the specimens for the subsequent longer-term air oxidation, steam oxidation and chlorine-induced fireside corrosion tests. For cold spray, the coatings were deposited at the Xi'an Jiaotong University, China, by using the university's custom-made cold spray equipment with one set of the recommended parameters. There was no optimised process parameter window for the laser cladding of the Ni50Cr powder using the setup at the University of Nottingham, and hence, the laser cladding process parameters was optimised and shown in the published work of author [49]. The process of selecting suitable laser cladding process

parameters is quite different from that of the HVOLF and the HVOGF process parameters. The thickness of the coatings, dilution, and the metallurgical quality of the beads [39] are the main criteria for deciding the optimised process parameters.

- The high temperature exposure of the deposited coatings in air, steam and simulated chlorine-containing atmosphere and the subsequent characterisation of the samples after oxidation/corrosion exposure were carried out. After depositing the four types of coatings with the recommended/optimised process parameters, we placed the specimens were placed in a high temperature box furnace, a simulated steam oxidation test rig and a simulated chlorine-induced corrosion rig that we built in the laboratory to conduct the high temperature oxidation/corrosion test. The exposed specimens in the rigs were collected at a certain time point and provided abundant information about the oxidation/corrosion performance of the deposited coatings in various atmosphere including air, steam and chlorine-containing gas at 700 °C. By comparing the differences in the high temperature oxidation/corrosion behaviour of the coatings, we determined the most suitable coating deposition technique for high temperature oxidation/corrosion applications. In addition, a thorough understanding of the mechanisms of air and steam oxidation and the chlorine-induced corrosion of Ni50Cr coatings was gained, thereby filling the knowledge gap mentioned earlier.

This thesis is divided into six chapters. Chapter 1 is the introduction, and Chapter 2 presents a review of the literature on the main subjects presented in this thesis. In Chapter 3, the methodology and, the experimental equipment materials utilised in the

study are described. Chapter 4 discusses the optimisation of the HVOF thermal spray process parameters and the subsequent shortlisting process of one HVOLF coating and one HVOGF coating with the lowest oxidation rate according to the TGA results. The results of the conducted oxidation test of select HVOLF, HVOGF coatings, cold sprayed coatings and laser cladded coatings are also presented in Chapter 4. In Chapter 5, the high temperature chlorine-induced corrosion of the four coatings is investigated and discussed in detail. Finally, the key conclusions are presented in Chapter 6. Four journal papers that were published using the results and discussion in this thesis are attached at the end of this thesis.

Chapter 2 Literature review

2.1 Introduction

This chapter addresses the high temperature air and steam oxidation as well as the chlorine-induced fireside corrosion of Ni50Cr coatings. In addition, background knowledge about the coating deposition techniques and oxidation/corrosion mechanisms of NiCr alloys/coatings is provided. Literature relating to the oxidation/corrosion of NiCr alloys/coatings is summarised to provide a comprehensive view of the current research status in this area, and thus a clear knowledge gap in this area is identified.

2.2 High temperature chlorine-induced corrosion of biomass fuel boiler materials

A typical thermal power plant boiler system includes a fuel feeding system which continuously supplies fuel (such as fossil/biomass/municipal solid waste (WTE)) to the combustion chamber in which energy stored in the fuel is released in the form of heat. The heat energy from the high temperature flame is transferred to the cold water flowing in the heat exchanger-tubes, finally producing steam at high temperature and pressure. The steam can be used to drive steam turbines to generate electricity.

Heat exchangers are just steel tubes/pipes of various sizes and geometries that transfer heat from one medium to another efficiently [58, 59]. However, the harsh service environment (high temperature and large pressure) poses a challenge to the service performance of the heat exchanger material. For instance, the temperature of the gas usually reaches 1400 °C near the furnace side in the boiler [60]. The pressure

of the steam inside the heat exchanger tube before it arrives at the turbine is around 20 MPa to provide as much energy as possible [60]. Therefore, two categories of heat-resistant steels are used as the boiler material to combat such problems: 'ferritic/martensitic' and 'austenitic' steels [60]. The ferritic and martensitic steels have the same bcc structure as Fe. A small amount of Mn, Mo, Cr, Si and N is added into the Fe–C matrix to strengthen the alloy by precipitation and improve their high temperature creep resistance. The presence of Cr also increases the high oxidation resistance of ferritic steels owing to the protection effect of the Cr_2O_3 scale. Compared with those in ferritic steels, the Cr content and the total minor alloying content in martensitic steels increases from 1–3 wt.% to 9–12 wt.% and < 5 wt.% to 10–20 wt.% respectively. Despite the fact that the high temperature and high-pressure performances of martensitic steels is better than that of the plain carbon steels, these steels cannot operate under conditions of ultra-high temperature and high pressure. Hence, martensitic steels are modified further by adding V, Nb and Ni into their matrix. Sufficient addition of Ni into the Fe–C matrix could transform the crystal structure from bcc to fcc, which is referenced as austenitic. The representatives of austenitic steels include P/T91 (P stands for pipe and T for tube), X10CrMoVNb9–1 and P/T92. Their strength, ductility and high temperature creep resistance are significantly improved when compared with those of the ferritic/martensitic steels. In the case of austenitic steels, an improvement in the properties brought about by adding a large amount of beneficial alloying elements increases production cost, which limits the application of these steels. Therefore, these steels are only used at locations inside the boiler where the temperature of the steam is above 650 °C.

Unfortunately, the composition and the microstructure of boiler steels as mentioned above are tailored to combat the high temperature corrosion and steam oxidation that occur in the traditional fossil fuelled boiler [61-65]. These boiler steels are not suitable for operating in a high temperature chlorine-containing environment.

Plant and animal substrates including wood from forests, crops, seaweed, material left over from agricultural and forestry processes, and organic industrial, human and animal wastes are all classified as biomass [66-69]. Any organic matter that is derived from plants can be referred to as biomass. Further, any biomass substrates that could be burned in the boiler and thereby release the solar energy stored in them are called biomass fuel. Zero carbon emission is the most obvious merit of using biomass fuels, as the net increase in CO_2 is zero when the biomass is burnt [66]. Yet, the burning of the biomass fuel will lead to a severe failure to these boiler materials because of the unique corrosion attack related to the chlorine and the alkali metal in the biomass fuel.

According to Liu *et al.* [64], a more severe material degradation of T91, 12Cr1MoVG and TP347H is caused by firing a high-chlorine fuel at a relatively high tube wall temperature. Pronobis *et al.* [70] proposed a method for the calculation of the material losses in the tubes of steam superheaters and clearly showed that the chlorine content in the fuel can promote the external corrosion rate. As summarised in James *et al.* [71] a large ratio of material failures in the boiler system is the direct/indirect consequence of the severe loss of steel, which is brought about by the fireside corrosion. Fuel chemistry, particularly the chlorine content in the fuel caused a large amount of severe fireside corrosion issues. The contents of the alkali metal (Na and K), Mg, and Cl are much higher in the biomass fuel than in the fossil fuel. For instance, according to Baxter *et al.* [72], the contents of K in biomass fuels fluctuates between 0.033 and 1.66

wt.% (dry fuel) and the concentrations of Cl is between 0.025 and 2 wt.% (dry fuel) in 11 various types of biomass. Furthermore, 0.2–1.9 wt.% K, 0.1–1 wt.% Cl and 0.1–0.2 wt.% S were found in Danish straw according to a dry basis analysis [7]. Although the concentration of Cl (0.04–0.2 wt.%) in coal increases with an increase in the coal seam depth, it is much lower than the content of Cl in biomass, as mentioned above [73]. Hence, the chlorine-induced corrosion in a biomass fuelled boiler is considerably more severe than that in the traditional boiler. The co-combustion of fossil and biomass fuel and/or the limiting operation temperature (usually < 500 °C) are a common measure to combat the high temperature chlorine-induced fireside corrosion of boiler steels [70]. However, the drawbacks of such a measure are evitable: 1. The low mix ratio (18–49 % according to Hansen *et al.* [8]) of the biomass in the co-combustion fuel reduces the effort of zero carbon emission. 2. The low operation temperature of the boilers results in a low heat transfer efficiency, as there is a proportional relationship between temperature and heat efficiency [74]. The deposition of protective coatings onto the boiler steel substrate is a promising approach to address the corrosion problem, as a considerable number of coatings have been applied in the oxidation/corrosion/erosion areas [26, 27, 31, 45-47, 75-79].

2.3 Properties of NiCr alloys and their applications in high temperature oxidation/corrosion field

NiCr alloys can operate under various severe conditions, such as high temperature, high pressure, corrosive atmosphere/environment and their combinations [80]. These versatile capabilities are brought about by the various excellent properties of Ni and Cr [80, 81].

Pure Ni can retain excellent toughness and ductility owing to its fcc crystal structure at high temperatures that are quite close to its melting point (around 1450 °C [82]). Therefore, Ni and nickel-based alloys are readily fabricated and manufactured into powder metallurgy products. As most of the feedstock materials required in the coating deposition industry are in a powder form, this readiness is particularly important to the application of nickel-based alloys.

A wide range of alloying elements can be used as solute atoms in the Ni matrix owing to its fcc crystal structure. Cu and Fe can form a complete solid solution with Ni and Cr has a maximum solubility of 35 wt.%. For other alloying elements, the solubility is around 20 wt.% in the W and Mo cases and it reduces to 5–10 wt.% in the Mn, Ti, Al and V cases [83]. A further addition of alloying elements that exceeds the solubility limit can form dispersoid as well precipitate particles, which strengthens the alloys on the basis of the solid solution strengthening. Ni exhibits good corrosion performance in various environment such as air, natural freshwaters, mono-oxidising acids, and caustic alkalis [83]. Therefore, Ni offers the considerably useful corrosion resistance when acting as a matrix of the alloys. Large soluble Cr in the NiCr alloys can form a dense and thick chromia scale at the surface of the fresh metal in various atmospheres at high temperature [20], which is the basis of the high temperature oxidation/corrosion application of NiCr alloys.

The merits of NiCr alloys mentioned above promotes its wide application in the field of high temperature oxidation/corrosion [14, 20, 79, 83, 84]. It is necessary to discuss the NiCr binary phase before discussing the deposition and oxidation/corrosion performance of NiCr alloys/coatings. The NiCr binary phase diagram is a simple

eutectic system as shown in Fig. 2.1. The eutectic point for NiCr alloys is located at 53 wt.% Cr at 1345 °C. At lower temperatures, the solubility of Ni in Cr is subject to a large limitation, while solubility of Cr in Ni is not restricted (up to 20 wt.%). A Ni20Cr phase in the orthorhombic structure occurs when the temperature is lower than 580 °C. The nickel-rich single-phase region (γ–Ni) extends up to approximately 37 wt.% Cr. To decrease the melting temperature and increase the solidification temperature range of the Ni–Cr system, minor elements such as B are added into the NiCr solid solution, forming hard Ni_3B phases and decreasing the minimum heat input required for the fusion of the substrate [84].

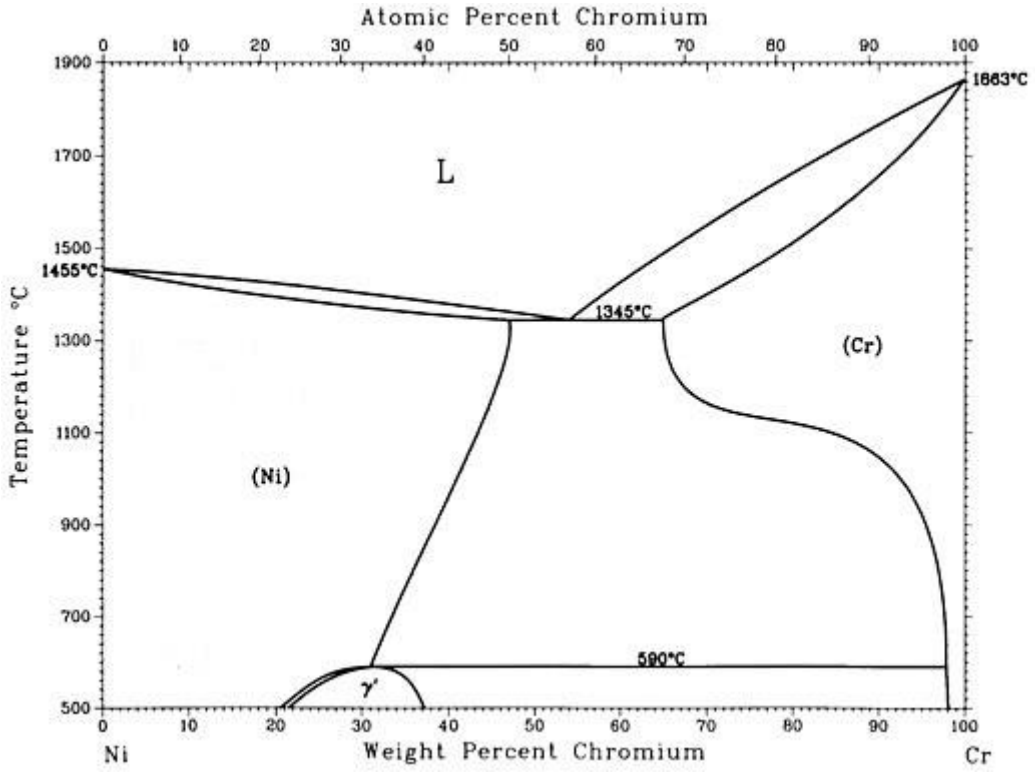

Fig. 2.1 Binary phase diagram of Ni-Cr system [82].

2.4 Surface engineering

Surface engineering is a subject that engages the design and the modification of the surface of the substrate (bulk material) to ensure the desired surface properties such as bio-inertness, oxidation/corrosion resistance, electronic properties, friction coefficients and thermal insulation. The surface modification can be obtained by adding a material having the desired properties to the surface with an energy source to build a coating having the required phase, microstructure and properties. For instance, the high velocity oxygen–fuel (HVOF) thermal spray process and the cold spray process can be used to deposit the desired surface layers through the mechanical interlocking effect among several powder particles and between the powder particles and the substrate [36]. A combination of the surface layer and the substrate is established through the metallurgical bonding effect in the laser cladding process [38, 39].

2.4.1 HVOF thermal spray process

In the HVOF thermal spray process, the energy source is the combustion flame of the fuel mixture; it transfers enough energy to the powder particles, leading to the particles heating up, accelerating and deforming upon striking the substrate. The denser microstructure and the higher bonding strength with the substrate are the obvious advantages of the HVOF thermal sprayed coatings over the other coatings. These benefits can be attributed to the high kinetic energy stored in the ejected powder particles during flight when these particles strike at the substrate [85, 86]. Moreover, the relatively low flame temperature does not cause the powder particles to oxidise

too much and/or decompose during flight, finally attaining the original properties of the powder particles to the maximum degree.

High velocity gas acts as the kinetic energy transfer medium in the HVOF thermal spray process. It is obtained through the following process: A large quantity of the mixture of fuel (in the gas/liquid form) and oxygen is injected into a chamber in small size under high pressure. Then, the mixture is ignited and thus combusts intensively in the chamber of considerably restricted size. The hot burning gas at high temperature and under high pressure expands instantly and injects from the outlet nozzle. The nozzle having a specially designed geometry can accelerate the hot gas to the rate of 1800 m s^{-1} [87]. The powder is injected into the hot gas jet using a carrier gas by two methods, i.e. either directly into the combustion chamber or downstream in the nozzle with an inert carrier gas. The powder particles are heated and accelerated by the rapidly expanding gases along the nozzle and ejected from the gun as a stream of molten or softened particles. When they hit the substrate, the high kinetic energy of the particles produces a strong bond with the substrate or the previously coated layer.

The HVOF thermal spray mainly uses two types of fuels: liquid (such as kerosene) and gas (such as hydrogen, methane, propane, propylene and natural gas) [36]. The liquid fuelled HVOF (HVOLF) thermal spray can achieve a relatively large spray rate and thus a high deposition efficiency because of the more homogeneous distribution of the sprayed particles during the HVOLF process [30, 36, 88-90]. Moreover, the in-flight oxidation of the powder particles varies in the HVOF thermal spray processes using different fuels, as the flame in the gas fuelled HVOF (HVOGF) gun is hotter than that in the HVOLF gun.

As shown in Fig. 2.2, the lamellar and heterogeneous microstructures are the most obvious feature of the cross-section of the HVOF thermal sprayed coatings [91]. According to Sharma *et al.* [91], a typical coating structure usually consists of lamellae (formed by splats) separated by interlayer pores, cracks and/or a second phase (usually an interlayer oxide in metallic coatings). Other micro- and nano- structural characteristics such as segregated oxide within the splats (intra-layer oxide precipitates), intra-splat cracks and regions of true contacts (where two splats are connected to each other via a metallurgical junction) are also distributed throughout the coating.

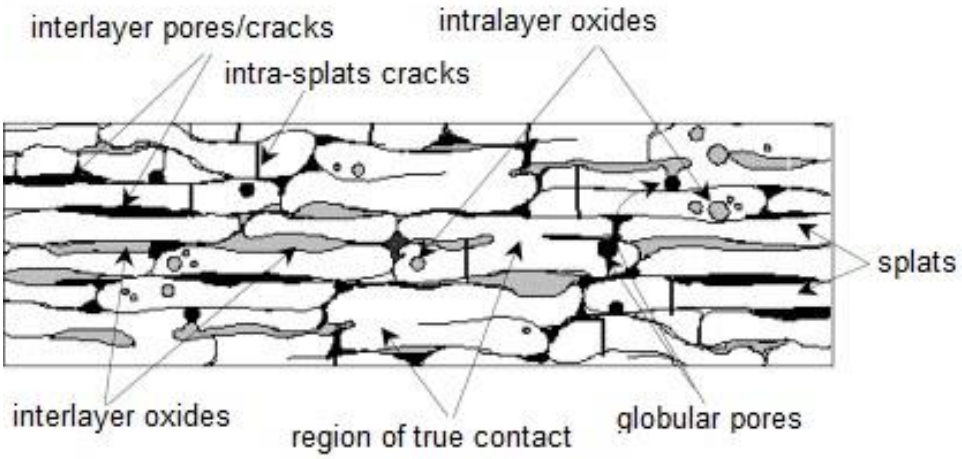

Fig. 2.2 Schematic representation of the microstructural features associated with typical HVOF spray coatings according to Sharma *et al.* [91].

Several factors such as the particle's (or splat's) states during and after spray, its physical properties and its interactions with the surroundings may bring about the chemical and/or microstructural inhomogeneity to the lamellae. The interactions with the surroundings mainly include the following: The phases present in the particles can be oxidised by the atmospheric oxygen in several microseconds. The minor phases

begin to dissolve into the molten or partially molten powder particles. The molten region of the powder particles resolidifies at high cooling rates when these particles hit the substrate. Therefore, the formation of the HVOF thermal sprayed coating microstructure is complicated and depends strongly on precise process conditions.

According to Brandt's classification [92], the HVOF process parameters include the primary and the secondary ones. The Composition, morphology, size and feed rate of the feedstock powder; composition and flow rate of the fuel; the oxygen–fuel gas ratio, composition, flow rate and pressure of the carrier gas; and the gun design such as nozzle type and dimensions are the primary factors. The secondary category contains the standing-off distance, rotational speed of the fixture, gun movement speed and the parameters related to the substrate, such as material type, geometry, grit blasting or preheating prior to spray and cooling during spray. The factors mentioned above in combination, can influence the physical and chemical structure and thus, various properties (e.g. bond strength, porosity and corrosion resistance).

2.4.2 Cold spray process

In the cold spray process, the powder transport and injection method are like that in the HVOF thermal spray process. The hot, pressurised gas (up to 30 bar) [93] can be accelerated to supersonic velocity in the axial (thrust) direction after passing through a de Laval-type nozzle, which can convert the heat energy of the mass flow to kinetic energy [94-96]. The de Laval-type nozzle is often referred to as the convergent-divergent nozzle (CD nozzle), as it is designed to have such geometry. The feedstock powder is fed into the gas stream at the inlet of the nozzle such that it can be carried by the accelerating gas in the CD nozzle and ejected to the coated substrate.

As summarised by Moridi *et al.* [97] and shown in Fig. 2.3, the cross-section structure of the cold sprayed coatings is considerably similar to that of the HVOF thermal sprayed coatings except that there are almost no interlayer and intra-layer oxides, as the gas temperature is not sufficiently high to induce the oxidation of the powder particles during the flight of the powder from the nozzle to the coated substrate. However, the porosity and the cracks of the as-sprayed coatings are very clearly as shown in Fig. 2.3 a, b and c, which indicates that the powder particles are not in the partially plastic state upon impact with the substrate or the previously coated particles. However, with a deposition material of suitable hardness and optimised parameters, cold sprayed coatings having a dense and crack-free microstructure can still be manufactured.

During the cold spray process, the particles undergo adequate deformation so that the mechanical interlocking among various particles can occur, which guarantees the connection of the coating and the substrate. This behaviour requires that the velocity of the powder particles be above a certain value so that the kinetic energy of the particles is sufficiently high to bring about deformation as a result of the impact between the particles and the substrate [33, 98].

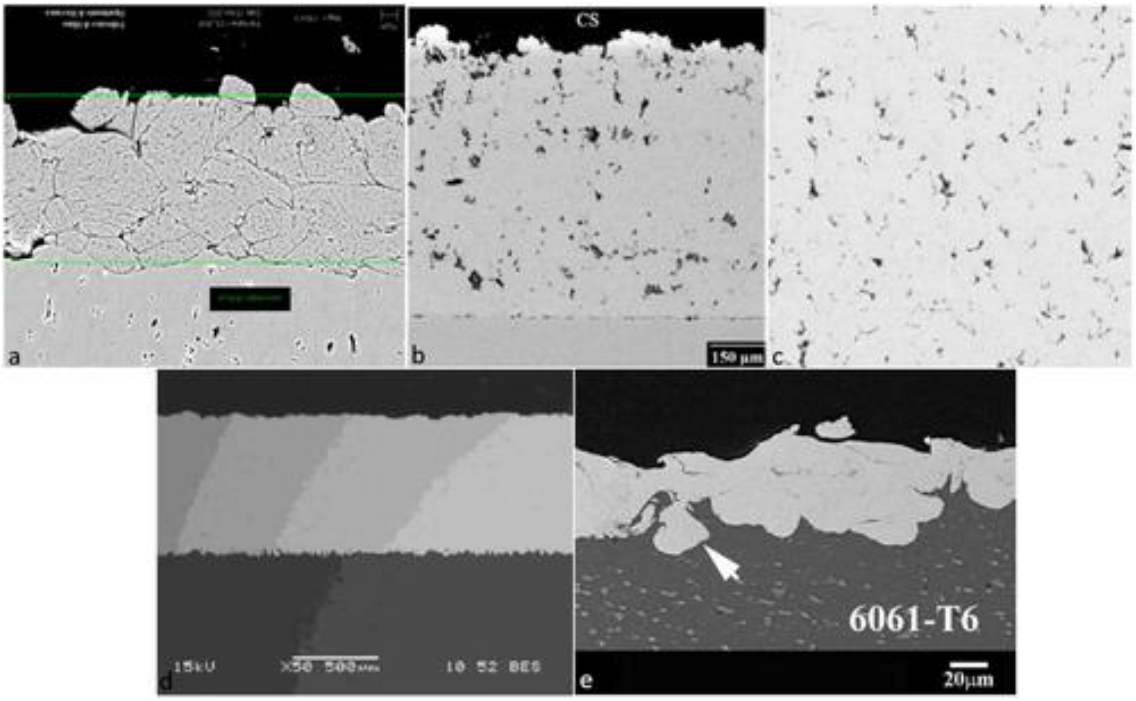

Fig. 2.3 Various metallic cold sprayed coating cross-sections summarised by Modiri *et al.* showing the typical microstructure of cold sprayed coatings: (a) Al 6082 on Al 6082; (b) Ti on Ti6Al4V, (c) Inconel 718 on Al alloy, (d) Ta on Al, (e) Ni on Al alloy [97].

The minimum velocity required for this is called the critical velocity and is determined by each individual powder material [33, 99]. The main parameter in the cold spray process can affect the velocity of the particles including the type of powder carrier gas, carrier gas pressure and temperature. The Influences of the type of gas and the gas temperature on the gas velocity can be described as follows [33, 98], and there is a positive relationship between the gas velocity and the particle velocity:

$$a = \sqrt{(\gamma RT/M_w)} \qquad \text{Eq. 2.1}$$

Where a is the gas speed, γ is the specific heat ratios, R represents the gas constant, Tdenotes the temperature and M_w is the molecular weight of the gas. Helium (He) has a smaller molecular weight (4) than nitrogen (N_2) (28), and the gas velocity increases

accordingly. Usually, N_2 is preferentially selected, as it can be used to spray most of the materials suitable for the cold spray process without any significant oxidation and is very cost-effective. The use of a mixture of N_2–He and pure He is only considered when the feedstock material needs greater critical velocity to deposit on the surface of the substrate because of the high cost of He.

Van Steenkiste *et al.* [100] identified the effect of gas pressure on the gas velocity. The air velocity does not increase with an increase in gas pressure, as the pressure of the gas in the downstream of the CD nozzle is 52.8 % of that in the upstream. The throat of the CD nozzle is choked under this condition and thus, isolates the beneficial effect of pressure on the gas velocity.

Before entering the CD nozzle, the powder carrier gas is usually heated up to 650 °C [98] to heat the powder particles. Then, the greater the heat energy stored in the gas, as well as powder, the more it can be converted into kinetic energy in the CD nozzle. Obviously, 650 °C is considerably lower than 2000–3000 °C that usually appears in the HVOF thermal spray [101]. Therefore, the drawbacks of the HVOF thermal spray process connected to the large heat input including oxidation and undesired phase changes during the spray process can be eliminated or minimised in the cold sprayed coating.

2.4.3 Laser cladding process

Laser is an acronym for ‘Light Amplification by Stimulated Emission of Radiation’ and has been widely accepted after it was first proposed by Schawlow and Townes [102] in 1958 and officially published by Gordon Gould in 1959 [103]. As its name suggests,

laser can be produced through the stimulated emission phenomenon [104]. Once an atom is excited from its ground state to a higher energy level, it becomes relatively unstable and always spontaneously returns to its ground state by losing originally absorbed energy. The energy is released chaotically in the form of photon and dissipates in nature. In contrast, in the case of laser, the release of photons from the energised atoms is controlled (amplification process), and thus a light beam (photon beam) of high energy is generated.

Ideally, if a metal is irradiated with a short pulse of ultraviolet light, its interaction with the electromagnetic waves can result in high-frequency conductivity and the skin-effect [105]. The free movable charge carriers of the metals are shifted in the electromagnetic field. The generated displacement current leads to heating according to the Joule effect [43, 106]. If the exposure time is sufficiently long, this will cause heating, melting and evaporation. A further increase in the field strength causes the field emission of electrons and finally results in plasma formation. With the heat produced by the Joule effect, rapid melting and solidification with the additive material of the substrate can be performed; this is called laser cladding. The treated area on the surface is heated by the absorption of the energy delivered by the laser beam. The heat input due to a high-power density laser beam is well confined and extremely intense, which leads to the large heating rate in the surface layer. After the passing of the laser beam, the diffusion of heat to the cold bulk and the atmosphere is so rapid that the self-quenched phenomenon occurs spontaneously. This thermal cycle continues unremittingly during a laser process as that in welding [107], finally leading to the following beneficial results: refined grain and the, formation of metastable phases and/or altered microstructures [108]. No information about the microstructure

of laser cladded Ni50Cr layer has been provided in the existing literature. Instead, the altered and fine microstructure of two-stage laser cladded Ni75Cr coating on grey cast iron is shown in Fig. 2.4 according to Zhong *et al*. [109]. The pre-eutectic austenite (smoother and darker features shown in Fig. 2.4 (a) and (b)) phase is surrounded by the ledeburties (white and pattern features shown in Fig. 2.4 (a) and (b)) phase, building a fine hypoeutectic metastable structure. This is attributed to the restraining of the normal γ phase to the M phase transformation in the cast iron during solidification due to the solid solution of the high Ni content in the austenites by alloying. The microstructure of the interface between the coating and the substrate shows a satisfactory microstructural transition and a strong metallurgical bond, which indicates the advantage of the laser cladding process over the thermal spray process.

In the laser cladding process, a wide variety of materials can be deposited on a substrate to form a layer with the thickness ranging from 5 μm to 2000 μm and the width as narrow as 400 μm [38, 39]. A large number of operating parameters and physical phenomena determine the quality of the laser cladded coatings. In general, the inputs of the operating parameters are the laser, motion device, powder feeder set points, and the material and ambient properties. The designed combination of these input parameters can finally obtain a satisfactory output, i.e. the required geometry of the clad bead, fine cast microstructure, minimal crack porosity and residual stresses and dilution.

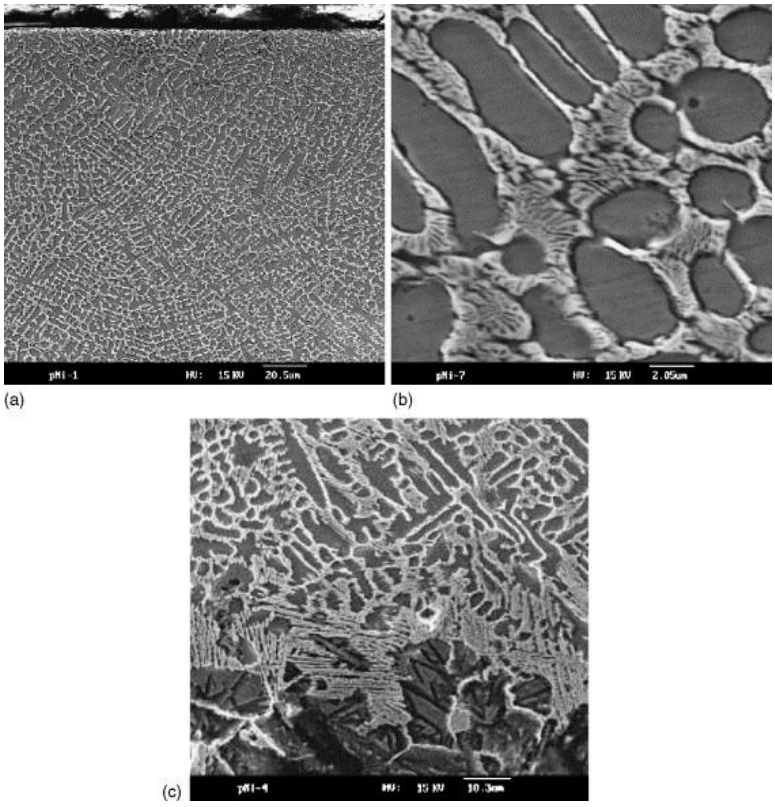

Fig. 2.4 Microstructure of the two-stage laser cladded Ni57Cr layer that is deposited by Zhong *et al*. [109]: (a) alloying zone; (b) image of (a) at higher magnification); and (c) interface between alloying zone and substrate.

2.5 High temperature oxidation of NiCr alloys and coatings

2.5.1 Basic high temperature oxidation process

When a material operates at high temperature it can be oxidised by the surrounding atmosphere and form an oxide layer at the surface. This reaction is called high temperature oxidation [14, 20, 22, 110] and is illustrated by Reaction 2.1. The atmosphere is not strictly restricted to air/oxygen. Any gases containing components with a low oxidising potential, such as CO_2, SO_2 and NO_2 can act as oxidants even in very small amounts at high temperature. Corrosion is a term used when complex atmosphere/deposits such as HCl, Cl_2 and Na_2SO_4. appear in the system. Essentially,

this can be considered oxidation behaviour, as the metal loses electrons and form compounds.

$$M(s) + O_2(g) \rightarrow MO_2(s) \qquad \text{Reaction 2.1}$$

An oxidation process is usually divided into two basic stages: the initial rapid oxidation stage and the subsequent slower stage, as the developed oxide scale at the fresh metal surface can limit the contact opportunity of the oxidising atmosphere with the metal [14, 20, 22, 110].

The initial period of oxidation starts can be divided into four sub-stages according to Fromhold *et al.* [23]: 1. collision of O_2 with the clean metal surface; 2. physical adsorption [111] between O_2 and the metal surface; 3. Formation of a strong chemical bond between oxygen and the metal atom and 4. Formation of a thin chemisorbed oxide layer at the metal surface. In the literature, the oxidation kinetic of the initial stage is believed to be considerably rapid and follows the linear rate dependency and the logarithmic rate dependency [14, 20, 22, 23].

The second stage oxidation is considerably longer than the initial oxidation stage at the considered time scale. Either the metal ions from the clean metal under the oxide layer formed in the initial stage or the oxygen ions from the oxidising atmosphere must be transported in the opposite direction to maintain the continuous growth of the thicker oxide scale at this stage [14, 20, 22, 23, 110]. The major factor that controls the migration of the ions involved is their diffusion through the bulk lattice; the diffusion rate may be the key factor controlling the oxidation kinetics. Wagner's theory [112-114] can be used to describe the second stage oxidation: the activity gradients of metals and oxygen are established across the oxide scale because of the equilibrium at both

the interfaces (gas/oxide and oxide/metal). Therefore, it drives the counter-diffusion of the metal and oxygen ions throughout the scales (metal to gas/oxide interface and oxygen to oxide/metal interface). An electric field across the oxide scale is established when the metal ions are charged. However, the net migration of ions, electrons and electron holes is balanced to maintain the electro-neutrality condition. The oxidation kinetics in the second stage is determined by the diffusion rate of the ions, electron and electron holes and anions passing through the oxide scale. This diffusion rate shows the parabolic rate dependence [112]. Therefore, the oxidation behaviour in the second stage also follows the parabolic law [115]: i.e. the oxidation rate decreases with the increase in the scale thickness.

A practical high temperature oxidation of metals/alloys is usually not as simple as discussed above [14, 20, 22, 110]. For example, the oxidising atmosphere may not contain only one reactive component and alloys containing at least two components that may be involved in the oxidation process. In addition, the presence of various liquid and/or solid deposits may further increase the complexity of the oxidation process further [9]. Therefore, thermodynamic calculations are an essential tool to identify the possible reactions between the substrate and the oxidising atmosphere, predict potential oxidation products, and thus simplify the investigation and discussion of the practical oxidation process [20, 22].

The Ellingham diagram [116, 117] as shown in Fig. 2.5 is a Standard Gibbs' free energy of formation versus temperature diagram and is usually applied when determining the possible products of a reaction under the given conditions. By comparing the standard Gibbs' free energy (ordinate values) for various oxidation

reactions at the same temperature (horizontal ordinate value), the reaction indicated by the lower line will occur initially.

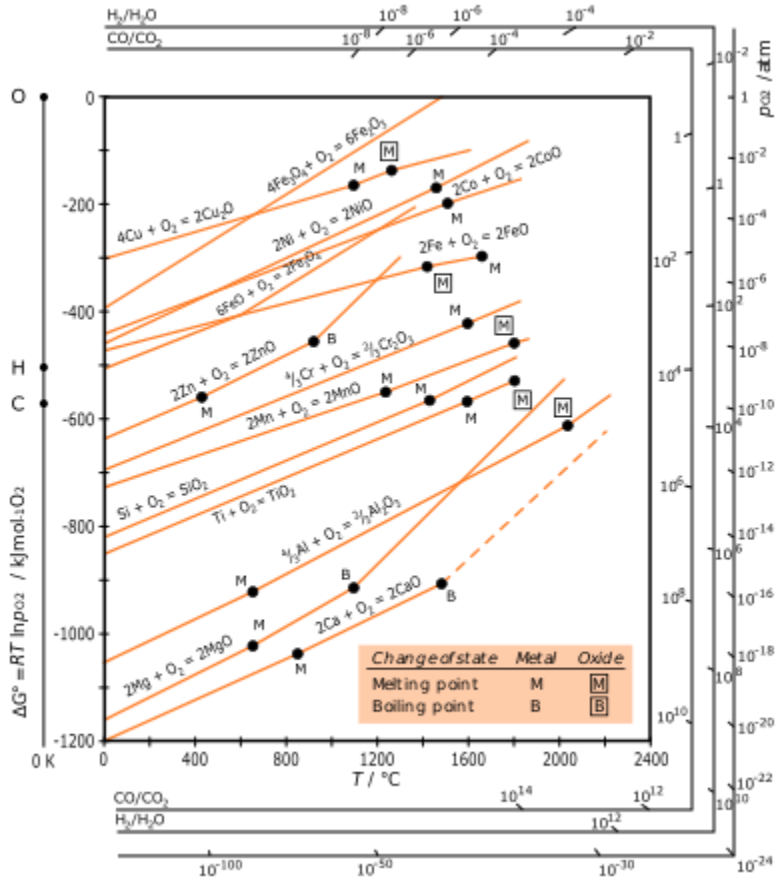

Fig. 2.5 Ellingham diagram showing the free energy of formation of metal oxides and the corresponding oxygen partial pressure at equilibrium [118].

2.5.2 High temperature oxidation of NiCr alloys and coatings

The information provided in Section 2.5.1 is only concerned about the oxidation process of a single metal component. The oxidation of alloys such as NiCr is more complex and will be presented in this section.

There are two types of oxidation reactions of NiCr alloys: transient oxidation and selective oxidation. The type of oxidation that occurs depends on the Cr content in the

NiCr alloys. The transient oxidation process [20, 119-121] is applied to the alloys whose Cr content does not exceed a critical value (around 30 wt.%).

Both Ni and Cr in the NiCr alloys can react with O to produce oxides such as NiO and Cr_2O_3 by following Reaction 2.2 and Reaction 2.3 respectively. However, according to the Ellingham diagram given in Fig. 2.7, the reaction line of Cr and O is considerably lower than that representing Ni and O at all temperatures. Therefore, it is concluded that Cr_2O_3 is more stable than NiO at high temperature, or Cr is preferentially oxidised by O when compared with Ni according to the minimum Gibbs' free energy criterion.

$$Ni(s) + 1/2\ O_2(g) \rightarrow NiO(s) \qquad \text{Reaction 2.2}$$

$$Cr(s) + 3/2\ O_2(g) \rightarrow 1/2\ Cr_2O_3(s) \qquad \text{Reaction 2.3}$$

Fig. 2.6 illustrates the transient oxidation process of a dilute NiCr alloy. Oxygen diffuses into the clean metal surface to oxidise the Ni and Cr and form oxides under the original metal surface respectively. Meanwhile, Ni in alloys near the original metal surface diffuses outwards (from the metal to the atmosphere) and comes into contact with O, as Ni is the major matrix of alloy, forming the NiO layer on the original metal surface. In this stage, the nickel-containing oxides grow much more rapidly than Cr_2O_3, and a significant amount of NiO and $NiCr_2O_4$ forms before the development of a continuous Cr_2O_3 layer [14, 20, 110]. Among them $Ni_2Cr_2O_4$ is the reaction product of NiO and Cr_2O_3 as shown in Reaction 2.4.

$$Cr_2O_3(s) + NiO(s) \rightarrow NiCr_2O_4(s) \qquad \text{Reaction 2.4}$$

Therefore, a triple-layered oxide scale can form at the surface of the oxidised dilute NiCr alloys (Cr < 30 wt.%) as shown in Fig. 2.6. The outermost layer is the NiO layer,

and it grows on the original metal surface. The middle layer is a mixture of NiO and $NiCr_2O_4$. The innermost layer is chromia and Ni as the alloy matrix.

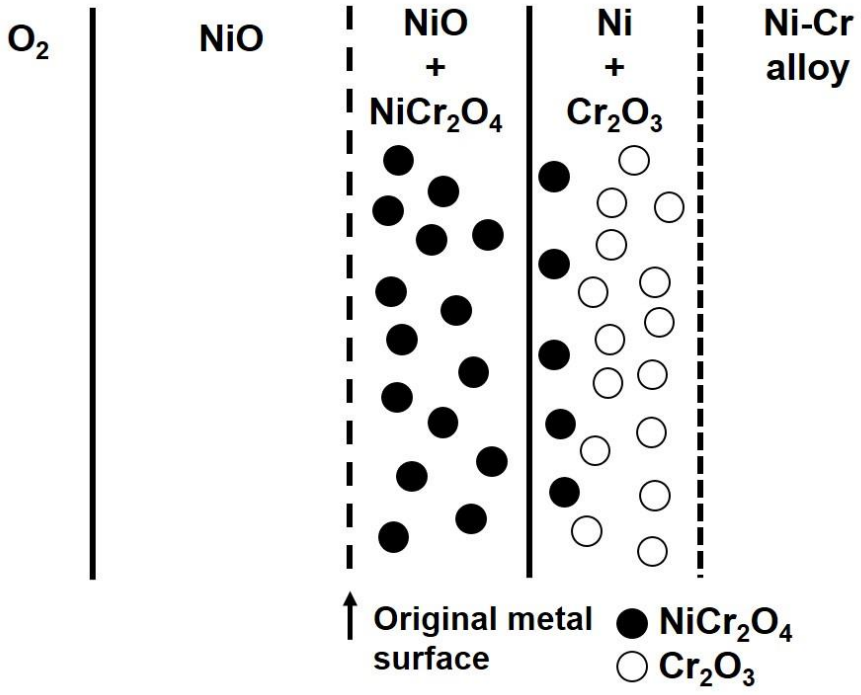

Fig. 2.6 Schematic representation of the oxide scale of dilute NiCr alloys [20].

When the Cr content increases to 30 wt.%, the solute Cr is oxidised preferentially to the parent Ni as mentioned above and forms a slowly growing, dense and protective chromia scale, which suppresses the formation of NiO. This process is called the selective oxidation of Cr in NiCr alloys and it is the basis for the oxidation protection of all the NiCr alloys and coatings used at high temperature.

In general, Cr_2O_3 scale is robust and stable when facing the mild oxidising atmosphere such air and CO_2; it will not fail for a considerably long-term. However, its destiny, in severe oxidising environment such as with the presence of steam and chlorine-containing species, is not satisfactory and will be discussed in following sections.

A significant body of literature exists on the air oxidation of NiCr bulk alloys [54, 122-127]. Ul-Hamid *et al.* [122, 123] performed a detail TEM study on the air oxidation of three dilute NiCr alloys (Ni10Cr, Ni20Cr and Ni30Cr) at 750 °C and 1000 °C for 100 h. They confirmed that the lowest critical value of the Cr content for the generation of α-Cr_2O_3 protective scale is 30 wt.% by investigating the microstructure and the composition of the oxide scale developed on various dilute NiCr alloys using TEM. A multi-layered oxide scale formed on the surface of the NiCr alloys as shown in Fig. 2.7 according to their investigation.

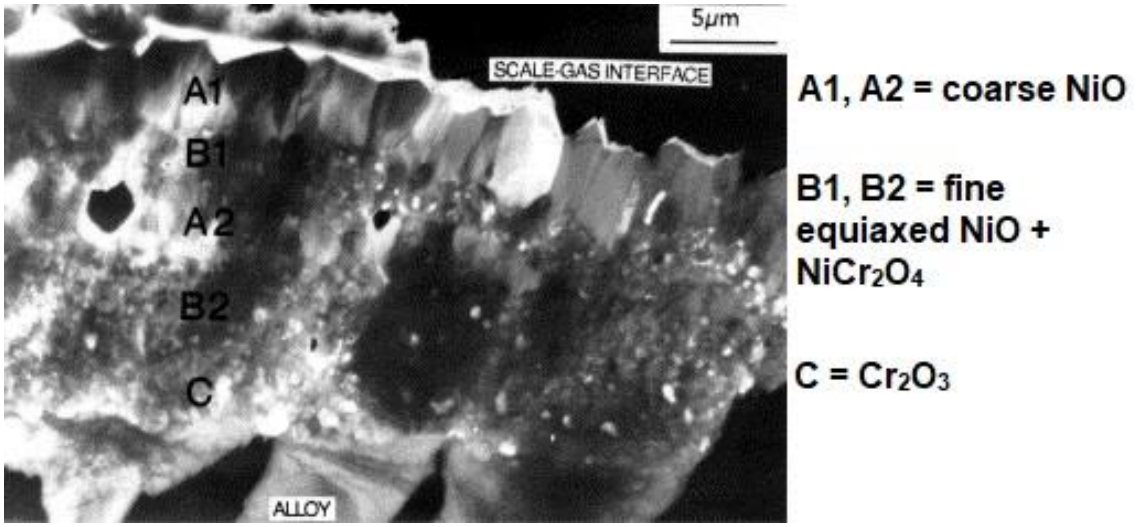

Fig. 2.7 TEM image of oxide scale developed at the surface of dilute NiCr alloys by Ul-Hamid *et al*. [123], showing the triple-layered structure of oxide scale.

The outermost NiO layer and the inner NiO+$NiCr_2O_4$ layer shown in Fig. 2.6 are clearly visible in Fig. 2.7. A1 and A2 were relatively coarse NiO, while B1 and B2 were mixed oxide layers consisting of fine equiaxed NiO and $NiCr_2O_4$. The innermost layer C was Cr_2O_3. Moreover, the composition of the oxide scale was not determined by the exposure temperature, as the oxide scale samples obtained at 750 °C and 1000 °C were compared. Finally, Ul-Hamid also provided the top surface morphology of single

and double layer oxides, which is quite useful when identifying the type of oxides generated at the metal surface.

Calvarin *et al.* [128] also used TEM to study the air oxidation behaviour of the Ni20Cr alloy. However, the sample was manufactured as 100 µm thick and 200 µm thick foils. The exposure time considered was similar to that considered in the study of Ul-Hamid [122, 123]. Calvarin *et al.* [128] found that the exposure temperature affects the composition of the oxides. The temperature determines the composition of the oxide scale by controlling the time required for the lateral extension of the Cr_2O_3 islands along the metal surface. Rhines *et al.* [126] investigated the oxide microstructure and the growth stresses in the NiO scale at 1000 °C. A layer of NiO elongated crystals developed at the surface of the fresh hot-worked Ni bar because of the generation of the stresses parallel to the oxide/metal interface. Moreover, the top faceted morphology of NiO was also confirmed by them. Stott [125] provided a good summary of the information about the establishment of the Cr_2O_3 scale discussed in previous publications. The thickness of chromia may reduce at quite high temperature (1000 °C) after long-term exposure. An oxidising gas with a large flow rate further promotes this trend. The reason behind this phenomenon is the continuous volatilisation of CrO_3 at high temperature, which is the oxidation product of Cr_2O_3 at a large oxygen partial pressure. Stott [125] also indicated that Cr_2O_3 is usually generated at the oxide/gas interface following the outward diffusion of Cr^{3+}. A wide range of the oxidation kinetics of chromium was reported by Hindam *et al.* [127]; several factors contributed this large diversity, such as the formation of the volatile oxide (CrO_3), the different preparation and exposure methods used in each study, and the short-circuit paths.

In summary, most of the literature concerning NiCr alloys describes the oxidation of bulk alloys rather than the coatings. Information about the oxidation performance of NiCr bulk alloys is abundant [23, 121, 129-133], while little information is available on the NiCr coatings. Therefore, it is necessary to investigate the air oxidation behaviour of the coatings deposited in this study. With the investigation result, knowledge about the oxidation of NiCr coatings could be enriched; it can also serve as the basis of an investigation of the oxidation/corrosion of NiCr coatings in other atmospheres.

2.5.3 High temperature steam oxidation of NiCr alloys and coatings

Unlike the mechanisms of air oxidation of NiCr alloys, the oxidation behaviour of alloys containing Cr in the presence of steam is still not been fully understood [54]. Researchers have proposed several mechanisms to explain the oxidation behaviour of chromia forming alloys.

The oxidation of chromium-containing alloys in the presence of steam follows the same reaction principle as the air oxidation process discussed in Section 2.5.2 except that the dissociation of H_2O at high temperature serves as the source of O^{2-}. However, it has been commonly recognised by researchers [54, 131, 132, 134-138] that the steam oxidation of an alloy is usually accelerated when compared with the case in the presence of air. Several previous studies contributed to the explanation of this acceleration effect. For instance, Ikeda *et al.* [135] confirmed that in the presence of micro-cracks and pores, oxygen and water vapour can pass through them and immediately arrive at the metal surface to participate in the oxidation process after investigating the gas penetration rate under wet and dry conditions. Steam could in turn increases the frequency of scale cracking and prevent the healing of the scale in

this transport process. This mutual assistance behaviour between the transport of the steam and the scale cracking contributes to the increased oxidation rate of alloys under the wet condition. This finding is very useful when evaluating and discussing the steam oxidation performance of coatings deposited in this study, as there are usually more porosities and cracks inside the sprayed coatings than inside the forged alloys.

The calculation results reported by Honda *et al*. [136] indicated that oxygen could be supplied via steam faster than under a dry condition. Another possible mechanism accounting for the rapid steam oxidation behaviour was proposed by Armanet *et al.* [83]. The evaporation of the volatile Cr species (mainly $CrO_2(OH)_2$) primarily along the grain boundaries brings about the scale cracking and spallation of the oxide scales in the presence of steam. They exposed a selection of alloys to pure oxygen, air and wet air. The oxidation products of Ni20Cr in both dry and wet air included NiO, Cr_2O_3 and their spinel ($NiCr_2O_4$). When there was no steam, the NiO phase gradually disappeared with time, as it combined with Cr_2O_3 to produce the spinel as discussed in the previous section. However, the NiO phase survived under the wet condition. Moreover, significant cracking and spallation of oxide scale occurred during the wet exposure. The following mechanism could explain these phenomena: chromium-rich compounds such as CrO_3 and $CrO_2(OH)_2$ volatilise easily at high temperature and exert an over-pressure to the oxide scale, finally leading to the rupture of the oxide layer. Considering that the Cr_2O_3 layer is continuous at the alloy/oxide interface, the rupture of oxide layer causes the breakdown of the NiO and $NiCr_2O_4$ layers initially. The Cr_2O_3 layer then comes into contact with the atmosphere after the spalling of oxide containing Ni and would volatilise as CrO_3 and $Cr_2O_2(OH)_2$. The depletion of Cr in the alloy leads to the production of a new layer of NiO. Meanwhile, the $NiCr_2O_4$ spinel

develops. This process can be described simply by using the following equations (Reaction 2.5, Reaction 2.6 and Reaction 2.7) and continued in such a manner that the steady oxidation state observed during the dry oxidation is not retained.

$$Cr_2O_3(s) + 3/2\,O_2(g) \rightarrow 2CrO_3(g) \quad \text{Reaction 2.5}$$

$$Cr_2O_3(s) + 1/2O_2(g) + 2H_2O(g) \rightarrow 2CrO_2OH_2(g) \quad \text{Reaction 2.6}$$

$$CrO_3(s) + 2H^+ \rightarrow CrO_2OH_2(g) \quad \text{Reaction 2.7}$$

The H^+ ion that are the dissociation product of water can dissolve as protons in the alloys. The point defects within the oxide scale such as vacancies, substitutional sites and interstitial sites may be altered due to the introduction of the additional protons. The diffusion rate may be enhanced accordingly. This is another possible explanation for the accelerating oxidation process in steam.

Saunders *et al.* [137, 139] summarised the practical oxidation behaviour of NiCr alloys reported in previous publications under wet conditions. Furthermore, 50% and 100% steam tests of the Nimonic 75 alloy (Ni80Cr with minor Ti and C) for 25 h were conducted by Rahmel *et al*. [138]; they found that the steam oxidation behaviour of this alloy did not differ with that under 50% O_2 + 50% CO_2 condition. Similar results were obtained by Wood *et al.* [132], but they changed the wet condition to 10% H_2O + 90% Ar. England and Virkar compared the dry and wet oxidation behaviours of a series of thin foil nickel-based alloys at 700–1000 °C [140]. The relationship between the rate of steam oxidation and the rate of air oxidation is not consistent with the expected value when the temperature changes, as with the increase in temperature, the evaporation of volatile Cr species becomes more intense and the oxidation rate increases. The oxidation rate was increased in steam at 800 °C by factors of 8 and 30

and decreased in steam at 1100 °C by a factor ranging between 1.5 and 13 as compared to that in air. The authors attributed this behaviour to the microstructure of the oxide scale developed at the metal surface. The oxide scale developed at 1100 °C was thicker than that developed at 800 °C in steam. Hussain *et al.* [141] reported that a protective scale at the surface of Hastelloy C-4 in 100% steam at all temperatures (600–1200 °C), while the scale formed in air ruptured. They also believed that oxides containing Ni are not affected by steam. Holcomb *et al.* [142] investigated the effect of adding minor elements on the steam oxidation of NiCr alloys. When 0.01 wt.% Y was added to the NiCr alloy, no evaporation of the Cr species as $CrO_2(OH)_2$ was observed even when the sample was oxidised in air + 5% H_2O at 950 °C for 4000 h. The additions up to 3 wt.% Mn did not prevent the spalling of the scaling because of the evaporation of Cr species in same alloy.

As shown in Fig. 2.8 that was obtained by Aguero *et al.* [143], the thickness of the oxide scale increases at the surface of Ni20Cr HVOF thermal sprayed coating and was around 3 μm even after 20,000 h in steam; no coating degradation or substrate attack was observed, showing the protective effect of the HVOF thermal sprayed Ni20Cr coating. The authors indicated that since there was no obvious chromium-depletion area within the coating under the oxide scale, the evaporation of volatile $Cr_2O_2(OH)_2$ was marginal.

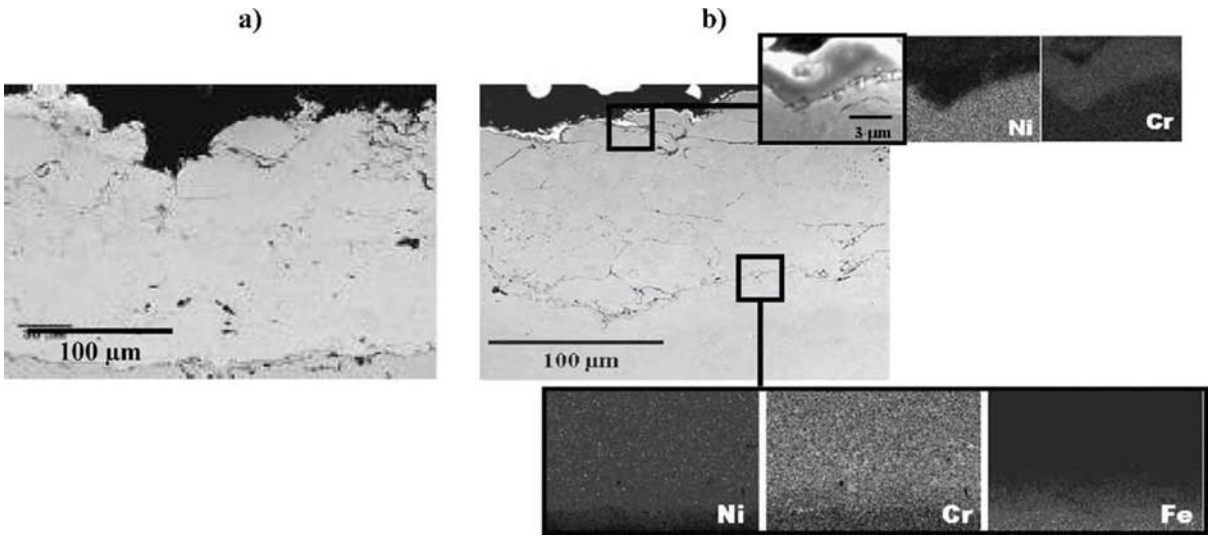

Fig. 2.8 FESEM image of the cross-section of as-sprayed Ni20Cr HVOF coating (a) and coating after 20,000 h steam exposure at 650 °C (b) by Aguero *et al*. [143].

Limited information is available on the steam oxidation behaviour of NiCr coatings [143-145], as most of the NiCr-based coatings in the steam application area are deposited on the surface of the key components such as steam turbine blades, pistons and valves for wear resistance. Sundararajan *et al.* investigated [144, 145] the steam oxidation resistance of the HVOF thermal sprayed Ni20Cr and Ni50Cr coatings at 600–750 °C. They found that the HVOF coatings can protect the substrate for up to 1000 h at 650 °C. The major indicator that they used to evaluate the oxidation degree was the initiation of scale at the metal/coating interface. The composition of this scale was mainly Cr_2O_3, as Ni diffused from the coating into the substrate. A thin Cr_2O_3 scale also developed at the surface of the coatings. This scale increased in thickness when the Cr content of the coatings increased.

According to the above discussion, researchers did not reach an agreement about the mechanisms of the steam oxidation of NiCr alloys. Each mechanism could explain the

experimental phenomena in an individual study but may not be applied to all the previous studies. Therefore, care is needed in the evaluation and discussion of the steam oxidation performance of the coatings deposited in this study. Moreover, the difference between the sprayed and the cladded coatings and the forged bulk alloys should be taken into consideration.

2.6 High temperature chlorine-induced corrosion of NiCr-based alloys and coatings

2.6.1 Basic high temperature chlorine-induced corrosion process

When metals such as boiler steels and NiCr alloys are exposed to an oxidising environment at high temperature, the material will gradually oxidise to the thermodynamically stable oxides (Cr_2O_3) and form an oxide scale adjacent to the metal. This Cr_2O_3 scale is thick and dense and can thus provide a barrier for the further diffusion of the oxidant [146, 147]. Therefore, the oxide growth rate reduces with an increase in the thickness of the oxide scale. However, chlorine generated by the burning of the biomass fuel with a high chlorine content can diffuse through the oxide scales (presumably through pores and cracks as they are the short-circuit paths) rapidly and react with metals at the oxide/metal interface to form the chlorides of metallic alloying elements as follows [26, 27]:

$$Cr(s) + 3/2\, Cl_2(g) \rightarrow CrCl_3(s) \qquad \text{Reaction 2.8}$$

The vapour pressure of $CrCl_3$ (3.17×10^{-5} atm) [148] is sufficiently high at 500 °C to maintain the continuous evaporation of $CrCl_3$. Then, the gaseous $CrCl_3$ passes through the cracks and the pores within the scale outwards. When it arrives in the

regions with a sufficient oxygen partial pressure (Oxygen continuously diffuses inwards because of the presence of the O^{2-} gradient between two interfaces), the Cr^{3+} ions can be oxidised to Cr_2O_3. Simultaneously, the Cl^- ions transform into gaseous Cl_2 again.

$$2CrCl_3(g) + 3/2\,O_2(g) \rightarrow Cr_2O_3(s) + 3Cl_2(g) \qquad \text{Reaction 2.9}$$

New Cr_2O_3 growing from the vapour phase near or at the scale surface is very fragile. Moreover, the growth sites of such new oxides are randomly distributed at the surface of the scale because of the random distribution of the short-circuit paths within the oxide scale. These two phenomena lead to the fact that these new oxides cannot act as the precursor of a dense and protective scale. The chlorine produced in Reaction 2.9 may enter the atmosphere but will mostly re-enter the scale and continue its catalytic effect in the reaction sequence Reaction 2.8 and Reaction 2.9. Since the continuous oxidation of the clean metal is activated and maintained, this mechanism is called active oxidation and is illustrated in Fig. 2.9.

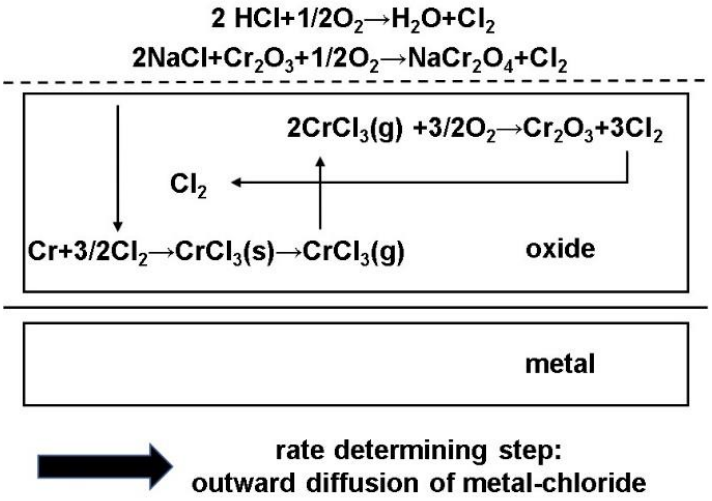

Fig. 2.9 Schematics of the reaction circuit in active oxidation of alloy containing Cr.

The condition discussed above is the oxidising atmosphere in which chlorides can be oxidised to chlorine. While under a reducing condition, the oxide phases are not sufficient to oxidise the chlorides to produce catalytic chlorine for an active oxidation circuit. The rate of corrosion depends only on the volatilisation of the metal chloride that is governed by the temperature. Usually, the most common gaseous chlorine-containing species in the biomass-fired boiler are HCl and Cl_2. The former is the dominant chlorine species in the bulk gas, while Cl_2 may be present locally at relatively high temperatures in the absence of moisture. Moreover, the thermal decomposition of HCl in a reducing environment may produce Cl_2 [149].

Besides the direct volatilisation of Cl in a biomass fuel, the alkali chloride in the residual burnt fuel will be oxidised to produce Cl to initiate the active oxidation process. Simultaneously, some desired oxide scale such as Cr_2O_3 will be broken, as it acts as the oxidising agent for the alkali chloride [50, 73, 149, 150].

$$2NaCl(s,l) + Cr_2O_3(s) + 1/2\,O_2(g) \rightarrow Na_2Cr_2O_4(s,l) + Cl_2(g)$$

Reaction 2.10

The sulphidation of the alkali chlorides deposited on the surface of a component after combustion can produce Cl^{-1} and Cl_2 and thus accelerate the corrosion based on the following reactions.

$$2KCl(s,l) + SO_2(g) + 1/2\,O_2(g) + H_2O(g) \rightarrow K_2SO_4(s,l) + 2HCl(g)$$

Reaction 2.11

$$2KCl(s,l) + SO_2(g) + O_2(g) \rightarrow K_2SO_4(s,l) + Cl_2(g)$$

Reaction 2.12

2.6.2 Thermodynamic stability of metal oxides and chlorides

The chlorine-induced corrosion of the NiCr coatings and the boiler steel under them is quite complicated because Fe and Ni can also be oxidised by Cl catalytically as under the abovementioned condition of Cr. To simplify the complexity of this issue, researchers have developed the predominance phase (phase stability) diagram (Fig. 2.10) of Fe/Ni/Cr–Cl/O to predict the presence of thermodynamically stable corrosion products at the given temperature and gas partial pressure. This diagram is drawn using the minimisation of Gibbs' free energy principle and a hypothesis combination of the phase stability diagrams of Fe–Cl–O, Ni–Cl–O and Cr–Cl–O. It neglects the inter-influence between the components in the Fe–Ni–Cr system and can approximately predict the corrosion product phase. With this diagram, the stability of various oxides of the metals under different conditions can be judged conveniently. For instance, the metal chlorides ($CrCl_3$, $NiCl_2$, $FeCl_2$ and $CrCl_2$) become stable in an atmosphere containing O_2 at a low partial pressure and Cl_2 at a high partial pressure.

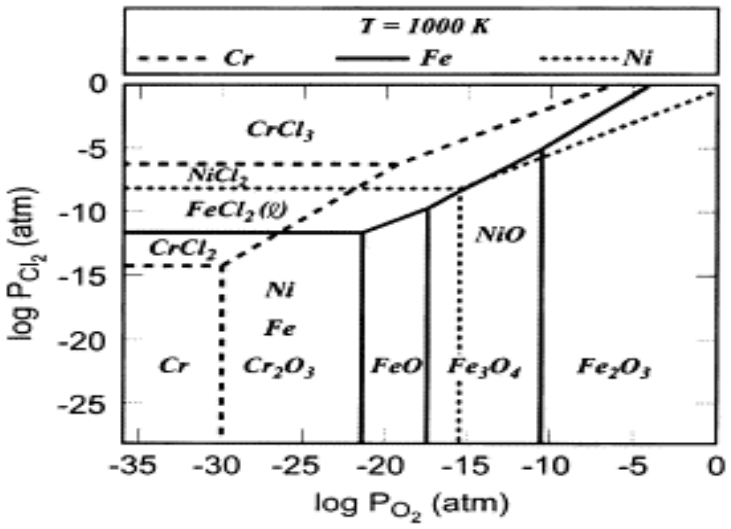

Fig. 2.10 Predominance phase (phase stability) diagram of Cr/Fe/Ni–O–Cl at 1000 K showing the most stable phases under various conditions [9].

2.6.3 Previous studies on the high temperature chlorine-induced corrosion of NiCr alloys and coatings

The corrosion mechanism of NiCr alloys and coatings is mostly obtained from the investigation and experience of bulk alloys rather than coatings [9, 26, 27, 45-47, 50, 52, 64, 71, 77, 79, 149, 151, 152]. Researchers summarised the chlorine-induced corrosion mechanism of the NiCr system according to the investigation results of the NiCr alloys and reported the corrosion performance of the NiCr alloys. However, publications concerning the corrosion of NiCr coatings have mainly reported the corrosion performance of the deposited coatings and no comprehensive discussion of the mechanism of corrosion of coatings with a different microstructure from that of bulk alloys has been presented.

Grabke *et al.* [149] believed that the evaporation can be the rate dominating step in the entire corrosion process if the vapour pressure of the metal chlorides exceeds 10^{-4} atm. Metal chlorides such NiCl, $FeCl_2$ and $CrCl_3$ have high vapour pressures when the temperature exceeds 500 °C even though they are still in the solid state. The high vapour pressures of metal chlorides imply that they will evaporate continuously and lead to a rapid loss of the metal from the coating surface.

The acceleration effect of metal chlorides in the molten liquid states when the temperature was increased further was also confirmed by Grabke *et al.* [150]; they reported that the presence of liquid chlorides causes the fluxing of the oxide scale and thus accelerates the mixed oxidation–chlorination process, as the ions participating in the corrosion transport faster within the oxide scale after the fluxing. Lang *et al.* [148] also proposed another two other points to explain the acceleration effect of liquid

chlorides on the corrosion of NiCr alloys: 1. The chemical reaction proceeds faster in the liquid phase because of the large surface activity of the liquid. 2. The liquid phase can act as a short-circuit path and thereby provide an electrolyte or a pathway for the ionic charge transfer, which can accelerate the electrochemical corrosion.

The melting points and the temperatures at which the evaporation of metal chlorides is intense (vapour pressures reach 10^{-4} atm) for different metal chlorides are summarised in Tab. 2.1. The metal chlorides can be molten only in a narrow temperature range, which is just above their melting point. A further increase in the temperature will promote the intense evaporation of chlorides According to Tab. 2.1, if the operation temperature of a biomass boiler increases to 650 °C, the volatilisation of $NiCl_2$ and $CrCl_3$ becomes intensive, which is a challenge for the application of the NiCr coatings in a biomass boiler at increased temperature.

Tab. 2.1 Melting point (T_m) and temperatures at which the chloride vapour pressure equals to 10^{-4} atm (T_4) [52].

Chloride	T_m(°C)	T_4(°C)
$FeCl_2$	303	536
$FeCl_3$	676	536
$NiCl_2$	1030	607
$CrCl_2$	820	741
$CrCl_3$	1150	611

Recently, researchers have focused on the investigation of the chlorine-induced fireside corrosion of thermal sprayed NiCr coatings. The excellent corrosion resistance of the HVOF thermal sprayed NiCr9Mo, NiCr16Mo and NiCr10Al coatings was

confirmed by Oksa *et al.* [26] with a two-year field test in a practical biomass boiler. Yet, their conclusion may not be robust, as the field test temperature was low. For instance, the temperature of the flue gas before the cold economiser was around 360–400 °C, and before the hot economiser, it was approximately 520–800 °C. The NiCr16Mo and NiCr9Mo coatings performed very well for two years at the surface of the cold economiser. Their performance at a higher temperature still needs to be studied further. NiCr10Al showed excellent corrosion resistance when deposited at the surface of the hot economiser. However, considering that there was 10 wt.% Al in the exposed coatings, the individual protection effect of Cr in the chlorine-containing environment is doubtful, as the Al_2O_3 scale can also act as a good oxidation resistance layer. Oksa *et al*. [26] also confirmed that the oxidised lamellar boundaries and pores in the coatings are the preferential transport path for the oxidising ions. In other words, the HVOF thermal sprayed coatings of less porosity and the oxidised splats perform better under the high temperature corrosion condition.

In another study by Oksa *et al.* [27], they increased the boiler running temperature up to 750 °C since it is a biomass-coal co-firing boiler. There was a 10 µm layer of Cr_2O_3 generated at the surface of the coatings. The HVOF thermal sprayed Ni50Cr coatings survived after 5900 h of heat treatment. This revealed the promising potential of the application of HVOF thermal sprayed Ni50Cr coatings for preventing high temperature chlorine-induced corrosion. Another useful result reported by Oksa *et al.* was the effect of Cr content on corrosion resistance of NiCr coatings. The In625 coating (21 wt.% Cr) corroded catastrophically at 750 °C and was consumed completely on the windward side. The corrosion had proceeded into the substrate material A263, which had experienced severe corrosion as compared to the uncoated A263 specimen. The

reason for the failure of the In625 coating could be the low content of Cr within the coating, which was not sufficient to continuously diffuse outwards and supply Cr to form an oxide scale adjacent to the surface of the as-sprayed coating. The evaporation of chromium chloride also contributed to this consumption of Cr within the coating.

Corrosion tests lasting for 100 h, 400 h and 1000 h were conducted on the HVOF thermal sprayed Ni50Cr/Ni57Cr coatings under the chlorine-containing condition by Uusitalo *et al*. [45-47]. These Ni50Cr/Ni57Cr coatings provided satisfactory corrosion protection according to the authors' experimental data. The Ni50Cr (Ni49Cr2Si) coating could provide the complete protection effect to the substrate in the chlorine-containing atmosphere at a high temperature, as no signs of corrosion were identified at the substrate/coating interface. The Ni57Cr HVOF thermal sprayed coatings after the laser re-melting process also survived after 1000 h of exposure. Oxides that partially covered the coating surface after the laser re-melting contained Cl in a small amount, and the other areas of the coating surface were free of the corrosion attack phenomenon. Briefly, the corrosion performance of the HVOF thermal sprayed coatings is reduced by the interconnected porosity, oxide-containing splat boundaries, voids formed at the splat boundaries and the compositional homogeneity caused by the process. However, the coated low-alloy boiler steel could survive from the chlorine-containing corrosion for a short dwell time because of the presence of the HVOF thermal sprayed NiCr coatings, and the laser re-melting could significantly promote the corrosion resistance of the sprayed coatings by improving the as-sprayed microstructure. Therefore, the laser cladded coating are expected to have better chlorine-containing corrosion resistance than the HVOF thermal sprayed coatings,

because there are no included oxides and extensive porosity in the laser cladded coatings as under the condition of the thermal sprayed coatings [39].

Other researchers have also reported the potential application of laser cladded NiCr-based coatings in the corrosion area. Li *et al.* [77] investigated the performance of the laser cladded Hastelloy C22 alloy (Ni–Cr–Mo) coatings on the TP347H stainless steel in an environment containing HCl. The laser cladded C22 layer performed better than both the naked steel and the bulk C22 alloys. The build-up of the protective chromia layer at the surface of the coating and the refined grains of the oxide scale as well as the coating contributed the superior chlorine-induced corrosion resistance, which was caused by the laser cladding process.

According to the literature summarised above, the NiCr coatings can provide protection for the boiler material from high temperature chlorine-induced corrosion to some extent [26, 153-155]. However, whether the performance of the laser cladded coatings is better than that of the coatings deposited using the HVOF thermal process and the details of the mechanism of the corrosion of NiCr coatings are still not clear, which will be the main objective of this study. Moreover, the application of mechanism of chlorine corrosion of NiCr alloys on the explanation of the chlorine corrosion of NiCr-based coating is doubtful and need investigation in this study.

2.7 Summary

According to the above literature review, information for the thermal spray and laser cladding of Ni50Cr coatings for high temperature applications can be summarised as follows:

- The currently popular boiler steels such as T/P 22 and 92 cannot perform satisfactorily at high temperature in the presence of a burning biomass because of their high chlorine and alkali metal content.
- It is necessary to deposit a protective layer on the surface of a boiler material to extend the operation life of the boiler and thus reduce the maintenance and repair costs of the boiler.
- NiCr alloys are a promising candidate for the protective layer owing to their excellent and versatile properties.
- In general, among the surface engineering techniques (HVOF, cold spray and laser cladding), the most suitable technique for the deposition of high temperature chlorine-induced corrosion resistant NiCr coatings in the biomass boiler is not clear and has no consensus according to previous researchers as each technique has its own merits and drawbacks. A comparison of the oxidation performance of coatings deposited using these techniques can help to determine the most suitable one and thus fill the knowledge gap in this area.
- Unlike the high temperature oxidation/corrosion of bulk NiCr alloys, the oxidation/corrosion behaviour of NiCr-based coatings deposited using various techniques has not been studied much. Whether the oxidation mechanisms extracted from the observation of bulk alloys can be used for explaining the oxidation behaviour of the coatings without any modification needs further investigation.
- Even in the case of oxidation/corrosion of NiCr bulk alloys, the results and the conclusions obtained by various researchers under different conditions are in mutual contradiction. This indicates that the high temperature oxidation of alloys

is a delicate science and needs careful investigation when conducting experiments and discussions.

- The air oxidation mechanisms of the NiCr alloys such as transient and selective oxidation have been widely recognised and investigated by researchers. However, the literature on the air oxidation of NiCr coatings is not as abundant as that on the bulk alloys and there is a gap that is hoped to be filled by this study.
- The presence of steam accelerates the oxidation of NiCr when compared with the dry condition. Several researchers have hypothesised possible mechanisms to explain this acceleration effect. However, there is consensus on the dominant mechanism. The experimental results and the related discussion may provide reinforcements to a certain mechanism. Meanwhile, whether the different microstructure and phase composition of the NiCr coatings from the bulk alloys could lead to different oxidation performance is another interesting point.

Chapter 3 Experimental

3.1 Introduction

In this chapter, an overview of the liquid fuelled HVOF (HVOLF) thermal spray, gas fuelled HVOF (HVOGF) thermal spray, cold spray and laser cladding equipment used in the deposition of the coatings is provided. Besides, a series of experimental devices in which the coatings were exposed in specific atmospheres (i.e. air, steam and chlorine containing gas) at 700 °C are also introduced. To characterise the as-deposited coatings as well as the coatings after oxidation/corrosion, analysis techniques such as X-ray Diffraction (XRD), Scanning Electron Microscopy (SEM) and Energy Dispersive X-ray Spectroscopy (EDX) are compulsory. Hence, sample preparation procedures for these characterisation processes, and the equipment as well as principles of those characterisation methods are also included in this chapter.

3.2 Materials

3.2.1 Feedstock powders

Two commercially available gas atomised Ni50Cr-based powder, Praxair 1260F (Praxair Surface Technologies Ltd., Swindon, UK) and Sandvik Osprey 50/50 NiCr (Sandvik Osprey Ltd., Neath, UK), were used in this study. These two powders have quite similar compositions as shown in Tab. 3.1. The Praxair powder was used in the HVOLF, HVOGF and laser cladding processes, and the Sandvik powder was used in the cold spray process. The Praxair powder has a larger size distribution than that of the Sandvik powder; thus, it is more robust to the deposition techniques which bring about a large amount of heat into the powder particles such as the HVOF process and the laser cladding process [156]. The nominal size ranges were specified as -53+15

μm for the Praxair powder and -25+5 μm for the Sandvik powder. The nominal compositions of the powders given by manufacturer are listed in Tab. 3.1.

Tab. 3.1 Chemical composition (wt.%) of material (powder and substrate) used in this study.

Material	C	Cr	Fe	Ni	O	Si	Mn	S	P	Other
Praxair 1260F	0.1	46	1.0	Bal.	0.03	2.0	–	–	–	1
Sandvik Osprey	0.2	50	–	Bal.	–	0.3	0.3	–	–	–
ASTM 304	0.08	18.6	–	7.9	–	0.4	1.8	0.03	0.1	–

3.2.2 Substrates

In the case of the HVOLF, HVOGF and cold spray processes, An ASTM 304 austenitic stainless steel plate was cut into coupons of dimension 60 mm × 25 mm × 2 mm and used as the substrates. The composition of ASTM 304 steel that was measured by using the spark atomic emission spectroscopy (AES) is reported in Tab. 3.1. The surface preparation of these coupons before deposition process differed according to which kind of HVOF coatings is required. For instance, to obtain the freestanding HVOF coatings for the subsequent mercury intrusion porosity (MIP) measure, density investigation and thermogravimetric analysis (TGA), the substrates were ground using the SiC grinding paper of grit 220. This grinding process brought about a substrate of lower roughness and thereby weaken the mechanical interlocking [157] between the coatings and the substrates. Then the freestanding coatings were removed from the ground substrates easily using benchwork tools. The other substrates were grit blasted with the brown alumina of ~250 μm particle size to increase the surface roughness, finally promoting the mechanical interlocking between the coatings and the substrates.

Consequently, the coatings having strong connection with the substrates were obtained.

In the laser cladding process, ASTM 304 stainless steel 304 was also used as the substrate material. Plates of dimension 100 mm × 180 mm × 6 mm were prepared and degreased with acetone before the cladding process. In addition, pre-cleaning of the surface of substrate was conducted by scanning the total area of substrate with a laser beam of minimum (0.2 kW) power to reveal the fresh metal surface.

3.3 Coating deposition processes

3.3.1 HVOLF and HVOGF processes

Two HVOF systems were used to deposit the Praxair powder onto the substrates: one is a HVOLF setup and the other one is a HVOGF setup. The major difference between these two setups is the spray gun. Other components such as the powder feeder and the fuel control console are same in both setups. Schematic diagrams of these two HVOF thermal spray guns are shown in Fig. 3.1. As shown in Fig. 3.1 (a), the HVOLF gun operates as follows: kerosene in liquid and oxygen are fed into the combustion chamber where the kerosene is vaporized and mixed with the oxygen. The mixture burns before passing through the converging-diverging nozzle that accelerates the gas to a Mach number between 1.5 and 2. Powder is fed radially into the gas stream through two ports which are located downstream of the throat. The gas and the entrained powder then flow along the nozzle, before emerging as a free jet [158]. In the case of the HVOGF process (Fig. 3.1 (b)), powder is fed axially into the rear of the combustion chamber where oxygen and fuel (H_2) are mixed and combusted. The hot gas and the entrained powder are then accelerated through the combustion chamber

and the parallel sided nozzle, which is approximately 220 mm long, before emerging as a free jet. The HVOLF thermal spray gun system used in this study was a Metjet IV system (Metallisation Ltd., Dudley, UK), while the HVOGF one is a Top Gun system (GTV Verschleiss-Schutz GmbH, Germany).

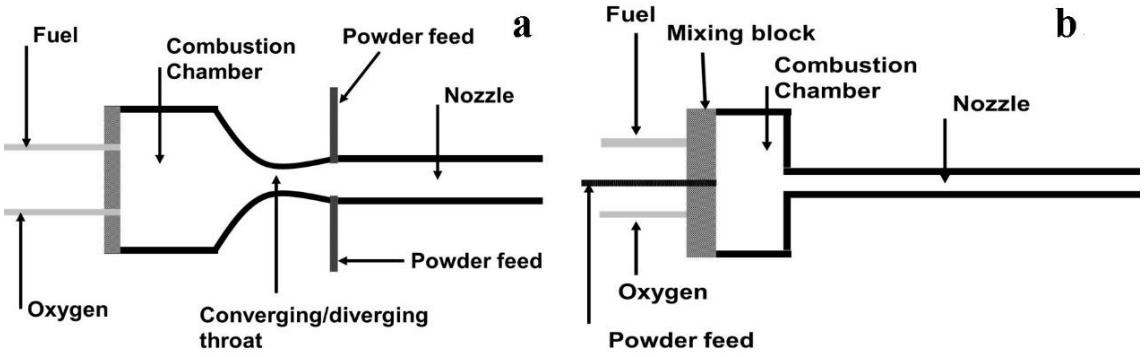

Fig. 3.1 Schematic diagrams of two types of HVOF thermal spray guns: (a) HOVLF; (b) HVOGF.

To deposit coatings onto substrates, flat coupons of ASTM 304 stainless steel were mounted vertically on the circumference of a turntable with a vertical axis of rotation and the spray gun was positioned at the front of the rotating coupons at a fixed standing-off distance to give a horizontal spray jet.

3.3.2 Cold spray process

A cold spray system developed at the Xi'an Jiaotong University [19] was used to deposit the Sandvik powder on ASTM 304 stainless steel substrates. This system consists of gas pressure regulators, a gas preheater, a powder feeder and a spray gun. As show in Fig. 3.2, the spray gun includes a gas pre-chamber and a convergent-divergent accelerating nozzle. This nozzle has a throat diameter of 2 mm and an exit diameter of 6 mm. The length from the throat to the exit is 100 mm. The cold spray

gun operates as follows: powder is fed axially into the upstream of the nozzle from the back of the gun and accelerating gas is introduced from the gas inlet into the pre-chamber. The gas temperature and pressure in the pre-chamber are measured via the thermocouple and pressure gauge that are mounted on the spray gun. N_2 is used as the accelerating gas that operating at a desired pressure in the pre-chamber. N_2 is also used as powder carrier gas. During the deposition, the gun is manipulated by a robotic arm (Motoman, Yaskawa Drives and Motion, America), with which the gun can move relatively to the substrate. Coatings of certain thickness can be produced through the continuous relative movement of the gun to the substrate.

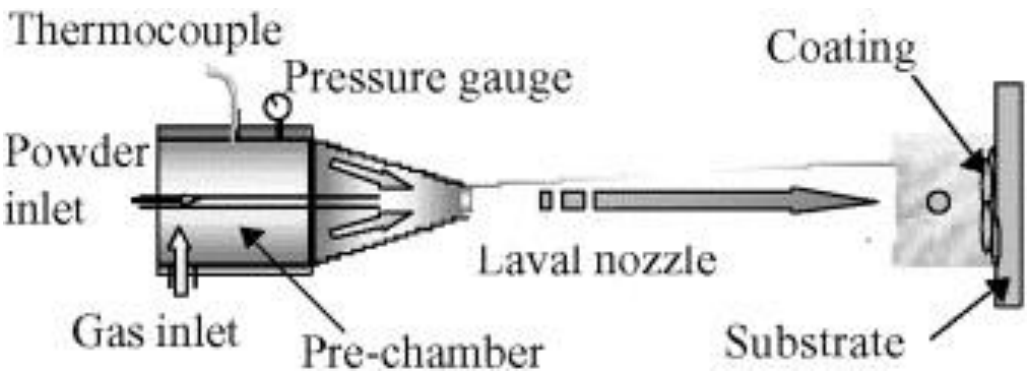

Fig. 3.2 Schematic diagram of the cold spray gun developed and used in the Xi'an Jiaotong University [33].

3.3.3 Laser cladding process

The laser cladding process of Praxair powder was carried out using a 2 kW Ytterbium doped fibre laser system (IPG Photonics Ltd., Bristol, UK) and other auxiliary equipment such as a powder feeder and a computer numerical control (CNC) machine tool. A Prectec YW50 fibre laser head (Laser Trader Ltd., Chesterfield, UK) was mounted on a 4-axis gantry system with a CNC worktable, which is shown in Fig. 3.3.

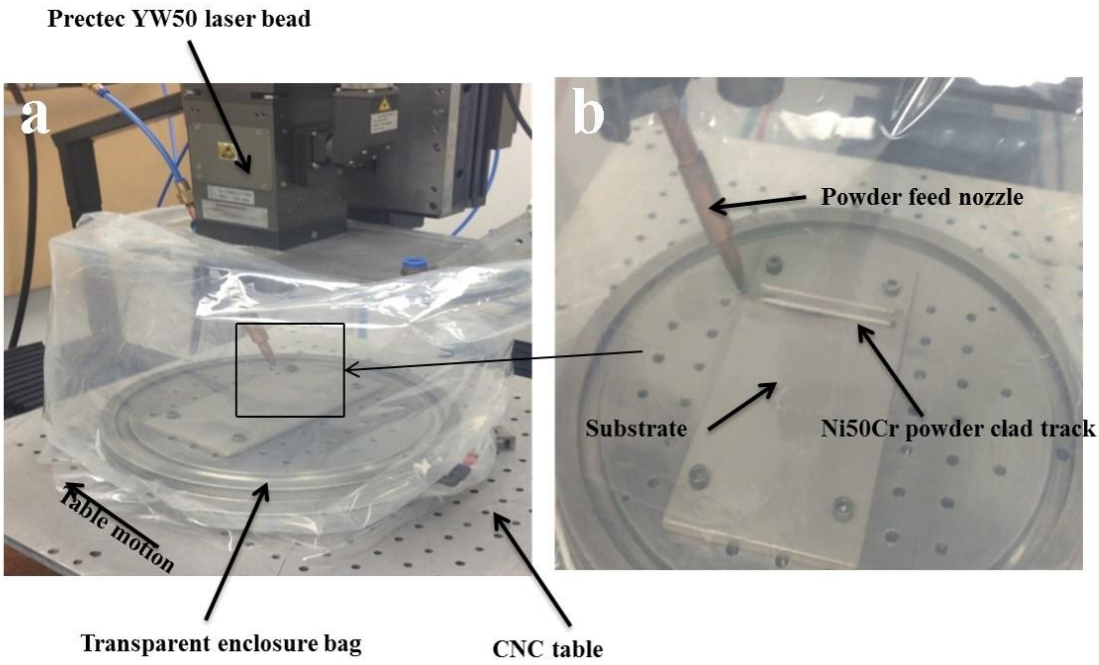

Fig. 3.3 Laser cladding deposition of Praxair powder setup: (a) entire setup including the laser bead, CNC table and enclosure bag; (b) deposited clad track on the substrate.

The Prectec YW50 laser head operates at 1070 nm wavelengths, and produce a beam which focuses to a round spot of about 3.1 mm at 20 mm away from focus, finally giving a 212 mm working distance with a Gaussian energy distribution [159]. To prevent oxidation, all laser cladding deposition are carried out inside a transparent enclosure that is evacuated and back-filled with high purity Ar. The Praxair Ni50Cr powder was ejected from the powder feed nozzle with the assist of the powder supply gas. Meanwhile, a laser beam produced by the laser bead scanned and melted the powder as well as the substrate that were under the laser beam. After beam passing, melted powder particles and substrate began to cool and solidify, finally forming a clad. Three major input process parameters of the laser cladding process are laser power (kW), scanning speed (mm min $^{-1}$) and powder feed rate (g min $^{-1}$), which can be adjusted by manipulation of the output power of the laser beam head, the rotation

speed of the disc inside the powder feeder, and the movement speed of the CNC table, respectively.

3.4 Thermogravimetric analysis (TGA)

TGA is a technique that measures weight of samples continuously at specific temperatures and in various atmospheres. The curve of weight change versus time can be used to calculate the oxidation rate, and thereby deduce the oxidation kinetics of samples. An SDT Q600 thermogravimetric analyser (TA Instruments, Herts, UK) was used to obtain the thermogravimetric curves of the freestanding as-sprayed HVOLF and HVOGF coatings in bottle air for 4 h.

To prepare the samples for TGA analysis, a square section of dimension approximately 3 × 3 mm was cut from a freestanding coating by using a precision diamond tipped cutting disk. The dimensions were measured using a micrometre to an accuracy of 1×10^{-3} mm. The thickness of the freestanding coatings was measured by investigating the cross-sections of coating using SEM.

Before carrying out the TGA test, the samples were cleaned using industrial methylated spirit (IMS), dried and weighed using a precision balance (1×10^{-4} g). Then the oxidation exposures were carried out in commercial grade bottled air (flow rate of 20 mL min^{-1}) at 700 °C. The samples were held in a recrystallized alumina pan and heated at a rate of 5 °C min^{-1} to 700 °C. This temperature was maintained for 4 hours before the heat treatment chamber of the SDT Q600 cooled down to room temperature, also at a rate of 5 °C min^{-1}. The TGA data obtained before the temperature reached

700 °C was not taken into consideration to examine the isothermal behaviour of samples at 700 °C.

As mentioned chapter 2, metal/alloy which has excellent oxidation resistance often exhibits an oxidation behaviour in parabolic law [160]. The parabolic law oxidation behaviour is described by Monceau *et al.* [161]:

$$(\Delta m/A)^2 = k_p t \qquad \text{Eq. 3.1}$$

Where Δm is the mass change, A is the total surface area of samples, t is time and k_p is the parabolic rate constant.

However, Eq. 3.1 needs modification when it is utilised to evaluate practical oxidation behaviour since the transient oxidation period of non-parabolic kinetics cannot be neglected in most oxidation resistance alloys. The modified version of Eq. 3.1 is written as follows, by assuming the oxide layer grown at $t > t_i$ has the same protective properties as the scale grown at $t < t_i$:

$$(\Delta m^2 - \Delta m_i^2)/A^2 = k_p(t - t_i) \qquad \text{Eq. 3.2}$$

In the TGA data process of this study, the t_i was selected as the time point at which the temperature arrived at 700 °C, initially. Whether the plot of the square of the mass gain per unit area versus time can be fitted with a straight line is used to decide the oxidation kinetics of the tested freestanding coatings. The gradient of the fitted straight line is the parabolic rate constants k_p, whose value is an indicator of the oxidation resistance. The coefficient of determination demonstrates the robustness of straight line fitting.

3.5 High temperature exposure of deposited coatings in air, steam and chlorine-containing atmosphere

3.5.1 Sample preparation before conducting high temperature exposure

Before placing deposited coated samples in the test furnace/rig, cold sprayed coatings were ground to remove several layers of splats that are of around 300 μm thick, as these layers contained a lot of pores. This measure was adopted to guarantee all the three thermal sprayed coatings (HVOLF, HVOGF and cold spray) had porosity of similar level of the surface that contacts with oxidising/corrosive atmosphere. Top surface of laser cladded coatings is not flat, and thereby not suitable for the XRD characterisation. Hence, laser cladded coatings were also ground to obtain a flat surface before conducing the high temperature oxidation/corrosion exposure. XRD patterns of as-deposited laser cladded coatings is also obtained using the flat surface sample to retain consistency of experimental results.

3.5.2 High temperature air oxidation test in furnace

A long-term (compared with the TGA dwell time) air oxidation exposures of four coatings at 700 °C were carried out in a box furnace (Lenton ECF 12/6, Lenton Thermal Design Ltd., UK). Twelve coated samples were placed in twelve crucibles that are made from high-density alumina and placed into the chamber of the furnace, respectively. At the beginning of the exposure, the temperature went up to 700 °C at a heating rate of 5 °C min^{-1} from room temperature. At the end of the exposure cycles, the samples were furnace cooled to room temperature also at a rate of 5 °C min^{-1}. Three exposure cycles (1 h, 10 h and 100 h) of samples were adopted to investigate the oxidation behaviour of the coatings at various time point.

3.5.3 High temperature steam oxidation exposure in a simulated rig

To investigate the steam oxidation resistance of the deposited coatings using four techniques (HVOLF, HVOGF, cold spray and laser cladding), a test rig that could simulate the desired exposure condition (100% steam at 700 °C) was built in the lab. Fig. 3.4 is a schematic diagram of this exposure rig. In this rig, water was transported from the reservoir to the ceramic exposure tube (alumina liner) inside the steel shell (stainless steel reaction vessel), by a peristaltic pump. When water flows through the hot exposure tube, it turns into steam and thereby simulates the steam condition in the steam tubes in power plants. N_2 is mainly used to remove the residual air from the pumped water, and thus protect the coating before steam filled the whole exposure tube. After passing the exposure vessel, steam was cooled by a heat exchanger and return to the reservoir. Water recycled in reservoir could be utilised to provide continuous steam resource in a closed loop setup.

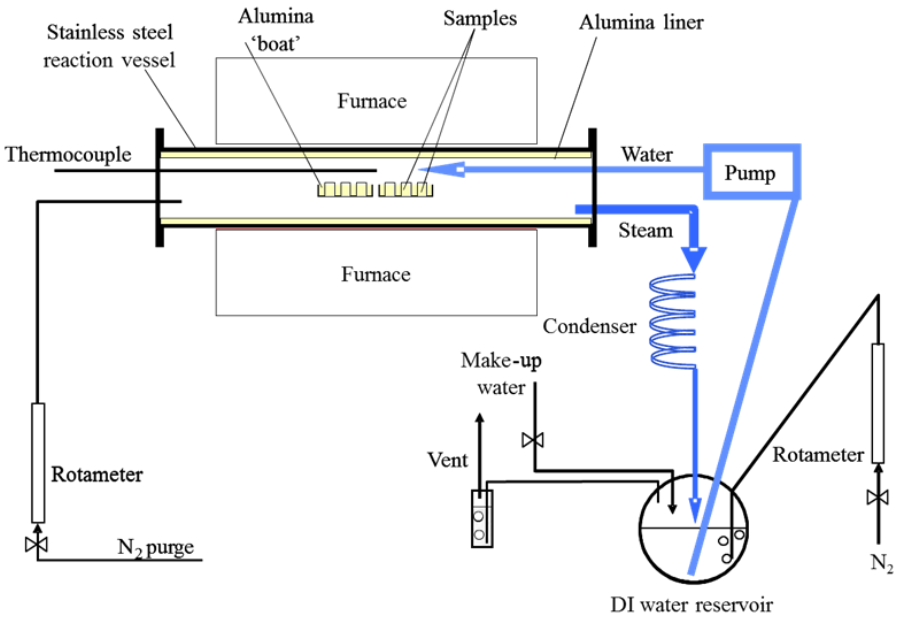

Fig. 3.4 Schematic diagram of the atmospheric pressure steam oxidation setup.

The heating and cooling rates were both 5 °C min^{-1}, as that was applied in the air oxidation exposure. To make sure all the spallation from the exposed sample could be collected, steam oxidation samples were placed into 99.8% alumina crucibles initially; then, these crucibles containing samples were placed in the abovementioned rig. The exposure continued for 1000 h that consisted of four 250 h dwells. After each 250 h dwell, exposure was stopped to remove samples that experienced 250, 500, 750 and 1000 h high temperature steam oxidation. Investigation of the samples collected at various time points can be used to elevate the steam oxidation performance of the deposited coatings.

3.5.4 High temperature chlorine-induced fireside corrosion exposure in a simulated rig

The high temperature fireside corrosion exposures were carried out in an alumina lined horizontal controlled-atmosphere furnace, using simulated biomass fuel combustion gases. The furnace holds 12 exposure specimens at one time in individual alumina crucibles in the hot zone. Pre-mixed gases were supplied to the controlled-atmosphere furnace through mass flows controllers to achieve the desired atmosphere. The schematic diagram of the furnace-setup is shown in Fig. 3.5. The gas mixture reached the entrance of furnace is of following composition: 500 ppm HCl, 5% O_2, N_2 Bal. The exhaust gas mixture from the furnace passed through a scrubber solution (NaOH), before finally being released into the atmosphere to avoid potential contamination. Besides the atmosphere, a mixture of 10 wt.% KCl in deionised water slurry was applied on the top surface of certain samples with a brush, which after drying deposited an average of 14±1 mg of KCl on each sample. This measure can help check the

influence of the presence of KCl on the high temperature corrosion of as-deposited coatings.

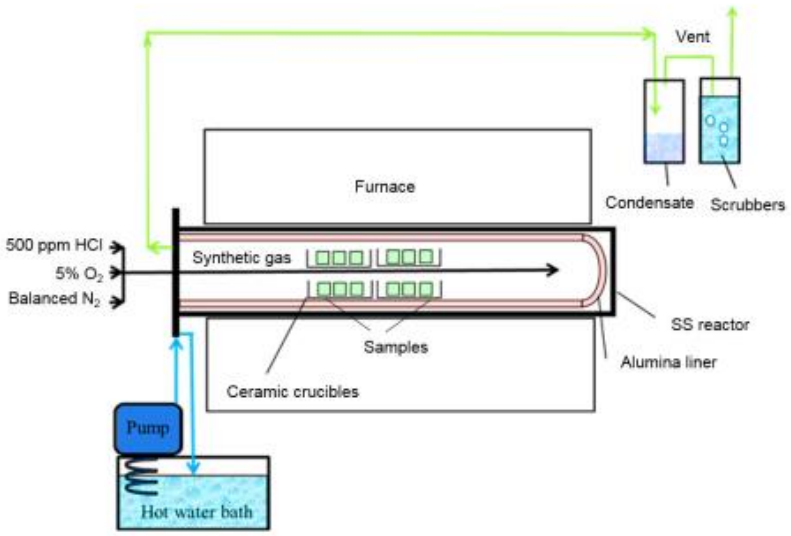

Fig. 3.5 Schematic of the controlled environment test setup for high temperature fireside corrosion.

The temperature of fireside corrosion exposure was also 700 °C. The heating and cooling rates were both 5 °C min^{-1}. A 250 h exposure cycle was conducted to study the effect of gas phase and deposit on the chlorine-induced corrosion of coatings.

3.6 Characterisation of feedstock powder and coatings

3.6.1 Sample preparation for various characterisation processes

Top morphology of ad-deposited coatings was examined directly in the SEM machine by placing them onto carbon stubs, as the coating and the substrate are both conductive.

As-deposited coatings were mounted in a conductive resin, ground and polished to a 1 µm diamond finish for the SEM cross-section examination. High temperature

exposed coatings were mounted in a mixture of cold setting resin and micro glass ball (50/50 volume ratio) to prevent the spalling of oxidation scale on the top surface of coating during the metallurgical preparation (grinding and polishing). To increase the conductivity of exposed sample in the cold setting resin for distinguish SEM observation, the samples were connected with sample holders using conductive aluminium tape.

3.6.2 Volume measurement using helium pycnometer

The volume of the freestanding HVOF coatings was measured using a helium pycnometer AccupycTM 1330 (Micromeritics Instrument Corporation, USA). As shown in Fig. 3.6, this device works by pumping helium gas into the sample chamber until helium completely surrounds the sample. The expansion valve then opens, allowing the pressure to equilibrate, after which the device calculates the volume of the sample by comparing it with the empty reference chamber. The skeletal (as opposed to the bulk) density is then calculated using the sample weight, which is determined separately and inputted into the pycnometer. Working principle of this device is given in Eq. 3.3:

$$V_s = V_c + V_r/(1 - P_1/P_2) \quad \text{Eq. 3.3}$$

Where V_s is the sample volume, V_c is the volume of the empty sample chamber (known from a prior calibration step), V_r is the volume of the reference volume (again known from a prior calibration step), P_2 is the first pressure (i.e. in the sample chamber only) and P_1 is the second (lower) pressure after expansion of the gas into the combined

volumes of sample chamber and reference chamber. Note that, only the open porosity in the samples can be measured using the helium pycnometer.

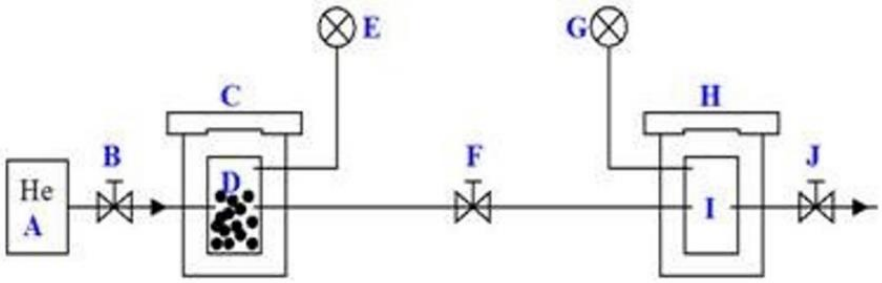

A - Helium gas tank; B - Fill valve; C - Sample cap; D – Sample chamber; E – Sample pressure transducer; F – Equilibration valve; G – Reference chamber pressure transducer; H – Reference chamber (internal); J – Vent valve

Fig. 3.6 Schematic of the AccupycTM 1330 pycnometer.

3.6.3 LECO oxygen content analysis

Oxygen contents of the freestanding as-sprayed HVOLF and HVOGF coatings were measured using a LECO oxygen analyser (LECO ON736, LECO Instruments UK Ltd, Stockport, UK). LECO oxygen content analysis is a combustion method that can determine the oxygen content of solids [162]. It has been widely used because of its rapid determination rate, simple operation and high accuracy. The LECO analysis works as follows: free-standing coatings are placed into a pure graphite crucible and heated, under a flowing stream of He; at high temperature. All the oxygen element in the free-standing coatings existed as metal oxide, and the carbon could deoxidise the metal oxide easily. Thereby, following reaction occurs:

$$C(graphine) + 2O(element\ in\ sample) \rightarrow CO_2(g) \qquad \text{Reaction 3.1}$$

The infrared absorption and thermal conductivity of the combustion gases are measured and recorded by the analyser in a form of spectrum. The reaction product, CO_2 of Reaction 3.1, has its unique infrared absorption and thermal conductivity spectrum, which can be identified in the total spectrum of the combustion gases mixture. Therefore, the quantity of CO_2 can be calculated using the spectrum. Since all the oxygen is in the presence of CO_2, its weight can be calculated knowing the quantity of CO_2.

3.6.4 Mercury intrusion porosimetry (MIP)

To measure the porosity of the as-sprayed freestanding HVOF coatings, a mercury intrusion porosimeter (Autopore IV 9500, Micromeritics, Hexton, UK) was used. Mercury intrusion porosimeter utilises the unique properties of mercury. Since mercury does not wet most substances and does not spontaneously penetrate pores by capillary action, it must be forced into the pores by the application of external pressure. The required equilibrated pressure is inversely proportional to the size of the pores; only slight pressure is required to intrude mercury into the large macro-pores, whereas much greater pressures are required to force mercury to penetrate the small pores. From the pressure versus intrusion data, the MIP instrument generates volume and size distributions of pores inside the sample using the Washburn equation (Eq. 3.4) [163], where D is the diameter of pores, γ is the surface tension of mercury, θ is the wetting angle of mercury and P is the pressure of mercury. However, MIP cannot detect close pores and its pore size detect limitations are between 30 nm–440 µm.

$$D = -4\gamma \cos\theta / P \qquad \text{Eq. 3.4}$$

3.6.5 Optical microscopy

As shown in Fig. 3.7, optical microscopy uses visible light and a system of lenses to magnify images of specific small area on samples. Optical microscopes are the oldest design of microscope and were possibly invented in their present compound form in the 17th century. Basic optical microscopes can be quite simple, although there are many complex designs which aim to improve resolution and sample contrast.

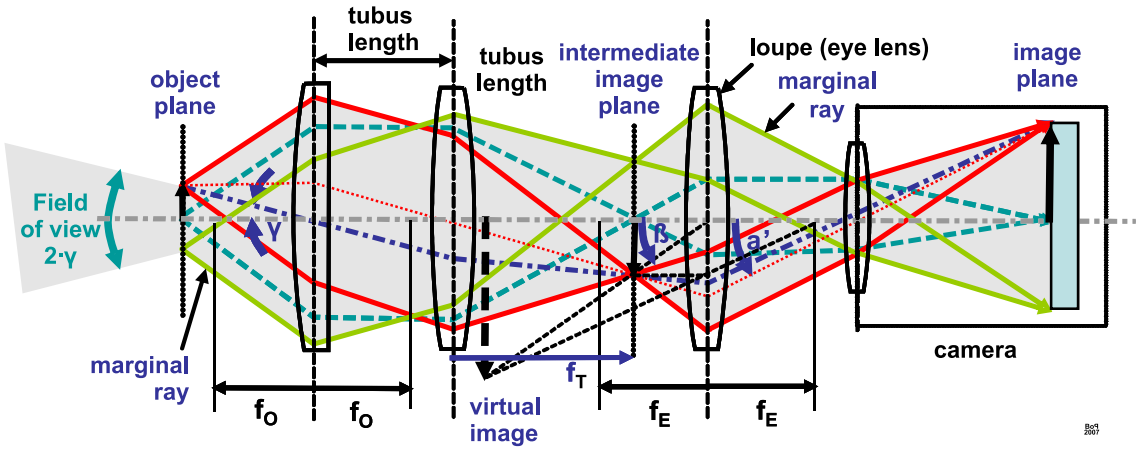

Fig. 3.7 Optical path in an optical microscope [164].

The image from an optical microscope can be captured by normal light-sensitive cameras to generate a micrograph. Purely digital microscopes are now available, which use a charge-coupled device (CCD) camera to examine a sample, showing the resulting image directly on a computer screen without the need for eyepieces. The actual power or magnification of a compound optical microscope is the product of the powers of the ocular (eyepiece) and the objective lens. The maximum normal magnifications of the ocular and objective are 10× and 100× respectively, giving a final magnification of 1000×.

The optical microscope (Nikon Eclipse Lv100ND with attached Nikon DS-Ri1 camera) in corporation with ImageJ analysis software was used to measure the dimensions of the cross-section of a laser cladded bead and investigate the microstructure of the as-sprayed HVOF thermal sprayed coatings before the SEM characterisation.

3.6.6 X-ray Diffraction (XRD) analysis

XRD analysis is a routine material characterisation technique that can determine the phase composition of crystals. It works as follows and is shown in Fig. 3.8: crystals are regular arrays of atoms, and X-rays can be considered as waves of electromagnetic radiation. Atoms scatter X-ray waves, primarily through the atoms' electrons. Just as an ocean wave striking a lighthouse produces secondary circular waves emanating from the lighthouse, an X-ray striking an electron produces secondary spherical waves emanating from the electron. This phenomenon is known as elastic scattering, and the electron is known as the scatterer. A regular array of scatterers produces a regular array of spherical waves. Although these waves cancel one another out in most directions through destructive interference, they add constructively in a few specific directions, determined by Bragg's law:

$$n\lambda = 2d\,sin\,\theta \qquad \text{Eq. 3.5}$$

Here d is the spacing between diffracting planes, θ is the incident angle, n is any integer, and λ is the wavelength of the beam. These specific directions appear as spots on the diffraction pattern called reflections. Thus, X-ray diffraction results from an electromagnetic wave (the X-ray) impinging on a regular array of scatterers (the repeating arrangement of atoms within the crystal).

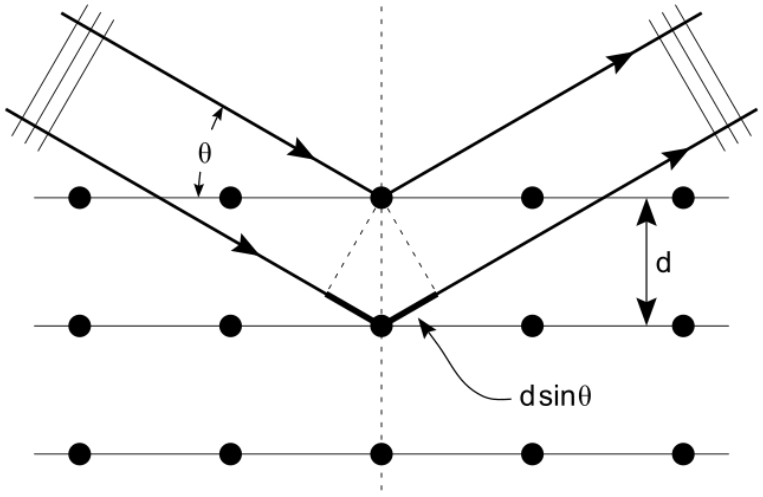

Fig. 3.8 Schematic of Bragg diffraction from a cubic crystal lattice [165].

Peak identification and phase determination using XRD patterns were performed according to the principle mentioned above and with the aid of the Joint Committee on Powder Diffraction Standards (JCPDS) powder diffraction files (PDF). Usually, a given substance consists of crystals in different composition, phase and orientation. These crystals can give out various specific Bragg peaks, which can form a characteristic diffraction pattern like a fingerprint of the substance to be identified. Yet, diffraction can show the presence of a compound, whereas chemical analysis can only exhibit the presence of separate substrates. Substances are classified using the PDF. In this system, any powder is classified in terms of d spacing or 2θ positions and relative intensities.

In this study, the XRD scanning was carried out using a Siemens D500 diffractometer that was equipped with a DACO-MP X-ray source. The X-ray source operated at 40 kV and 20 mA to generate CuK_α radiation at a wavelength of 1.540 Å. Diffractograms were obtained using the CuK_α radiation with a step size of 0.05° and a 5 second counting time for a range of 2θ values (20°–90°).

3.6.7 Scanning Electron Microscopy (SEM) and Energy Dispersive X-ray Spectroscopy (EDX)

The scanning electron microscope (SEM) is a type of electron microscope capable of producing high resolution images of the sample surface [166]. The working principle is demonstrated in Fig. 3.9: an electron beam is thermionically emitted from an electron gun fitted with a tungsten filament cathode. Tungsten is normally used in thermionic electron guns because it has the highest melting point and lowest vapour pressure of all metals, thereby allowing it to be electrically heated for electron emission. The electron beam, which typically has an energy ranging from 0.2 keV to 40 keV, is focused by one or two condenser lenses to a spot about 0.4-5 nm in diameter. The beam passes through pairs of scanning coils or pairs of deflector plates in the electron column, typically in the final lens, which deflect the beam in the x and y axes, so that it scans in a raster fashion over a rectangular area of the sample surface. The energy exchange between the electron beam and the sample, when the beam contacts with the sample, results in the reflection of high-energy electrons by elastic scattering, the emission of secondary electrons by inelastic scattering and the emission of electromagnetic radiation, each of which can be detected by specialised detectors. The beam current absorbed by the specimen can also be detected and used to create images of the distribution of specimen current. Electronic amplifiers of various types are used to amplify the signals, which are displayed as variations in brightness on a computer monitor. Each pixel of computer video memory is synchronised with the position of the beam on the specimen in the microscope, and the resulting image is therefore a distribution map of the intensity of the signal being emitted from the scanned area of the specimen.

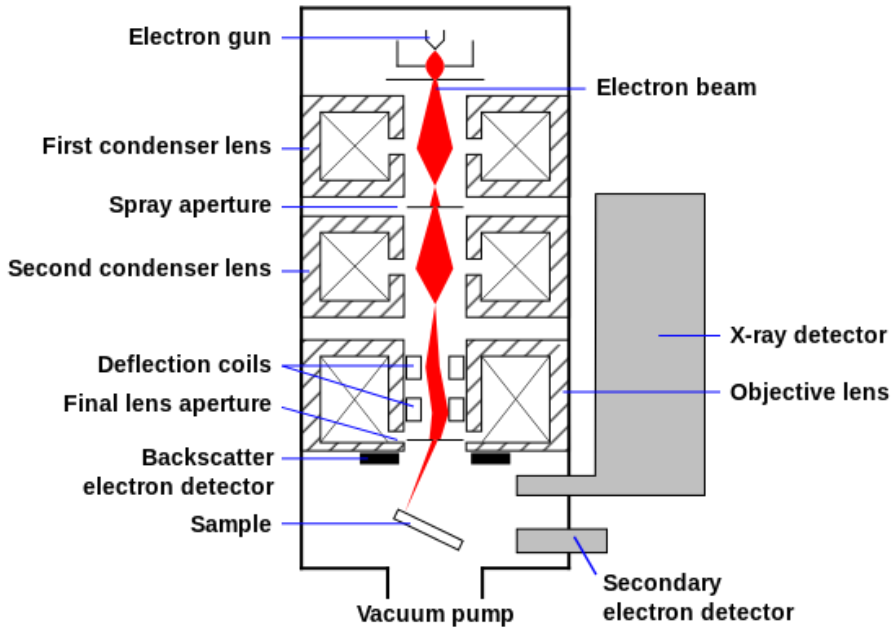

Fig. 3.9 Schematic of an SEM device [167].

Energy-dispersive X-ray spectroscopy (EDS, EDX, or XEDS) is an analytical technique used for the element analysis or chemical characterisation of a sample. It relies on the interactions of X-ray excitation and samples, and the fundamental principle that each element has a unique atomic structure allowing a unique set of peaks on its electromagnetic emission spectrum [166].

To stimulate the emission of characteristic X-rays from a specimen, a high-energy beam of charged particles such as electrons that can be produced by the electron gun in an SEM, is focused into the sample being studied. Then as shown in Fig. 3.10, an atom within the sample contains ground state (or unexcited) electrons in discrete energy levels or electron shells bound to the nucleus. The incident beam may excite an electron in an inner shell, ejecting it from the shell while creating an electron hole where the electron was. An electron from an outer, higher-energy shell then fills the hole, and the difference in energy between the higher-energy shell and the lower

energy shell may be released in the form of an X-ray. The number and energy of the X-rays emitted from a specimen can be measured by an energy-dispersive spectrometer. As the energies of the X-rays are characteristic of the difference in energy between the two shells and of the atomic structure of the emitting , EDX allows the al composition of the specimen to be measured [166].

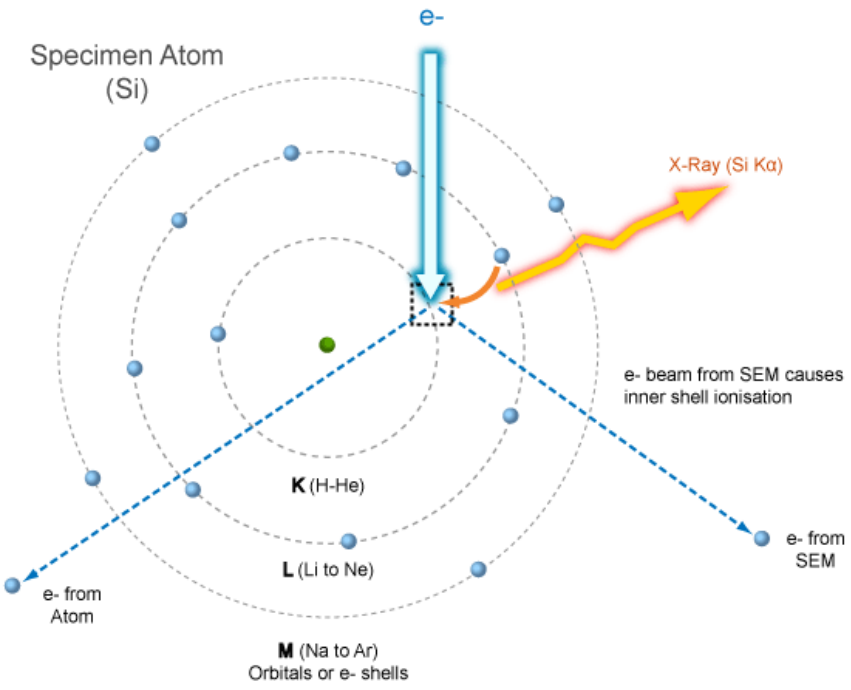

Fig. 3.10 Foundation of EDX analysis: emission of characteristic X-rays from an atom (Si) [168].

A Philips FEI XL30 SEM (FEI Company/Philips electron Optics, Eindhoven, Netherlands) was used for analysis and characterisation of feedstock powder, as deposited coatings and coatings after high temperature test with an accelerating voltage of 20 kV in secondary and backscattered electron modes. EDX scan was conducted using an Oxford EDX system (Oxford instrument, Oxford, United Kingdom) in combination with the XL30 SEM to identify the composition of specimens.

Chapter 4 Process parameter optimisation and oxidation behaviour of coatings

4.1 Introduction

In this chapter, detail investigation of the deposition of Praxair Ni50Cr powder using a liquid fuelled HVOF (HVOLF) and a gas fuelled HVOF (HVOGF) thermal spray process is provided. The characteristics of the as-sprayed coatings obtained using various techniques and the results of the thermogravimetry analysis (TGA) performed on five freestanding HVOF (3 HVOLF + 2 HVOGF) thermal sprayed coatings are presented here. The final session reports the oxidation behaviour of the four coatings (a HVOLF coating and a HVOGF coating that are shortlisted according to the TGA results, a cold sprayed coating and a laser cladded coating) in air and steam.

4.2 Parameter selection for HVOLF and HVOGF thermal spray processes

The most important adjustable parameters for the HVOF thermal spray are the oxygen–fuel ratio and the total mass flow rate. These two parameters for the HVOLF thermal spray of Praxair Ni50Cr powder were selected according to the chart shown in Fig. 4.1, which was provided by the manufacturer (Metallisation Ltd., Dudley, UK) of the HVOLF thermal spray equipment used in this study. The chart shown in Fig. 4.1 was plotted according to the combustion reaction formula between kerosene and oxygen, which is shown in Reaction 4.1.

$$C_{12}H_{26}(l) + 18.5O_2(g) \rightarrow 12CO_2(g) + 13H_2O(g) \qquad \text{Reaction 4.1}$$

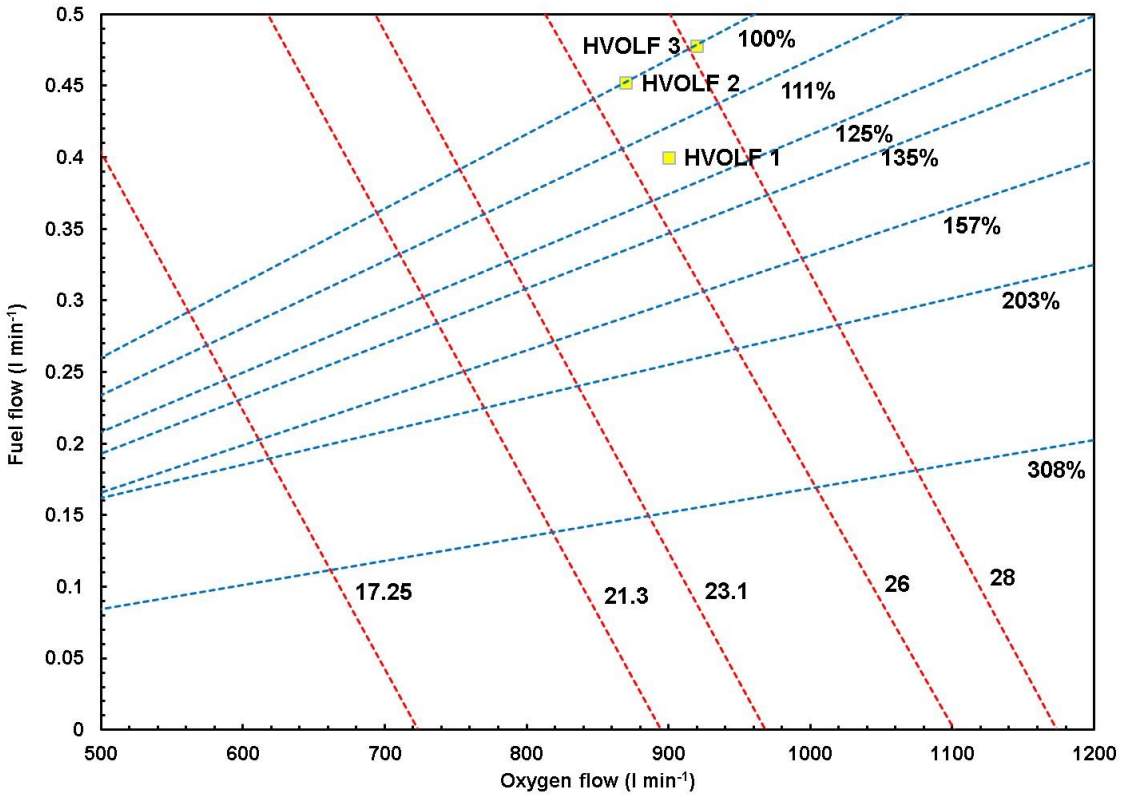

Fig. 4.1 Plot showing oxygen and kerosene flow rate for various total flow rate (red dash lines) and stoichiometry percentages (blue dash lines) that can be used to shortlist spray conditions in the Metjet IV HVOLF thermal spray gun.

At the 100% stoichiometry (the uppermost blue dash lines), 1 mole of kerosene react with 18.5 mole of oxygen in theory, and thus all the kerosene and oxygen are consumed completely. The points on the other stoichiometry lines such as 111% and 125% implied an excessive 11 vol.% and 25 vol.% oxygen when the spray process was conducted under the corresponding conditions. The oxygen and fuel flow rates were determined from Fig. 4.1 by using the following rule: Moving across the stoichiometry lines from a higher percentage to a lower percentage leads to a decrease in the excess oxygen of the flame, which results in an increase in the flame temperature due to the reduced cooling effect of oxygen and thus a higher percentage

of particle melting [36]. The 100% stoichiometry line was the lower threshold in Fig. 4.1 for practical applications as the condition below the 100% line led to an excessive amount of unburnt kerosene. The residual kerosene might contaminate the coating and would be a wastage of fuel. Furthermore, the total mass flow rate (red dash line) represents the total mass input into the combustion including kerosene and oxygen. The higher the total mass flow rate, the higher was the flame temperature. However, the influence of moving across the total mass flow lines on the flame temperature was not as obvious as moving across the stoichiometry lines [169].

A similar principle was applied when deciding the process parameter combinations for the HVOGF thermal spray process. However, the stoichiometry line under this condition was calculated with H_2, as the Top Gun setup utilises it as a fuel. The combustion of hydrogen was as follows:

$$H_2(g) + 0.5O_2(g) \rightarrow H_2O(g) \qquad \text{Reaction 4.2}$$

The parameters for both the HVOLF and the HVOGF trials of Ni50Cr were selected with the help of the stoichiometry and the total mass flow rate charts, and the detailed spray parameters are listed in Tab. 4.1.

HVOLF 1, HOVLF 2 and HVOLF 3 are the spray parameters for the HVOLF thermal spray process, and HVOGF 1 and HVOGF 2 are the parameters for the HVOGF thermal spray process. Moreover, the oxygen–fuel ratio and total mass flow, powder feed rate and standing-off distance for the deposition in the respective groups were adjusted according to previous experience.

Tab. 4.1 Process parameters of HVOLF and HVOGF thermal spray of Praxair Ni50Cr powder.

Parameter	HVOLF 1	HVOLF 2	HVOLF 3	HVOGF 1	HVOGF 2
Oxygen flow rate (L min $^{-1}$)	900	878	920	245	243
Fuel flow rate (L min $^{-1}$)	0.400	0.445	0.470	480	614
Oxygen stoichiometry (%)	117	100	100	100	80
Total mass flow rate (g s $^{-1}$)	26.5	26.5	28		
Gun traverse speed (mm s $^{-1}$)	5	5	5	5	5
Powder feed rate (g min $^{-1}$)	72	72	72	42	42
Carrier gas flow rate (L min $^{-1}$)	6	6	6	6	6
Standing-off distance (mm)	355	355	355	254	254
Number of passes	10	10	10	20	20

4.3 Influence of process conditions on the characteristics of as-sprayed HVOLF and HVOGF coatings

4.3.1 Phases and microstructure of feedstock powder

Phases and microstructure of feedstock powder have significant effect on the characteristics of thermal sprayed coatings. Hence, it is necessary to investigate and discuss those features of feedstock powder prior to the investigation of as-sprayed coatings. The XRD pattern of the Praxair Ni50Cr powder is provided in Fig. 4.2 together with the XRD pattern of the HVOF as-sprayed coatings for the comparison. The powder pattern consists of three main peaks (2θ = 43.5°, 51° and 76°) corresponding to the fcc γ–(Ni, Cr) solid solution and three minor peaks (2θ = 45°, 65.5° and 83°) corresponding to the bcc α–Cr according to the identification of the crystal structure using the powder diffraction file (PDF) database. The position of these main peaks shifted slightly to the left in the pattern as compared to that of the pure fcc

Ni phase peaks because of the expansion effect of the Cr atoms in the Ni lattice, which is in turn was caused by the rapid cooling of the (Ni, Cr) super-saturated solution during the gas atomisation process. The XRD pattern of the feedstock powder revealed that there were no oxide phases or at least the fractions of any oxides phases were below the limit of detection (around 1–2 wt.% [170]).

The morphology of powder particles is an important factor that can affect the thermal spray process and is illustrated in Fig. 4.3 (a). The figure shows the typical powder morphology of the inert gas atomised powders, as most of the particles were almost spherical. It also reveals the presence of some smaller satellite particles around the larger particles. The polished cross-section image of a powder particle shows a dendritic solidification pattern of the powder because of gas atomisation (Fig. 4.3 (b)).

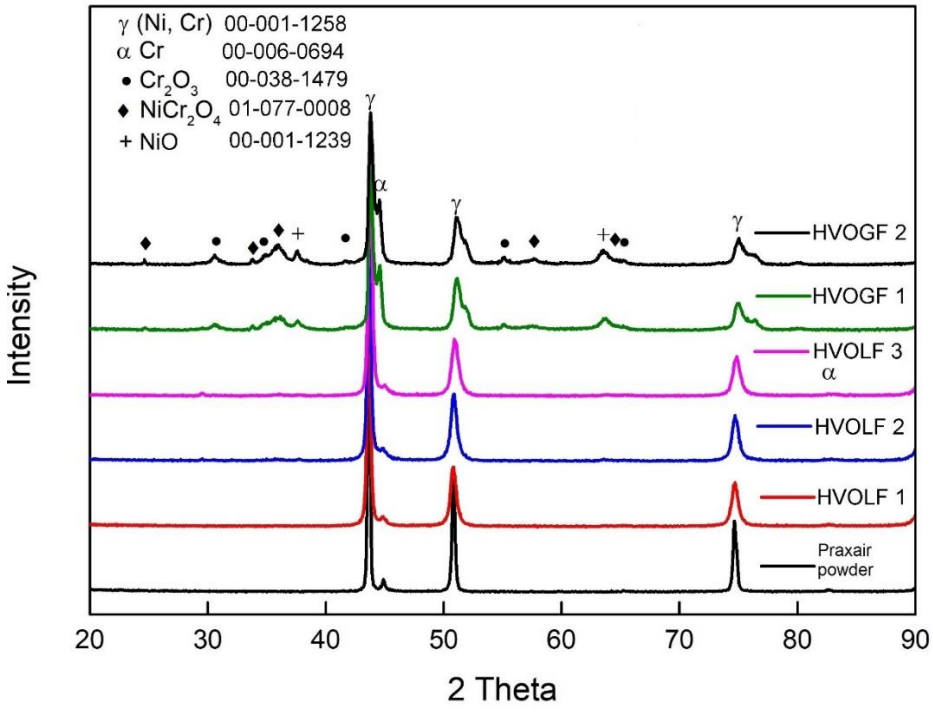

Fig. 4.2 XRD patterns of as-received Praxair feedstock powder, three HVOLF as-sprayed coatings and two HVOGF as-sprayed coatings.

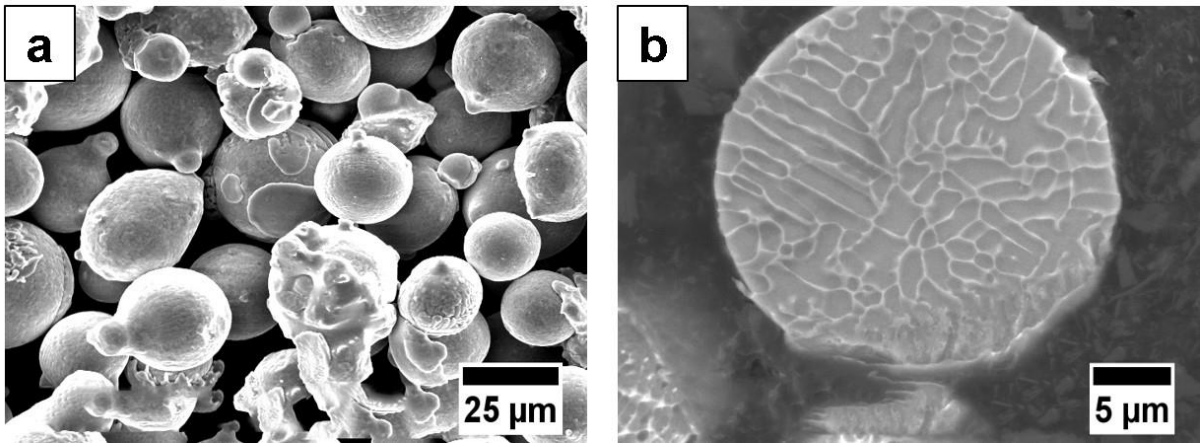

Fig. 4.3 SEM images of as-received Praxair Ni50Cr powder: (a) powder particles morphology, (b) polished cross-section of single powder particles showing dendritic pattern.

4.3.2 Phases and microstructure of as-deposited coatings

The XRD patterns of three HVOLF as-sprayed coatings in Fig. 4.2 show peak positions almost identical to the peak position of the powder, indicating that no new phases appeared during the spray process. Moreover, no obvious difference can be observed among the XRD patterns of these three coatings. The as-sprayed HVOLF coatings retained the main fcc γ–(Ni, Cr) solid solution phase. The corresponding peaks broadened because of the lattice distortion that occurred during the spray process [171]. The two minor α–Cr peaks ($2\theta = 65.5°$ and 83°) could not be clearly identified in the three as-sprayed coatings. Note that no oxide phase peaks were detected in the XRD patterns of the as-sprayed coatings within the detection limit of the XRD.

For the two HVOGF as-sprayed coatings, the evolution of the phases of the powder during the spray process was different to that observed in the case of the HVOLF coatings (Fig. 4.2) Several oxide phases were identified after the thermal sprayed process as can be seen from the corresponding XRD patterns in Fig. 4.2. The oxides

phases included NiO, $NiCr_2O_4$ spinel and Cr_2O_3. Furthermore, NiO (2θ = 38° and 63.5°) and $NiCr_2O_4$ (2θ = 18.5°, 31°, 36°, 57.5° and 64.5°) appeared to be the two major oxidation products in the as-sprayed coatings, as the intensity of their peaks was considerably larger than that of Cr_2O_3. The α–Cr phase could not be detected in the as-sprayed coatings; instead, three new peaks (2θ = 44°, 52° and 76.5°) corresponding to the fcc Ni phase were identified. Moreover, no obvious difference was observed between the phases of the two HVOGF coatings.

The top morphology of the as-sprayed coatings was examined using SE imaging and is displayed in Fig. 4.4 (HVOLF coatings) and Fig. 4.5 (HVOGF coatings). As can be seen from the six images of Fig. 4.4, a large amount of unmelted/semi-melted powder particles remained on the top surface of the as-deposited coatings, which had a hemispherical geometry. This was representative of the coating morphology typically observed after the HVOLF thermal spray process, in which powder particles are not fully molten because of the low flame temperature of the liquid fuel (usually kerosene) and the short dwell time at high temperature. However, more un-melted particles were observed on the surface of the HVOLF 1 coating (Fig. 4.4 (a) and (b)) than on the surfaces of HVOLF 2 the coating (Fig. 4.4 (c) and (d)) and the HVOLF 3 coating (Fig. 4.4 (e) and (f)), indicating that the powder particles during the spray process under the HVOLF 2 and HVOLF 3 conditions were sufficiently heated and thus experienced more significant deformation, verifying the effect of oxygen–fuel ratio on the microstructure of the as-deposited coatings.

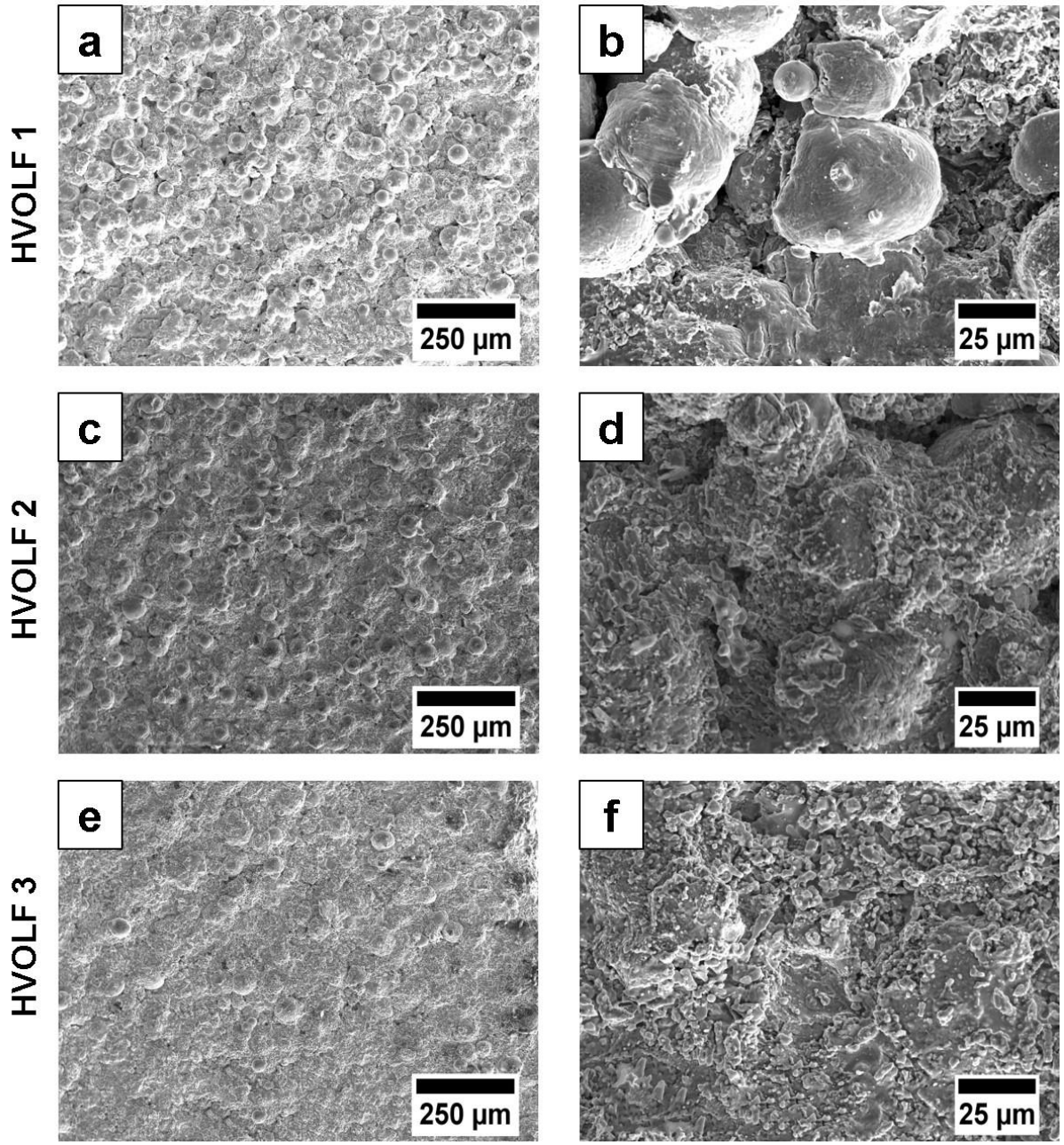

Fig. 4.4 SEM SE top surface morphology of as-sprayed HVOLF coatings in two magnifications: (a & b) spherical and unmelted splats at the surface of HVOLF 1 coating, (c & d) semi-melted splats in deformation at the surface of HVOLF 2 coating, (e & f) semi-melted splats in larger deformation at the surface of HVOLF 3 coating.

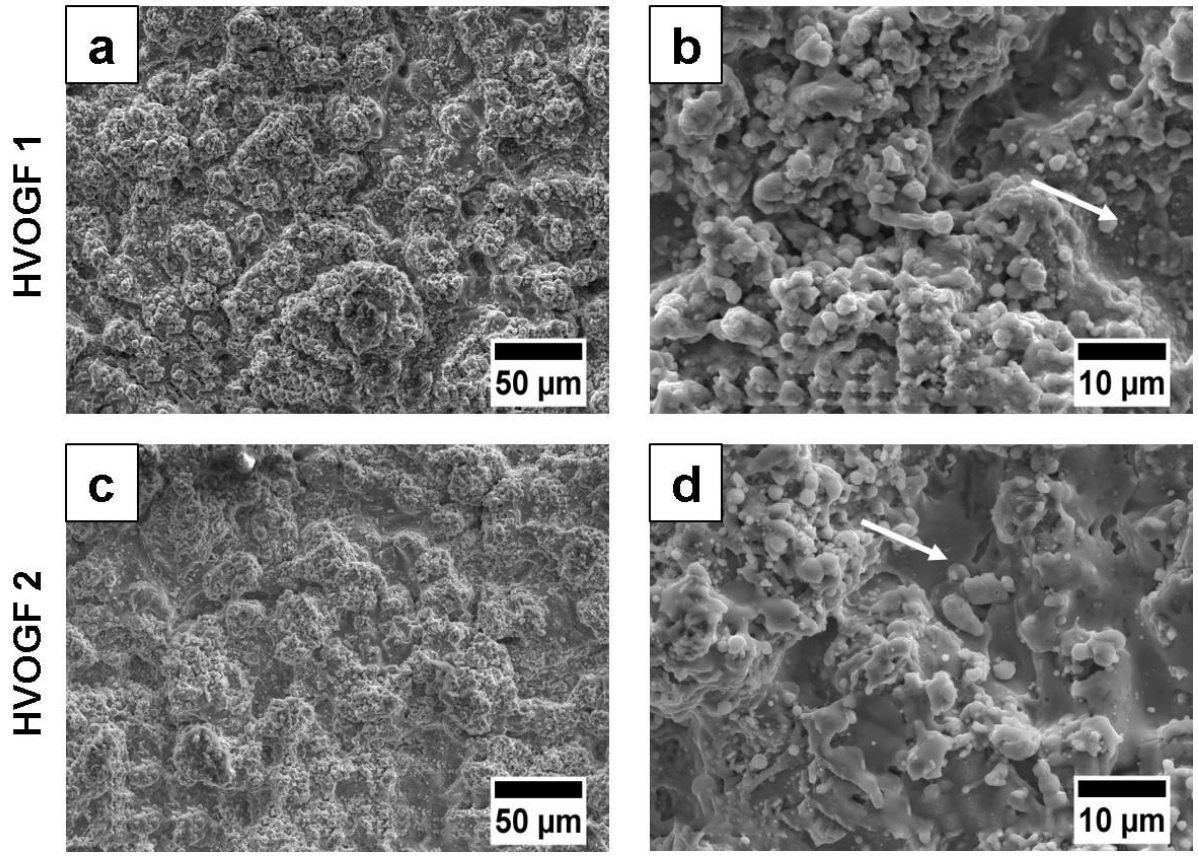

Fig. 4.5 SEM SE top surface morphology of as-sprayed HVOGF coatings in two magnifications: (a & b) semi-melted splats in large deformation at the surface of HVOGF 1 coating, (c & d) semi-melted splats also in large deformation at the surface of HVOGF 2 coating.

For the HVOGF as-sprayed coatings, no un-melted splats were observed on the top surface of both the coatings and the deformation of the powder particles (splats) during the spray process was more significant than that of the powder in the HVOLF spray process, as revealed by a comparison of Fig. 4.5 and Fig. 4.4. Fig. 4.5 (a) and (c) revealed that none of the splats retained the spherical geometry and all of them were flattened to the lamellar geometry after the thermal spray process. However, the small satellites on the surface of the large splats (white arrows in Fig. 4.5 (b) and (d)) still retained the original spherical geometry. This phenomenon indicated that these small satellites in the spherical geometry had a lower degree of deformation than the large

splats during the thermal spray process. Interestingly, this phenomenon was not observed in the case of the HVOLF thermal spray process. As shown in Fig. 4.4 (d) and (f), most of the minor satellites on the surface of the splats seemed to have a cubic geometry, which was obviously different from that of the feedstock powder particles. There were no oxides that could be observed in the morphology of the HVOGF coatings at the magnification in Fig. 4.6 (b) and (d). Yet, the XRD pattern confirmed their existence.

Fig. 4.6 displays the cross-section images of three HVOLF coatings obtained using BSE imaging. The black features above the coating cross-section is the black conductive resin. All the three images for the HVOLF coatings (Fig. 4.6 (a), (c) and (e)) showed a typical lamellar thermal sprayed microstructure. No delamination and cracks were observed between the coating and the substrate in any of the coatings. All the as-sprayed coatings were around 250 µm thick, and porosities were present in the top layer (~50 µm). The porosity was most obvious in HVOLF 1, as shown in Fig. 4.6 (a). The grey pixels in the BSE images around the splats that were darker in the images indicated the existence of a thin oxide layer [172]; this was also confirmed by the EDX analysis.

Note from Fig. 4.6 (a), (c) and (e) that there was less oxide surrounding the splats in the HVOLF 1 coating than in the HVOLF 2 and HVOLF 3 coatings. The higher magnification images of the cross-sections of the three coatings are shown in Fig. 4.6 (b) (d) and (f). In the case of the HVOLF 1 coating, the pores and the gaps between the splats (thin black area surrounding the splats) were observed in Fig. 4.6 (a). The microstructure of the HVOLF 2 and HVOLF 3 coating was better than that of HVOLF 1 coating, as there was almost no gaps and pores among the splats. It can also be

concluded that there were more grey pixels in Fig. 4.6 (d) and (f) than in Fig. 4.6 (b). These grey features were oxides according to previous research on similar coatings [172]. The HVOLF 2 and HVOLF 3 coatings experienced more intense oxidation during the spray process.

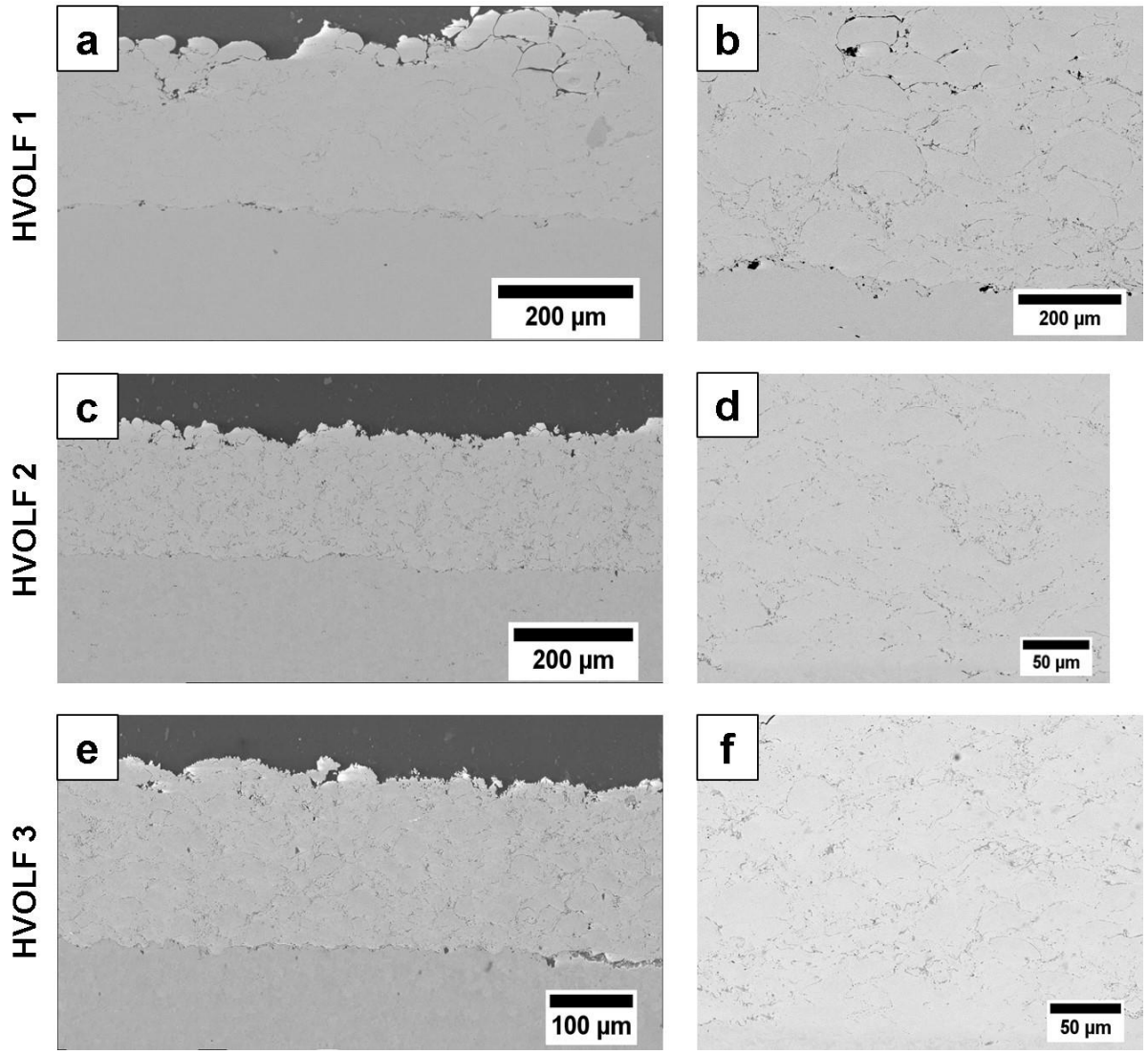

Fig. 4.6 SEM BSE cross-section images of HVOLF as-sprayed coatings: (a, c & e) microstructure of coatings in total view showing the thickness, the porosity, and the interface bonding of coatings, (b, d & f) microstructure of coatings at larger magnification showing the splats connection and the oxidation degree of splats in each coating.

The HVOGF coatings shown in Fig. 4.7 (a) and (c) were around 300 µm in thickness and had a good coating–substrate interface without any delamination or cracking at the boundary between the coating and the substrate.

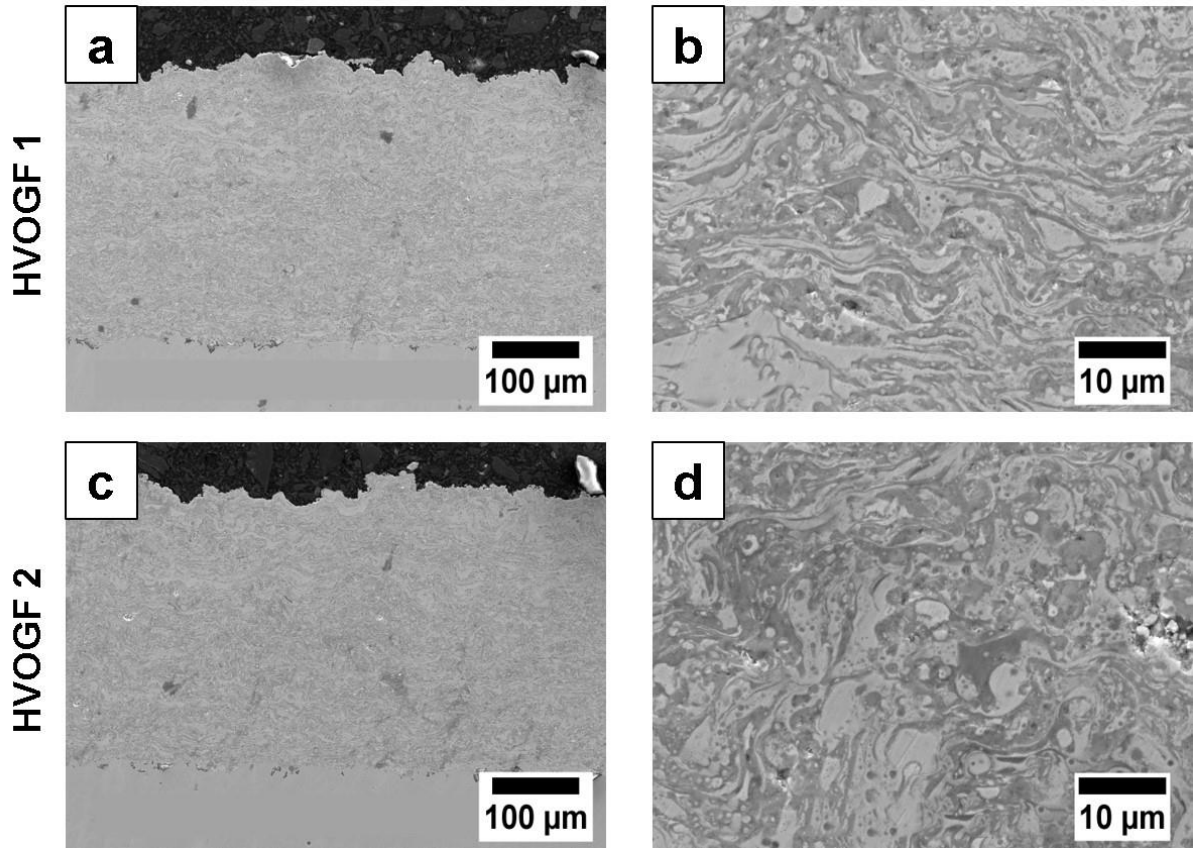

Fig. 4.7 SEM BSE cross-section images of HVOGF as-sprayed coatings: (a & c) microstructure of coatings in total view showing the thickness, porosity, and interface bonding of coatings; and, (b & d) microstructure of coatings at larger magnification showing the large splat deformation, splat connection and oxidation degree of splats in each coating.

The large deformation of the lamellar splats was the most obvious feature of these coating microstructures. The black features surrounding the splats were oxides according to the EDX analysis. Fig. 4.7 (b) and (d) clearly indicated the considerably more oxidation of the powder particles in the HVOGF thermal spray process than in the HVOLF thermal spray process. However, it was difficult to decide which coating

(HVOGF 1 and HVOGF 2) had more oxidation in terms of quantity just by using Fig. 4.7 (b) and (d). No obvious difference was observed between these two coatings.

4.3.3 Oxygen contents of freestanding coatings

The LECO infrared oxygen analysis results for all the five coatings are shown in Fig. 4.8. The oxygen content of the as-sprayed coatings represents the content of the oxide produced during the thermal spray process, as the oxygen is only present in the oxide compounds of Ni and Cr.

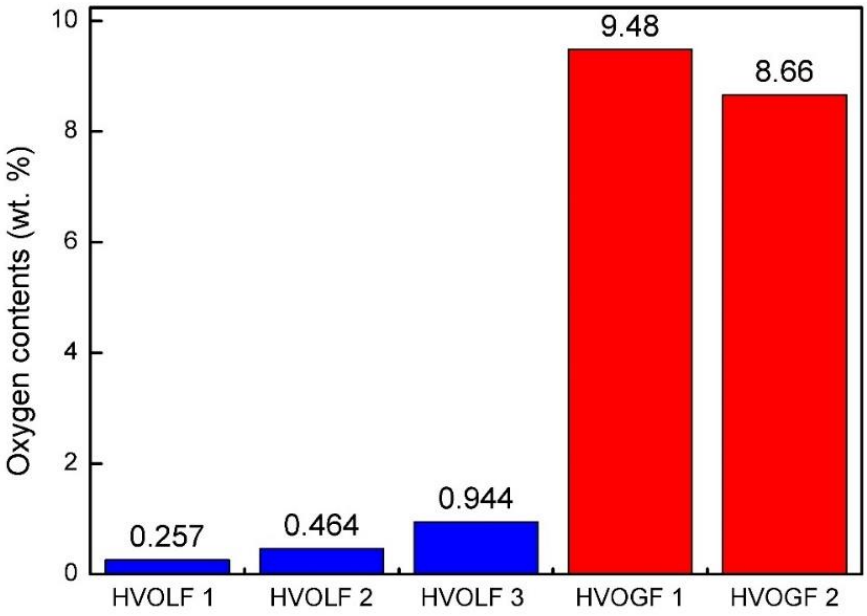

Fig. 4.8 Oxygen contents of HVOLF and HVOGF freestanding coatings that are measured using LECO infrared method.

As compared to the oxygen contents of the HVOGF coatings, the corresponding indexes of the HVOLF coatings do not have the same magnitude. The oxygen contents of the HVOLF 1, HVOLF 2 and HVOLF 3 coatings do not exceed 1 wt.%, and

the HVOLF 3 coating has the highest level (0.944 wt.%). While in the HVOGF coatings, the oxygen contents are almost around 10 wt.%.

4.3.4 Porosity of freestanding coatings

Mercury intrusion porosimetry (MIP) is the most accurate method to provide information about the size distribution of the pores and the volume percentage of the open inter-connected porosity. This information is useful for evaluating the oxidation performance of the coatings, as pores inside the HVOF coatings are the main transport path of the oxygen ions [173]. The diffusion of oxygen ions and the other corrosive species is considerably faster in the pores than in the metal and the oxide scales [174]. The incremental intrusion of mercury (Hg) versus the pore sizes in all the five as-sprayed coatings is plotted in Fig. 4.9.

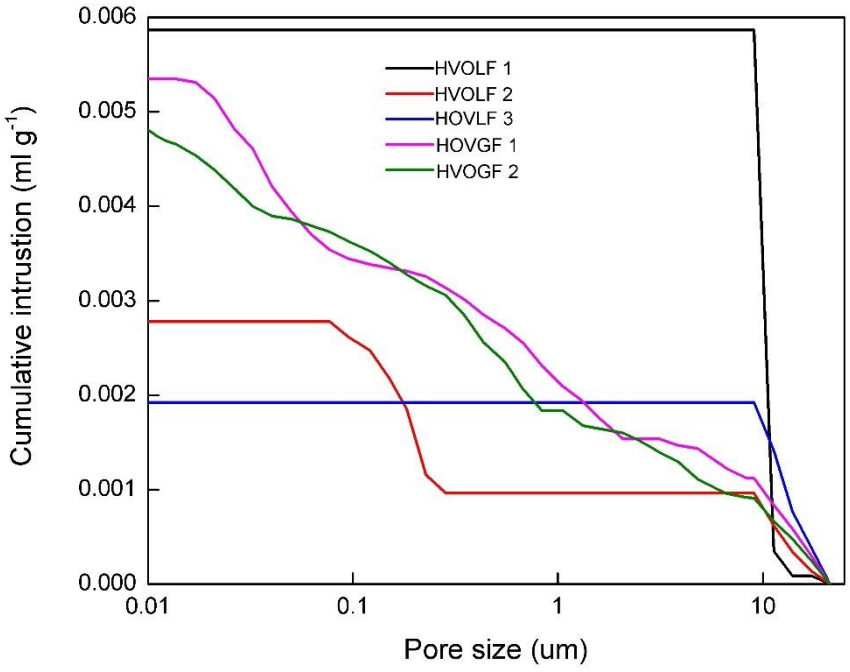

Fig. 4.9 Incremental intrusion of mercury *vs*. pore size of five coatings.

The size distribution of the pores inside the HVOLF 1 coating was concentrated at 8–13 µm and 13–20 µm. The size distribution of the pores inside the HVOLF 2 coating fell into two distinctive ranges; i.e., one distribution was between 0.06–0.3 µm and the other distribution was between 8–20 µm. For the HVOLF 3 coating, the size distribution of most of the pores was 8–20 µm. For coating HVOGF 1, the size distribution of the pores almost occupied all the entire considered range except 0.09–0.2 µm and 2–2.5 µm. The HVOGF 2 coating also had a wide range of pore size distribution except several minor pore sizes such as 0.04 µm, 0.83 µm and 8.2 µm.

Fig. 4.10 summarises the cumulative intrusion of mercury versus the pore sizes for all the coatings. The HVOLF 1 coating had the largest cumulative intrusion (0.0059 mL g $^{-1}$), which was almost twice that of the HVOLF 2 coating (0.0028 mL g $^{-1}$) and the HVOLF 3 coating (0.0019 mL g $^{-1}$). For the HVOGF coatings, the cumulative intrusions were 0.0053 mL g $^{-1}$ (HVOGF 1 coating) and 0.0049 mL g $^{-1}$ (HVOGF 2 coating) respectively. Ignoring the oxides in the coating and knowing the density of the feedstock material, the cumulative intrusion of mercury can be converted into the volume percentage of porosity by using the following equation:

$$porosity(vol.\%) = V_{Hg}/V_{bulk} \times 100\% \quad \text{Eq. 4.1}$$

where V_{Hg} is the cumulative volume of the mercury intrusion and V_{bulk} is the bulk volume of the freestanding coating, which can be determined from the density of the Ni50Cr powder and the mass of the coating.

Taking the density of the feedstock powder as 8.2 g cm $^{-3}$ as the density of the freestanding coatings, porosities of the coatings were calculated to be: 4.83 vol.% in

the HVOLF 1 coating, 2.30 vol.% in the HVOLF 2 coating, 1.59 vol.% in the HVOLF 3 coating, 4.35 vol.% in the HVOGF 1 coating and 4.02 vol.% in the HVOGF 2 coating.

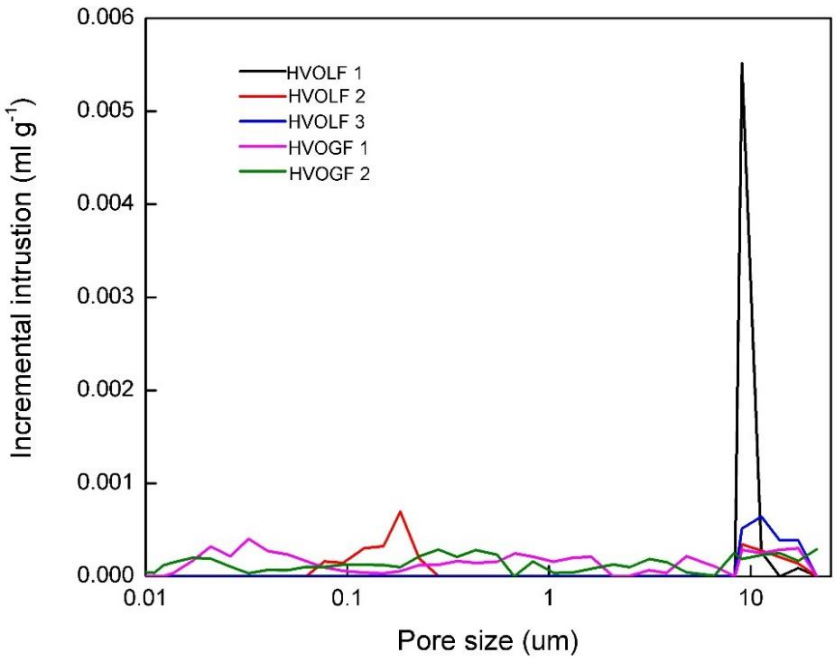

Fig. 4.10 Cumulative intrusion of mercury *vs.* pore size of five coatings.

4.3.5 Effect of fuel type on the characteristics of HVOF thermal sprayed coatings

The feedstock powder contains a range of particle sizes and these particles follow different trajectories through the gas stream during the thermal spray process. In the HVOF thermal spray process, some particles arrive at the point of impact in the semi-molten and/or molten condition, and the others in a fully solid condition [175]. Extensive deformation of the particle occurs if the particle arrives in a semi-molten state, whereas, the plastic deformation of the fully solid particles is more difficult. In the HVOGF coatings, the splats are mostly lenticular because of extensive melting and deformation upon impact. The metallic splats were 5–15 μm thick and, were

separated by 1–2 μm thick oxide sheets, as shown in Fig. 4.7 (b) and (d). Hewitt calculated the flame temperatures and the excess oxygen in the flame for a range of gases and oxygen–fuel ratios [176]. The combustion of hydrogen and oxygen can theoretically reach 2850 °C, and the melting temperature of the Ni50Cr alloy according to the phase diagram is 1345 °C [82]; albeit, the particle temperature in the spray plume depends on the residence time and the size of the particles, as 2850 °C was more than two times 1345 °C.

The coating built up in the HVOLF thermal spray process is the same as that described in the HVOGF thermal spray process, but with a reduced degree of particle melting. It is generally accepted that the particle bonding in the HVOLF thermal spray process is better, as a significant proportion of particles from the powder arrive in the unmolten state. In the HVOLF thermal spray process, the particles are injected directly into a supersonic high temperature jet whereas in the HVOGF thermal spray process, the particles enter the slow, subsonic gas before being accelerated down the nozzle. Consequently, the residence time of the particles in the HVOLF thermal spray process is shorter, meanwhile, the particles are exposed to lower gas temperatures. Therefore, only a thin shell on the surface of the powder particles melted in the HVOLF thermal spray process, whereas a considerably larger proportion of the particles melted in the HVOGF thermal spray process (for a given particle size). This high degree of melting also resulted in the higher oxidation of the HVOGF coating; this is proven by the LECO infrared oxygen analysis of the five coatings considered in this study. Although the HVOGF 2 coating was sprayed at the 80% oxygen stoichiometry, excess oxygen remained in the flame because of the decomposition of the combustion products at high temperature and the turbulent mixing of the gas steam with air [175], which

promoted the oxidation of the powder particles during the flight from the spray gun nozzle to the substrate.

The degree of particle melting could also explain the differences in the porosity measured by MIP. The level of porosity in the HVOGF coatings (HVOGF 1 and HVOGF 2 in Fig. 4.10) was larger than that of the HVOLF coating except in the case of the HVOLF 1 coating. This difference is mainly attributed to the poor inter-splat bonding (oxide around the splats) and localised pinhole pores in the HVOGF coating. The exception of the HVOLF 1 coating might be attributed to its poor microstructure, as shown in Fig. 4.6 (a) and (b). The large pores on many of the top layers contributed to the increase in the MIP curve for the HVOLF 1 coating. In the HVOLF coatings, the porosities were mostly in the range of 0.007–0.03 μm, and these pores were mostly present at the inter-splat boundaries. A typical powder particle in the thermal spray process consists of a fully molten liquid shell, a solid unmolten core and a semi-solid region due to the temperature gradient [158]. This liquid shell can react with oxygen in the flame and results in the formation of the oxides in the coating. The inter-splat bonding also relies on this liquid shell, and sub-micrometre porosities can arise when the particles are not packed well.

In the XRD patterns of the HVOGF 1 and HVOGF 2 coatings, significant peak broadening of the main fcc peaks was observed in the coating as compared to the gas atomised powder. Peak broadening in the thermal spray process is generally attributed to the microstrain and the fine grain size. Both factors are present in both two types of coatings. The microstrain in the HVOLF 1, HVOLF 2 and HVOLF 3 coatings is probably higher because of the solid particle impact. Ni peaks were observed in the XRD pattern of the HVOGF coating; this could be attributed to the reduced alloying content of the

coating. The Ni peaks were also attributed to the presence of Cr_2O_3 and the $NiCr_2O_4$ oxides found in the coating. Zhang *et al.* [158] reported that during the heating of the powder the alloying Cr is preferentially oxidised from the fully molten zone where the mass transport is considerably high. $NiCr_2O_4$, NiO and Cr_2O_3 were formed on the particle surface, leaving a chromium-depleted liquid droplet that solidifies on the impact of the particle with the substrate. Indeed, this was observed in the EDX scans where the centre of the splats contained more Cr than the periphery of the splats. Numerical models indicated that small particles followed the gas temperature and velocity more closely and therefore, reached relatively high temperatures [177]. It was evident from the microstructure of the thermal sprayed coatings that the particles became hot to melt. Molten particles were covered with an oxide skin, and the oxidation of Cr and the other elements proceeded relatively slowly from the liquid. If the oxide film ruptured, the oxidation proceeded more rapidly. The melting point of Cr_2O_3 is 2440 °C [178] and only the smallest particles reached this temperature. SEM revealed that a large number of the powder particles were less than sub-ten micrometres in size; this could account for the formation of nickel-rich regions in the coating. With respect to the composition of the oxide phase, the principal oxide phase for the oxidation of the HVOGF coatings was $NiCr_2O_4$ with small amounts of Cr_2O_3 and NiO. The Ellingham diagram data on the free energies regarding with the formation of oxides shows that the thermodynamic stability of the oxides increases from Ni to Cr. NiO, $NiCr_2O_4$ and Cr_2O_3 can all be formed in the NiCr-based alloys, but spinel is thermodynamically favoured at a higher oxygen partial pressure [20] and both Cr_2O_3 and spinel have been reported to form during the initial, transient oxidation.

The oxidation of NiCr alloys whose Cr content > 20 wt. % is expected to produce only Cr_2O_3 (selective oxidation) rather than the mixture of Cr_2O_3, NiO and $NiCr_2O_4$ (transient oxidation) [14]. However, in the case of the HVOGF thermal spray of Ni50Cr powder of this study, the oxidation products of Ni50Cr powder after the in-flight oxidation were the transient oxidation one, instead of the selective oxidation one. This phenomenon indicated that the completion of the selective oxidation of high-Cr alloys need longer time than that was taken during the HVOGF process; i.e. the coverage of the Cr_2O_3 oxide layer on the island of $NiCr_2O_4$ needs exposure of enough time, which has not been reported by previous researchers.

4.3.6 Effect of process parameters on the coatings

By altering the oxygen–fuel stoichiometry, it is possible to change the temperature and the exit velocity of the gas, and the momentum of the particles as they impact onto the substrate, which in turn affects the porosity and the bonding of the particles [179]. This explains the difference in the microstructure and porosity between the HVOLF 1 coating and the HVOLF 2 coating, where the HVOLF 1 coating was sprayed at a higher oxygen–fuel ratio (excess oxygen in the flame). The oxygen stoichiometry of the HVOLF 2 coating was 100%, which was lower than that of the HVOLF 1 coating. There was no excess oxygen for the combustion of kerosene during the spray of the HVOLF 2 coating, providing a higher gas flow rate and a higher exit velocity [177]. Wanphut [177] conducted a particle image velocimetry (PIV) study with DPV 2000 on the thermal spray process of an MCrAlY powder; it was reported that the average particle temperature increased and the average particle velocity decreased with the decrease in the oxygen stoichiometry. The particles in the HVOLF 2 coating were largely deformed because of the relatively high impact velocities, as compared to the HVOLF

1 coating. If the oxygen stoichiometry is greater than 100%, an oxygen-rich mixture or an oxidising environment is created by the unconsumed oxygen in the flame. Such a condition could result in the excessive oxidation of the molten powder particles if the powders are injected in the upstream of the gun during the HVOLF thermal spray process; however, the powders are injected in the downstream of the gun, and this excess oxygen does not contribute to the increased oxidation of the metallic coatings.

In the HVOGF thermal spray process, the powder particles are injected into the combustion chamber directly, and the oxygen ratio in the oxygen–fuel mixture has an obvious influence on it. When the oxygen stoichiometry was 100%, more oxides was produced on the HVOGF 1 coating during the spray, and thus the oxygen content of the HVOGF 1 coating was higher than that of the HVOGF 2 coating. Moreover, the high oxygen stoichiometry promotes the complete combustion of hydrogen and create a flame of a high temperature, which also contributed to the oxidation of the powder particles during the spray. The porosity of the HVOGF 1 coating was also larger than that of the HVOGF 2 coating. This is attributed to the fact that the large amount of oxides around the splats reduced the inter-splat bonding, as the strength of the mechanical bonding between the splats decreased in the case of very brittle oxide than in the case of plastic alloy contacts.

For the HVOLF coatings, the influence of the total flow rate on the in-flight particle temperature and velocity is less obvious; although it was suggested that the particle velocity increases with an increase in the total flow rate. A comparison of the microstructure of the HVOLF 2 and HVOLF 3 coating revealed that the degree of particle deformation was similar on the cross-section; however, the topography of the coatings showed the splashing of the splats, possibly due to the relatively high impact

energies of the splats in the HVOLF 3 coating. No obvious difference in porosity levels was observed between the HVOLF 2 coating and the HVOLF 3 coating in the MIP analysis. The major difference between these two coatings was investigated while determining the oxygen content of the coatings. The HVOLF 3 coating had almost twice the level of oxygen of the HVOLF 2 coating, which suggested that the particles went through a higher degree of in-flight oxidation. Although both the coatings were sprayed at a similar oxygen–fuel ratio, the higher total flow rate contributed to this higher level of oxidation. The most plausible explanation is that the particles achieved a higher temperature that resulted in this higher degree of oxidation.

4.4 Selection of candidate HVOF coatings in subsequent oxidation/corrosion tests

4.4.1 TGA results of coatings

The TGA results of five freestanding coatings for 4 h at 700 °C are shown in Fig. 4.11. The mass gain of these five coatings was attributed to the external oxidation of coating surface as well as the internal oxidation of splats inside the coating since there was porosity and pre-formed oxide surrounding the splats, which are the main transport path for oxidising ions. However, the contribution of the internal oxidation to the mass gain was little when compared with the external oxidation. The reaction surface area, in which oxygen contact with the fresh coating alloy, was much larger in the case of the external oxidation. The mass gain of the HVOLF 1 coating was about 0.536 mg cm^{-2} after 4 h, while the mass gain of the HVOLF 3 coating is 0.337 mg cm^{-2} and the mass gain of the HVOLF 2 coating was 0.135 mg cm^{-2}. The mass gains of the HVOGF coatings (HVOGF 1 and HVOGF 2) sample were 0.232 mg cm^{-2} and 0.166 mg cm^{-2}, respectively.

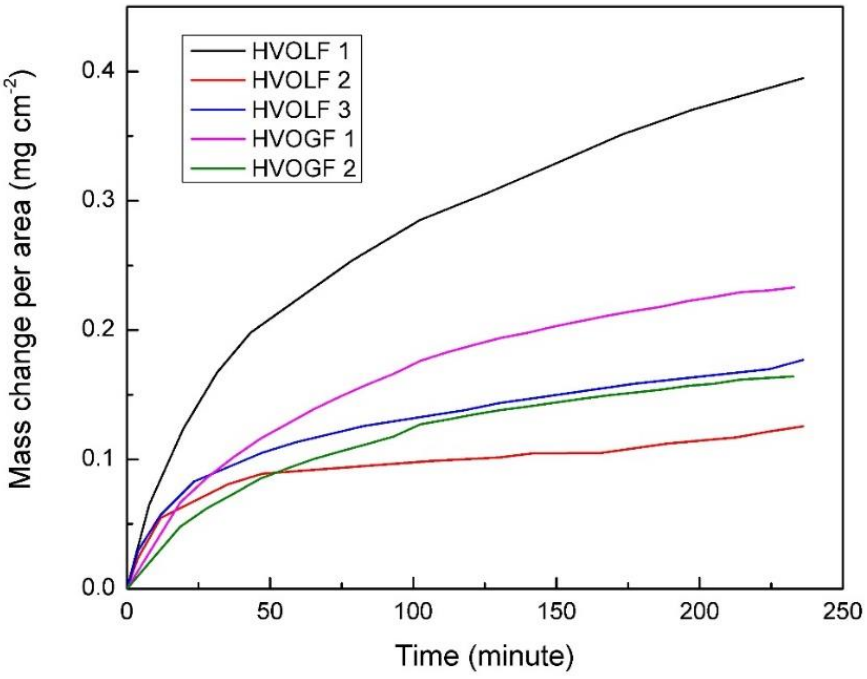

Fig. 4.11 TGA results of five freestanding coatings for 4 h at 700 °C (mass gain per area) showing the rank of weight change of coatings due to the oxidation process.

Traditionally, the square of the specific mass change versus time plot (Fig. 4.12) can be used to determine the oxidation rate [14, 20, 64]. The calculation the oxidation rate has been described in the experimental chapter. This method is usually applied to alloys/coatings that can produce a dense and thick protection oxide scale and whose rate of oxidation depends on the diffusion rate of the oxidation ions through the oxide scale [180]. In this study, the oxide does not form a dense scale on the top surface of the coating even after 100 h of air oxidation (the related are presented in the following section). Therefore, the practicality of fitting straight lines to curves is doubtful.

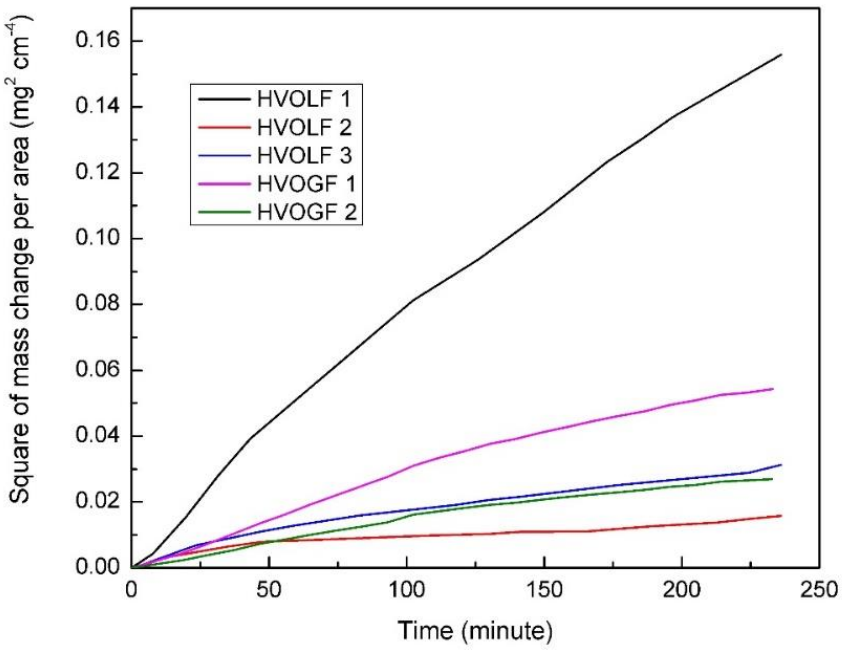

Fig. 4.12 TGA results of five freestanding coatings for 4 h at 700 °C (square mass gain per area) showing the rank of weight change of coatings due to the oxidation process.

The HVOLF 2 coating and HVOGF 2 coating had the lowest oxidation rates in each group, as indicated in Fig. 4.12. According to this rank, the HVOLF 2 coating and HVOGF 2 coating were believed to have better air oxidation resistance and were thus selected as the candidates for the subsequent isothermal oxidation/corrosion for longer time tests. For the ease of description, the HVOLF 2 and HVOGF 2 coatings are hereinafter referred to as HVOLF and HVOGF simply while presenting their high temperature exposure results along with those of the cold sprayed and laser cladded coating.

4.4.2 Short-term air oxidation of coatings

Tab. 4.2 summarised the porosity, oxygen content and oxidation performance (specific mass gain) of all the coatings to compare the oxidation performance of various

coatings. For ease of reference, the coatings deposited using the same thermal spray process were compared in the respective group initially. Then, the coatings have the best oxidation performance representing each group will be compared again.

Tab. 4.2 Oxygen contents, porosity and TGA mass gain per area of five coatings.

Coating	HVOLF 1	HVOLF 2	HVOLF 3	HVOGF 1	HVOGF 2
Oxygen content (wt.%)	0.257	0.464	0.944	9.48	8.66
Porosity (vol.%)	4.83	2.30	1.59	4.35	4.02
Mass gain per unit area (mg cm $^{-2}$)	0.536	**0.135**	0.337	0.232	**0.166**

The oxidation performance of the HVOLF 1 coating was worse than that of the HVOLF 2 and HVOLF 3 coatings, according to the TGA curves (Fig. 4.11 and Fig. 4.12). The HVOLF 1 coating had the lowest amount of oxide in the coating but the highest level of porosity. The porosity of the coating allowed oxygen to seep through it, which led to the oxidation of the splat boundaries. The pre-existing oxides from the as-sprayed coatings were also oxidised, contributing to the kinetic behaviour. The HVOLF 1 coating had the lowest amount of oxide content (no oxide was detected in the XRD within the detection range), and hence, the oxidation of the pre-existing oxides was not a major contributor. Moreover, at higher temperature, diffusion takes place, which can reduce the inter-splat porosity, but the exposure temperature in this study was not sufficiently high and/or the exposure time was not sufficiently long as the pre-existing splat boundaries could not be neglected. The porosity of the HVOLF 1 coating was almost two times higher than that of the rest of the coatings, and this high level of porosity was the key factor influencing the high parabolic rate constant.

Considering that the oxidation kinetics of the HVOLF 2 and HVOLF 3 coating, it is found that the second-stage rate constant of the coating HVOLF 2 was half of that of

the HVOLF 3 coating in spite of the fact that both the coatings had similar rate constants during the first stage of oxidation (red and blue curves in Fig. 4.12). According to the MIP measurements, both the coatings had similar porosity levels, and thus, the main difference here was the level of oxides.

The oxygen content of the HVOLF 3 coating was almost twice that of the HVOLF 2 coating, which implied considerably high amounts of inter-splat oxides and the oxides surrounding the splats in the HVOLF 3 coating. It has been reported in the case of bulk high-chromium alloys (Cr wt.% > 20%) [20] that the previously formed oxides at the alloy surface can aggregate to form a dense chromia scale to prevent the fresh metal surface under the scale to come into contact with the oxidising atmosphere [14]. However, the oxides surrounding the splats in the thermal sprayed coating do not have such a function, as they are less dense and cannot aggregate to their entirety. In contrast, the oxides surrounding the splats act as an oxidising ion transport path like pores do. Therefore, the fresh metal in the splats and the splats under the several top layers come into contact and react with the oxidising atmosphere; i.e. oxides in the thermal sprayed coating formed during the spray process are detrimental to the oxidation resistance of coatings. In coatings with similar porosity levels, the lower level of oxides led to a better oxidation performance.

In addition, the morphology and the size of the oxides on the top surface of the three coatings can result in different oxidation performance according to the SEM characterisation results of the top morphology of coatings after air oxidation [169]. The oxides on the top surface of the HVOLF 2 coating were of the largest in size, which implied that the density of their grain boundary was also the lowest. As the ions and atoms that participate in the oxidation process have the largest diffusion rate at the

grain boundary [181], a smaller portion of the grain boundary can slow down the transport and the contact of the oxidation ions and atoms, thereby retarding the further oxide scale growth.

In the case of the HVOGF coatings, the HVOGF 2 coating performed better in air than the HVOGF 1 coating. The oxidation performance agreed with the expectation of the porosity, oxygen content and oxide growth on the top surface. The HVOGF 2 coating had lower porosity and lower oxygen content, thus performing better in the high temperature oxidation than the HVOGF 1 coating. As mentioned above, porosity is the transport path for the oxidation ions, as these ions have largest diffusion rate inside the pores. In traditional view, more oxide means better oxidation resistance, as a large amount of oxide can build a thick oxide scale, acting as a barrier to insulate the fresh alloy and metal from the oxidation by increasing the difficulty of the ion movement. However, this view is not corroborated in this study of the thermal sprayed coatings, as the oxide in the as-sprayed coatings did not mainly form an oxide scale on the surface. Instead, most of the oxides were distributed in the area surrounding the splats. The oxides surrounding the splats, as mentioned above, provided another oxidising ion transport path like pores; thus, fresh metal inside the splats and the splats under the several top layers could come into contact with the oxidising atmosphere. In the thermal sprayed coatings with similar porosity levels, the lower level of oxides leads to a better oxidation performance. This principle also applied to the HVOGF coatings. The top morphology of the HVOGF 1 and HVOGF 2 coatings after 1 h of oxidation [182] clearly indicated that the oxides on the surface of the HVOGF 2 coating grew and developed more slowly than those on the surface of the HVOGF 1 coating in spite

of the fact that on both these as-sprayed coatings, the same oxides were detected (Cr_2O_3, NiO and $NiCr_2O_4$).

4.4.3 Determination of candidate coatings

Calvarin *et al.* [128] reported a two-stage oxidation kinetic behaviour of Ni20Cr at 700 °C where the first stage obeys a parabolic law and the second stage follows a complete law (with a linear and a parabolic component). The rate constant for Ni20Cr at 700 °C were 3.8 $\times 10^{-4}$ mg ^{2} cm $^{-4}$ min $^{-1}$ for the first stage and 2.6 $\times$ 10 $^{-7}$ mg ^{2} cm $^{-4}$ min $^{-1}$ for the second stage. This method may be useful in the investigation of the kinetic behaviour of the HVOF thermal sprayed coatings in this study. This method was only applied to the HVOLF 2 and HVOGF 2 coatings, as both had best oxidation resistance in each category according to Fig. 4.11 and Fig. 4.12 and were selected as the candidates for subsequent oxidation/corrosion exposure. The air oxidation of the HVOLF 2 coating and the HVOGF 2 coating was assumed to follow a two-stage mechanism; the fitting results is shown in Fig. 4.13 . The rate constant for the HVOLF 2 coating in the first stage is 1 $\times$ 10 $^{-4}$ mg ^{2} cm $^{-4}$ min $^{-1}$, which reduces to 6 $\times 10^{-5}$ mg ^{2} cm $^{-4}$ min $^{-1}$ in the subsequent stage of oxidation. For the HVOGF 2 coating, the first stage of oxidation ends at around 100 minutes, and the corresponding rate constant is 2 $\times$ 10 $^{-4}$ mg ^{2} cm $^{-4}$ min $^{-1}$. The rate constant decreases to 8 $\times$ 10 $^{-5}$ mg ^{2} cm $^{-4}$ min $^{-1}$ in the second stage.

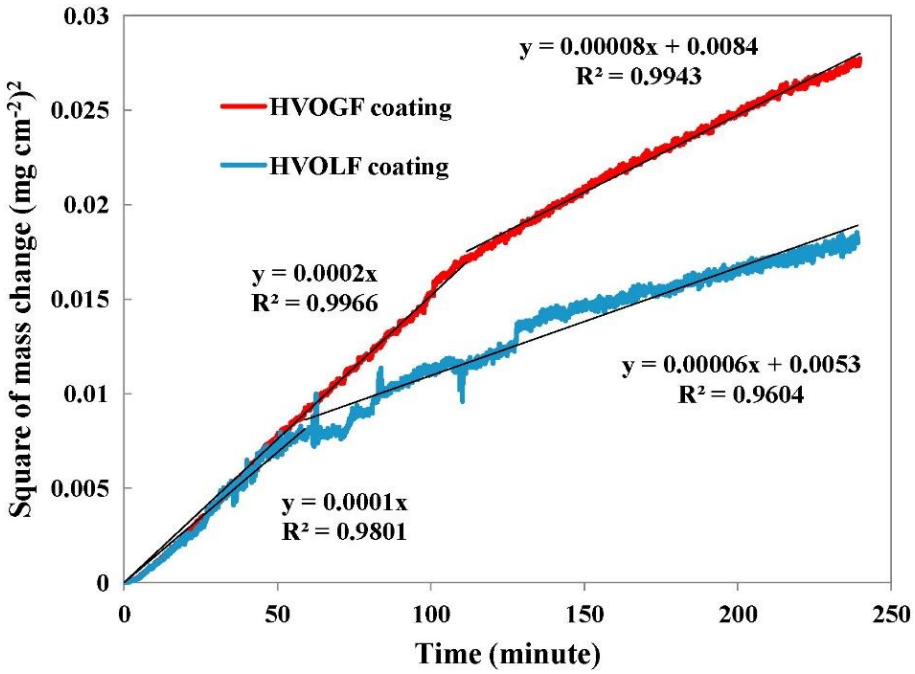

Fig. 4.13 Two-stage straight line fitting result of HVOLF 2 and HVOGF 2 TGA curves.

The abovementioned results can be compared with those obtained from the experiment of the bulk alloys of similar compositions, which were reported in the literature. Another study by Essuman *et al.* [183] reported the oxidation kinetics of Ni25Cr in an atmosphere of Ar–20% O_2 at 1100 °C, which is 1.66 × 10 mg ^{2} cm $^{-4}$ min $^{-1}$. Therefore, the results obtained for the best HVOLF and HVOGF coatings in this study were broadly in line with the reported data [128, 183]. The surface morphology and the microstructure of the HVOF thermal sprayed coatings vary from those of the bulk alloys; therefore, some degree of variation is expected. The parabolic behaviour indicates that the HVOLF and HVOGF coatings can develop a barrier for air oxidation.

For the ease of reference, HVOLF 2 and HVOGF 2 thermal sprayed coatings are called HVOLF and HVOGF coatings immediately in the following discussion of the oxidation/corrosion performance of the HVOF thermal sprayed coatings.

4.5 Characteristics of the as-sprayed cold sprayed and laser cladded coatings

The cold sprayed coating shown in Fig. 4.14 was deposited using a custom-made cold spray gun made by Xi'an Jiaotong University in China. The set of parameters recommended by the research group was adopted to deposit the oxidation/corrosion exposure coatings in this study.

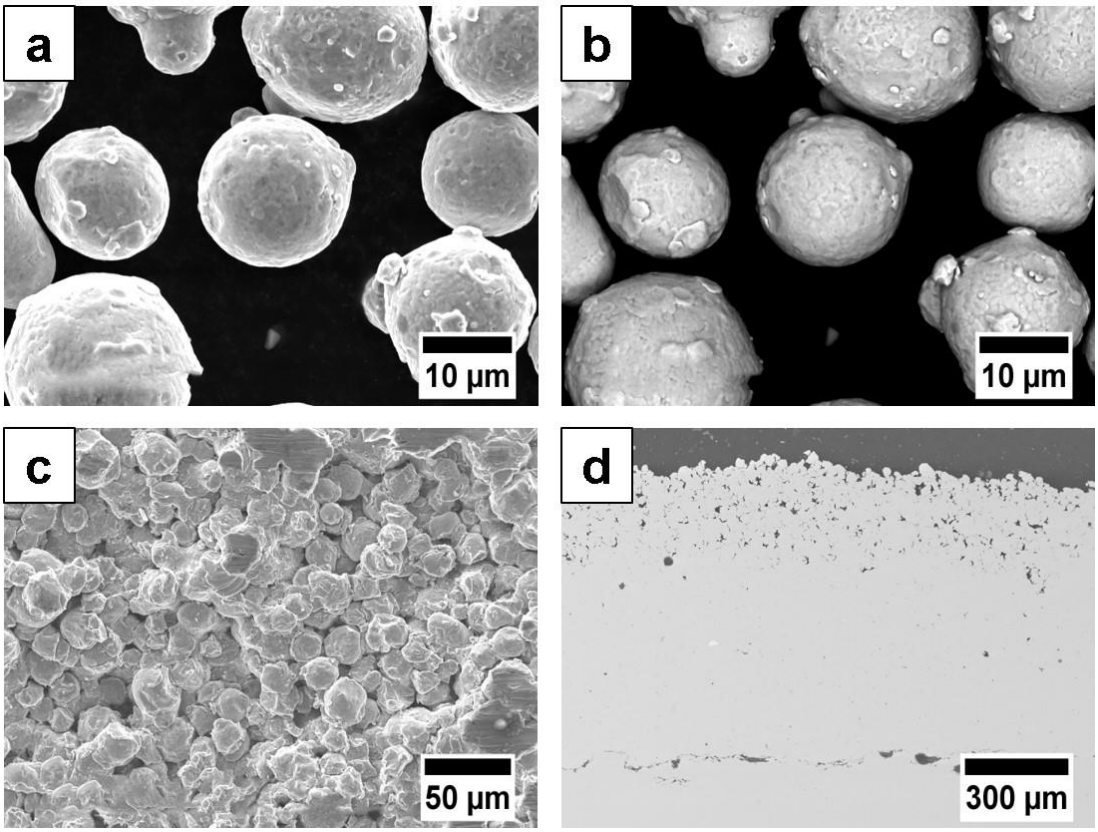

Fig. 4.14 SEM morphology of Sandvik Ni50Cr powder in SE mode (a) and BSE mode (b); top surface morphology (a) and BSE cross-section (b) images of as-deposited cold sprayed coatings.

To provide a full set of data of the phase and the microstructure of the as-deposited coatings, the top surface morphology and the cross-section of them are presented in this section (Fig. 4.14) to facilitate the readers' understanding of the as-sprayed

coating before the discussion on its oxidation performance. Moreover, the morphology of the feedstock powder for the cold spray process, Sandvik Ni50Cr, is shown in Fig. 4.14. The XRD patterns of the as-sprayed coatings showing the phase compositions are displayed together with the XRD patterns of the coatings after air and steam oxidation so that the readers can observe the phase evolution of the coatings immediately and conveniently.

As shown in Fig. 4.14 (a) and (b), the Sandvik Ni50Cr powder particles had spherical geometry and were of around 15 μm in diameter; they displayed a pattern similar to that observed on the surface of the Praxair Ni50Cr powder, as both of these two powders are manufactured using gas atomisation methods. The BSE image (Fig. 4.14) of the powder particles indicates that no obvious inhomogeneity was present in the powder composition, as the grey scale inside each particle was quite similar.

According to Fig. 4.14 (c), the splats at the top surface of the cold sprayed coating still retained the spherical geometry of the feedstock powder after the cold spray process. No obvious deformation of the splats was observed. Moreover, because of the insufficient plastic deformation of the powder particles, the bonding between the splats was poor in several top layers, leading to a porous structure. This feature can also be confirmed from the cross-section image shown in Fig. 4.14 (d). Under the porous microstructure, there were splats of satisfactory bonding. Robust adhesion was also observed between the coating and the substrate. The total thickness of the coating was around 1200 μm, and the porous layers were 300 μm thick.

The laser cladded coatings were deposited using the parameter sets after optimisation process, which is shown in detail in the paper attached at the end of this thesis. The

top morphology and cross-section of the laser cladded coatings are shown in Fig. 4.15. The XRD pattern of the as-deposited coatings is also shown along with the XRD patterns of the coatings after air and steam oxidation for convenient comparison and discussion.

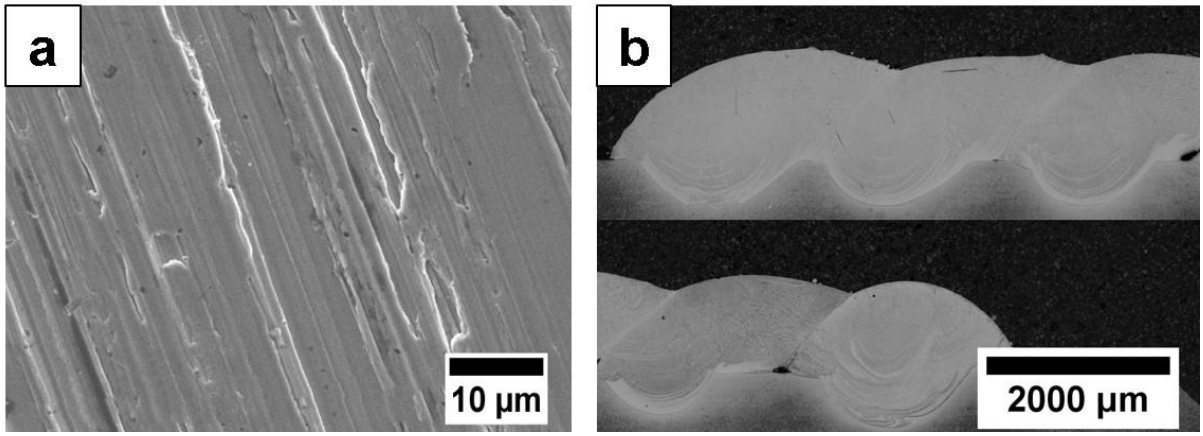

Fig. 4.15 SEM SE top surface morphology (a) and OM cross-section (b) images of as-deposited laser cladded coatings.

In Fig. 4.15 (a), the grain in the laser cladded coatings was too fine to be distinguished even at 5000× magnification. A cross-section of a laser cladded coating that consisted of five overlapped laser cladded tracks is shown in Fig. 4.15 (b). The thickness of the laser cladded coating was around 1200 µm, and the metallurgical bonding between the clad and the substrate was satisfactory. The dendritic patterns were a typical feature shown in the laser cladded coatings/substrates. Moreover, because of the melting and re-solidification of the laser cladding process, the microstructure of the laser cladded coating was considerably denser than that of the coatings deposited using the HVOF thermal spray and cold spray processes.

4.6 High temperature oxidation of HVOLF coatings

4.6.1 Oxidation product phases affected by the oxidising atmosphere

The XRD patterns of the HVOLF as-sprayed coating and after 1, 10 and 100 h of exposure in air are plotted in Fig. 4.16. The intensity of α–Cr phase (2θ = 81.8°) increased initially after 1 h and 10 h of exposure, and the peak could not be detected after 100 h of exposure. No Ni phases were found in the initial as-sprayed coating; however, a Ni phase was detected after high temperature oxidation for 10 h and 100 h. The major oxide phase was Cr_2O_3 for the 1 h and 10 h samples. New oxide phases including NiO and $NiCr_2O_4$ were identified in the 100 h sample.

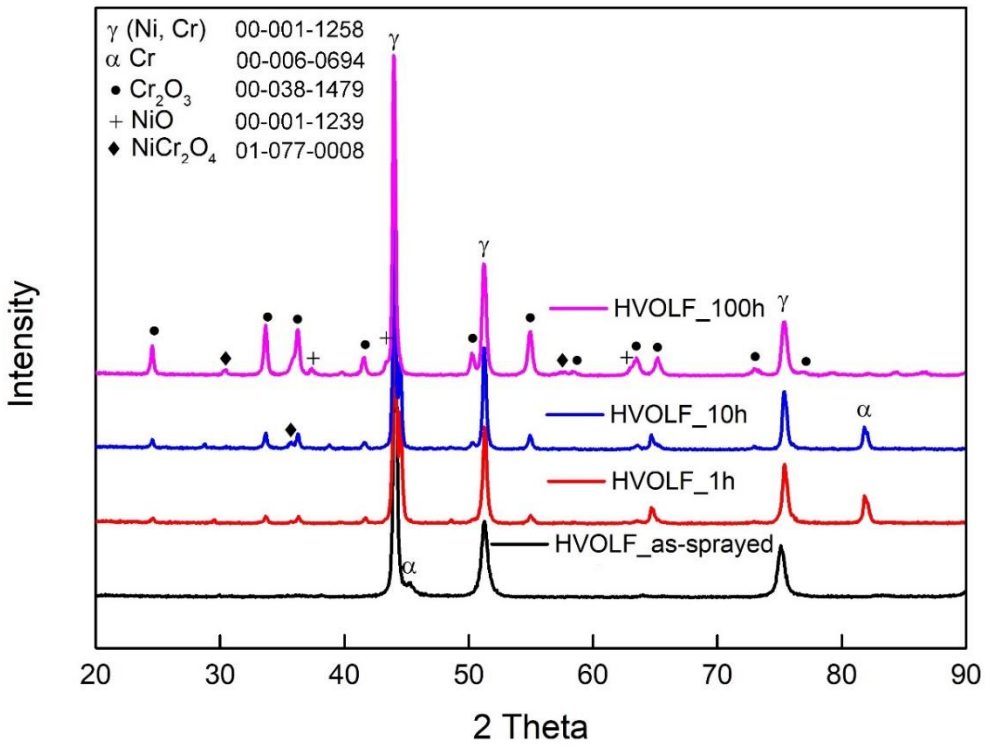

Fig. 4.16 XRD patterns of HVOLF coatings under as-sprayed condition and after high temperature air oxidation in air at 1 h, 10 h and 100 h.

As shown in Fig. 4.17, after steam oxidation for various dwell times, the XRD phases of the oxidation products did not show a significant evolution of the new phases. After 250 h in steam, besides the original peaks corresponding to the (Ni, Cr) phases and Cr phases in the pattern of the as-sprayed coating, peaks corresponding to Cr_2O_3 appeared. No phase peaks of NiO and $NiCr_2O_4$ were identified in the XRD pattern. Such phenomenon (Cr_2O_3 was the major oxide phase) also occurred in the air oxidation of the HVOLF coatings.

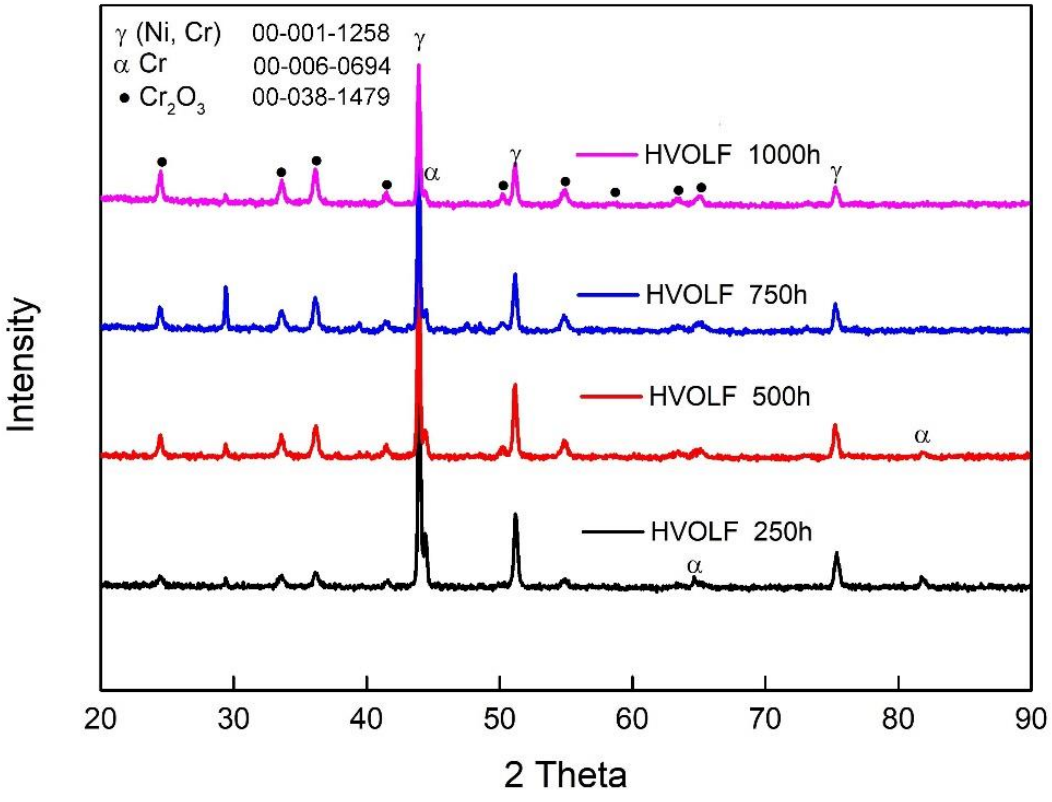

Fig. 4.17 XRD patterns of HVOLF coatings after high temperature oxidation in steam at 250 h, 500 h, 750 h and 1000 h.

When the exposure time in steam was increased, no peaks corresponding to NiO and $NiCr_2O_4$ appeared after 500 h, 750 h and even 1000 h of steam oxidation. The intensity

of the oxide phase peaks increased, and the intensity of the metal phase decreased continuously, as revealed by a comparison of the intensity of peaks at the same 2θ position in various patterns. For instance, the α–Cr peak at 2θ = 81.8° in the HVOLF 1000 h pattern almost disappeared. In general, the oxidation products in air after 100 h included Cr_2O_3, NiO and their spinel combination. In contrast, in steam, Cr_2O_3 was the only detectable oxide phase after 250 h and up to 1000 h of exposure. Therefore, the change in the oxidising atmosphere can be inferred to change the final oxidation product composition.

4.6.2 Oxide morphology variation in air and steam

To show the evolution of oxides produced in air above the surface of the coatings, the SE images of the top morphologies of the oxide scale on the HVOLF coating after 1, 10 and 100 h of air oxidation at 700 °C are presented in Fig. 4.18.

According to Fig. 4.18 (a), the complete coverage of oxides in flake geometry on the surface of the HVOLF coating was completed within 1 h of exposure. With the increasing exposure time, the oxide flakes thickened significantly after 10 h of exposure, as shown in Fig. 4.18 (c) and (d). This thickening trend of the oxides continued up to 100 h (Fig. 4.18 (e) and (f)). Finally, most of the oxides transformed into large well-defined flake oxides (arrow 1 in Fig. 4.18 (f)) around 2 μm in size, which were considerably thicker than the original oxide flakes produced at the surface of the 1 h specimen. In addition, some smaller hexagonal oxides appeared near the major oxides, as shown by arrow 2 in Fig. 4.18 (f).

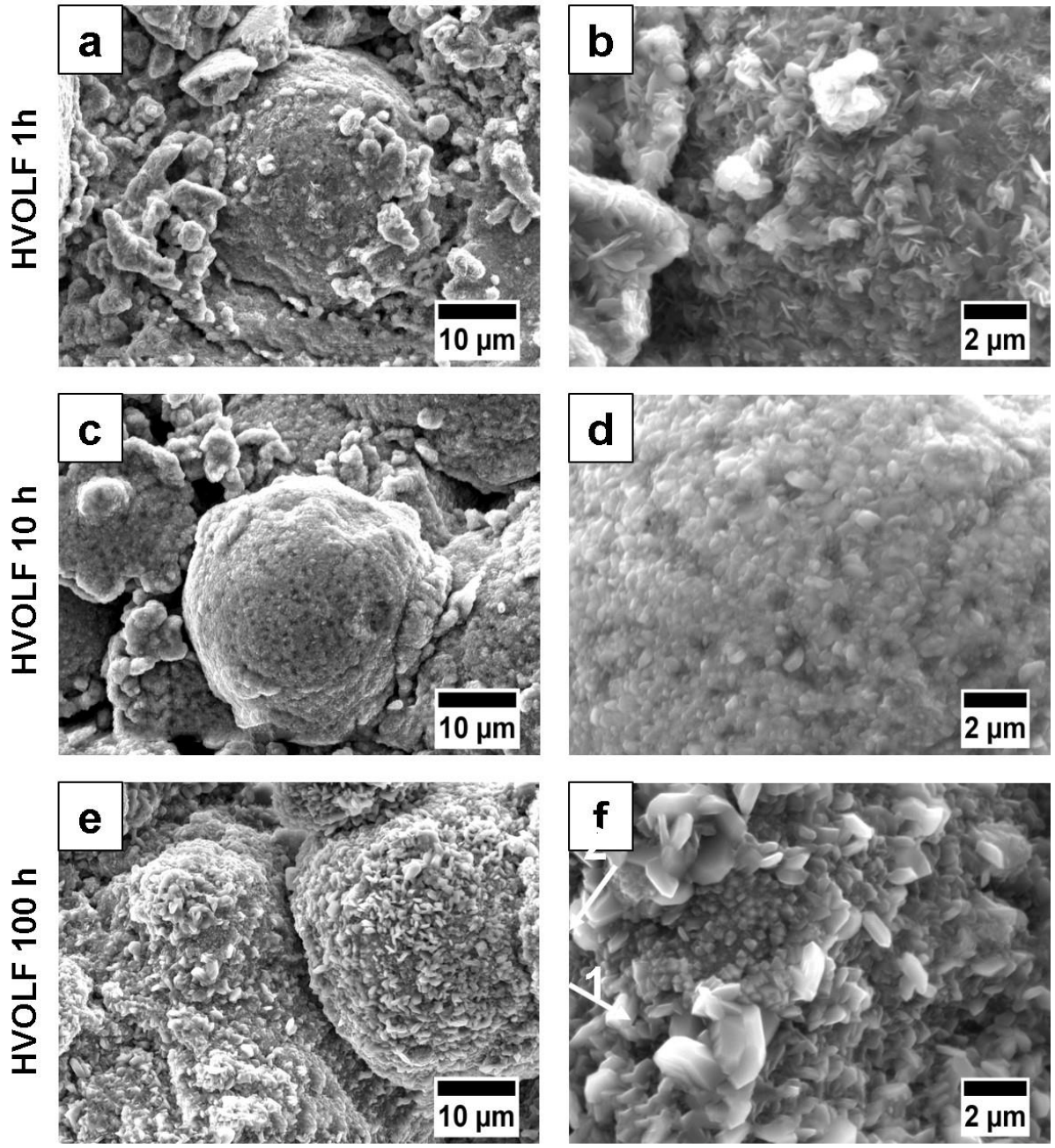

Fig. 4.18 SEM SE top surface morphology of HVOLF coatings after 1 h (a & b), 10 h (c & d) and 100 h (e & f) in air at 700 °C, showing the distribution and geometry of oxides.

The top morphology of the oxide scale of the HVOLF coatings produced in steam at various times is displayed in Fig. 4.19.

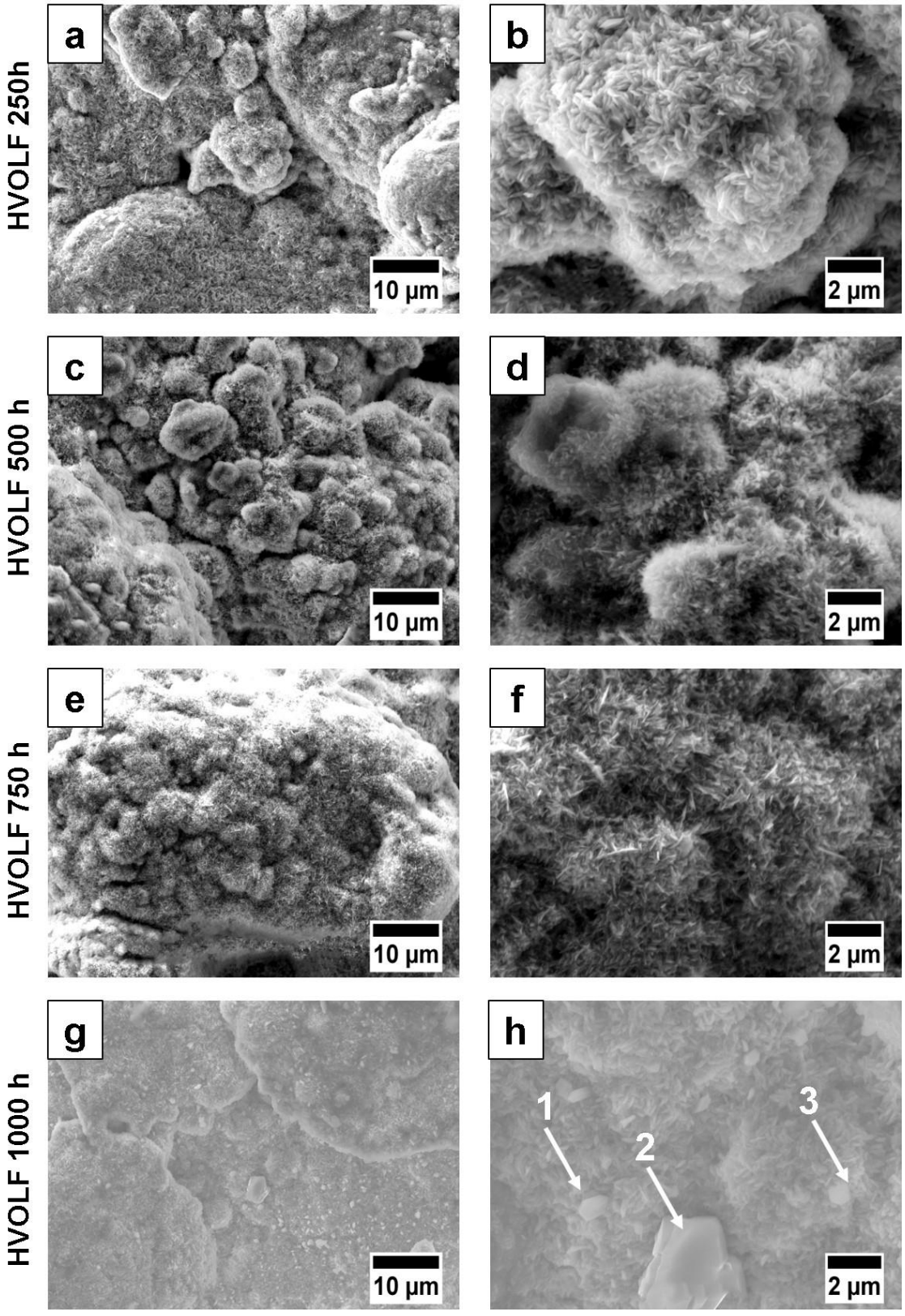

Fig. 4.19 SEM SE top surface morphology of HVOLF coatings after 250 h (a & b), 500 h (c & d), 750 h (e & f) and 1000 h (g & h) in steam at 700 °C, showing the distribution and geometry of oxides.

After 250 h (Fig. 4.19 (a) & (b)), the oxides in the flake geometry grew on the entire surface of the splats. The growth orientation of these flakes was radial; they surrounded the powder particles. Hence, they exhibited a cluster-like feature when observed using SEM. With a further 250 h of exposure (Fig. 4.19 (c) & (d)), the density of these oxides increased; therefore, a cluster-like feature in the finer scale appeared. This trend continued up to 750 h of steam exposure (Fig. 4.19(e) & (f)). On the top surface of the 1000 h sample (Fig. 4.19(g) and (h), several oxide polyhedral crystals are indicated by arrows 1, 2 and 3; they could be the accumulation products of the oxide flakes, which clearly displayed the growth and development process of oxides.

After comparing the morphology of the oxides developed at the surface of the coatings in two different atmospheres, it is obvious that the presence of steam significantly slowed down the development process (size increase) of the oxides. In air, large well-defined flakes were identified in the 100 h sample; a similar phenomenon was observed after 1000 h in steam. Moreover, the oxide size in the two atmospheres was considerably different: the oxides developed in steam were smaller than those developed in air.

4.6.3 Loose accumulation of oxides inside the thick scale

The BSE image of the cross-sections of the HVOLF coatings after 100 h of air oxidation is shown in Fig. 4.20. The oxide scale developed on the surface of the HVOLF coating after 1 h and 10 h of the heat treatment was too thin to distinguish from the BSE cross-section image; thus, it is not shown in Fig. 4.20. The oxides on the interface between the coating and air did not from a dense and uniform scale, as shown in Fig. 4.20 (a); they formed an accumulation of oxides (white rectangle in Fig.

4.20 (b)) rather than a dense layer which can act as a precursor of the oxidation barrier. This unique growth and development method of oxides on the HVOLF coating may undermine the oxidation resistance of the coating, as the complete development of the dense scale needs more time than that occurring during the oxidation of bulk alloys. The EDX analysis shows that these oxides were mostly chromia with silicon and contained a very small amount of Ni. The bulk coating microstructure following the heat treatment presented a dual-phase. The darker island phase in the splats (in the BSE images) contained around 60–80 wt.% Cr, while the lighter phase included approximately 50–60 wt.% Ni.

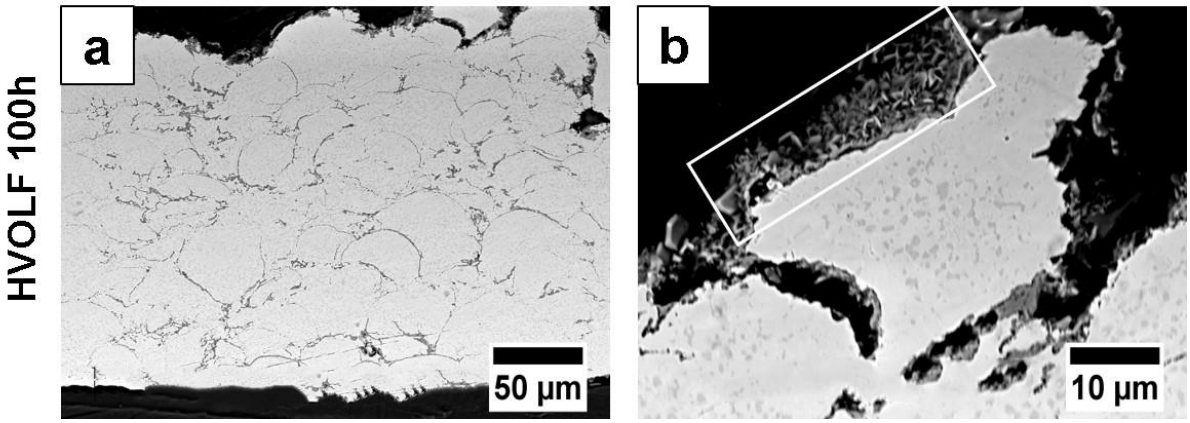

Fig. 4.20 SEM BSE cross-section images of HVOLF 2 coatings after 100 h in air at 700 °C, showing: (a) distribution of oxide scale and (b) microstructure of oxide scale.

A relatively thin oxide scale was observed on the top surface of the HVOLF coatings with up to 1000 h of exposure, as shown in Fig. 4.21. Furthermore, even after 1000 h of steam oxidation, the thickness of the oxide scale did not exceed that of the scale developed in air for 100 h (Fig. 4.21 (d) compared with Fig. 4.20 (a) and (b)). The thickness of the oxide scale increased with an increase in the exposure time, as revealed by a comparison of Fig. 4.21 (d) with Fig. 4.21 (a), (b) and (c); however, the

extent of increase was marginal. A dual-phase structure was the most obvious feature of all the splats irrespective of the increase in the exposure time, as the heat treatment time was increased. In both air and steam, the thicknesses of the oxide scales were small, and the microstructure of the oxide scale was not as dense as that produced at the surface of the bulk alloys. Moreover, the oxide scale produced in steam was thinner than that produced in air because of the presence of steam. The damage effect of steam on the Cr_2O_3 scale is believed to be responsible for this thinning behaviour [134].

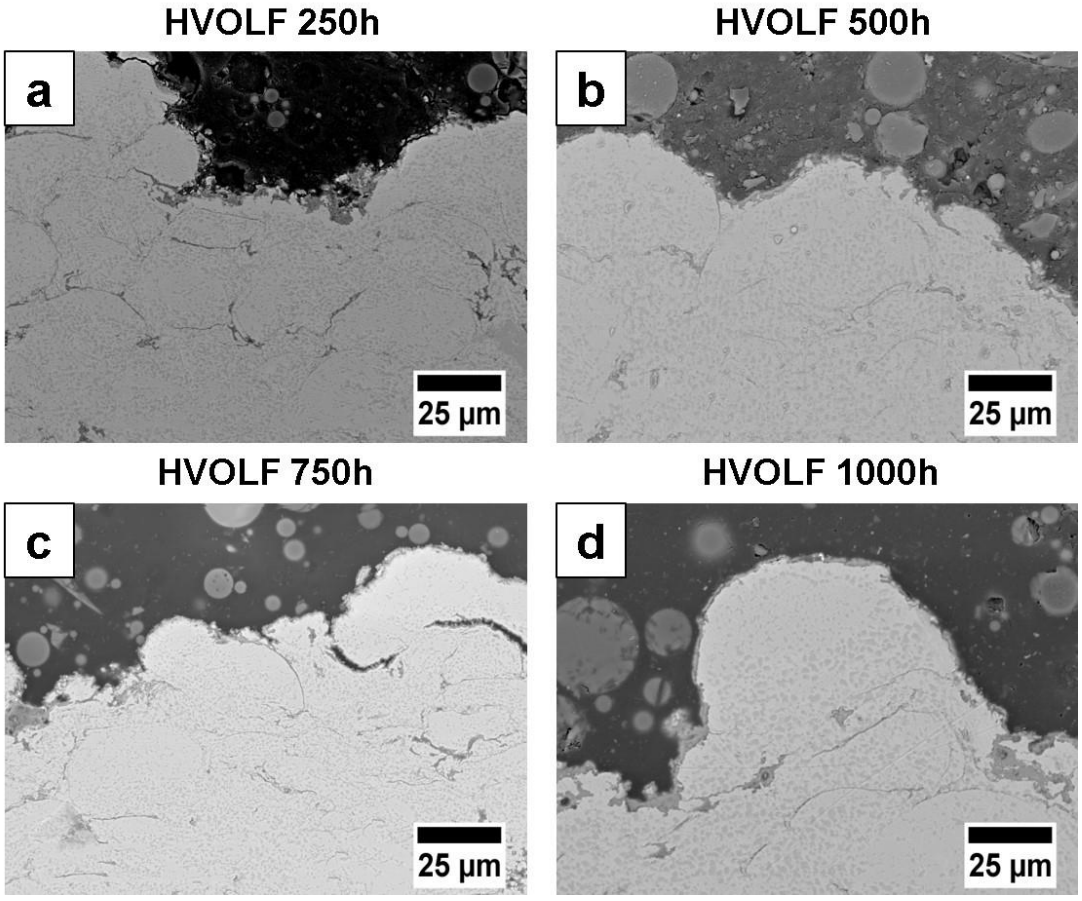

Fig. 4.21 SEM BSE cross-section images of HVOLF coatings after 250 h (a), 500 h (b), 750 h (c) and 1000 h (d) in steam at 700 °C, showing the distribution and microstructure of oxide scale on the coating.

4.7 High temperature oxidation of HVOGF coatings

4.7.1 Evolution of oxidation product phases in air and steam

The XRD patterns of the HOVGF coatings after air oxidation are shown in Fig. 4.22.

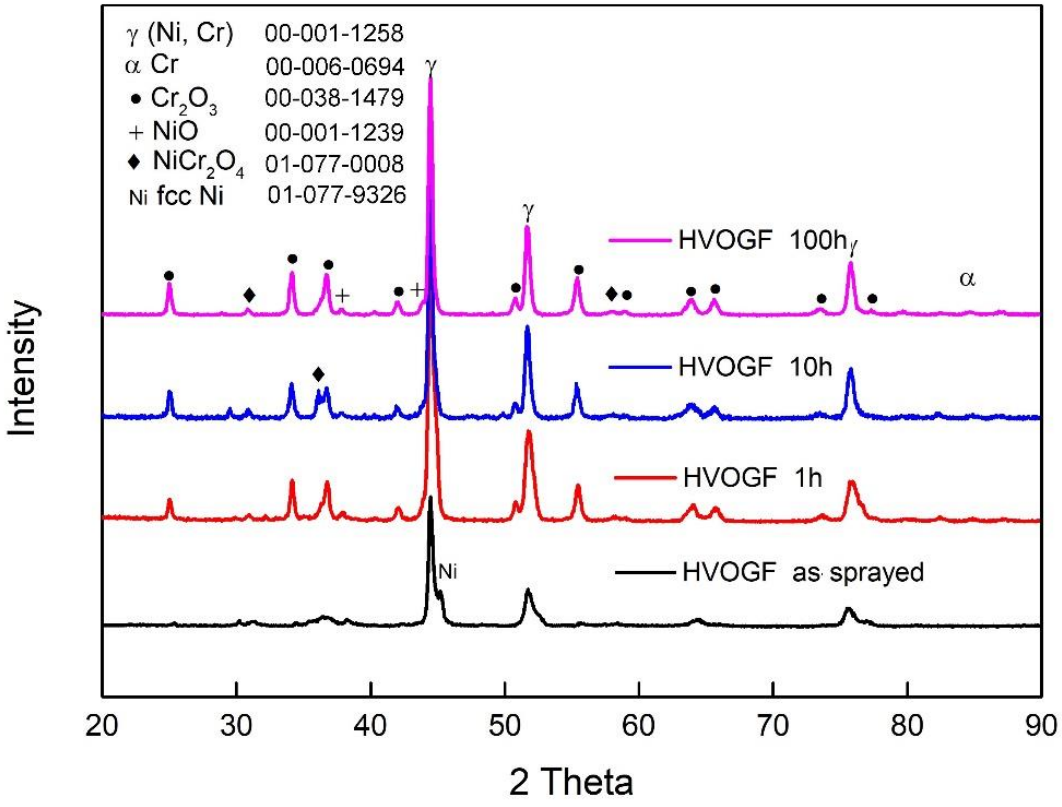

Fig. 4.22 XRD patterns of HVOGF coatings under as-sprayed condition and after high temperature air oxidation (1 h, 10 h and 100 h).

When the exposure time increased, the metallic phases of the coatings always included the γ–(Ni, Cr) solid solution phase and fcc Ni phase; no minor Cr phase was identified in the as-sprayed coatings. After 100 h, only one minor Cr peak with marginal intensity at a large 2θ appeared. The oxide phases in these coatings included Cr_2O_3, NiO and $NiCr_2O_4$; all of them began to appear on the surface of the as-sprayed coating and did not disappear when the exposure time increased up to 100 h. The twin peaks

at around 2θ = 37° representing the $NiCr_2O_4$ and Cr_2O_3 phases in the HVOGF 10 h pattern changed to one Cr_2O_3 peak in the HVOGF 100 h pattern, which indicated that NiO might be covered by the Cr_2O_3 scale at some locations, and thus, the X-ray could not irradiate it.

The phase evolution of the steam oxidation products of the HVOGF coatings is shown in Fig. 4.23.

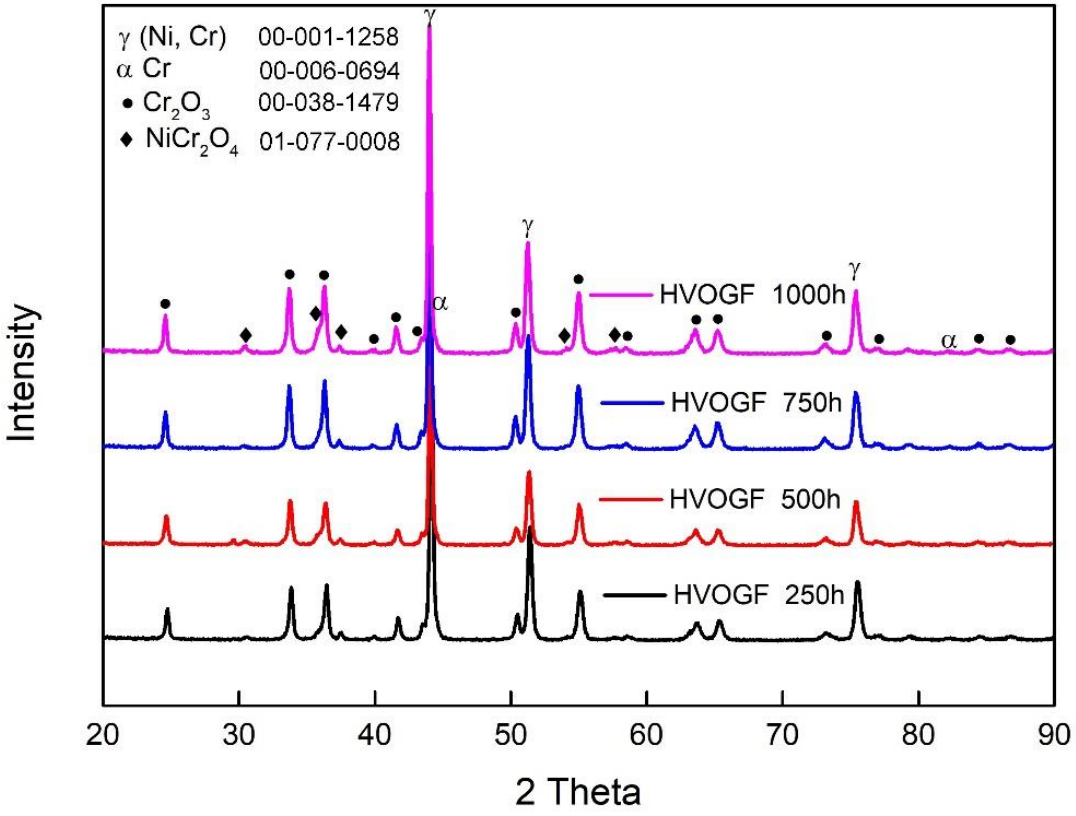

Fig. 4.23 XRD patterns of HVOGF coating after high temperature steam oxidation (250 h, 500 h, 750 h and 1000 h).

The HVOGF 250 h pattern shown in Fig. 4.23 clearly indicated that there were peaks corresponding to the $NiCr_2O_4$ spinel developed after 250 h in steam. Meantime, a number of Cr_2O_3 peaks (2θ = 58.4°, 73.0° and so on) appeared in the HVOGF 250 h

pattern when compared with the HVOLF 250 h XRD pattern. The continuous increase in the intensities of the Cr_2O_3 peaks at the same 2θ locations implied the constant build-up of the Cr_2O_3 scale with the increasing exposure time. For the metal phases, only peaks corresponding to the (Ni, Cr) solid solution phases could be identified in these XRD patterns. The intensities of the peaks representing he Cr phase were too small to be identified clearly even from the HVOGF 250 h pattern.

In the air 100 h sample, the oxides were Cr_2O_3, NiO and $NiCr_2O_4$. While in the steam 250 h sample, no trace of NiO was found; this absence of NiO was confirmed even in the steam 1000 h XRD pattern. The presence of steam changed the phase composition of the oxides that grew at the surface of HVOGF coatings, but the change effect was not same as that observed under the HVOLF coating condition.

4.7.2 Growth processes of oxides in various oxidising atmosphere

Oxides on the top surface of HVOGF coatings are shown in Fig. 4.24. On the surface of 1 h air oxidation specimen of the HVOGF coatings (Fig. 4.24 (a)), the size of the oxides was so small that most of the oxides were difficult to distinguish even at 20,000× magnification (Fig. 4.24 (b)). As shown in Fig. 4.24 (b), no oxide flakes of two different sizes formed on the surface of the splats. The larger ones were around 1 μm and the smaller ones were in the nanometre size range. After 10 h, as shown in Fig. 4.24 (c) and (d), thin oxide flakes grew into the larger cubic oxides at the peak of the splats, while the oxides in the valley of the splats retained the flake geometry. The difference in the oxygen partial pressure at the various levels of the splats was considered to result in this difference in the oxide growth. As shown in Fig. 4.24 (e), some oxides grew sufficiently large to be distinguished at the 2000× magnification.

The detailed geometry and size of these oxides are shown in Fig. 4.24 (f). A polyhedron with well-defined edges was the most obvious feature of these oxides; further, these oxides developed into an oxide scale in which their edges could not be distinguished.

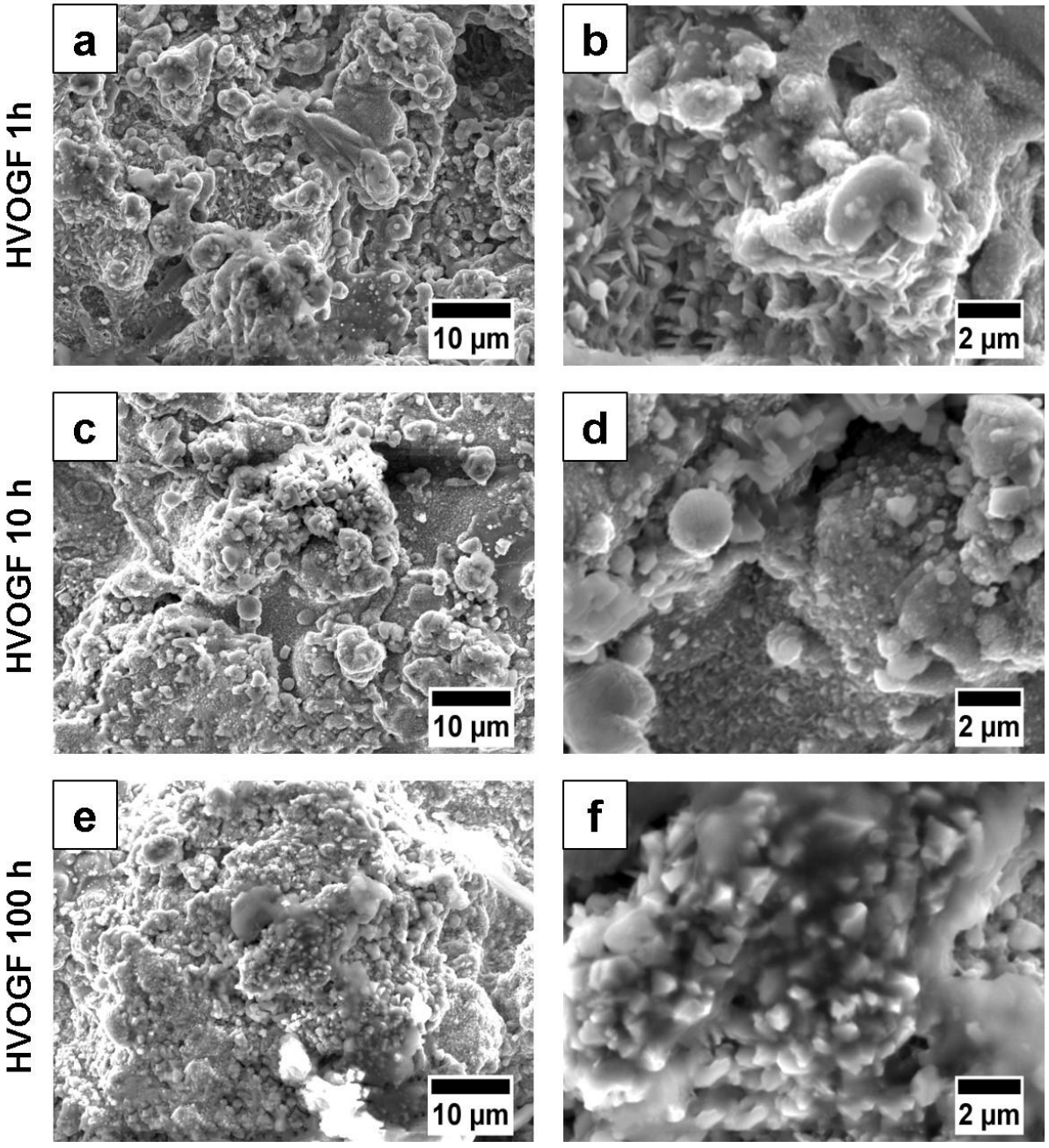

Fig. 4.24 SEM SE top surface morphology of HVOGF coatings after 1 h (a & b), 10 h (c & d) and 100 h (e & f) in air at 700 °C, showing the distribution and geometry of oxides.

The evolution of the top morphology of the HVOGF coatings after various dwell times in high temperature steam is demonstrated in Fig. 4.25.

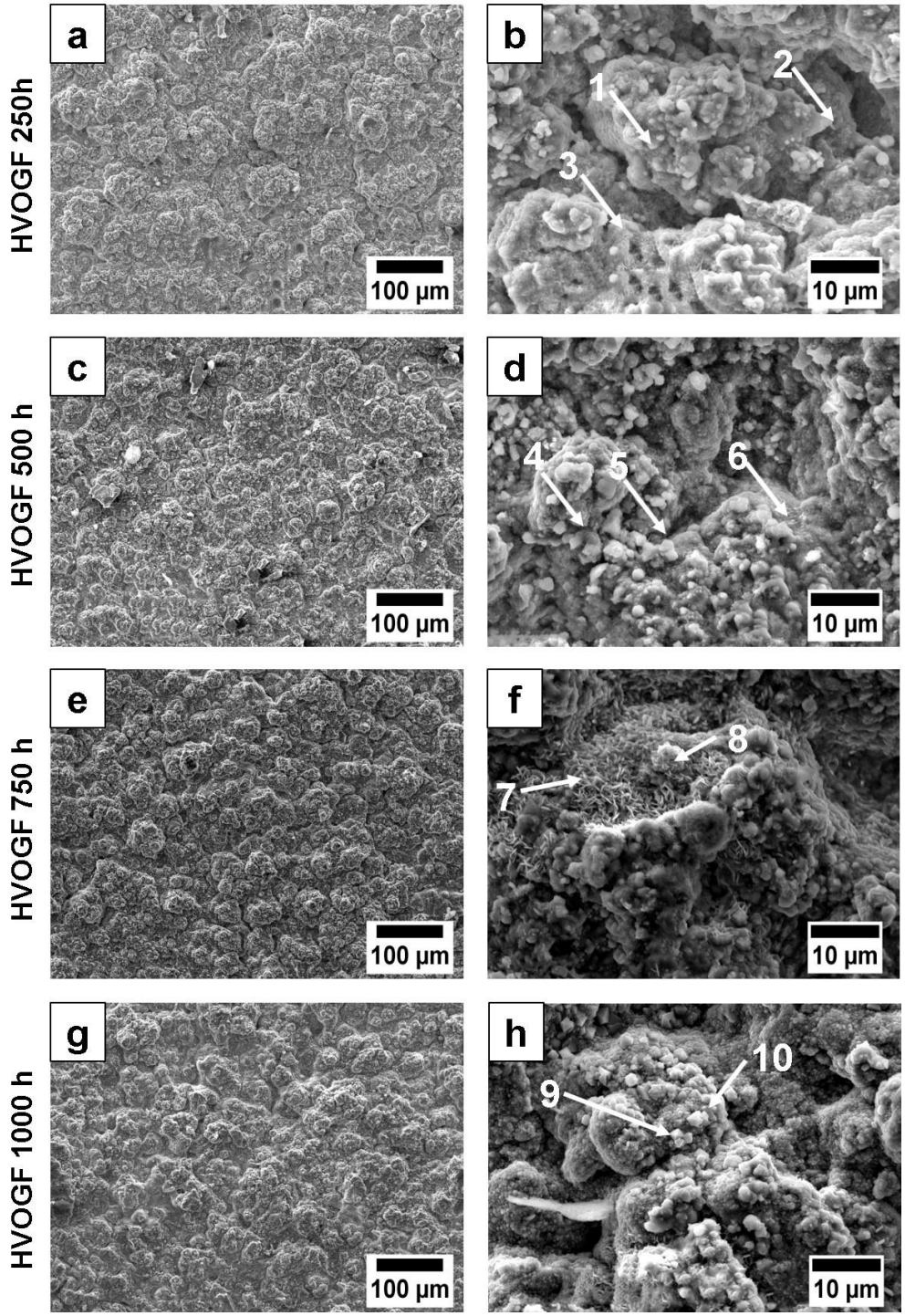

Fig. 4.25 SEM SE top surface morphology of HVOGF coatings after 250 h (a & b), 500 h (c & d), 750 h (e & f) and 1000 h (g & h) in steam at 700 °C, showing the distribution and geometry of oxides.

As shown in Fig. 4.25 (a), the top surface of the coating exhibited a uniform feature. The details of this feature are shown in Fig. 4.25 (b). Further, the cracked and flatten splats seemed to be covered with oxides. The growth and development of those oxides varied at the different locations of the splats. For instance, the area indicated by arrow 1 showed a feature of the lay-up of the lamellar oxide grains. While in area 2, the surface of the splat was quite considerably smooth, as only a few tiny oxides grew on it. In area 3, the geometry of the oxides resembled needles. Most of these oxides were Cr_2O_3 according to the XRD pattern.

No obvious difference was revealed by a comparison of Fig. 4.25 (c) with Fig. 4.25 (a). However, in Fig. 4.25 (d), some oxides began to develop into a very large polyhedral crystal, as indicated by arrows 4, 5 and 6. Further 250 h steam oxidation promoted the growth and development of the oxides.

Fig. 4.25 (e) and (f) revealed the oxide morphology of the samples after 750 h of steam oxidation. These cluster-like features (arrow 7) were oxides in the flake geometry. The feature indicated by arrow 8 clearly demonstrated the formation of an oxide having polyhedral geometry; i.e. oxide flakes in various orientations accumulated to form a polyhedral crystal. Finally, after 1000 h of steam oxidation (Fig. 4.25 (g) and (h)), a large number of oxides on the surface of the splats developed into a regular octahedron, as indicated by arrows 9 and 10. At this point, almost the entire splat surface was covered with polyhedral oxides of various sizes. The EDX analysis of spots 9 and 10 clearly showed that the composition of these polyhedral oxides was $NiCr_2O_4$.

4.7.3 Microstructure of oxide scales and nearby coatings

Fig. 4.26 (a) and (b) show the cross-section images of the HVOGF coatings after 100 h of air exposure. As in the case of the HVOLF coatings, no uniform oxide scale covered the surface of the HVOGF coatings. The thickness of scale varied at different locations, and the maximum thickness was around 5 μm. The internal oxidation of the splats could not be evaluated from Fig. 4.26 because of the large amount of oxides surrounding the splats before exposure. Moreover, no evident dual-phase phenomenon in splats can be confirmed in the splats, as a considerable amount of the Cr in the splats γ–(Ni, Cr) solid solution was consumed during the HVOGF thermal spray process.

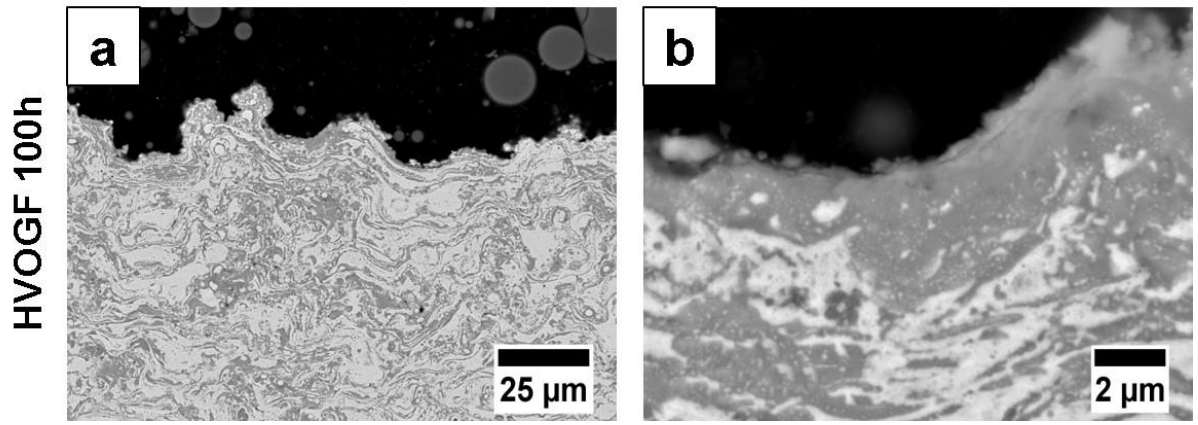

Fig. 4.26 SEM BSE cross-section images of HVOGF coatings after 100 h in air at 700 °C, showing: (a) distribution of oxide scale and (b) microstructure of oxide scale.

As shown in Fig. 4.27, no continuous thick oxide scale covered the original coating even after 1000 h of steam oxidation (Fig. 4.27 (d)). The thickness of the oxide scale varied at different locations on the surface of the coatings. The average thickness of the oxide scale was around 2–3 μm, and the maximum thickness at a certain point was around 5 μm. The dark features surrounding the top layer splats were Cr_2O_3

according to the EDX analysis (70–75 wt.% O and 20–22 wt.% Cr). It was difficult to determine whether the thickness of oxide scale continuously increased with an increase in the exposure time, as the oxide scale did not have no uniform thickness and the imaging of oxide scale for the samples was random.

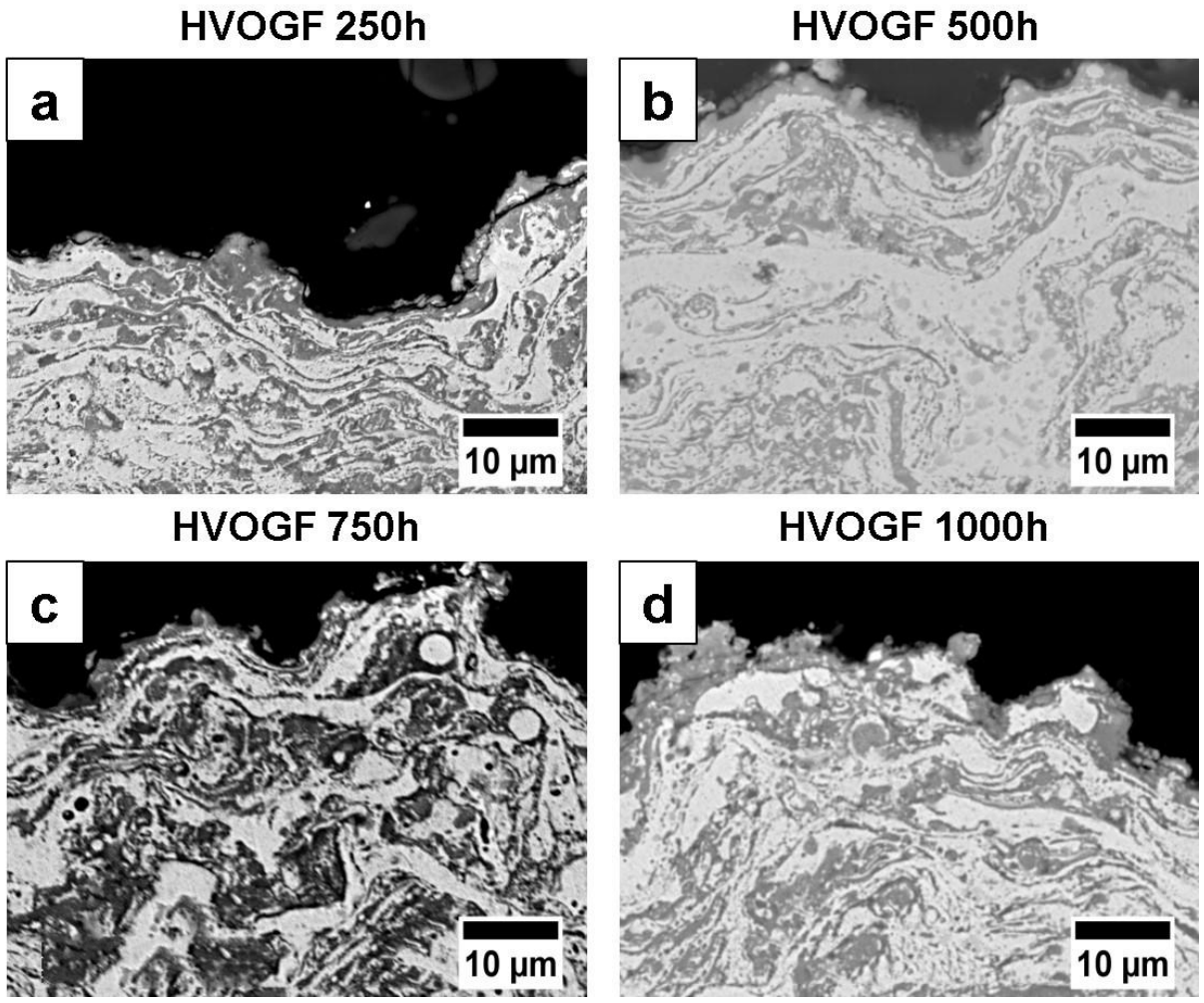

Fig. 4.27 SEM BSE cross-section images of HVOGF coatings after 250 h (a), 500 h (b), 750 h (c) and 1000h (d) in steam at 700 °C, showing the distribution of oxide scale and microstructure of oxide scale.

The dark features under the top layer of splats were also oxides. However, the actual phase of these oxides could not be determined only on the basis of the EDX results, as the actual EDX scan area is much larger than these spots; i.e. information from the

composition of the matrix can obscure the composition information of the oxides surrounding the splats. A dual-phase feature was observed in Fig. 4.27 (b) (500 h sample) and could not be identified in the 250 h sample, which indicated the increasing oxidation degree of the splats with increasing exposure time.

4.8 High temperature oxidation of cold sprayed coatings

4.8.1 Effect of the oxidising atmosphere on the phases of oxidation products

The phase compositions of the cold sprayed coatings after air oxidation for various dwell times are displayed in Fig. 4.28.

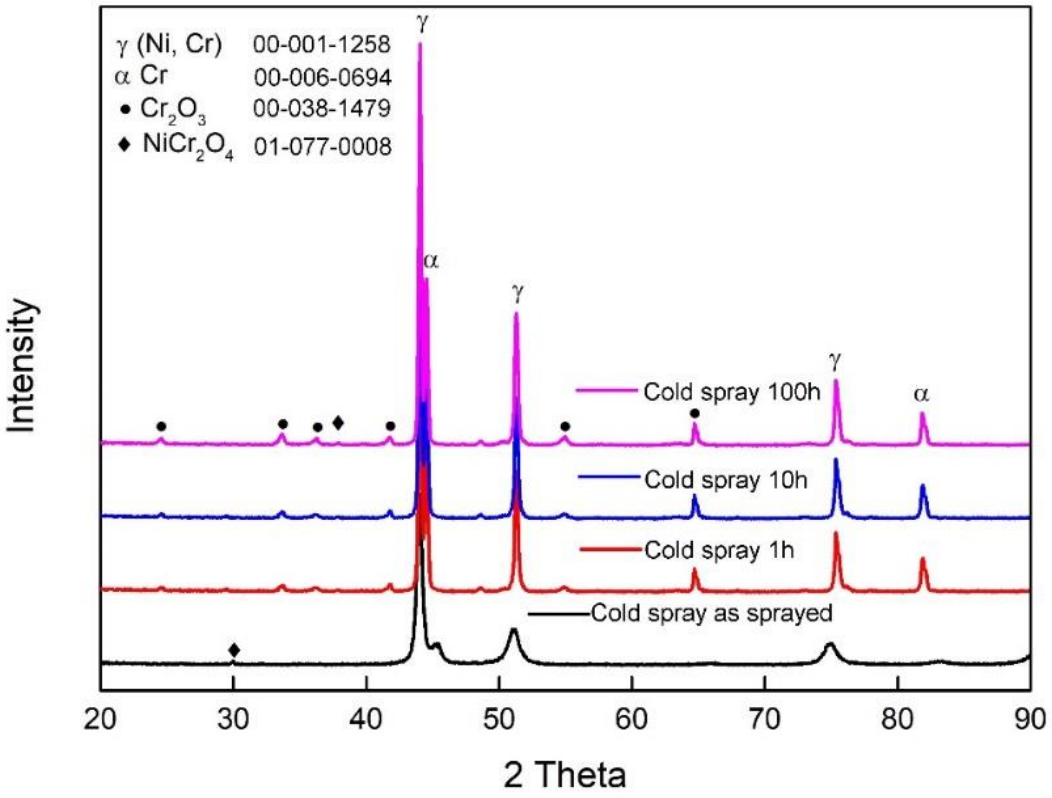

Fig. 4.28 XRD patterns of cold sprayed coatings under as-sprayed condition and after high temperature air oxidation (1 h, 10 h and 100 h).

In the as-sprayed coating, metal phases including the γ–(Ni, Cr) solid solution and the α–Cr could be identified from the pattern. No peaks corresponding to the oxide phases were observed, indicating the small oxidation degree of the splats during the cold spray process, which could be attributed to the low temperature (~500 °C) during the spray process. Further, the N_2 carrier gas acted as a protective atmosphere that isolated the splats from the oxidising environment. In the oxidised coatings, Cr_2O_3 was the major phase, and an α–Cr peak was observed at 2θ = 81.8°. Up to 10 h, no new phase appeared on the surface of the oxidising coating. After 100 h of exposure, a peak corresponding to the $NiCr_2O_4$ phase (2θ = 38°) could be identified in the XRD pattern, although the intensity of this peak was marginal. This phenomenon indicated the actual start time point of the transition oxidation is around 100 h. The intensity of the peaks at the same 2θ locations but in different XRD patterns did not change with the exposure time, indicating that the surface of the as-sprayed coating was not completely screened by the growing oxide scale. The thickness increase of the oxide scale that could fully cover the surface indicated that the X-rays penetrated through the scale and thus led to a decrease in the intensity of the peaks corresponding to the metal phases (γ–(Ni, Cr) and α–Cr).

The phase evolution of the steam oxidation products of the cold sprayed coatings with time is shown in Fig. 4.29. In the cold spray 250 h XRD pattern, besides the original metal alloy phases (γ–(Ni, Cr) and α–Cr phase), the oxide phases included the Cr_2O_3 and $MnCr_2O_4$ spinel; however, the spinel phase was a minor phase when compared with the Cr_2O_3 phase. With an increase in the exposure time, the intensity of the peaks corresponding to the Cr_2O_3 phase showed a decreasing trend. The evolution of the $MnCr_2O_4$ peaks also demonstrated a similar trend. For instance, the peak at 2θ = 29.8°

almost disappeared after the 500 h steam oxidation. The appearance of the Mn spinel ($MnCr_2O_4$) instead of the Ni spinel ($NiCr_2O_4$) was attributed to the Mn content in the Sandvik Osprey Ni50Cr powder. However, such a phenomenon did not occur in the air oxidation of the cold sprayed coatings. It was obvious that the presence of steam promotes the production of spinel containing Mn.

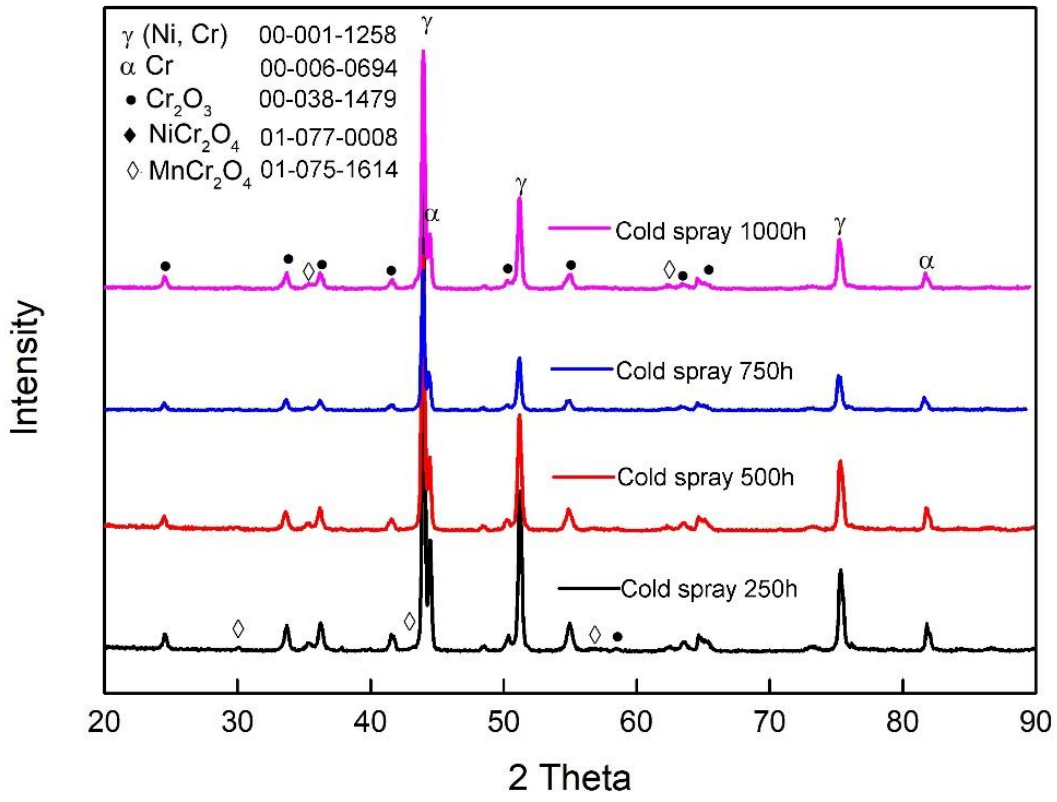

Fig. 4.29 XRD patterns of cold sprayed coatings after high temperature steam oxidation (250 h, 500 h, 750 h and 1000 h).

4.8.2 Oxides in small size and uniform geometry

The morphology of the oxide scales produced after 1 h in air on the surface of the cold sprayed coatings is shown in Fig. 4.30 (a) and (b).

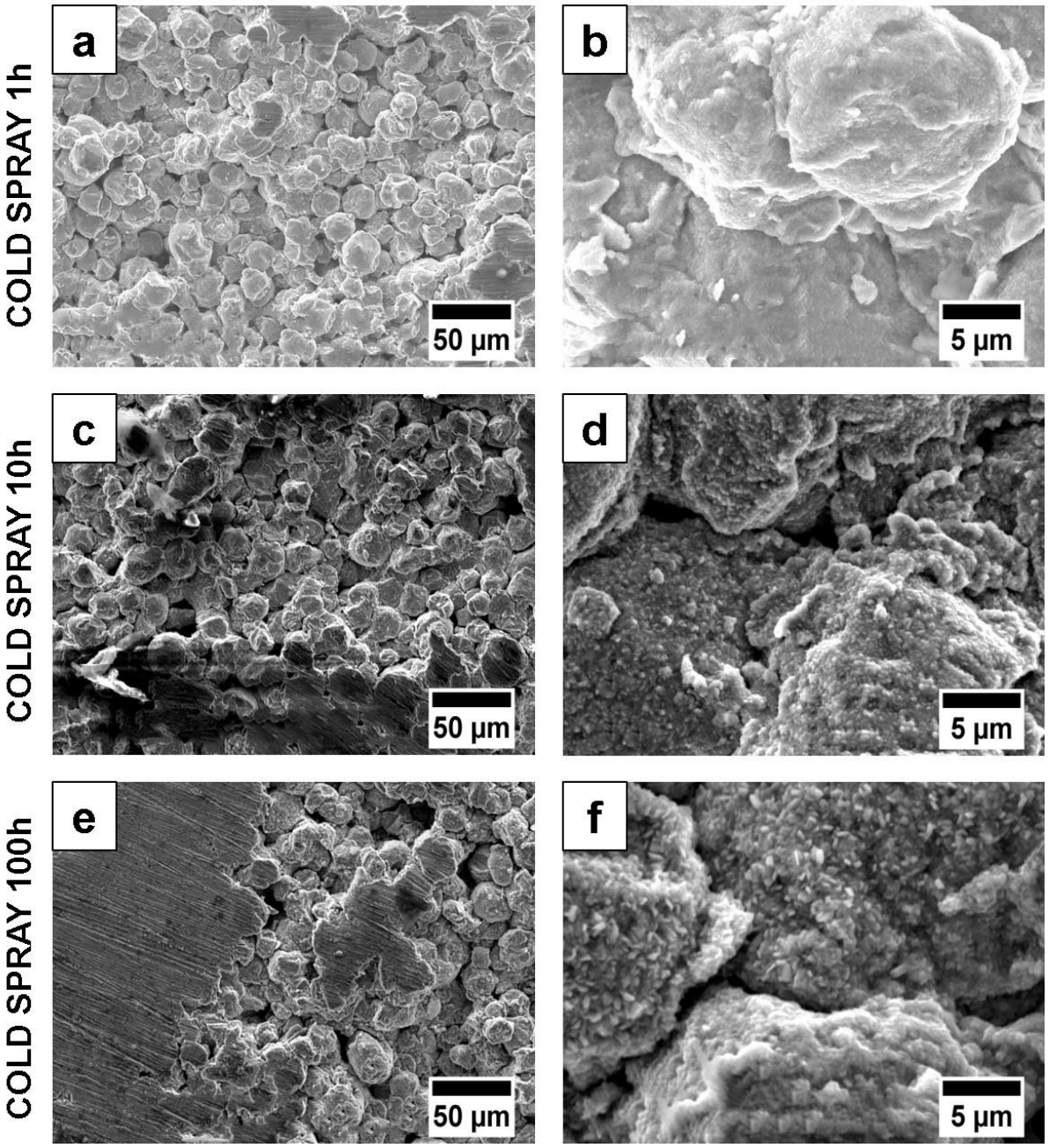

Fig. 4.30 SEM SE top surface morphology of cold sprayed coatings after 1 h (a & b), 10 h (c & d) and 100 h (e & f) in air at 700 °C, showing the distribution and geometry of oxides.

The surface of all the splats was covered with oxides in a considerably fine scale (~hundreds of nanometres). The particle size of the oxides is so small that these oxides can only be distinguished in the 10,000× magnification image. Moreover, most of the oxides share the same flake geometry. According to the XRD phase

identification shown in Fig. 4.28, the composition of these oxides is Cr_2O_3. The morphology of the oxides on the surface of the 10 h air oxidation sample indicated a size increase of the oxides and no geometry change of oxides with an additional 9 h of exposure. After 100 h of high temperature oxidation, the oxides on the surface of the splats still retained the flake geometry and maintained the enlargement progress.

Fig. 4.31 reveals a significant difference in the top morphology of the cold sprayed coatings after 250 h, 500 h and 750 h of steam oxidation; i.e. the amount and distribution of oxide flakes reduced with an increasing in the exposure time, although all the splats were covered with these oxide flakes. These small oxide flakes (size < sub-micrometres) did not show a trend to combine and form one large oxide polyhedron, as in the case of the HVOGF coating (Fig. 4.25 (f) arrow 8). Instead, they distributed over all the surface of the splats; the size of these oxides was limited by the finite growth space. After 1000 h of steam oxidation (Fig. 4.25 (g) and (h)), some large oxide flakes appeared, and no trace of a large oxide polyhedron was found. Although an $MnCr_2O_4$ phase was identified in the cold spray 1000 h XRD pattern, the EDX spot scan of the areas of interest did not show a large amount of Mn.

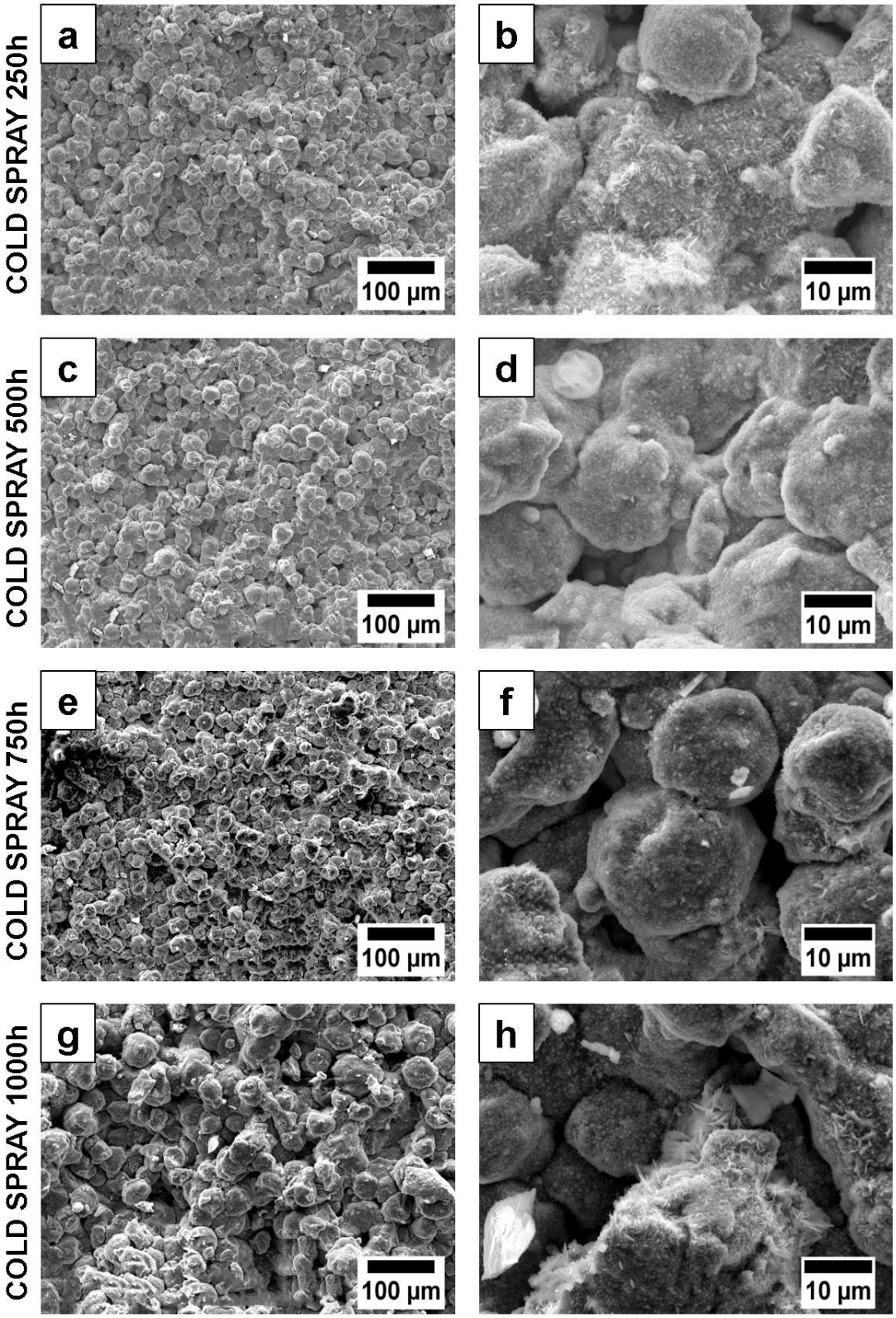

Fig. 4.31 SEM SE top surface morphology of cold sprayed coatings after 250 h (a & b), 500 h (c & d), 750 h (e & f) and 1000 h (g & h) in steam at 700 °C, showing the distribution and geometry of oxides.

4.8.3 Discontinuous thin oxide scale on the coating surface

Cross-section images of the cold sprayed coating after 100 h of air oxidation are shown in Fig. 4.32 (a) and (b). No continuous oxide scale developed on the surface of the fresh coating (Fig. 4.32 (a)), and the thickness of the oxide scale was less than 1 μm, according to Fig. 4.32 (b). The dual-phase phenomenon observed in case of the cold sprayed coating was more significant than that observed in the case of HVOLF and HVOGF coatings. This is attributed to the fact that the poor microstructure of the several top layers of the splats in the cold sprayed coating could not limit the opportunity for air to come into contact with the splats effectively. The oxidation of Cr in the γ–(Ni, Cr) solution could promote the diffusion of Cr from the core of the splats to outside and thus relocate the distribution of Cr within the splat. As shown in Fig. 4.33 (a), (b), (c) and (d), no thick oxide scale developed on the top surface of the cold sprayed coating after steam oxidation for various dwell times. The thickness of the oxide scale was also small and did not increase with an increase in the exposure time.

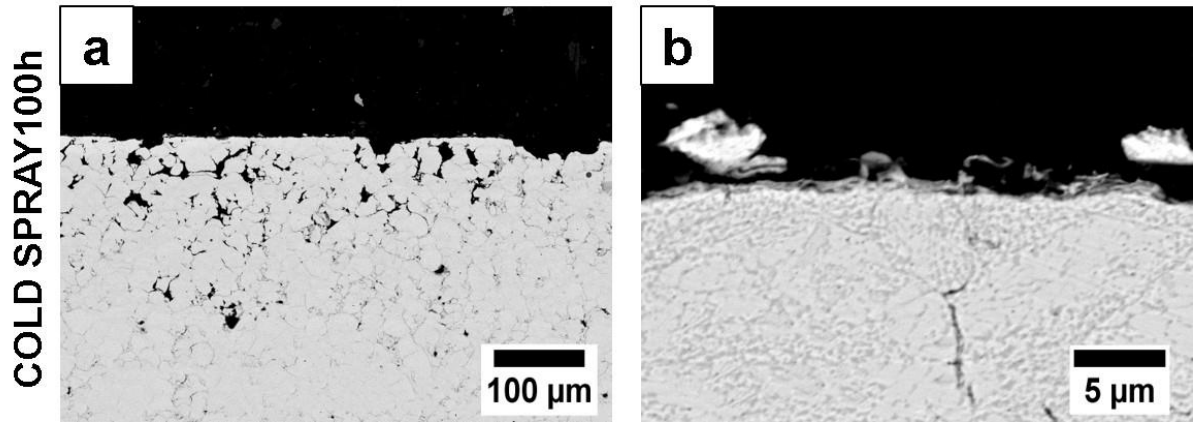

Fig. 4.32 SEM BSE cross-section images of cold sprayed coatings after 100 h in air at 700 °C, showing the: (a) the distribution of oxide scale, (b) microstructure of oxide scale.

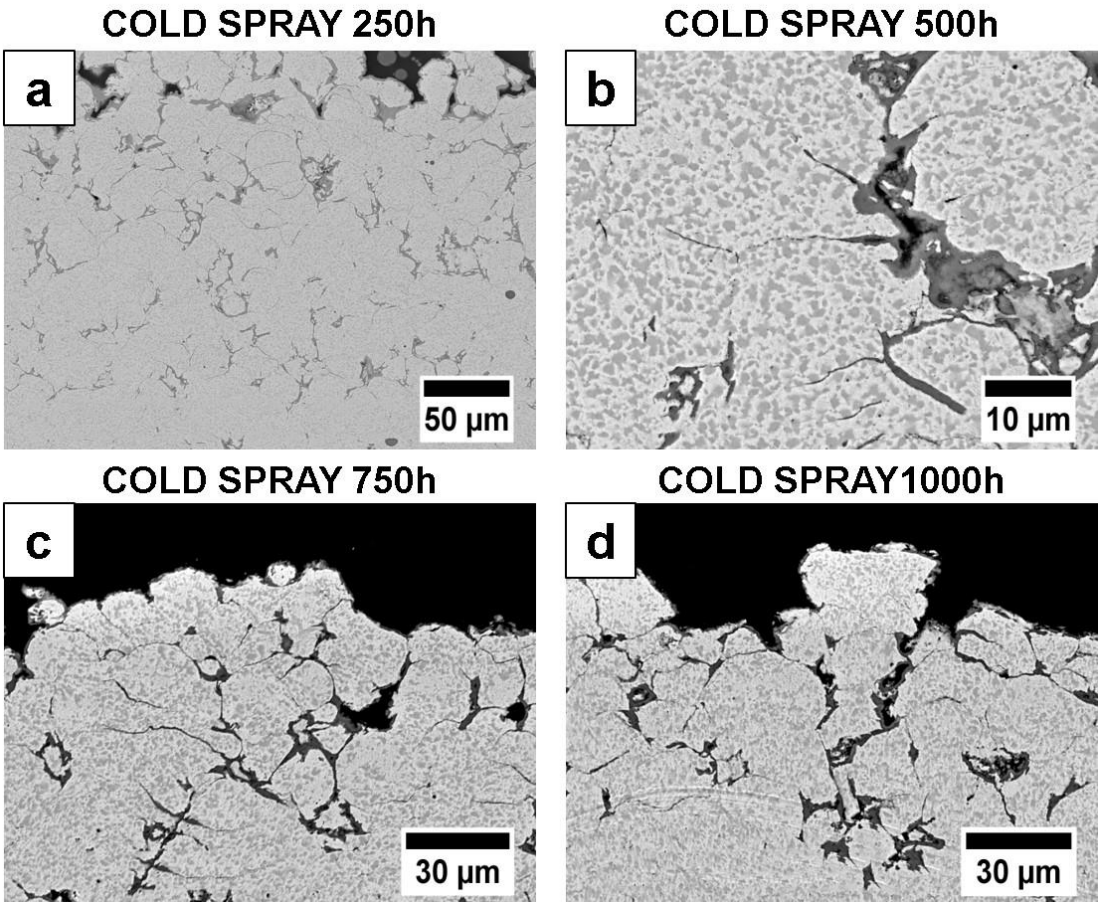

Fig. 4.33 SEM BSE cross-section images of cold sprayed coatings after 250 h (a), 500 h (b), 750 h (c) and 1000 h (d) at in steam 700 °C, showing the distribution of oxide scale and microstructure of oxide scale.

The microstructure of the cold sprayed coating was not as dense as that of the HVOLF and HVOGF coatings and thus led to the deep penetration of the oxidising ions into the coating. The dark feature surrounding the splats in the coating was oxide, which could be used as a measure to determine the oxygen ion penetration during steam oxidation, as there was little or no oxidation of the splats during the cold spray process. According to the distribution of the dark features in the coating, there were oxidised splats even at the bottom of the coating and near the coating–substrate interface. A

significant dual-phase structure was found in all the splats and this feature was observed in the samples exposed for 250 h, 500 h, 750 h and 1000 h.

4.9 Oxide scales developed on the thermal sprayed coating surface

In the case of the HVOLF, HVOGF and cold sprayed coatings, no continuous and uniformly thick oxide scales developed on the surface of the coatings. The maximum thickness of the oxide scales did not exceed 5 μm, which was consistent with the results reported by Aguero *et al*. [143]. In their case, the thickness of the oxide scale was only 3 μm even after 20,000 h of steam oxidation. The dense degree of the oxide scale is not sufficient to prevent the penetration of the oxidising ions into the fresh metal surface, as the oxides were accumulated within the scale in a loose method, rather than growing along one direction, which is observed during the oxidation of the bulk alloys condition.

The oxide scale thickness at a small magnitude as mentioned above might be attributed to two reasons: 1. low oxidation rate of NiCr-based coatings in air and steam and 2. thinning effect of steam on the oxide scale. Obviously, in air, there are no factors such as OH^- ions that could lead to the deterioration and thinning of the oxide scale [134, 141-145, 184, 185]. Hence, the low oxidation rate of the NiCr alloys is the dominant factor that contributed to the small thickness of the oxide scale. In this study, the maximum air oxidation duration was 100 h. The oxidation rate was not sufficient to guarantee that an oxide scale of satisfactory thickness grew and built up on the fresh metal surface within 100 h. However, there was a continuous increasing trend of the oxide scale in thickness with an increase in the exposure time. The coating might exhibit satisfactory long-term air oxidation resistance on the basis of this deduction.

When the oxidising atmosphere changed to steam, the oxidation rate of the coatings was actually augmented according to other publications [54, 186] and the experimental results obtained in this study. However, the thickness of the oxide scale that developed in steam was not as thick as expected. The intense evaporation of $Cr_2O_2(OH)_2$ at high temperature in the presence of steam interrupted the build-up process of Cr_2O_3 within the oxide scale, and thereby reduced the thickness of the scale significantly. The thickness of scale that developed on the 1000 h steam oxidation samples confirmed this undermining effect of steam and showed a poor potential for the long-term steam oxidation resistance application. If the thickness of the oxide scale does not increase with an increase in the exposure time, the barrier effect of the scale on the transport of the oxidising ions cannot be retained.

The loose packing of the oxides within the oxide scale on the surface of the thermal/cold sprayed coatings in this study resulted in the weakened points to the oxide scale that do not exist in the oxidation of the bulk alloys. In the oxidation of bulk alloys, the preferred path for the transport of ions and atoms involved in the oxidation process is the grain boundaries, as they are the combination zone of various oxide grains [187-189]. The point, line and plane defects in the crystal concentrate near the grain boundary [190-192] and make it easier for the oxidising ions to diffuse and shift between the vacancies in lattice. In the oxide scale developed on the surface of the thermal/cold sprayed coatings, besides the grain boundary, gaps among several oxide crystals which are not packed in the closest pattern possibly act as the preferred transport path for the oxidising ions. The transport rate of the ions inside these gaps is much larger than that inside the grain boundaries, as there is vacuum or gas rather than lattice defects inside these gaps.

4.10 High temperature oxidation of laser cladded coatings

4.10.1 Insufficient chromium oxide in the oxidation products

The XRD patterns of the as-deposited laser cladded coating and the samples after various dwell times of air oxidation are shown in Fig. 4.34. In the as-deposited coatings, $Ni_{2-3}Fe$ is was major phase since there was round 10 wt.% Fe diluted in the coating. The α–Cr phase was a minor phase, and its intensity was small that only one peak at 2θ = 83° could be identified in the as-deposited laser cladding pattern.

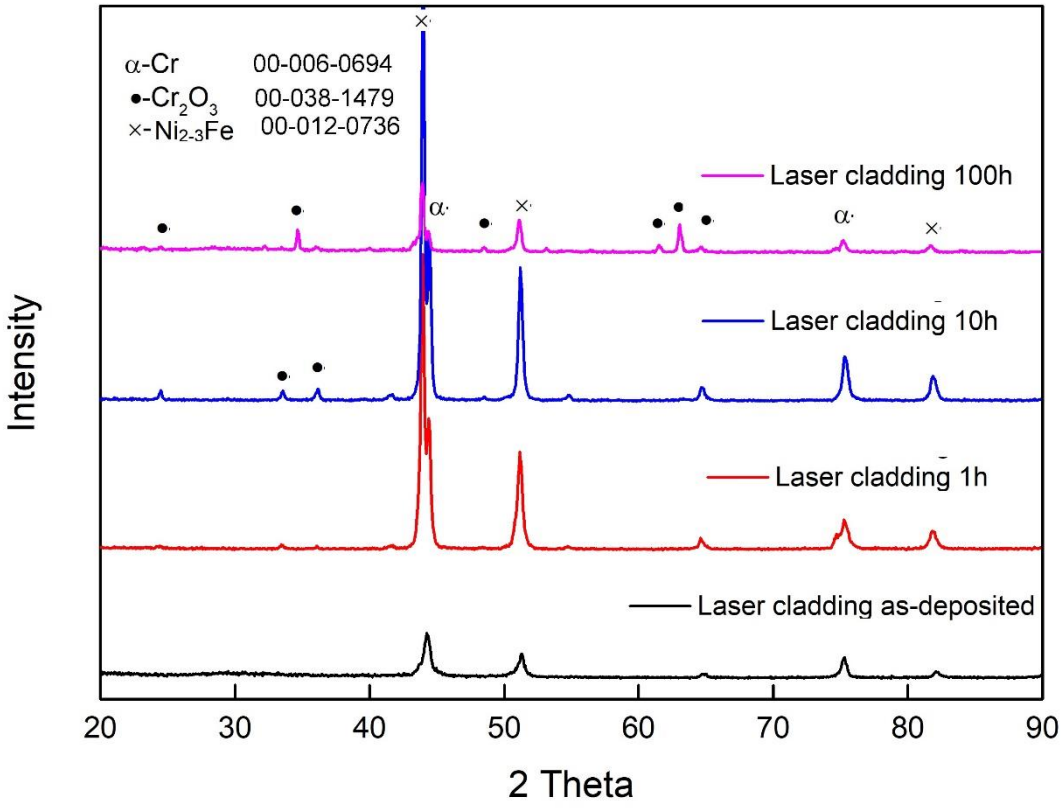

Fig. 4.34 XRD patterns of laser cladded coatings under as-sprayed condition and after high temperature air oxidation (1 h, 10 h and 100 h).

The evolution of the $Ni_{2-3}Fe$ phase peaks in the XRD patterns corresponding to the air oxidising coatings for various dwell times indicated that the production of the Cr_2O_3

scale that could cover the entire coating surface completed at a certain time point between 10 h and 100 h, and even at 100 h, the microstructure of the oxide scale was not satisfactory. It is obvious that the $Ni_{2-3}Fe$ peaks in the laser cladding 1 h and laser cladding 10 h XRD patterns were considerably stronger than those in the laser cladding 100 h XRD pattern; the intensity of the $Ni_{2-3}Fe$ peaks increased with an increase in the exposure time before 10 h. The increasing trend of the $Ni_{2-3}Fe$ phase peaks before 10 h could be explained as follows: Cr in the original NiCr solid solution was oxidised to Cr_2O_3 selectively and the residual Ni could combine with dilute Fe to form the $Ni_{2-3}Fe$ phase instead of being oxidised to NiO since, as Fe could be oxidised preferentially when compared with Ni. This might be attributed to the fact that there were no phase peaks corresponding to iron oxide in the XRD pattern because of the evaporation of iron oxide, as the exposure temperature was 700 °C. The decreasing trend of the $Ni_{2-3}Fe$ phase peaks between 10 h and 100 h might be attributed to the increasing coverage of the Cr_2O_3 scale on the fresh coating, which led to fewer X-rays required for the irradiation of the coating and thus produced fewer diffraction signals of the coating material.

As shown in Fig. 4.35, the main metal phases in the four steam oxidised coatings were $Ni_{2-3}Fe$. No peaks corresponding to the γ–(Ni, Cr) and α–Cr phases were identified, indicating that in the top area of the cladded coatings, the dilution of Fe into the original matrix γ–(Ni, Cr) + α–Cr microstructure significantly change the phase composition. There are also no peaks corresponding to the iron oxide were found in the XRD patterns of the steam oxidation samples. Instead, Cr_2O_3 is the only oxidation product of the laser cladded coatings at high temperature and in steam. A small difference was observed among the peaks of Cr_2O_3 at the same 2θ position in various XRD patterns.

Therefore, it was difficult to conclude the promotion effect of the steam oxidation time on the oxidation of the laser cladded coatings.

In general, Cr_2O_3 was the major oxidation product of the laser cladded Ni50Cr coatings in both air and steam. Iron oxides were not identified in the XRD patterns of the samples after the oxidation exposure, and the major metallic phase for the laser cladded coatings was the $Ni_{2–3}Fe$ phase.

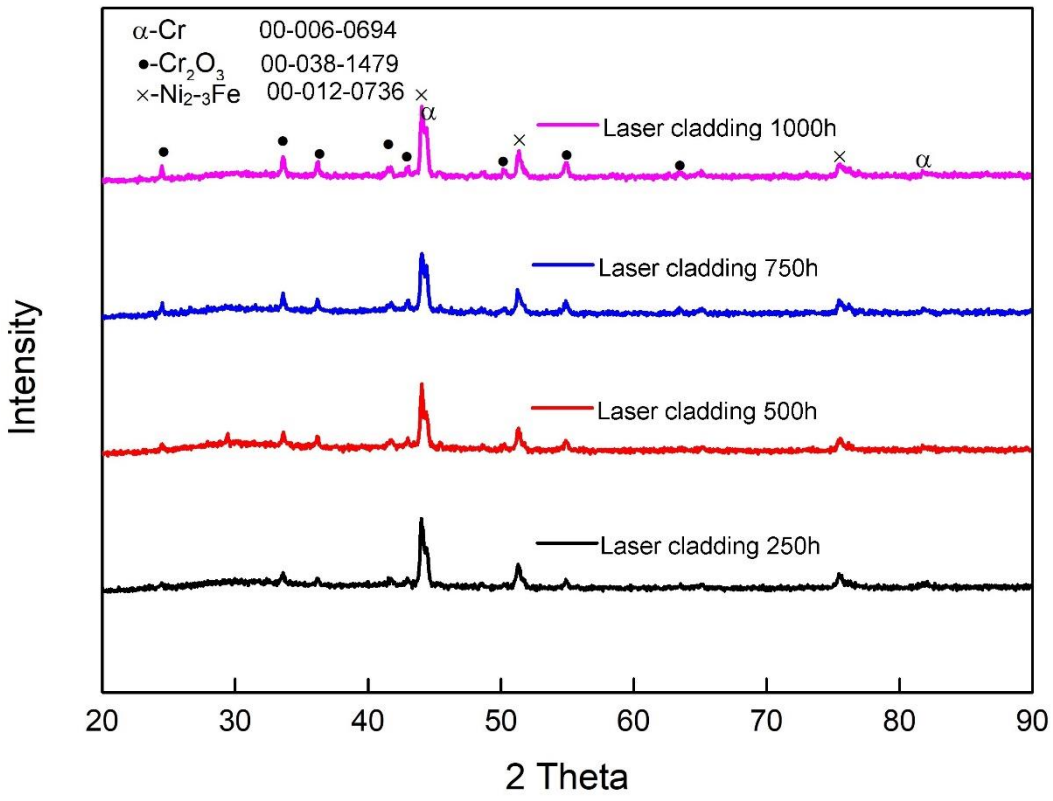

Fig. 4.35 XRD patterns of laser cladded coatings after high temperature steam oxidation (250 h, 500 h, 750 h and 1000 h).

4.10.2 Continuous enlargement of oxides

The morphology of the laser cladded coatings after various oxidation periods is shown in Fig. 4.36.

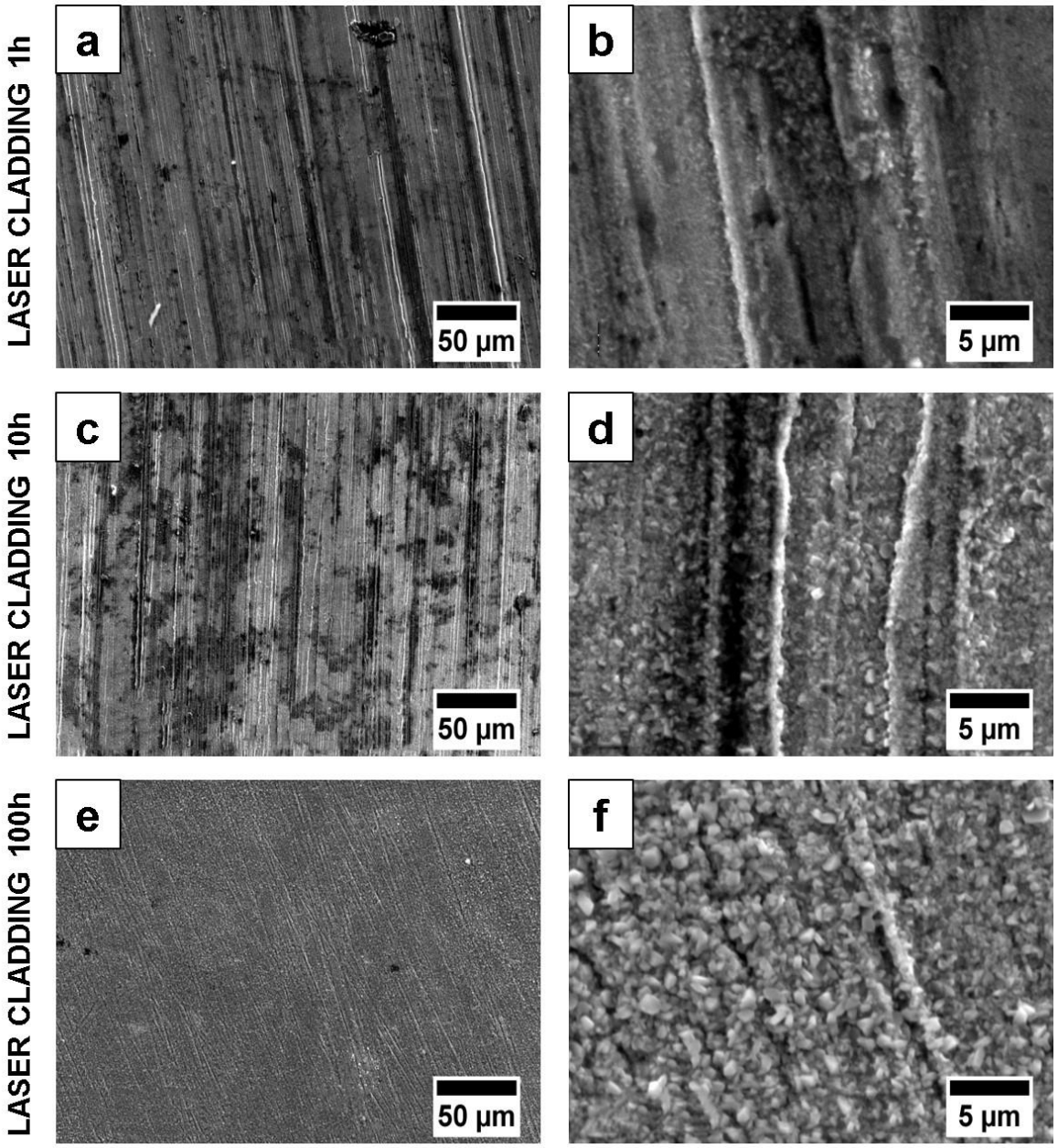

Fig. 4.36 SEM SE top surface morphology of laser cladded coatings after 1 h (a & b), 10 h (c & d) and 100 h (e & f) in air at 700 °C, showing the distribution and geometry of oxides.

In the 1 h sample, the oxides were very fine and had flake geometry. In the 10 h sample, these oxides were enlarged and began to show polyhedron geometry at some locations. In the 100 h sample, the oxides were in the mixture of the flakes and the polyhedrons and significantly increased in size when compared with those on the 1 h

and 10 h sample. The coverage of oxides at the coating surface is satisfactory. Yet, the X-ray can still penetrate this layer of oxides and contact with the fresh coating surface. Hence, it is concluded that this Cr_2O_3 scale was still thin.

The morphology of the oxides on the top surface of the laser cladded coatings after steam oxidation is shown in Fig. 4.37 (a), (b), (c) and (d), and the oxide flakes of various sizes were its most obvious features. Only one thick flake geometry of these oxides was identified on the coating surface. No polyhedral oxides were identified in the four samples of various oxidation dwell times. With an increase in the exposure time, the size of the oxide flakes continuously increased up to the 750 h exposure. After 750 h of steam oxidation, further exposure did not promote any increase in the size of oxides, which was concluded from a comparison of Fig. 4.37 (f) and (h). These oxide flakes were Cr_2O_3 according to the XRD pattern shown in Fig. 4.35.

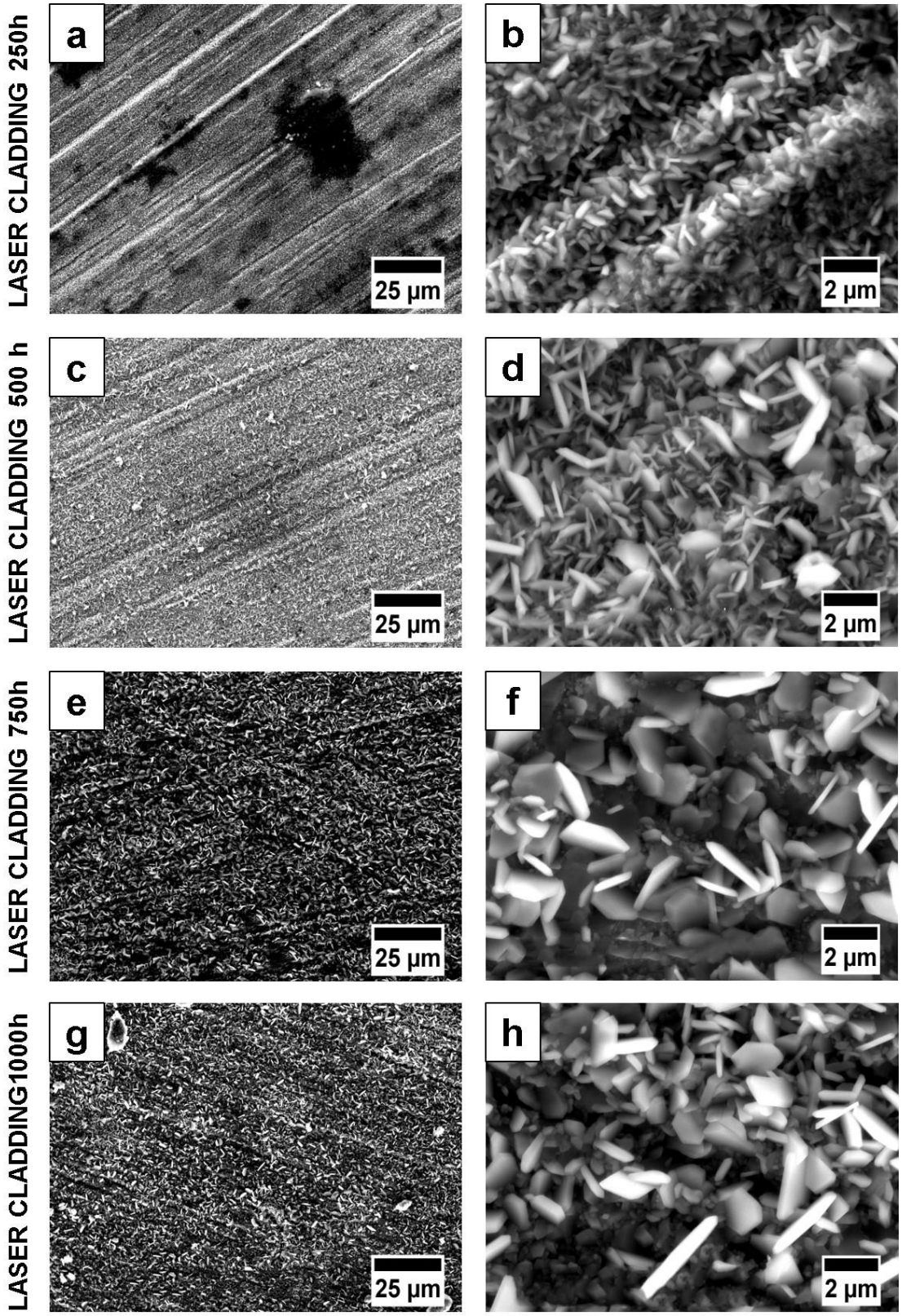

Fig. 4.37 SEM SE top surface morphology of laser cladded coatings after 250 h (a & b), 500 h (c & d), 750 h (e & f) and 1000 h (g & h) in steam at 700 °C, showing the distribution and geometry of oxides.

4.10.3 Thickness variation of oxide scale in air and steam

As shown in Fig. 4.38, the oxide scale developed on the surface of laser cladded coating after 100 h in air was so thin that it could not be observed in Fig. 4.38 (a). The image at a higher magnification, of the oxide scale exhibited the slow oxidation rate of the laser cladded coating, as the thickness of the oxide scale was in the range of nanometre.

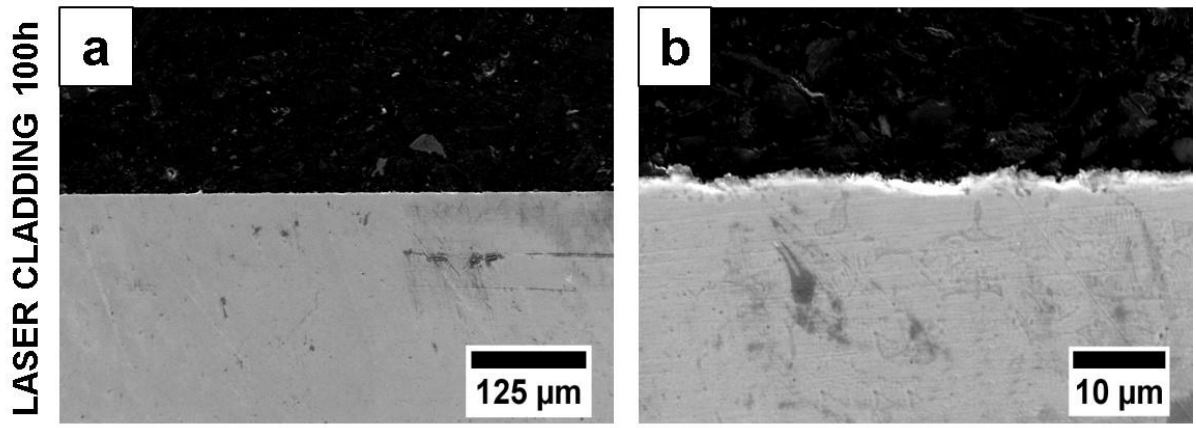

Fig. 4.38 SEM BSE cross-section images of laser cladded coatings after 100 h in air at 700 °C, showing: (a) entire oxide scale, (b) oxide scale detail at higher magnification.

Fig. 4.39 (a) shows an absence of a continuous oxide layer on the top surface of the laser cladding 250 h steam oxidation sample. With the increase in the exposure time, the oxides were observed in Fig. 4.39 (c) and (d). These oxides were Cr_2O_3 according to the EDX analysis and the XRD phase identification. The morphology of the oxides was flake geometry, as shown in Fig. 4.37.

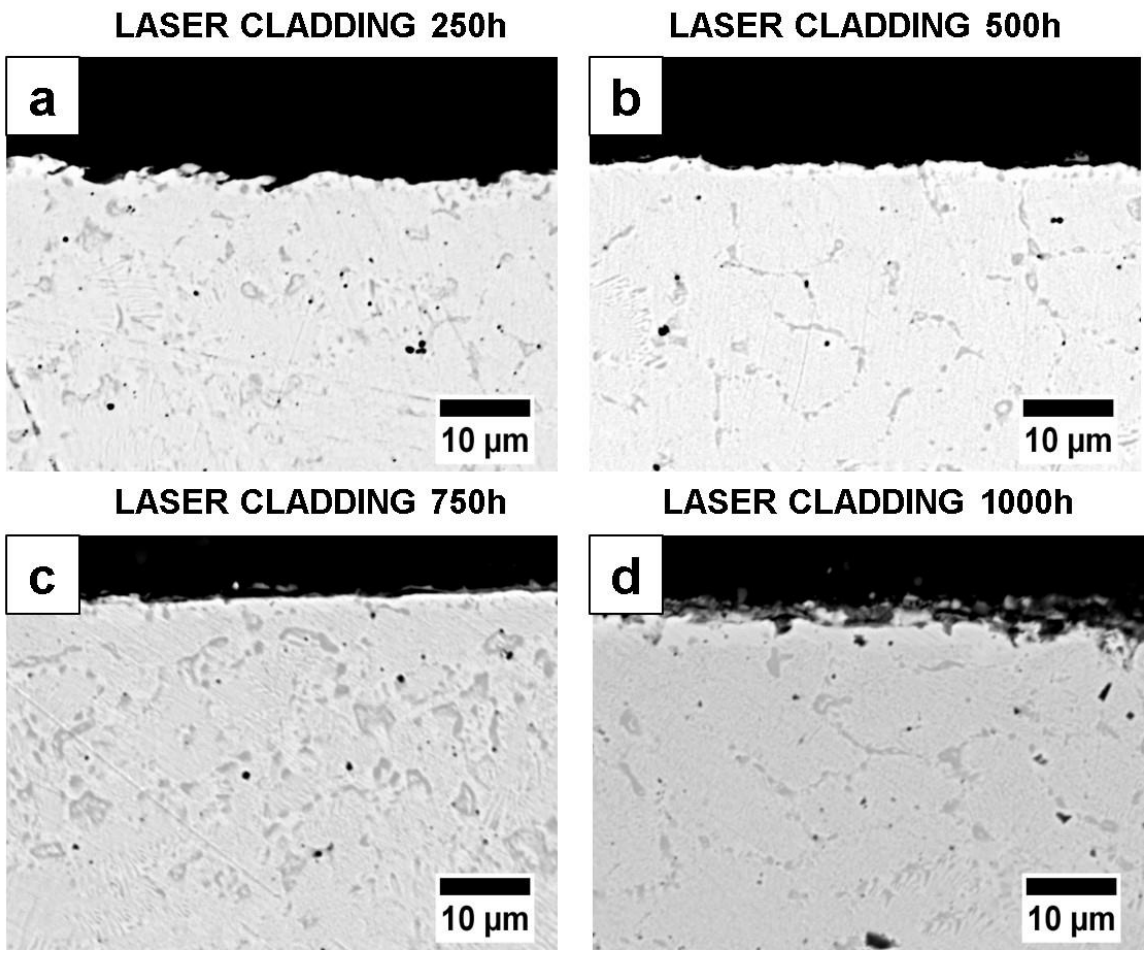

Fig. 4.39 SEM BSE cross-section images of laser cladded coatings after 250 h (a), 500 h (b), 750 h (c) and 1000h (d) in steam at 700 °C, showing the distribution of oxide scale and microstructure of oxide scale.

These oxides did not form a dense scale within 1000 h of exposure. This layer could not provide long-term steam oxidation resistance for the coatings under it. The dark features developed at the boundary of the resolidification grains of the NiCrFe alloy were oxides. The penetration of the oxidising ions was evaluated using these features as a tracer. The gaps at the grain boundary had a sharp feature, which was not detected in the as-deposited laser cladded coating. The steam oxidation promoted the formation of these gaps.

4.11 Oxidation behaviour of coatings

A short summary of the characteristics of four coating after oxidation is given in following paragraphs to provide an intuitive comparison of different oxidation behaviour of coatings.

In the case of HVOLF coatings:

- Cr_2O_3 was the major oxidation product in air and the only product in steam. Oxide phases containing Ni were also identified in the 100 h air oxidation sample.
- In air, the oxides in the thin flakes began to grow on the surface of the splats after only 1 h of exposure and kept increasing in thickness up to 100 h. In steam, the edge of these oxide flakes was sharp because of the presence of steam, which resulted in the cluster-like features of the oxides on the coating surface.
- The cross-section images of the oxide scale confirmed that the thickness of the oxide scale under both conditions was considerably low, and the microstructure of this oxide scale was a cluster of oxide flakes.

For the HVOGF coatings:

- In air, there was Cr_2O_3, NiO and $NiCr_2O_4$ were identified on the surface of coatings up to 100 h. In contrast, there was no trace of NiO in steam.
- The evolution of oxides that grew on the surface of the splats in both air and steam exhibited the same trend: initially, the thin oxide flakes increased in thickness and size; then, the thick oxide flakes accumulated to form a

polyhedron with well-defined edges; and finally, these oxide polyhedrons developed into an *in-situ* oxide scale.

- The oxide scales on the surface of the coatings that developed in both air and steam were thicker than those developed on the surface of the HVOLF coatings. Moreover, a positive correlation was observed between the thickness of the oxide scales and the high temperature exposure time. However, the extent of increase in the oxide scale was not obvious even when the exposure time reached 1000 h.

The characteristics of the cold sprayed coatings after air and steam oxidation were different from those of the HVOLF and HVOGF coatings because of the composition and the microstructure of the as-sprayed coatings:

- The oxides that developed in air were Cr_2O_3 and $NiCr_2O_4$. While in steam, $MnCr_2O_4$ appeared as the secondary oxide phase.
- The oxides on the surface of the coatings in both air and steam always retained the flake geometry during each exposure time (100 h in air and 1000 h in steam).
- The cross-sections of the air and steam oxidising coatings confirmed that the oxide scales under both conditions were thin and not continuous.

The characteristics of the laser cladded coating after oxidation can be summarised as follows:

- The main produced oxide in both air and steam was Cr_2O_3.

- Oxides produced in air exhibited small and cubic geometries while that produced in steam exhibited large and flake geometries, which confirmed the thinning effect of steam on the oxides.
- The oxide scales on the surface of the coating after air oxidation were too thin to be observed, even the exposure time extended to 100 h. In steam, the thickness of the oxide scale increased with the exposure time and was thick enough to make the scale distinguished after 750 h of exposure.

4.12 Growth direction of the oxides on the coating surface

The top morphology of the HVOLF coating indicated that the oxides preferred a specific growth direction. As shown in Fig. 4.18 and Fig. 4.19, the oxides exhibited a cluster-like feature when observed from the top. The sharp edges of the flat polyhedral oxide flakes brought about this feature of the top morphology. Most of the flat polyhedral flakes grew and increased in size in the plane defined by their largest cross-sections. These largest cross-sections are mostly parallel to the radial direction of the splats.

On the top surface of the HVOGF coatings, the accumulation of oxides was different from that on the top surface of HVOLF. The polyhedral flakes were parallel to the splat surface and thereby showed a laminar stacking layer by layer (Fig. 4.24 and Fig. 4.25).

On the top surface of cold sprayed coatings (Fig. 4.30 and Fig. 4.31), most of the oxide crystals showed a cubic polyhedron feature, which was quite different from that of the oxides on the top surface of the other three coatings. The thin flakes appearing at the

surface of the 1000 h sample (Fig. 4.31 (h)) are believed to be another layer of oxides that grew above on the old polyhedral oxides.

On the surface of the laser cladded coating after air oxidation, oxides in approximately equiaxed polyhedron geometry accumulated as shown in Fig. 4.36. When the oxidising atmosphere changed to steam, the cluster-like feature on the top surface of sample (Fig. 4.37) is not so obvious as that shown on the top surface of the HVOLF coating; instead, the large flat surface of the polyhedral flakes could be easily identified at most locations.

These differences might be attributed to the residual strain status on the top layer of the coatings. The splats on the top layer of the HVOLF and HVOGF coatings experience some degree of deformation upon impact and are usually in compression [35], and the deformation of the HVOGF spray splats is larger than that of the HVOLF spray splats. The splats in the cold spray process experience almost no deformation, as the temperature is relatively low and thus all parts of the powder particles retain in the solid and unmolten states [97]. Tensile strain is produced in the splats that are in the deformation state because of the compression states of these splats [193]. The direction of the tensile strain of these splats is from the geometrical centre of the deformed splats to the edge of the splats [194].

In the HVOLF spray splats, the deformation of the splats is medium, and they retain a near spherical geometry. The strain in them appears to have a roughly radial distribution. In the HVOGF splats, the deformation of the splats is so large that these splats transfer to lamellar geometry. In the lamellar splats, the strain is approximately parallel to the expansion direction of the splats. In contrast, in the cold spray splats,

there is no deformation in most of the splats and the strain in them distributes in a perfectly spherical pattern. The difference in the strain direction determines the growth orientation of the oxides on the surface of splats; these oxides are perpendicular to the growth surface and extend their area in one plane (two dimensions), and this plane is defined by the largest cross-section of the polyhedron and the direction of strain. The strain in each direction is almost same for the splats of cold sprayed coatings. Hence, size of oxides on the surface of cold sprayed coating increased in three dimensions rather than two dimensions, as that occurring in the case of the HVOLF and HVOGF coating.

The strain in the laser cladded coatings is attributed to the melting and the resolidification of the melt pool [195, 196]. Cycling heat input and output throws a thermal impact on the melt pool, and thereby produce a thermal strain state in the clad [197, 198]. The direction of this thermal strain is from the centre of the melt pool to certain points at the boundary of melt pool. The largest strain direction for each oxide varies slightly because of the thermal disturbance in the melt pool.

4.13 Oxidation mechanisms of coatings in air and steam

According to the results that were showed above, oxides produced in the same atmosphere of various coatings have different morphologies despite their same composition. Moreover, the morphologies of oxides that developed at the surface of a coating varied with a change in the atmosphere.

On the top surface of the HVOLF coatings, the air oxidation product up to 100 h of exposure was Cr_2O_3 and a small amount of $NiCr_2O_4$. The morphology of Cr_2O_3 appeared to have transformed into large well-defined flakes measuring around 2 μm.

Moreover, some smaller hexagonal oxides covered the area that was not occupied by the flakes. While in the steam oxidation 250 h sample, these Cr_2O_3 flakes seemed to be finer in size and had a sharper edge than those developed in air. With the increase in the steam oxidation time, the sharpening trend was retained up to 750 h. This trend was attributed to the evaporation of the volatile Cr species as abovementioned. Such evaporation behaviour prefers to occur along the grain boundary during the oxidation of the alloys, as in which there is a largest surface area. Yet, under the condition of coating oxidation, the evaporation may occur along the two largest surfaces of the oxide flakes. The continuous evaporation of the Cr atoms of the two largest surfaces leads a decrease in the thickness of oxide flakes, which brings about a sharpening and thinning effect on the oxide morphologies. In the air atmosphere, no evaporation of the Cr ions occurs; hence, the thickness of Cr_2O_3 continues to increase accordingly.

Unlike in the case of the HVOLF coatings, the oxide phases on the top surface of the HVOGF coating were complex. At 100 h, in the air oxidation sample of the HVOGF coating, Cr_2O_3, NiO and $NiCr_2O_4$ were all identified, which indicated that the oxidation process of this coatings is a transition oxidation, rather than a complete selective oxidation of Cr. The threshold point between the transition oxidation and the selective oxidation is 20 wt.% Cr in the NiCr-based alloy [20]; i.e. when the Cr concentration in the NiCr alloys exceeds 20 wt.%, there will be the selective oxidation of Cr occurring and the surface of coating will be covered by the Cr_2O_3 scale. However, this principle can only be applied to the oxidation of alloys which have a surface of low roughness according to the evidence shown in this study; it did not work in the investigation of the oxidation of NiCr-based coatings. The production of a complete chromia scale comes from the suppression effect of Cr on nickel-containing oxides such as NiO and

$NiCr_2O_4$. The oxide islands containing Ni in the scale could be covered by Cr_2O_3 if the concentration of Cr exceeds the limit, thereby losing the contact opportunity with the oxidising atmosphere. This isolation behaviour is determined by not only the chemical dynamic and thermodynamic properties of Cr_2O_3 but also the structure and the integrity of the chromia scale. Obviously, the scale developed on the surface of the thermal sprayed coating could not retain uniform thickness and microstructure because of the considerable roughness of the as-sprayed coatings. Splats having various degrees of deformation lead to an oxide scale that could not grow and develop on a relatively flat surface. The distribution and the magnitude of stress in the scale varies according to the morphology of the nearby coatings under the local scale. This made it difficult for oxides to grow at an approximately equal rate and along the same outward direction. Hence, the suppression influence of Cr_2O_3 scale on the production of nickel-containing oxides could not be achieved in the thermal sprayed coatings rapidly. For instance, in this study, the nickel-containing oxide phases remained on the surface of the coatings even after 100 h of air oxidation.

Besides the less suppression effect of Cr on the growth of NiO and $NiCr_2O_4$, the evaporation of chromium-rich compounds contributes to the survival of NiO during the steam oxidation of the HVOGF coatings. In the steam oxidation samples, even after 1000 h of exposure, the NiO phase identified in the XRD pattern remained (Fig. 4.23). The stable chromia layers did not cover the surface of fresh coatings entirely and could not be retained for the further protection of the substrates. The oxide scale of the NiCr alloys consisted of three layers: the inner chromia layer, the middle layer of a mixture of Cr_2O_3 and NiO, and the outer NiO layer. Chromium-rich compounds such as $CrO_2(OH)_2$ volatilise easily at high temperature, resulting in a burst of the Cr_2O_3 layer.

The bursting of the chromia layer leads to the subsequent spalling of NiO and $NiCr_2O_4$ that grow at the basis of Cr_2O_3 layer. Then the fresh chromia layer comes into contact with the steam atmosphere again. Considering the large partial pressure of water under the 100% steam condition, the volatilization of $CrO_2(OH)_2$ and CrO_3 becomes sever. The Cr in the fresh coating surface is consumed in abovementioned method, and the residual Ni is oxidised again. This reaction circuit (evaporation of Cr_2O_3–spalling of NiO–exposure of fresh metal to atmosphere) operates in cycles, and finally an oxide scale cannot be steadily built and retained on the surface of the coating in the presence of steam. The two oxide behaviours discuss above leads to the formation of the unstable oxide scale for the steam oxidation coatings.

The feedstock powder of the cold sprayed coatings had a different composition from that used in the HVOLF and HVOGF processes. The 1–2 wt.% Mn in the Sandvik Ni50Cr powder did not result in the formation of a new oxide phase in the identification of the XRD pattern of the air oxidation samples of the cold sprayed coatings Fig. 4.28. The Cr_2O_3 and spinel phases developed on the coating surface. However, when the oxidising atmosphere changed from air to steam, the composition of the spinel changes from nickel-containing to manganese-containing accordingly. Moreover, the relative intensity ratio between the $MnCr_2O_4$ peaks and the Cr_2O_3 peaks in the cold spray 1000 h steam oxidation XRD pattern (Fig. 4.29) was larger than that between the $NiCr_2O_4$ peaks and the Cr_2O_3 peaks in the HVOGF 1000 h steam oxidation XRD pattern (Fig. 4.23). This behaviour indicated that the Mn in the coating participated in the oxidation process. Considering the 1–2 wt.% content of Mn in the Sandvik Ni50Cr powder and Sandvik powdered coating, the $MnCr_2O_4$ peaks could not reach the same intensity as that reached by the $NiCr_2O_4$ peaks just by consuming the Mn elements in

the several top splat layers that are adjacent to the coating surface. Therefore, the Mn atoms in the several middle and bottom layers diffuses outwards through the coating as well as the oxide scale and produce manganese-containing oxides at the surface of coatings. Mn ions diffuses 100 times faster than Cr ions through the Cr_2O_3 lattice [199].

4.14 Summary

According to the discussion made above, following summary can be made:

- In general, HVOLF coatings had less oxide and larger porosity than HVOGF coatings.
- The oxides phases produced on the top surface of the HVOGF Ni50Cr coatings indicates that the occurring of selective oxidation of NiCr alloys needs a certain dwell time and the several seconds in the flame is not long enough.
- Chromium oxide was the main oxidation product for high temperature and steam oxidation of Ni50Cr coatings.
- Minor oxide phases such as $MnCr_2O_4$ spinel and $NiCr_2O_4$ spinel were identified on the surface of cold sprayed coating and HVOGF coating respectively.
- $NiCr_2O_4$ was developed during the spray process stage of HVOGF coatings, rather than consequent steam oxidation test stage, which indicated the presence of steam, the transient oxidation of NiCr alloys is not significant.
- Oxides of various morphology developed on the top surface of coatings. The morphology and growth direction of oxides are determined by the strain status of splats.

- Oxides of flake geometry appeared on the surface of HVOLF, HVOGF and laser cladded coatings. While on the surface of cold sprayed coatings, irregular cubic geometry was the main morphology for oxides.
- There was no thick and continuous oxide scale developed on the surface of four coatings in air after 100 h of exposure, which indicated the small oxidation rate of NiCr system. Moreover, in the cases of HVOLF, HVOGF and cold sprayed coatings, the larger surface roughness that was attributed to the splats undermined the microstructure of the oxide scale further.
- There was no thick and continuous oxide scale developed on the surface of four coatings although steam can promote the oxidation of NiCr alloys. Besides the abovementioned larger surface roughness, the damaging effect of the steam on the Cr_2O_3 scale cannot be neglected.
- Oxide scale on the surface of laser cladded coatings was the thickest. Yet, the steam oxidation of laser cladded coatings was not the best since there is evidence indicating oxidising ions penetrates through the scale and enter the coatings.
- HVOLF and HVOGF coatings had better steam oxidation resistance and are robust with the presence of steam during oxidation.

Chapter 5 High temperature chlorine-induced corrosion behaviour of coatings

5.1 Introduction

In this chapter, the high temperature chlorine-induced corrosion of the liquid fuelled HVOLF (HVOLF) and gas fuelled HVOF (HVOGF) thermal sprayed, cold sprayed and laser cladded coatings are reported. These coatings were exposed in a controlled corrosion environment test rig at 700 °C for 250 h in an atmosphere containing 500 ppm of HCl and 5 vol.% O_2 and N_2 in balance. The examination results of the exposed samples using various characterisation techniques are displayed here. The fireside corrosion performance of the coatings and the mechanisms behind the behaviour are discussed, followed by the conclusions.

5.2 High temperature corrosion of HVOLF coating

5.2.1 Effect of KCl deposit on the phase change of corrosion products

As shown in Fig. 5.1, in the XRD pattern corresponding to the HVOLF coating after 250 h of heat treatment in a simulated atmosphere, three peaks corresponding to the fcc γ–(Ni, Cr) phase at 2θ = 44.2º, 51º and 75.8º remained. The other peaks corresponding to the fcc γ–(Ni, Cr) phase and the α–Cr phase in the as-sprayed HVOLF coating (Fig. 4.2) disappeared. Cr_2O_3 was the main oxidation product of the HVOLF coating without the KCl deposit. In the XRD pattern corresponding to the coating deposited with KCl, one peak at 2θ = 30.8º representing the $NiCr_2O_4$ spinel appeared. $NiCr_2O_4$ was a minor oxide phase, as the intensity of the Cr_2O_3 phase peaks was much larger than that of the $NiCr_2O_4$ phase in the pattern. The intensity of the γ–(Ni, Cr) peaks was considerably higher than that of the Cr_2O_3 peaks. In contrast, in the

pattern for the HVOLF coating without the KCl deposit, the γ–(Ni, Cr) peaks had larger intensities than the Cr_2O_3 peaks. This evolution of the intensity of the two main phases in the XRD patterns of the two coatings was attributed to several factors such as the detrimental effect of the alkali metal ions (K^+) on the oxide scale microstructure and the active oxidation of NiCr in the presence of chlorine, whose discussion will be expanded in the discussion section of this chapter. Moreover, the intensity of the peaks in the HVOLF XRD pattern was considerably stronger than that in the HVOLF + KCl pattern XRD pattern, which indicated the reduction effect of KCl on the crystallinity of the alloy (γ–(Ni, Cr)) and the oxide (Cr_2O_3).

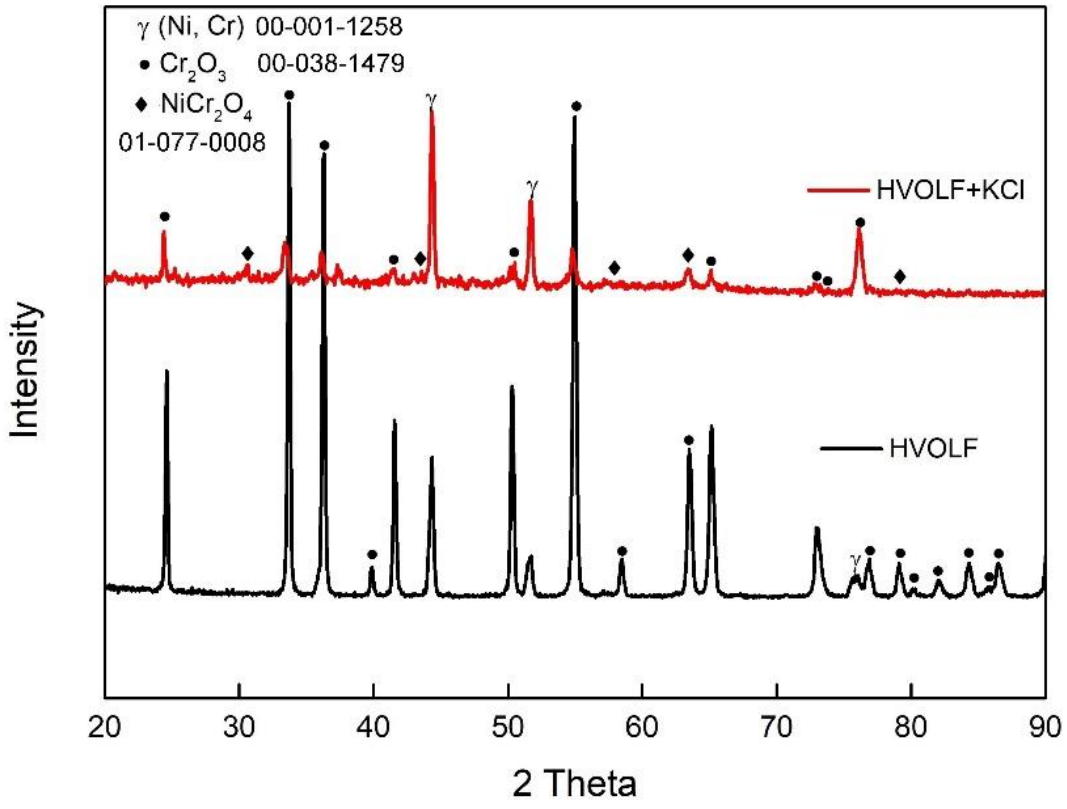

Fig. 5.1 XRD patterns of HVOLF coatings with and without the KCl deposits after chlorine-induced corrosion at 700 °C for 250 h.

5.2.2 Influence of KCl deposit on the crystallinity of oxide scale

The SEM images of the HVOLF coating without the deposit after exposure are shown in Fig. 5.2 (a), (b) and (c). A layer of oxide covering the entire coating surface can be seen in Fig. 5.2 (a). Two geometries of these oxides were observed: irregular polyhedron oxides, occupying at least 95% of the surface, and flake-like oxide geometry occupying the rest. Fig. 5.2 (b) and (c) provide the morphology information of the two oxides at a higher magnification. According to the EDX analysis, these oxides in both the polyhedron and the flake geometries were mainly Cr_2O_3 (spots 1 and 3: Cr 50–52 wt.% and O 48–50 wt.%), which was consistent with the XRD results mentioned above, as Cr_2O_3 was the only oxidation product identified. Smaller oxides at spot 2 in Fig. 5.2 (b) contained 28 wt.% Ni, which was quite close to the Ni content (26 wt.%) in $NiCr_2O_4$. Thus, this oxide could be the $NiCr_2O_4$ spinel according to the EDX analysis. However, no peak corresponding to the $NiCr_2O_4$ phase was observed in the HVOLF XRD pattern shown in Fig. 5.1. This was probably because the content of $NiCr_2O_4$ was too low to be detected using XRD (1–2 wt.%) [170] or the presence of Ni in the EDX result was due to the coating under the oxide scale.

Fig. 5.2 (c), (d) and (e) show the top morphology of the scale of the HVOLF coatings with the KCl deposit after the exposure. As seen in Fig. 5.2 (d), the presence of KCl obviously changed the morphology of the scale on the top surface of the HVOLF coating. The scale in certain areas cracked into blocks because of the presence of KCl [20] and developed into a parched earth-like pattern. The details of these blocks are shown in Fig. 5.2 (e). The gaps (indicated by black arrows) revealed the cross-section of the oxide scale on the top surface of the HVOLF coating in the presence of KCl. Fig.

5.2 (f) shows the amorphous oxides at a higher magnification. The geometry of the oxides was rather irregular in nature.

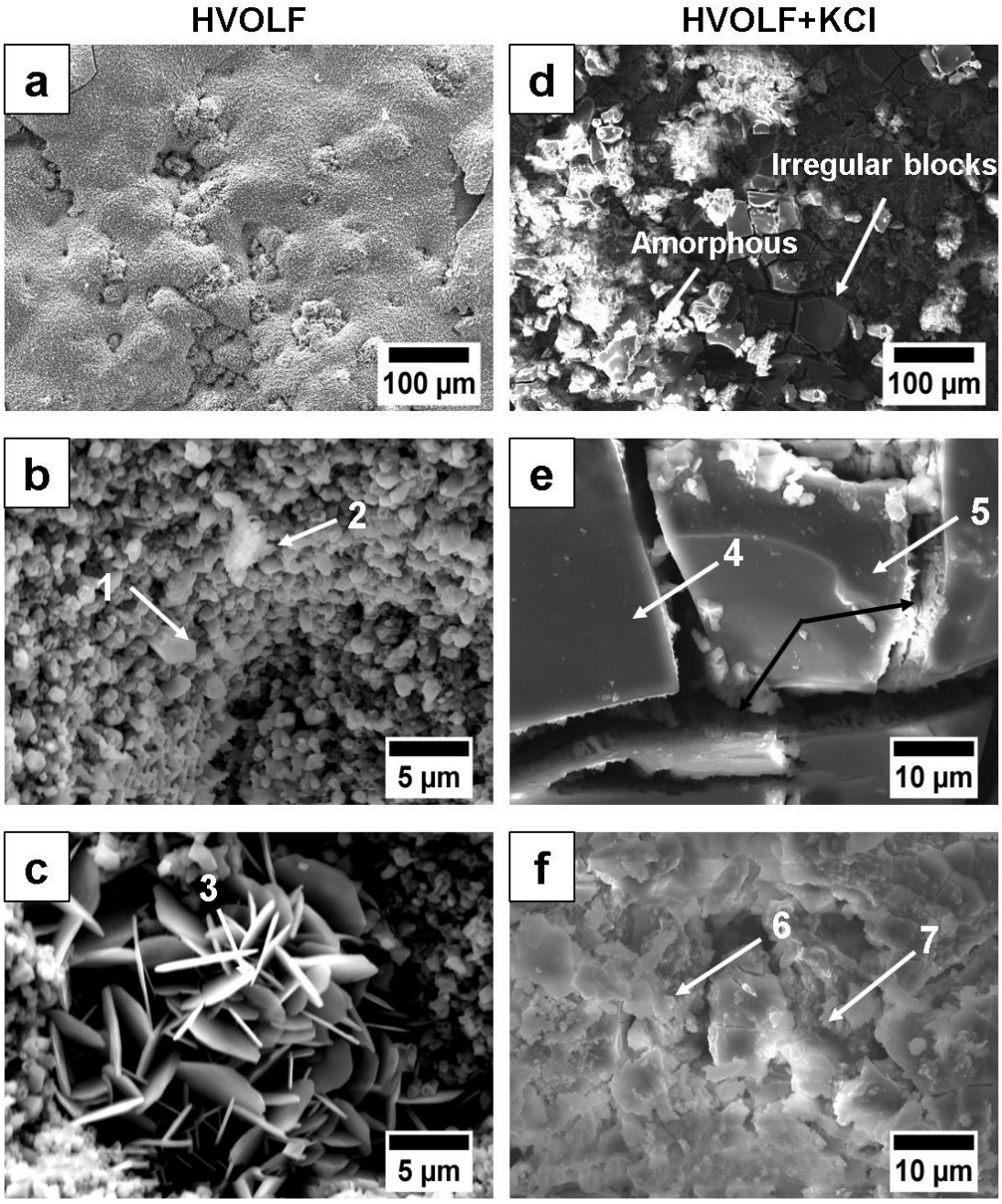

Fig. 5.2 SEM SE top surface morphology of HVOLF coatings after chlorine-induced corrosion at 700 °C for 250 h without the deposit: (a) overall view of the surface, (b) oxides in polyhedron geometry and (c) oxides in flake geometry; with the KCl deposit: (d) overall view of the surface, (e) cracked oxide scale and (f) amorphous oxide.

According to the EDX analysis, Cl was detected at all the four locations (spots 4, 5, 6 and 7) in non-negligible amounts (18–30 wt.%); in contrast, the presence of Cl was not detected in the XRD scans. This could be attributed to the fact that Cl is present in the amorphous scale according to literature [200]. Another piece of evidence that could reinforce the presence of the amorphous scale was the significantly reduced intensity of the phase peaks in the HVOLF + KCl XRD pattern (Fig. 5.1). The smaller the intensity of the pattern peaks, the less was the crystallinity of the alloy and the oxide and the larger was the amorphous degree of the scale.

Ni was also identified at all four spots, and its concentration ranged between 19 and 30 wt.%. These Ni contents could be attributed to two possible sources: $NiCr_2O_4$ or the underlying Ni50Cr coating. Considering the low intensity of the $NiCr_2O_4$ peak in the HVOLF + KCl XRD pattern shown in Fig. 5.1, most of the Ni signals in the EDX analysis could be attributed to the Ni50Cr coatings under the oxide scale, as the microstructure of the produced oxide scale was not free of defects; i.e. there were cracks through which the X-ray could irradiate the fresh coating surface easily.

5.2.3 Failure of the thickened oxide scale due to the KCl deposit

The entire cross-section of the HVOLF coating without the KCl deposit in Fig. 5.3 (a) clearly shows that a layer of oxide developed on the top surface of the coating; however, this layer was not continuous and did not have uniform thickness. A layer of splats was observed just under the oxide scale, which showed a brighter contrast in the BSE image shown in Fig. 5.3 (b). This was identified as the chromium-depletion area. The thickness of this chromium-depletion area was around 30 μm as indicated by the double-ended arrow in Fig. 5.3 (b). Gaps were observed not only at the

boundary between the splats but also within the splats, as shown in Fig. 5.3 (b); they were attributed to the Cl attack.

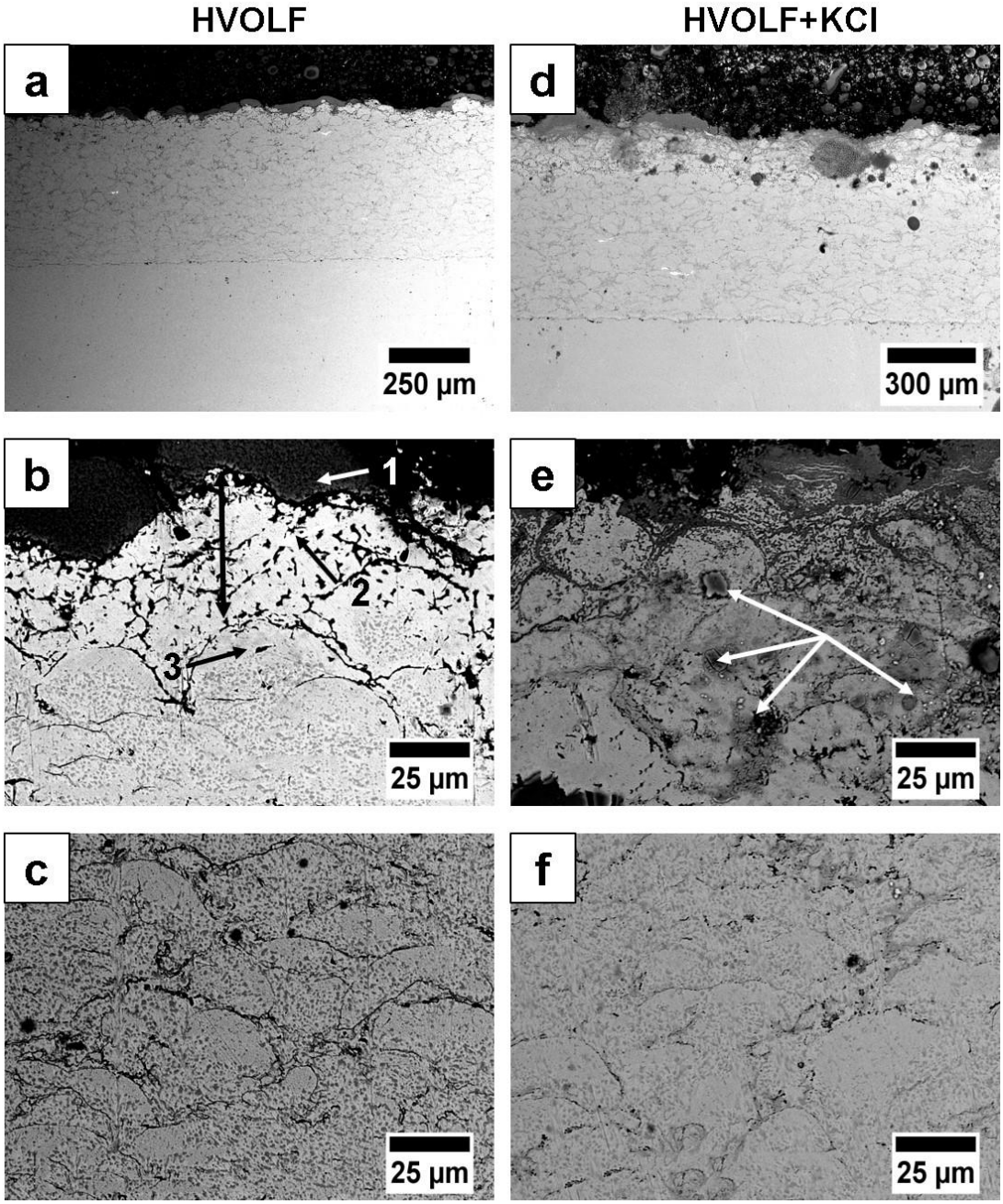

Fig. 5.3 SEM BSE cross-section images of HVOLF coatings after chlorine-induced corrosion at 700 °C for 250 h without the deposit: (a) overall view of coating cross-section, (b) oxide scale and chromium-depletion zone and (c) dual-phase microstructure of the bulk coating; with the KCl deposit: (d) overall view of the coating cross-section, (e) oxide scale and (f) dual-phase microstructure of the bulk coating.

According to Fig. 5.3 (b), under this chromium-depletion area, almost all the splats showed a chromium-depletion feature on the splat scale; i.e. the top half section of the splats was depleted in Cr, and the bottom half section of the splats contained a dual-phase microstructure. This dual-phase feature was also observed in the central region of the coating, as shown in Fig. 5.3 (c). The presence of the half chromium-depleted splats not only indicated the outwards diffusion direction of Cr but also could be used to confirm the transport path effect of the splats/grains boundary.

The EDX analysis results of spots 1, 2 and 3 supported the presence of a chromium-depletion layer under the oxide scale. The spectrum at spot 1 clearly indicated the presence of Cr_2O_3. At spot 2, the concentration of Cr reduced to 9 wt.%, which indicated the depletion of Cr. Moreover, 23 wt.% O was detected in the chromium-depleted area which confirmed the selective oxidation process of the coating.

The detrimental effect of KCl on the oxide scale is shown in Fig. 5.3 (d). Although the oxide scale was thicker in certain areas than on the surface of the HVOLF coatings exposed without KCl, in are some areas, the oxide scale completely spalled because of the attack of the K^+ ions. The role of KCl in the Cr depletion [149] was also confirmed from Fig. 5.3 (e). The thickness of the chromium-depleted zone under the oxide scale was 100 μm, which was two times larger than that without the deposit, as shown in Fig. 5.3 (a). The cracked blocky feature indicated by white arrows in Fig. 5.3 (e) also showed the detrimental effect of KCl on the coating [150], which was a result of the splats cracking within themselves. The elemental maps of the circular corrosion spot shown in Fig. 5.3 (d) as well as the nearby area are shown in Fig. 5.4. A large amount of Cl was observed in this spot; hence, it was believed to be rich in chloride [50]. Moreover, an obvious difference in the Cr content was observed between the area

inside the spot and that outside the spot. The Cr at the spot was consumed so much that there were almost no dots representing the Cr distribution, as shown in Fig. 5.4. These chloride ions acted as the catalyst during the active oxidation process of the NiCr coatings. Their concentration was an indicator of the poor corrosion performance of the HVOLF coatings in the presence of KCl. Obviously, such a porous and poor microstructure could not prevent the penetration of the corrosive species into the coating, and its expansion breached the oxide scale and lead to the failure of the coating. Three circular corrosion spots can be easily distinguished form Fig. 5.3 (d).

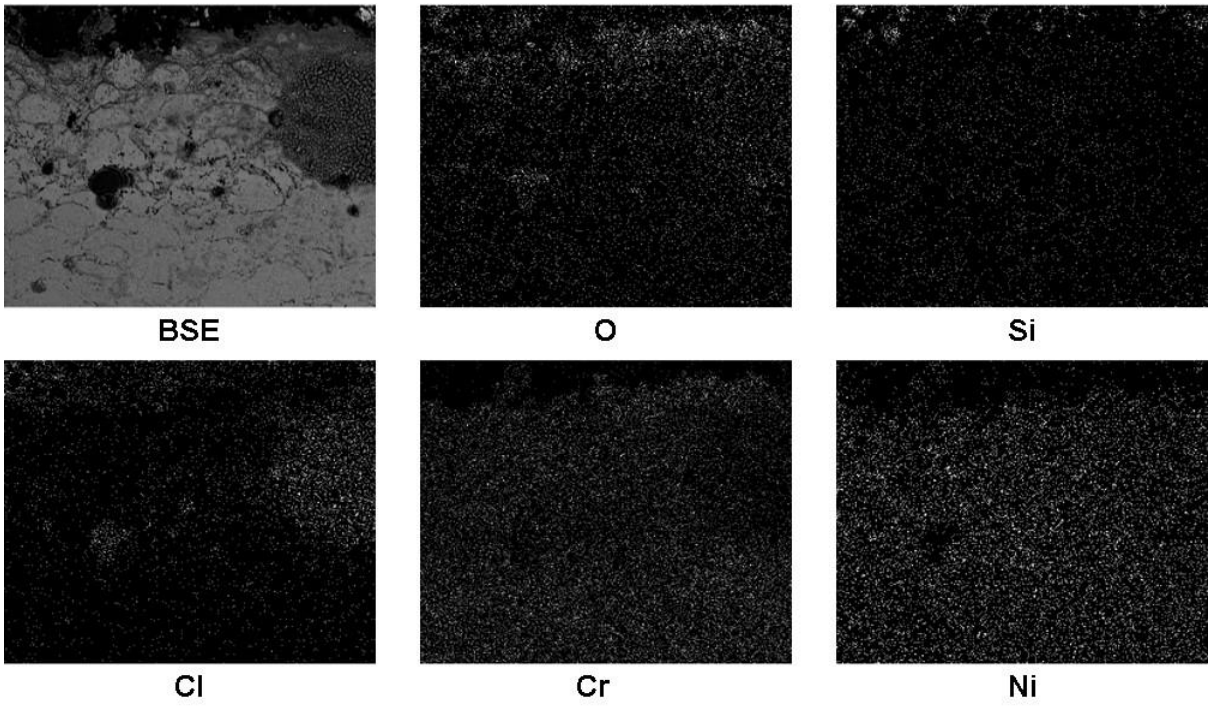

Fig. 5.4 EDX maps of the porous circular feature in the cross-section of HVOLF coating with the KCl deposit after chlorine-induced corrosion at 700 °C for 250 h.

5.2.4 Properties of oxide scale on the surface of coatings

As a barrier to isolate the fresh coating from the corrosive atmosphere and the substrate, the oxide scale produced on the surface of the coating that had a dense

structure and the desired composition were important for the oxidation/corrosion resistant coating [202]. Hence, it is important to summarise and discuss the properties, such as thickness, integrity, microstructure and composition, of the oxide scale which developed at the surface of coatings to evaluate the corrosion resistance of each coating.

In the case of the HVOLF coating with and without the KCl deposit, the oxide scale covered the surface of the fresh coating; however, obvious differences in the properties of these two oxide scales were observed. For instance, the oxides produced without KCl exhibited a well-defined geometry (polyhedron and flake) as shown in previous publication [126]. These oxides had no preferential growth direction, which was usually observed in the oxidation of the forged alloys and thus could not form the oxide scale produced in the traditional bulk alloys. The oxide scale that developed on the surface of the coatings was not as dense as that produced on the bulk alloys, as under the coating conditions, the growth of each oxide might not restrict the overall growth and development of the nearby oxides to one uniform direction–outwards from the coating to the atmosphere [22, 133, 203]. Individual oxides produced with the involvement of KCl on the surface of the HVOLF coating could not be distinguished, as some of them developed into a densely packed scale and the others grew in an amorphous pattern. The presence of KCl restricted the freedom of the growth direction of each oxide. Considering that the melting point of KCl is 760 °C [204], the formation of the two morphologies of the oxide scale on the surface of the HVOLF coating with KCl was attributed to the non-uniform distribution of the KCl salts. These salts were retained in the solid state at the test temperature of 700 °C and thus changed the morphology of the oxide scale under them. However, whether the parched earth-like

or the amorphous pattern corresponded to the KCl solid locations needs to be investigated further.

Although the thickness of the oxide scale on the surface of the HVOLF coating with KCl increased significantly as compared to that of the HVOLF coating without KCl, the integrity of the scale was impaired. Moreover, some locations were not covered by the oxide scale, according to Fig. 5.3 (d). The oxide scale on the surface of the HVOLF coating without the KCl deposit was thin but continuous, which was important for the corrosion resistance of the entire coating. The composition of the oxides on the surface of the two coatings (with and without KCl) differed and therefore, the oxidation processes occurring under the two conditions were different. Under the condition without KCl, the total oxidation process was just a selective oxidation process of NiCr alloys [17, 183, 205] with a relatively high rate because of the catalyst effect of Cl, as mentioned in Section 2.6, as the only oxidation product identified using XRD was Cr_2O_3. In contrast, additional $NiCr_2O_4$ spinels were found on the surface of the HVOLF coating with the KCl deposit, indicating that the transient oxidation of NiCr continued even after 250 h. This phenomenon was attributed to the detrimental effect of KCl. It was combined with Cr_2O_3 to produce $K_2Cr_2O_4$ which evaporated easily at 700 °C. As Cr continuously diffused from the coating to the interface of the atmosphere and KCl/coating, this elimination process of Cr_2O_3 with the $K_2Cr_2O_4$ carriers carried on because of the large supply of both K and Cr. The sustained consumption of Cr_2O_3 at the outmost layer of the oxide scale destroyed the classic sandwich structure of the oxidation products of NiCr (NiO–$NiCr_2O_4$–Cr_2O_3) and revealed the $NiCr_2O_4$ embedded in NiO. This explained the identification of NiO in the XRD pattern of HVOLF+KCl.

5.3 High temperature corrosion of HVOGF coating

5.3.1 Phases of corrosion products

In the XRD pattern of the HVOGF coating without the KCl deposit after high temperature corrosion shown in Fig. 5.5, three peaks corresponding to the fcc γ–(Ni, Cr) phase at 2θ = 44.2º, 51º and 75.8º were identified. As in the case of the corrosion of the HVOLF coating, only the Cr_2O_3 phase developed after the high temperature exposure on the top surface of the HVOGF coating without KCl.

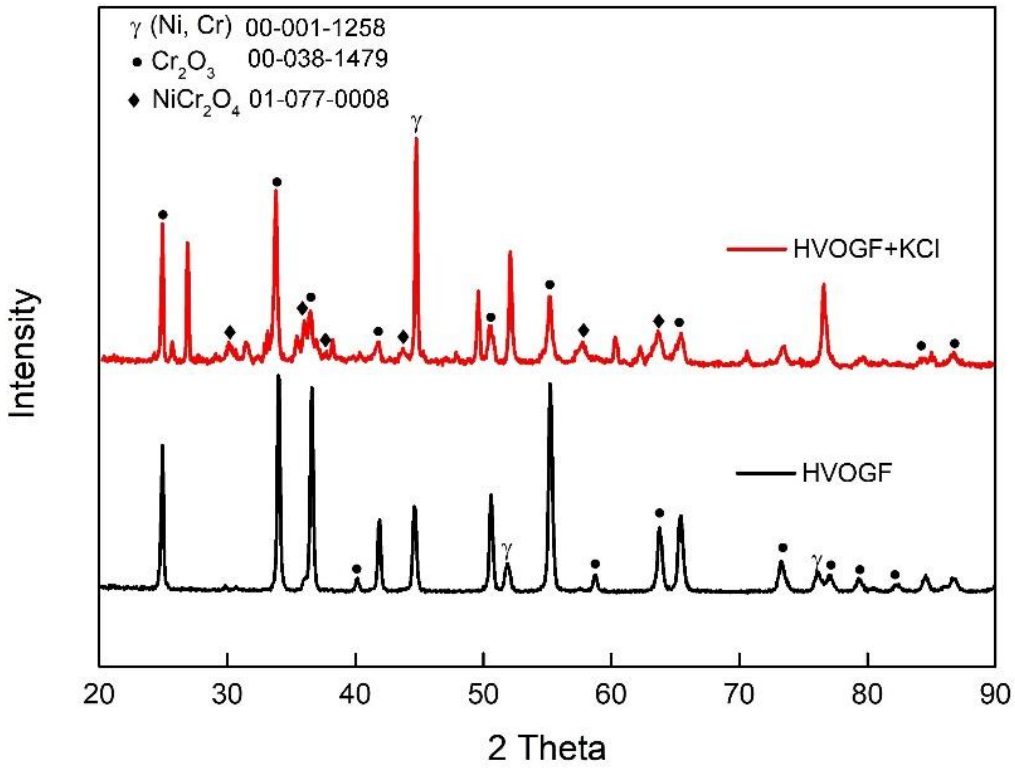

Fig. 5.5 XRD patterns of HVOGF coatings with and without the KCl deposits after chlorine-induced corrosion at 700 °C for 250 h.

In the XRD pattern of the coating exposed with the KCl deposit, peaks at 2θ = 30.8º, 35.7º, 43.5º and so on representing the $NiCr_2O_4$ spinel appeared. The $NiCr_2O_4$ content

increased significantly in the HVOGF coating covered with the KCl deposit compared with that in the HVOLF coating. The increase in the intensity of the γ–(Ni, Cr) peaks in the presence of KCl confirmed the detrimental effect of the K^+ ions on the oxide scale again, as it indicated the spalling or the thinness of the oxide scale in the local areas on the HVOGF coating surface; therefore, more X-rays from the coating rather than form the oxide scale were collected.

5.3.2 Evolution of oxide scale morphology with the addition of KCl deposit

The HVOGF coating experienced a corrosion attack like that experienced by the HVOLF coating. As shown in Fig. 5.6 (a), the surface of the HVOGF coatings after exposure was fully covered with oxides. Fig. 5.6 (b) shows the oxides of two geometries: irregular polyhedral and lamellar flake geometry. No significant composition difference was observed between these two types of oxides according to the EDX analysis. Both were believed to be Cr_2O_3 according to the EDX analysis as well as the XRD phase identification. Further 6–8 wt.% Ni was identified in spots 1, 2 and 3 in Fig. 5.6 (c), which might be attributed to the $NiCr_2O_4$ spinel, as a minor peak corresponding to this phase was observed in the HVOGF XRD pattern. The contribution of Ni in the underlying coatings could not be neglected.

The presence of KCl during the high temperature exposure obviously changed the morphology of the scale on the top surface of the HVOGF coating, as revealed by a comparison of Fig. 5.6 (d) and (a).

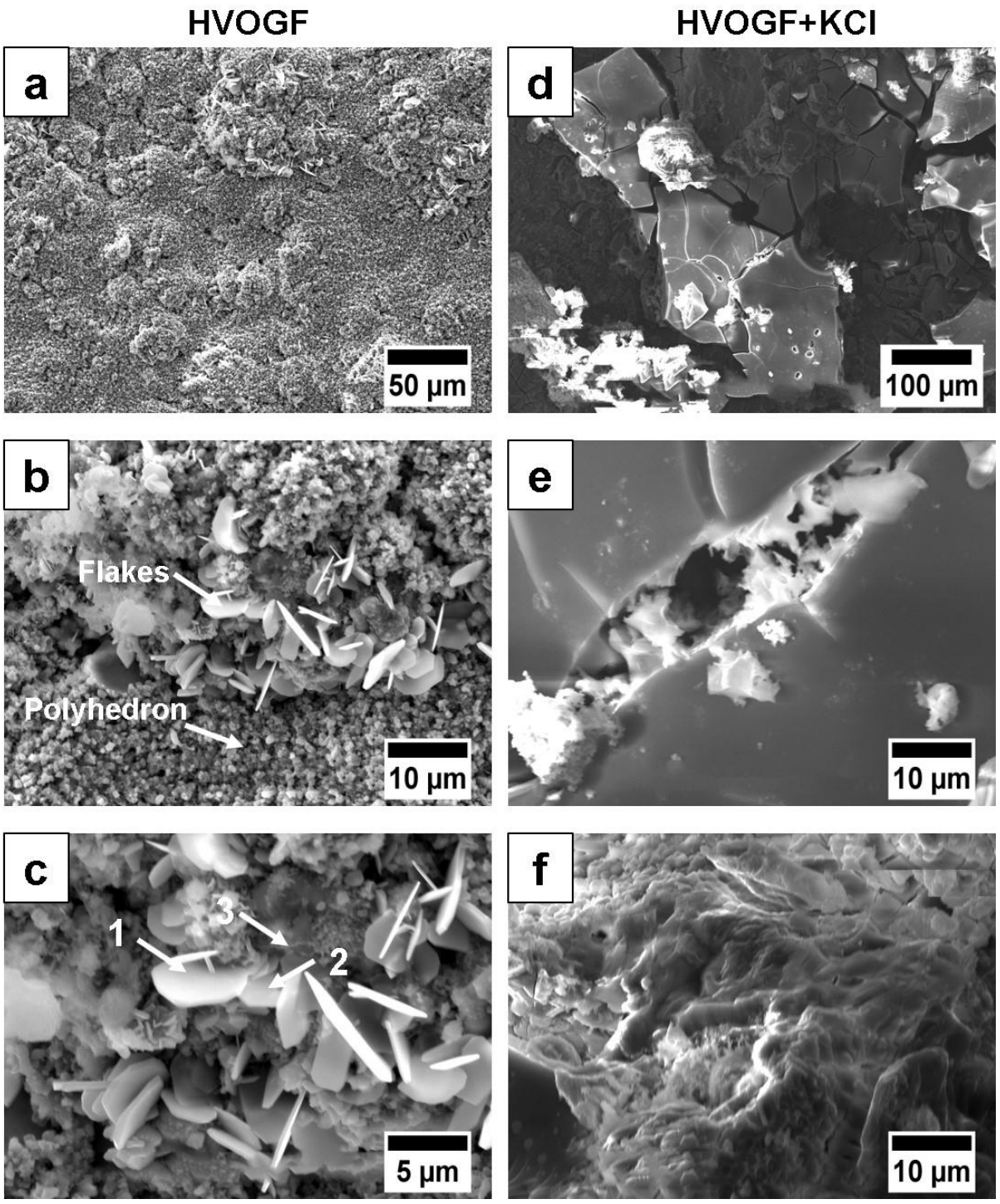

Fig. 5.6 SE top surface morphology of HVOGF coating after chlorine-induced corrosion at 700 °C for 250 h without the deposit: (a) overall view of the surface, (b) oxides in various morphologies and (c) higher magnification image of b; with the KCl deposit: (d) overall view of the surface, (e) oxide scale cracked into blocks and (f) irregular oxide scale.

The oxides within the scale in Fig. 5.6 (d) accumulated closely despite the fact that the scale cracked into large irregular blocks because of the presence of KCl. Fig. 5.6 (e) provides information about the cracks between two irregular blocks and the cross-section of the oxide scale. Fig. 5.6 (f) shows irregular oxides growing in an amorphous pattern. This phenomenon occurred on the surface of the HVOLF coatings with KCl after corrosion in the same manner.

5.3.3 Detrimental effect of chlorine-containing atmosphere and deposit on the oxide scale

A cross-section of the entire HVOGF coating without the KCl deposit after corrosion is shown in Fig. 5.7 (a). The oxide scale does not cover the entire top surface and shows cracks in certain areas, as shown in Fig. 5.7 (b). The oxide scale consists of Cr_2O_3 according to the EDX analysis result of spot 1 (48.4 wt.% O and 46.8 wt.% Cr). At spot 2, 80 wt.% Fe was identified. Such a high Fe content could be attributed to the corrosion of the steel substrate, i.e. vaporisation of iron compounds such as $FeCl_2$ at a high temperature, as only one surface of the rectangular P92 substrate was covered with the coating during the exposure and the other five surfaces of the substrate could contact the corrosive atmosphere. The EDX spectrum at spot 3 indicated that there was only 15 wt.% Cr in the splats under the scale, which was far less than the Cr content in the as-sprayed coating splats. Fig. 5.7 (c) shows the lamellar structure in the several middle layers of the coatings after exposure. It is difficult to evaluate the degree of oxidation in this area during chlorine-induced corrosion at 700 °C, as these splats experienced intense oxidation during the thermal spray process. The element maps shown in Fig. 5.8 clearly show a thin layer of the chromium-depleted area under the oxide scale; further, the oxide scale contained almost all the chromia.

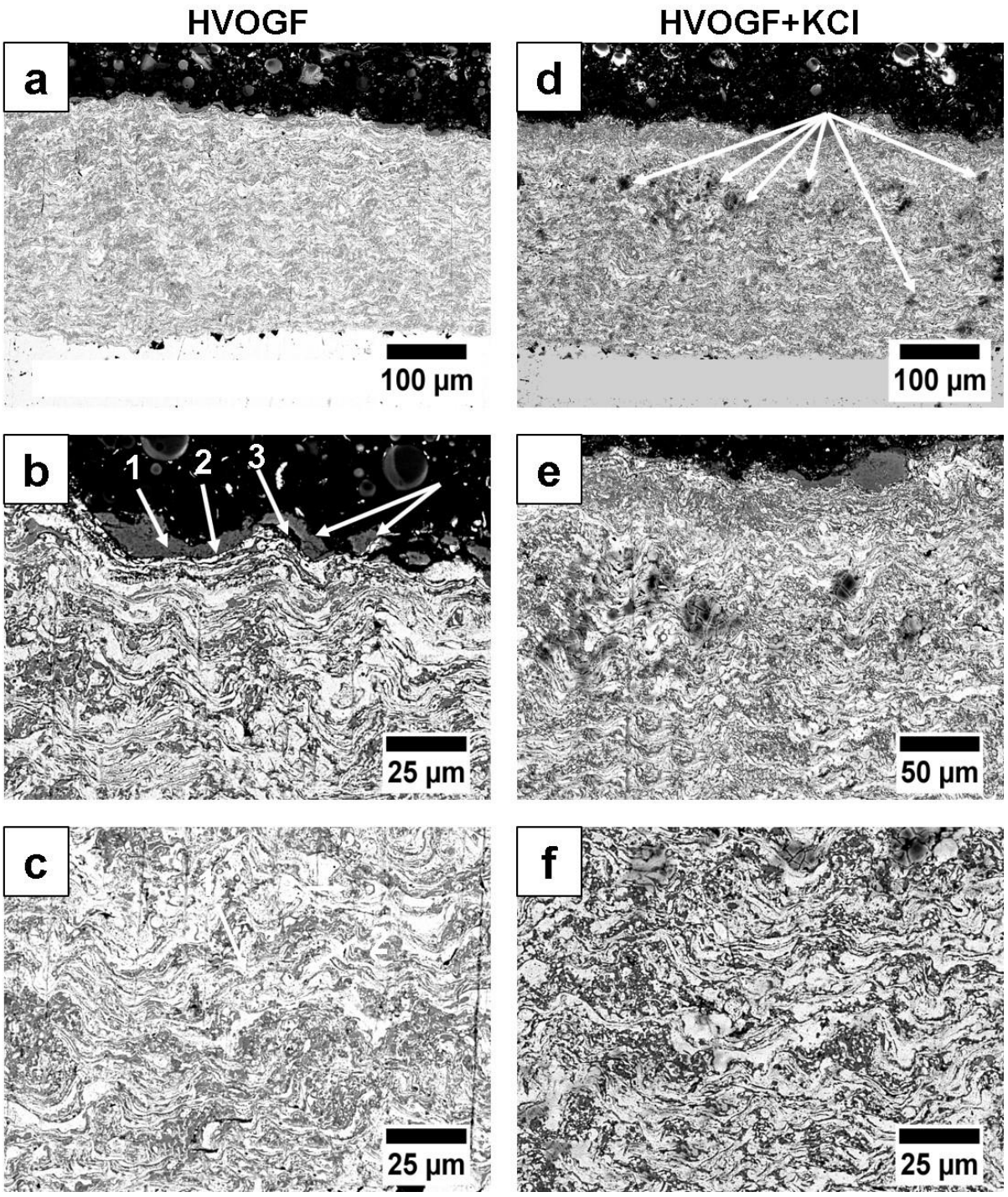

Fig. 5.7 SEM BSE cross-section images of HVOGF coating after chlorine-induced corrosion at 700 °C for 250 h without the deposit: (a) overall view of the coating cross-section, (b) oxide scale and (c) the central region of the coating; with the KCl deposit: (d) overall view of the coating cross-section, (e) oxide scale and (f) the central region of the coating.

The KCl attack on the oxide scale on the surface of the HVOGF coatings is also confirmed by Fig. 5.7 (d), as the oxide scale in some locations spalled. This phenomenon is very clearly seen in Fig. 5.7 (e). The cracks and the gaps within the splats indicated by white arrows in Fig. 5.7 (d) showed that the Cl content reached up to ~250 μm within the coating, which implied that the HVOGF coating might not provide satisfactory protection from chlorine-induced corrosion with the KCl deposit.

The penetration of the corrosive ions within the HVOGF coating was larger than that in the case of the HVOLF coating (~120 μm according to Fig. 5.3 (d)). As there was much more oxide within the as-sprayed HVOGF coating, the transport path effect of the corrosive ions in the oxides surrounding the splats was applicable here [26]. These corrosive ions had a larger transport/diffusion rate inside the oxides than inside coating itself.

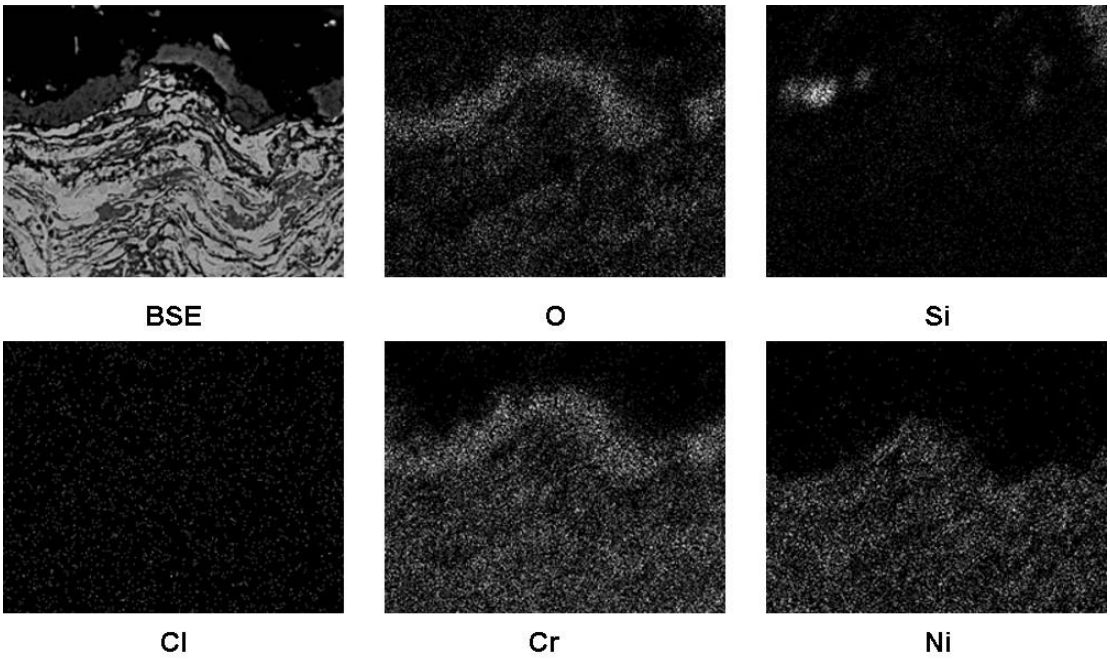

Fig. 5.8 EDX map of thin chromium-depletion area in the cross-section of HVOGF coating without the KCl deposit after chlorine-induced corrosion at 700 °C for 250 h.

5.3.4 Characteristics of oxide scale on the coating surface

In the case of the HVOGF coatings, the evolution of the oxidation scale under the conditions with/without KCl was almost the same as that in the case of the HVOLF coatings. The piled oxides in the well-define geometry grew along various directions without KCl and transformed into a dense but cracked oxide scale after the addition of the KCl deposit. The oxide scale increased in thickness and weakened in integrity when KCl participated in the corrosion process. The non-stop consumption of the outermost Cr_2O_3 in the presence of KCl revealed the NiO on the oxide scale surface.

5.4 High temperature corrosion of cold sprayed coating

5.4.1 Corrosion products including oxides of Cr, Ni and Mn

The XRD patterns of the cold sprayed coating after high temperature chlorine-induced corrosion are shown in Fig. 5.9. In the XRD pattern of the coating without the KCl deposit, the main peaks for fcc γ–(Ni, Cr) were still retained after exposure at 700 °C. Moreover, several types of oxides were produced, including Cr_2O_3, $MnCr_2O_4$ and $Mn_{0.63}Ni_{0.37}O$. Manganese nickel oxide was the major oxide, as the intensity of the peaks corresponding to this oxide was much stronger than that of the peaks corresponding to Cr_2O_3 and $MnCr_2O_4$. In the presence of KCl, the top surface of the cold sprayed coating after high temperature corrosion only contained two types of oxides and still retained the fcc γ–(Ni, Cr) phase, although the intensity of peak reduced significantly. $Mn_{0.63}Ni_{0.37}O$ almost disappeared from the top surface, as only one peak at $2\theta = 63°$ could still be identified. Instead, the peaks of Cr_2O_3 and $MnCr_2O_4$ significantly increased.

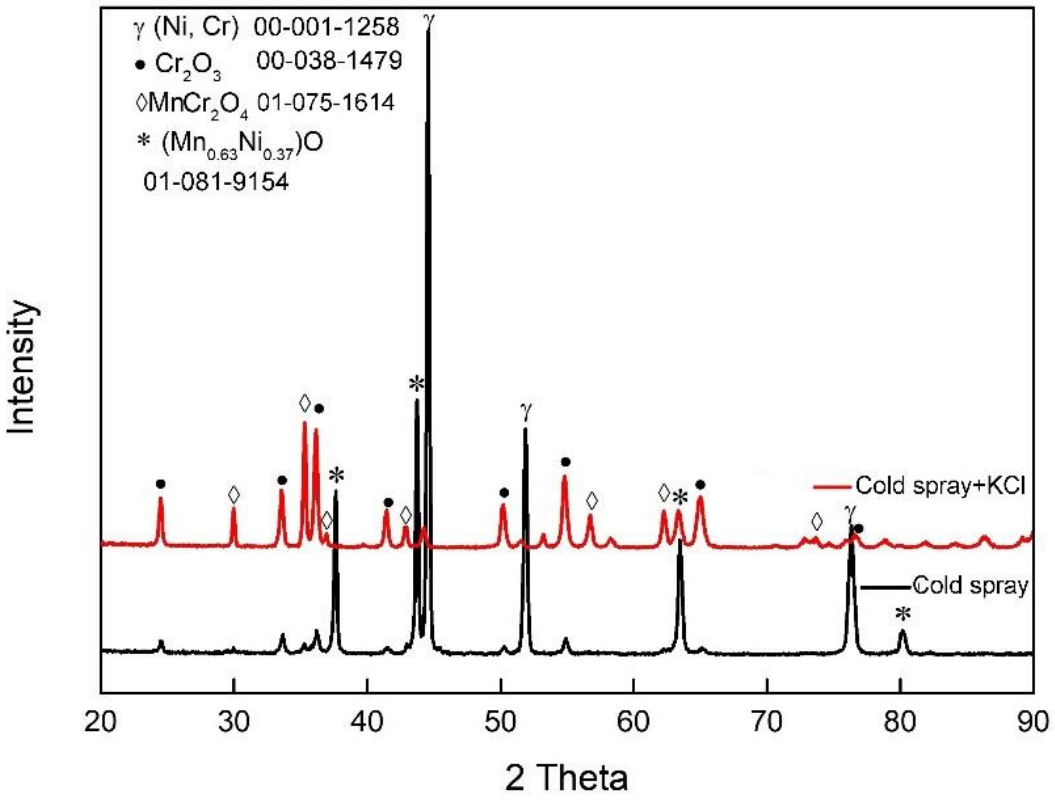

Fig. 5.9 XRD patterns of cold sprayed coatings with and without the KCl deposits after chlorine-induced corrosion at 700 °C for 250 h.

5.4.2 Well defined faceted oxides on the coating surface with the presence of KCl

The scratch pattern shown in the Fig. 5.10 (a) was left by the grinding procedure as mentioned in the experimental method. The porous structure was the most obvious feature of the scale morphology of the cold sprayed coatings without the deposit, as shown in Fig. 5.10 (a) and (b). Fig. 5.10 (c) provides the detailed microstructural information of the porous structure. These porosities are spherical and have a size distribution of 0.5–3 μm. The composition of the porous structure is mainly Cr_2O_3.

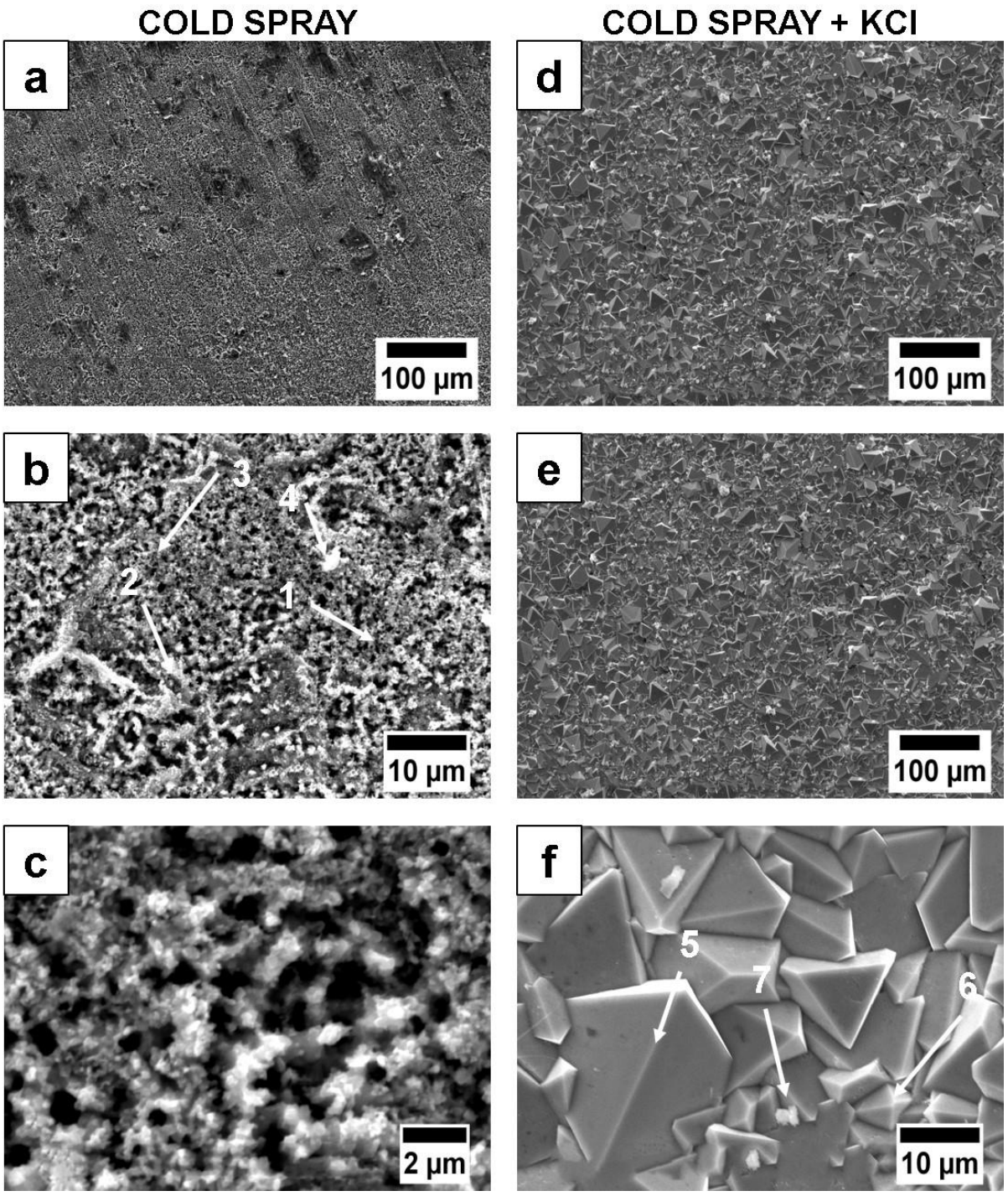

Fig. 5.10 SEM SE top surface morphology of cold sprayed coating after chlorine-induced corrosion at 700 °C for 250 h exposure without the deposit: (a) overall view of the surface, (b) and (c) high magnification images of the oxide scale; with the KCl deposit: (d) overall view of the surface, (e) oxides in faceted geometry and (f) faceted oxides in high magnification.

According to the EDX analysis, there is no Mn in spot 1, 2 and 3 but spot 4 contains around 15 wt.% Mn, which has a brighter appearance and it is likely to be a manganese nickel oxide.

The scale morphology of the cold sprayed coatings with the KCl deposit after high temperature chlorine-induced corrosion is shown in Fig. 5.10 (d) (e) and (f). The entire surface was covered with faceted oxides (Fig. 5.10 (e) and (f). These oxides were around of ~10 μm in size and had a well-defined geometry. They were closely packed.

The EDX analysis results for spots 5 and 6 indicated a trace amount of Ni (< 1.0 wt.%) and a large amount of Mn and Cr. Thus, these faceted oxides were a $MnCr_2O_4$ spinel with reference to the XRD results. The small bright particles indicated by spot 7 in Fig. 5.10 (f) had around 7.3 wt.% Fe, which might be the corrosion product of the substrate or contamination during the corrosion test.

5.4.3 Layered cross-section structure of oxide scale and coating

A triple-layered structure of the cold sprayed coating without the deposit can be observed clearly in Fig. 5.11 (a): 1. A mixed layer of Cr_2O_3, $MnCr_2O_4$ and $Mn_{0.63}Ni_{0.37}O$, 2. Oxidised splat layer and 3. Splats with a dual-phase microstructure. Layer 1 corresponds to the porous structure shown in Fig. 5.10 (b), as its cross-section features can still be seen in Fig. 5.11 (b). The dark features surrounding the splat structure was Cr_2O_3. There were also some cracks within the splats in this layer. Layer 2 consisted mainly of oxide splats. Cr at the core of the splats diffused outward, thereby forming a darker area around the boundary of the splats (darks features indicated by arrows in Fig. 5.11 (c) always appeared at the edges area of the splats).

A dual-phase microstructure was the most obvious feature in layer 3, which was also observed in the HVOLF and HVOGF coatings.

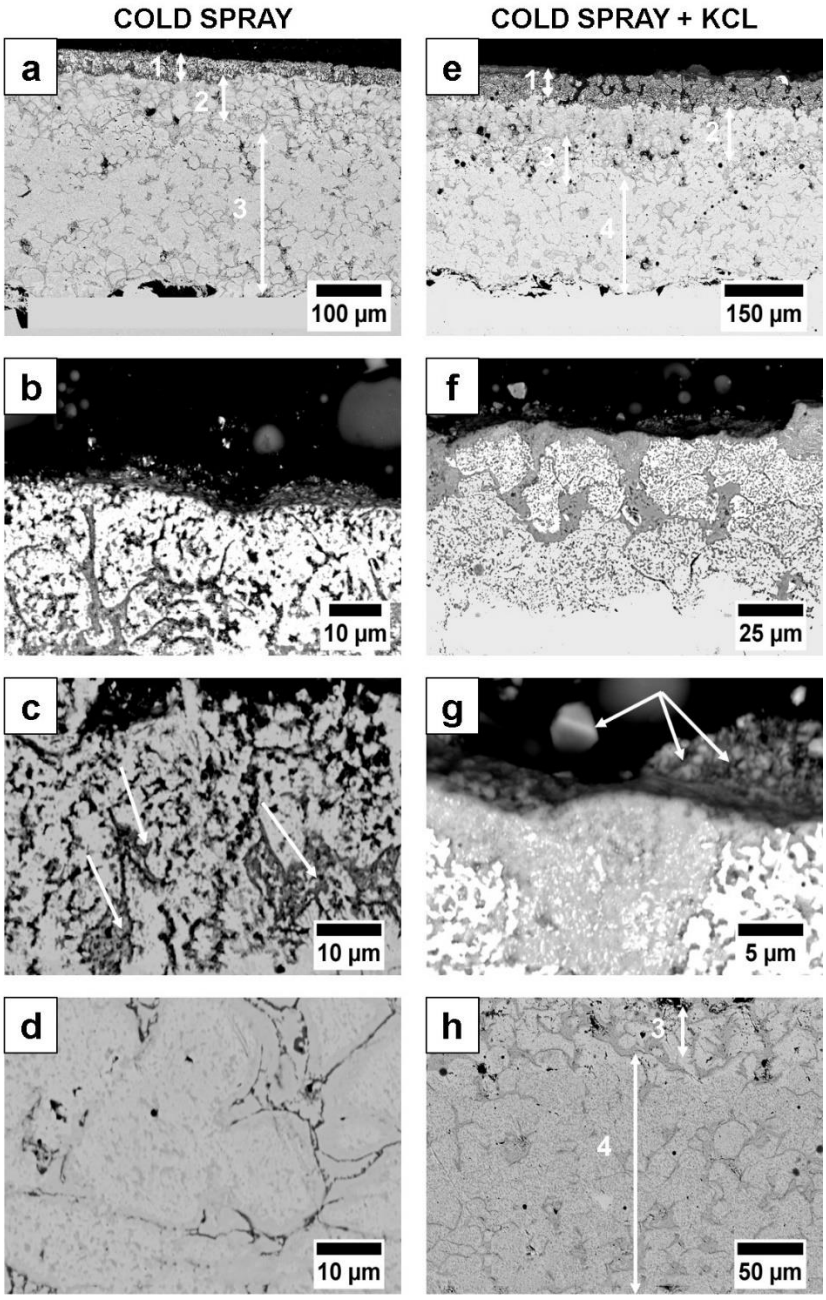

Fig. 5.11 SEM BSE cross-section images of cold sprayed coating after chlorine-induced corrosion at 700 °C for 250 h without the deposit: (a) overall view of the coating cross-section and (b–d) higher magnification image of the areas marked 1, 2 and 3; with the KCl deposit: (e) overall view of the coating cross-section and (f–h) higher magnification image of the areas marked 1, 2, 3 and 4.

In the presence of the KCl deposit, the coating was divided into four layers based on the distribution of Cr and O at the cross-section of the cold sprayed coating, as shown in Fig. 5.11 (e): 1. A layer in which Cr_2O_3 surrounded the oxidised splats ((f) and (g)), 2. A layer of chromium-rich and nickel-lean splats, 3. A layer of chromium-lean and nickel-rich splats ((h) and 4. A layer of dual-phase splats ((g)). Faceted $MnCr_2O_4$ can also be observed from Fig. 5.10 (f) as indicated by the arrows in (g).

According to the EDX maps shown in Fig. 5.12, the distribution of Cr in the different layers varied; this indicated the outward transport of Cr toward the gaseous atmosphere. The chromium-depletion layer (layer 3) had penetrated around 220 μm below the top layer of the coating. The Cr in these areas diffused outward to the top surface and did not form a dense and uniform Cr_2O_3 oxide scale. The oxidation phenomenon of the splats was observed at the scale–metal, which has a penetration depth of approximately 600 μm.

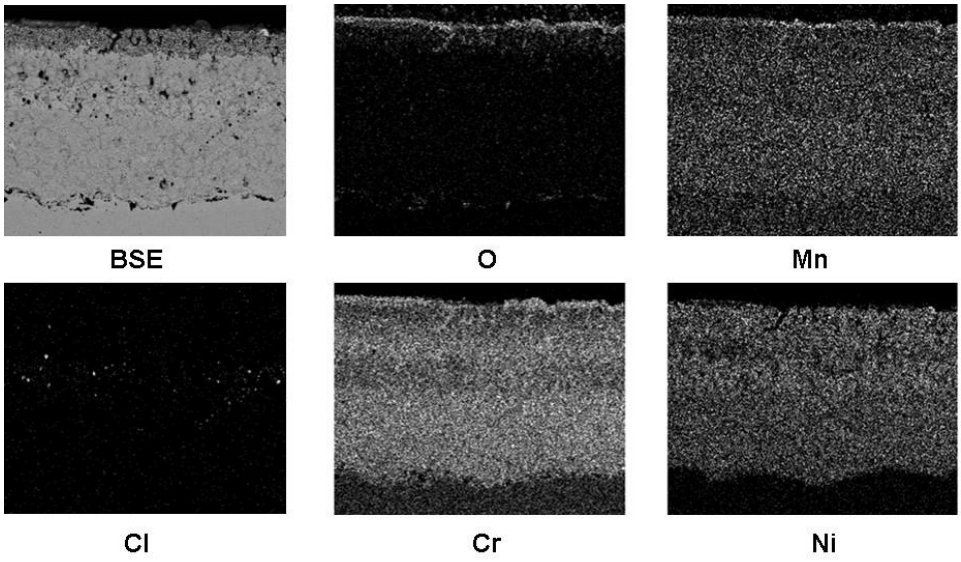

Fig. 5.12 EDX maps of the entire cold sprayed coating cross-section with the KCl deposit after chlorine-induced corrosion at 700 °C for 250 h.

5.4.4 Features of oxide scale on the coating surface

In the case of the cold sprayed coatings, the individual oxides in the sub-micrometre ranges grew freely on the surface of the original splats and a porous scale formed without the KCl deposit. These oxides transformed into a faceted geometry dramatically in the presence of KCl in the same atmosphere and at the same temperature. The reason that these $MnCr_2O_4$ spinels appeared to have such a well-defined and unique geometry is not clear. The addition of KCl promoted the elimination of the spinel containing Ni and Mn; this phenomenon might be attributed to the difference in the saturated vapour pressure of $K_2Cr_2O_4$, $K_2Mn_2O_4$ and K_2NiO_2. The thickness of the oxide scale also increased due to the presence of KCl in the cold sprayed coating. However, the integrity of the entire scale was impaired by KCl, as under the conditions observed in the case of the HVOLF and HVOGF coatings. Moreover, the oxide scale produced on the surface of the cold sprayed coating was not as dense as that produced on the surface of the HVOLF and HVOGF coatings (Fig. 5.11(g) compared with Fig. 5.7 (e) and Fig. 5.3 (e)). This difference was attributed to the different microstructures of the cold sprayed coating and the HVOF thermally sprayed coatings. The inter-splat adhesion of the HVOF thermal sprayed coatings was satisfactory, as the powder particles during the spray process partially transformed into an elastic state because of the heat of the flame. Considerably less porosity was observed in these HVOF thermal sprayed coatings than in the cold sprayed coating. The powder particles during the cold spray process did not absorb sufficient heat energy to soften partially because of the large difference between the carrier gas temperature (< 800 °C) and the melting point of the NiCr alloys (around 1400 °C). The oxide scales grew and developed on the surface of the original splats which came into

contact with the corrosive atmosphere. If there were large gaps among the splats in the cold sprayed coating, it was difficult for these oxides to grow completely and finally fill the gaps formed previously. Hence, the oxide scale was less dense than that developed on the surface of the HVOF thermal sprayed coatings.

5.4.5 Outward transport of Mn and its influence on the oxide scale

Although the Mn content in the feedstock powder of cold sprayed coatings was quite low (< 2 wt.%), its unique effect on the chlorine-induced corrosion was obvious. In the presence of Mn, the corrosion product of the Ni50Cr coatings in a single chlorine-containing atmosphere was a mixture containing a large amount of $MnCr_2O_4$ and $(Mn_{0.63}Ni_{0.37})O$ and a minor amount of Cr_2O_3 rather than only Cr_2O_3.

As suggested by Grabke *et al*. [149], the corrosion behaviour of the alloying elements in the oxidising-chloridizing environments could be explained mainly by the thermodynamic data shown in Fig. 5.13, which demonstrated that the Gibbs' free energy of the reaction metal + chlorine = metal chloride. The more negative this value was, the faster was the reaction in the metal matrix and the higher was the intensity of the corrosion attack. With respect to the oxygen pressure for the conversion of the evaporating chlorides into oxides, the lower this oxygen pressure was, the smaller was the distance from the metal surface on which the oxide was formed.

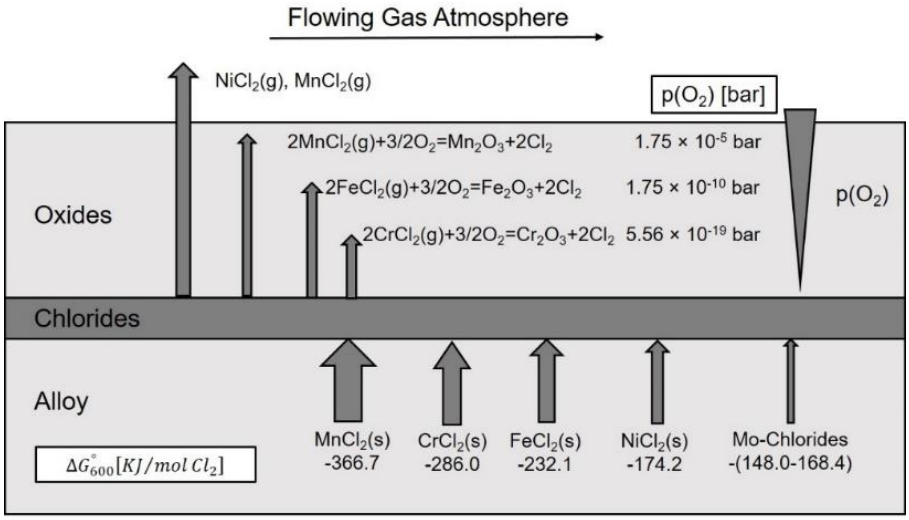

Fig. 5.13 Schematic representation of thermodynamics and reactions in the corrosion of the alloying elements of Mn, Cr, Fe, Ni and Mo in a flowing oxidising and chloridizing atmosphere [50].

The data shown in Fig. 5.13 revealed that $MnCl_2$ had the largest negative value of Gibbs' free energy, which implied that Mn could rapidly react with Cl to form $MnCl_2$. The oxygen pressure for the conversion of the Mn chloride into oxide was 1.75×10^{-5} bar, which was considerably larger than the value for Cr (5.56×10^{-19} bar). Therefore, the manganese-rich oxide layer ($MnCr_2O_4$ and $Mn_{0.63}Ni_{0.37}O$) should be outside the scale. The minor Cr_2O_3 peak in the cold sprayed coating, according to the XRD pattern shown in Fig. 5.9, might be attributed to the Cr_2O_3 under the manganese-rich oxide layer. The transport properties of the Mn inside the chromia scale also determined the composition of the outermost oxide layer. The Mn ions diffused 100 times faster than the Cr ions through the Cr_2O_3 lattice [207].

5.5 High temperature corrosion of laser cladded coating

5.5.1 Absence of iron oxide in the corrosion products

The XRD patterns of the laser cladded coatings after exposure are shown in Fig. 5.14.

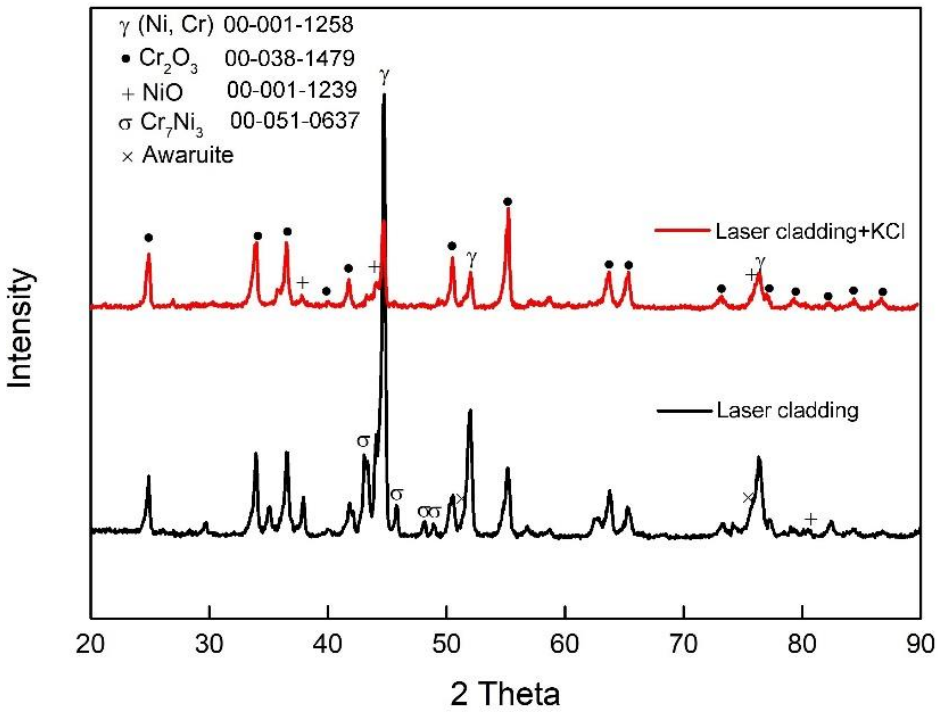

Fig. 5.14 XRD patterns of laser cladded coatings with and without the KCl deposits after chlorine-induced corrosion at 700 °C for 250 h.

In the laser cladded coating without the deposit, the metallic phase mainly contained the NiCrFe solid solution, Cr_7Ni_3 intermetallic compound and the $Ni_{2-3}Fe$ phase. The oxide phases were mainly composed of Cr_2O_3 and NiO. Cr_2O_3 was a major oxidation product, according to the intensity of the peaks. In the presence of KCl, the $Ni_{2-3}Fe$ phase disappeared from the top surface and the intensity of the peaks of the NiCrFe solid solution and Cr_7Ni_3 decreased significantly. In addition, NiO was present on the top surface.

5.5.2 Destructive influence of KCl deposit on the oxide scale

As shown in Fig. 5.15 (a), the top surface of the laser cladded coating after exposure without KCl included two different features. Fig. 5.15 (b) shows areas in which the

oxides of a flake geometry piled up loosely. These oxide flakes were Cr_2O_3, according to the XRD and EDX analysis.

The features shown in Fig. 5.15 (c) are from the areas where some oxides spalled and thereby produced web-like patterns. The web-like patterns might be attributed to the recession of the NiCrFe grain boundaries. The NiCrFe grain boundaries were the most easily attacked by the corrosive ions, and the spallation of the oxide grains preferably occurred in the weakest region. The composition of the oxides in this area corresponded to Cr_2O_3 and NiO according to the XRD results.

In the presence of the KCl deposit, a cracked scale (hydrated corrosion product) developed on the top surface of the laser cladded coating (Fig. 5.15 (d)). The morphology of this scale is shown in Fig. 5.15 (d) and can be divided into two types: the right section of the image shows a parched earth-like structure (Fig. 5.15 (e)), and the left section of the image shows the faceted oxides (Fig. 5.15 (f)).

The EDX spot analysis of 1, 2 and 3 revealed that there was 20 wt.% Cl in each spot in the area shown in Fig. 5.15 (e). The EDX results revealed that the faceted oxides (spots 4, 5 and 6) contained more Cr and less Ni than spots 1, 2 and 3. Moreover, the amount of Cl in spots 4, 5, and 6 was much lower than that in spots 1, 2 and 3.

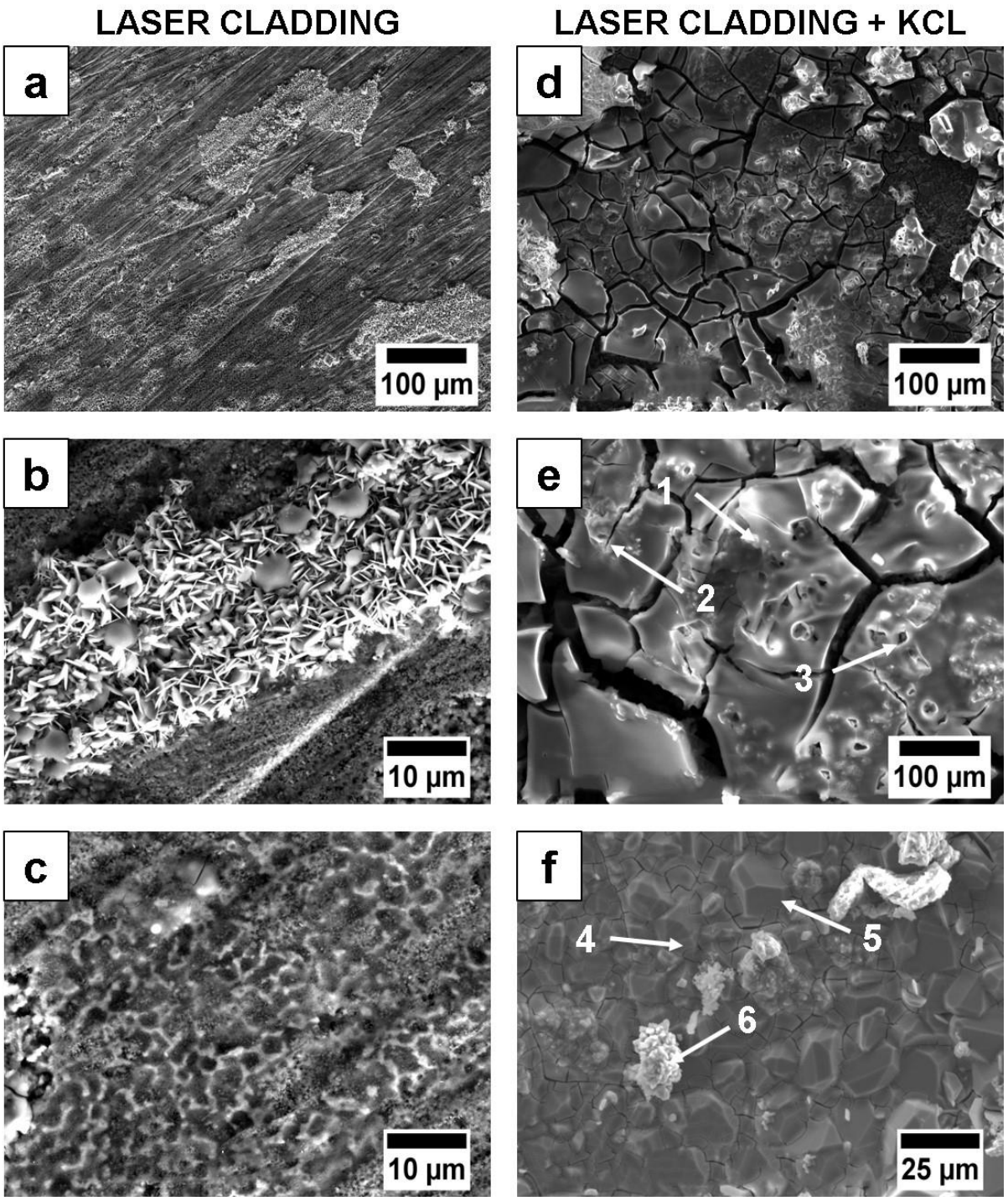

Fig. 5.15 SEM SE top morphology images of laser cladded coating after chlorine-induced corrosion at 700 °C for 250 h without the deposit: (a) overall view of the surface, (b) area in which loose oxides piled up and (c) web pattern due to spallation of oxides; with the KCl deposit: (d) overall view of the surface, (e) area with molten deposits and (f) polyhedron oxides at the scale surface.

5.5.3 Oxide scale in marginal thickness and grooving patterns in coatings

The cross-sections of the laser cladded coatings without the deposit are shown in Fig. 5.16(a) (b) and (c). These three images show an oxide scale occurring on the top surface. Features marked by the arrow in Fig. 5.16 (c) were Cr_2O_3 according to the EDX analysis. A gap of 3–4 μm was observed between the oxide scale and the coating. No Cl was identified in the scale, as well as within the coating.

The presence of KCl promoted the formation of a thicker scale according to Fig. 5.16 (e). Further, a layer of scale developed on the top surface although it was cracked at places. The maximum thickness of the scale was around 30 μm. The composition of the scale was analysed using EDX, and the results indicated that the scale was mainly Cr_2O_3.

The Cl ions attacked the coating along the grain boundaries, which could be observed from Fig. 5.16 (e). The gaps grew at the grain boundary initially and resulted in the grooving of the grain boundary [201]. The distribution of the grooves of the grain boundary was up to 80 μm under the surface of the coating. Fig. 5.16 (f) shows the BSE image of the grooving of the grain boundary at a higher magnification. These grooves acted as an easier transport path for the corrosive ions and developed into cracks in the microstructure of the coating, finally leading to the failure of the coating and the steel substrate under it.

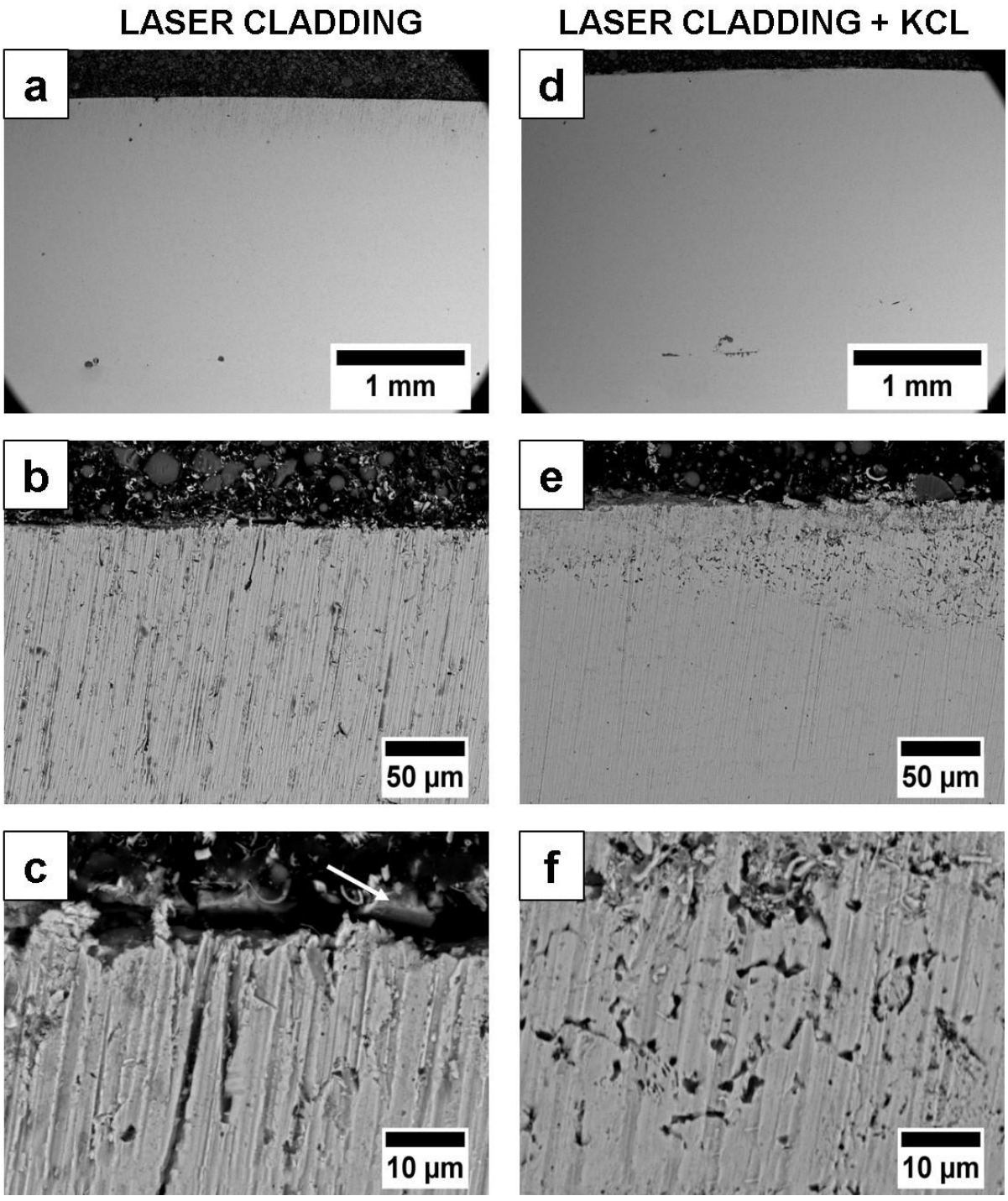

Fig. 5.16 SEM BSE cross-section of laser cladded coating after chlorine-induced corrosion at 700 °C for 250 h without the deposit: (a) overall view of the coating cross-section and, (b) and (c) oxide scale and the coating under it; with the KCl deposit: (d) overall view of the coating cross-section, (e) oxide scale and the coating under it and (f) grain boundary grooving.

5.5.4 Impaired oxide scale owing to the dilute Fe in coatings

Because of the presence of an average of 10% Fe in the as-deposited laser cladded coating, the oxide scale was expected to be different from that produced on the surface of the thermal sprayed and cold sprayed coatings. NiO was found on the surface of the laser cladded coating without the KCl deposit after corrosion, and its amount was obviously larger than that of the KCl deposit identified on the surface of the HVOLF and HVOGF coatings according to the intensity of the corresponding peaks in the respective XRD patterns. This might be attributed to the fact that the oxidation of NiCr slowed down in the presence of Fe. Fe was oxidised initially and easily in the simulated atmosphere, and the intense oxidation tendency of Fe in various oxidising atmospheres has been confirmed by several publications [131, 132, 135, 206]. The original O_2 used to produce Cr_2O_3 combined with Fe to form iron oxide, and this interrupted the amount of Cr_2O_3 produced per unit time, finally leading to the reduced coverage of Cr_2O_3 on the $NiCr_2O_4$ spinel island. This was the reason that more NiO was identified in the XRD pattern of the laser cladded coating after corrosion. Therefore, there should have been signals of iron oxide, such as those of Fe_2O_3 and Fe_3O_4, in the XRD pattern. However, no peaks corresponding to iron oxide were found in the XRD pattern; this could be attributed to the rapid evaporation of iron chloride at 700 °C. The produced iron oxides decomposed and combined with Cl to form iron chlorides such $FeCl_2$ and $FeCl_3$, which had a high vapour pressure at a high temperature. This process was like the chlorination process of Cr but had a larger reaction rate according to the chemical reaction kinetics data. Therefore, the chlorination of iron oxide resulted in an oxide scale containing no Fe. The web-like pattern of the oxide scale was attributed to the concentrated distribution of Fe at the

grain boundary of the NiCrFe resolidification grains. The cross-section of the laser cladded coating after corrosion without the KCl deposit showed the delamination of the oxide scale from the fresh coating surface; the degree of delamination was larger than that observed at the interface of the HVOF thermal sprayed coatings and the corresponding oxide scales. On the surface of the HVOLF and HOVGF thermal sprayed coatings, most of the areas were covered by the oxide scale. However, in the laser cladded coating, no adhesion was observed between the coatings and the oxide scale on at least 90% of the top surface. The presence of Fe aggravated the integrity and the compactability of the oxide scale because of the intense catalytic effect of Cl on the activation oxidation of Fe and the concentrated distribution of Fe at the grain boundary.

The disappearance of Cr_7Ni_3 and $Ni_{2–3}Fe$ on the surface of the laser cladded coating after corrosion in the presence of KCl proven the acceleration influence of K^+ on the chlorine-inducing fireside corrosion, as both the coatings (laser cladding without KCl and with KCl) faced almost the same test conditions except for the presence of the deposit. The disappearance of these two phases could be attributed to two possible reasons. The first one was the increase in the thickness of the oxide layer containing NiO and Cr_2O_3 on the coating surface, which masked the Cr_7Ni_3 and $Ni_{2–3}Fe$ underneath, in the fresh coating from the X-ray irradiation. However, considering the poor coverage of oxide scale on the surface of laser cladded coating, the other reason was more robust and convincing: the presence of the K^+ ions promoted the oxidation of Cr_7Ni_3 and $Ni_{2–3}Fe$. After 250 h of intense high temperature corrosion, only the major alloy phase γ–(Ni, Cr) survived under the attack of Cl and K^+. The grooving pattern in the cross-section of the coating also demonstrated the significant acceleration effect

of K^+ on the chlorine-induced corrosion. These grooving patterns were distributed along the entire coating length and their penetration depth could not be neglected.

5.6 Comparison of corrosion resistance of coatings

As the basis of the oxidation resistance, the oxide scale played a crucial role in the protection of the substrates from the oxidation. However, all the four coatings investigated in this study did not develop satisfactory oxide scales within 250 h that fully met the required of properties of the barrier scale, such as continuous, dense and good adherence to a substrate. Despite the ordinary or even poor properties in some cases of the oxide scales produced on the surface of each coating, the coatings themselves provided corrosion resistance to protect the substrate to some extent. The penetration depths of the corrosion ions, cracks, intense oxidising splat layer and grooving patterns acted as an indicator to evaluate the corrosion resistance of the coatings themselves.

Without KCl, all the coatings except the cold sprayed one provide acceptable oxidation resistance by developing an oxide scale and/or preventing the transport of the corrosive ions by themselves. In the HVOLF coating, the oxide scale on the surface of the coating was thin but continuous and was expected to isolate the coating from the corrosive atmosphere. Moreover, no obvious detrimental effect of the corrosive ions such as Cl^- shown in the cross-section was observed. The distribution of the chromium-depletion area in the coating including the breadth and the depth helped to determine the penetration of chlorine and oxygen in the coating up to 250 h. The chromium-depletion area was around 30 μm in thickness and was spread along the entire length of the coating. As the thickness of the as-sprayed HVOLF coating was

around 200 μm, the coating prevented the contact between the corrosive atmosphere including Cl and O and the substrate boiler steel up to approximately 1600 h. During this dwell time, the development of the Cr_2O_3 scale at the surface might retard the transportation of the corrosive ions (inward direction) and Cr (outward direction) and thus improved the operation life of the HVOLF coatings. In the HVOGF coating, the oxide scale was thickened compared with that in the HVOLF coating, but cracks were observed in some locations. Therefore, the oxide scale could not provide full coverage to isolate the coating and the substrate from the corrosive atmosphere, and its effect was uncertain. Because of the intense oxidation of the powder particles during the HVOGF spray process, it was difficult to distinguish the penetration depth of the corrosive ions by evaluating the distribution of the chromium-depletion area, as the splats showed the chromium-depletion features before the exposure. However, no other obvious corrosion phenomena in the coatings were observed, which confirmed that the HVOGF coating protected substrates underneath from corrosion. The poorest corrosion performance of the cold sprayed coating, shown in its cross-section image demonstrated that the porous structure of the coating could not prevent the corrosive atmosphere from coming into contact with each individual splat. In the HVOLF and HVOGF coatings, only the splats in the outermost layer had the opportunity to fully meet the atmosphere. Moreover, the contact direction between the atmosphere and the outermost layer of the splats was restricted from the atmosphere to the coating. In contrast, this condition changed in the porous cold sprayed coating, as all the spats many of the top layers of the cold sprayed coatings oxidised intensely and the connection between the splats began to be impaired. The original microstructure of the cold sprayed coating was destroyed, and this destruction area was believed to expand with the exposure time, finally leading to the failure of the entire coating. The

oxide scale of the laser cladded coating was neither thick nor continuous. Obvious gaps and cracks could be distinguished easily from the cross-section. However, the coating itself provided satisfactory corrosion resistance through its most dense and defect-free microstructure. The connection between the original powder particles (splats in the thermal and cold sprayed coatings) was metallurgical rather than mechanical, which increased the difficulty for the corrosive ions to pass through the boundary of these resolidified particles and thus reduced the transportation rate of the corrosive ions.

Unlike the condition without the KCl deposit, no coating provided a satisfactory corrosion performance when KCl was involved. The integrity of the oxide scale of the four coatings was impaired although there was a thickening trend in some locations of the oxide scale. The penetration of the corrosive ions into the coatings was clearly observed in the cross-section of each coating: In the HVOLF coating, the indicator for the penetration was the circular dots of chromium chloride and the cracks within splats. In the HVOGF coating, the indicator was the large cracks within and between the splats. In the cold sprayed coating, it was the intensely oxidised splat layer. In the laser cladded coating, the grooving pattern marked the location of the penetration of corrosive ions. The cold sprayed coating was still the poorest coating that faced the chlorine-induced corrosion in the presence of KCl. The HVOLF and HVOGF coatings did not provide acceptable corrosion resistance because of the contact between the atmosphere and the substrate in another 250 h of the heat treatment. Laser cladding had the longest operation life, as it was 1500 μm thick and the penetration rate of the corrosive ions in the coating was 0.3 μm h^{-1}.

5.7 Activation oxidation of coatings induced by chlorine

As described in Chapter 4, the oxidation of four coatings in air and steam was observed, but the oxidation rate was considerably small. Up to 100 h in air, the oxide scale thickness, according to the cross-section SEM images, did not exceed 1–2 μm, although the full coverage of oxides at the surface was observed in the top morphology clearly. The oxide scale did not show any obvious thickening even up to 1000 h in 100% steam. The investigation of the thickness of the oxide scale for the four coatings produced in a chlorine-containing atmosphere revealed that the oxidation of the NiCr coatings in steam was relatively low and that the oxidation rate of the same coatings in a chlorine-containing atmosphere significantly increased; i.e. once Cl was introduced into the reactive gas mixture, the scales formed on the top surface of coatings thickened.

Thermodynamic phase stability diagrams (predominance area diagrams) can be used to ascertain the stability of the corrosion products in the corrosion process and to investigate the corrosion mechanism to explain the effect of chlorine on the corrosion process of the Ni50Cr coatings [14]. The superimposed phase stability diagram for the Ni–Cr–Cl–O systems at 700 °C is plotted in Fig. 5.17. The diagram shown in Fig. 5.17 is a hypothetical combination of the phase stability diagrams of Ni–Cl–O and Cr–Cl–O. It can be used to predict the most stable corrosion product under a given condition by applying the minimisation of the Gibbs' free energy principle. One key assumption made in plotting the diagram is that the activities for all the solid components in the system are 1 and all the gases are regarded as ideal gas.

A new equilibrium was established when the mixed gases were pumped into the test rig. The calculated partial pressures of Cl_2 and O_2 were 15 Pa and 4.9 kPa, respectively, at 700 °C and marked with a black point (test condition) in Fig. 5.17. As the test condition point was in the area representing the NiO and Cr_2O_3 predominance phase, NiO and Cr_2O_3 were the stable metal oxide phases at 700 °C in the atmosphere simulated in this study. There were two reaction routes thorough which stable metal oxides were produced. The first one was the immediate oxidation of metal, as show in Reaction 2.2 and Reaction 2.3.

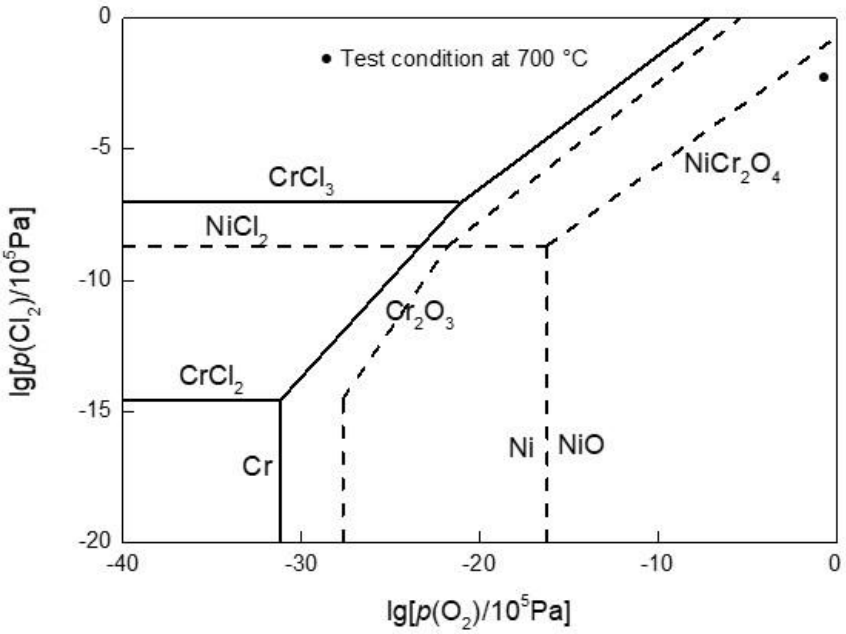

Fig. 5.17 Superimposed phase stability diagram for Ni–Cr–Cl–O systems at 700 °C.

The second one was the transformation of metal chlorides through the following reactions:

$$Ni(s) + Cl_2(g) = NiCl_2(s,g) \qquad \text{Reaction 5.1}$$

$$NiCl_2(s,g) + 1/2\,O_2(g) = NiO(s,g) + Cl_2(g)$$ Reaction 5.2

$$Cr(s) + Cl_2(g) = CrCl_2(s,g)$$ Reaction 5.3

$$CrCl_2(s,g) + 1/2\,Cl_2(g) = CrCl_3(s,g)$$ Reaction 5.4

$$2CrCl_2(s,g) + 3/2\,O_2(g) = Cr_2O_3(s,g) + 2Cl_2(g)$$ Reaction 5.5

$$2CrCl_3(s,g) + 3/2\,O_2(g) = Cr_2O_3(s,g) + 3Cl_2(g)$$ Reaction 5.6

For the equilibrium of the ternary oxide, $NiCr_2O_4$ reacted with Ni, Cr_2O_3 and O_2, or with Ni, $CrCl_2$ and O_2, or with $NiCl_2$, $CrCl_3$ and O_2. There was a line (above the $NiCr_2O_4$ label) whose range exceeded the Ni/NiO line on the O_2 partial pressure axis and exceeded the $NiCl_2$/NiO lines on the Cl_2 partial pressure axis, as shown in Fig. 5.17, which implied that $NiCr_2O_4$ was more stable than NiO. Therefore, the combination of Cr_2O_3 and NiO as shown in Reaction 2.4 could occur according to the above judgement.

Through several of the abovementioned reactions, an oxide scale formed on the surface of the coatings in the initial corrosion stage. The formed oxide scale could separate the alloy from the corrosive atmosphere and thus prevent the corrosion. However, this oxide scale could not stop the penetration of chlorine into the coating and the subsequent contact with the scale–coating interface because of the large chlorine pressure difference between the scale–gas interface and the scale–coating interface [9]. For example, the Cl^- pressure at the scale–coating interface was calculated to be 2.34×10^{-10} Pa at 700 °C when assuming $CrCl_2$ was in equilibrium with Cl_2. In contrast, in the gas mixture, the partial pressure of Cl^- was 15 Pa at 700 °C. Such a large Cl pressure difference acted as the driving force promoting Cl to permeate from the gas–scale interface to the scale–coating interface. At the scale–

coating interface, Cl reacted with the metal to form chlorides. Metal chlorides generally tend to volatilise at high temperature.

Tab. 5.1 lists the vapour pressure of the chlorides at 700 °C; all of them exceeded 10 Pa, which is considered to be the critical vapour pressure for a massive volatilisation to occur [52]. In a similar method, the partial pressure of oxygen in the oxide scale, fell from a high value at the gas–scale interface to a quite low value at the scale–coating interface. This helped to set up an oxygen pressure gradient opposite the partial pressure gradient of the volatile chlorides according to Reaction 5.2, Reaction 5.5 and Reaction 5.6, which promoted the diffusion of the chloride vapour [151]. Therefore, the chlorides volatilised, and the vapour of these chlorides diffused outward through the scale to the scale–gas interface. In the diffusion process of the chloride vapour in the scale, the Ni and Cr chlorides were converted into their corresponding oxides where oxygen pressure exceeded the level that the conversion by Reaction 5.2, Reaction 5.5 and Reaction 5.6 facilitated. As one of these reaction products, Cl_2 partially permeated through the scale into the scale–gas interface, where it reacted with the metal to form the metal chlorides again. This produced a Cl_2 circle catalysed by itself, which is called active oxidation [14, 20, 50, 149-151]. The active oxidation process increased the outward diffusion rate of the metal ions by the diffusion of the vapour chlorides, which in turn accelerated the corrosion rate.

Tab. 5.1 Physical properties of nickel and chromium chlorides (P_{700} denotes partial pressure at 700 °C) [204].

Chloride	Melting point (°C)	P_{700} (Pa)
$NiCl_2$	1030	0.182
$CrCl_2$	820	2.86
$CrCl_3$	1150	226

5.8 Acceleration and detrimental effect of KCl on the active oxidation of coatings

As explained above, the active corrosion of the Ni50Cr coatings occurred because of the Cr_2O_3 scale generated on the top surface of the coatings after exposure was either loose or porous and thus could not provide satisfactory protection. The poor structure of the oxide scale observed from the cross-section of the coatings after exposure supported this view. When the KCl as a deposit was introduced into the high temperature chlorine-induced corrosion process, the oxidation of the coatings accelerated, and the oxide scale in some areas thickened because of the acceleration. In contrast, the oxide scale was impaired by the attack of KCl according to the above summary of the oxide scale properties of the four coatings produced with and without the KCl deposit.

Fig. 5.18 displays the accelerated active oxidation process in the presence of the KCl deposit. Ions containing Cl (Cl_2 and Cl^-) acted as a catalyst to help build an active oxidation reaction circuit [150]. The Cr in the coatings that should originally be used to build protection barrier, was involved in the reaction circuit and thus transformed to $CrCl_2$, which evaporated continuously. The chromia as the oxidation product of the evaporating chloride could not form dense protective Cr_2O_3. The KCl deposit promoted

the reaction rate of this oxidation circuit by two means: 1. The KCl salt deposited on the surface of the as-sprayed coating dissolved into K^+ and Cl^{-1} at the high temperature of 700 °C. This behaviour supplied another source of Cl, which was the catalyst for the active oxidation circuit. 2. The Cr_2O_3 under the deposit combined with KCl and O_2 to form $K_2Cr_2O_4$, finally leading to the depletion of Cr_2O_3 in the scale. The consumption of Cr_2O_3 (reaction product of Reaction 5.5 and Reaction 5.6) promoted the rightward proceeding advance of these oxidation reactions to maintain the chemical balance of the entire system. Therefore, the oxidation of the NiCr coatings was significantly accelerated by the presence of KCl. However, even the oxide scale thickened because of the presence of KCl in some places, and the surface of the fresh coatings was not entirely covered by the thick scale. In some places, as the cross-section images of the coatings after exposure showed, oxide scale spalled because of the continuous evaporation of $K_2Cr_2O_4$, as illustrated in Fig. 5.18.

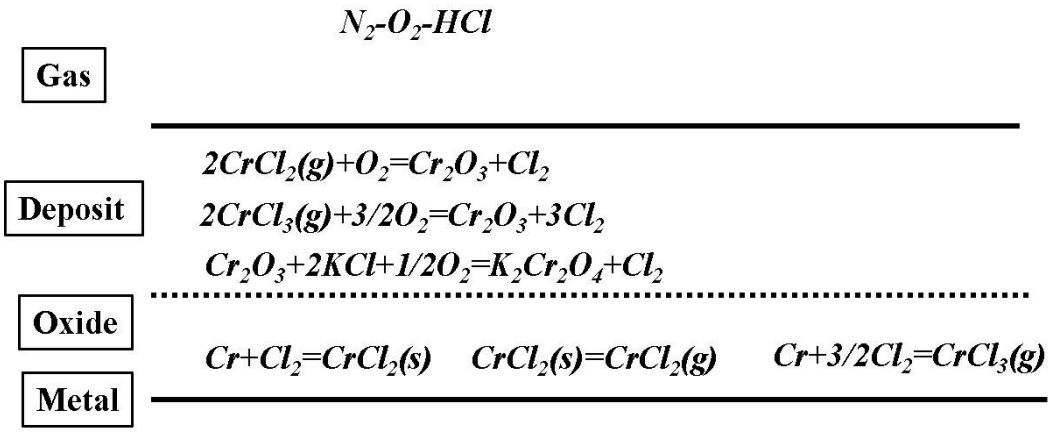

Fig. 5.18 Schematic diagram showing the effect of the KCl deposit on the activation corrosion of NiCr alloys [150].

5.9 Potential deposition routine of corrosion resistant NiCr-based coatings

An investigation of the performance of the various coatings in a chlorine-containing atmosphere with and without the KCl deposit revealed that the inferior corrosion resistance of the thermal sprayed coatings could be attributed to the inter-splat oxides and the small gap near the splat boundary. In these areas, the corrosive ions could transport at a much higher rate than passing through the coating itself. The inferior corrosion performance of the laser cladded coatings was attributed to the diluted Fe in the coating. The grain boundary was the weakest area in the laser cladded coating because of the region of the disordered atoms. The corrosive ions preferred to transport through the grain boundary because the crystal lattice defects in the grain boundaries could reduce the total repulsive force from the crystal lattice to the corrosive ions such as Cl and O. The concentration of Fe at the grain boundary aggravated this selective attack on the grain boundary, as Fe could be chloridized more easily than Cr. Therefore, to avoid the drawbacks and adopt the benefits of the thermal spray and laser cladding techniques simultaneously, the HVOLF thermal spray and post-laser remelting process is recommended. The HVOLF thermal spray process got rid of the detrimental effect of the Fe dilution in the deposited coatings, while the post laser remelting process improved the microstructure of the as-sprayed coating. With this two-step routine, the Ni50Cr coatings provided considerably better chlorine-induced corrosion resistance, particularly when facing an attack of the KCl deposit.

5.10 Summary

According to the above discussion, following summary were drawn:

- The oxide scale produced on the surface of the four coatings differed in phase, thickness, integrity and the connection with the coating, following the change of the coatings.

- Similar corrosion products developed on the top surface of each coating, except in the case of the cold sprayed coating. The main corrosion product was Cr_2O_3 for the HVOLF, HVOGF and laser cladded coatings. In the presence of KCl, a very small amount of NiO was observed on the surface. This was attributed to the consumption effect of K^+ on Cr_2O_3. The outermost Cr_2O_3 layer was removed and thus revealed the middle NiO layer in the selective oxidation products of the NiCr alloy.

- The oxides containing Mn was the main corrosion product for the cold sprayed coatings. This was attributed to the largest negative value of the Gibbs' free energy of $MnCl_2$ and the larger diffusion rate of Mn than that of Cr through the Cr_2O_3 lattice.

- The presence of KCl could change the scale morphology significantly. The scale morphology of the HVOLF, HVOGF and laser cladded coatings were quite similar irrespective of the presence of the KCl deposit. Without the KCl deposit, the Cr_2O_3 oxides piled up to form a thin scale, and on the surface of this scale, individual oxides could still be distinguished. With the KCl deposit, a cracked scale of oxide that looked like parched earth appeared. The other areas of the scale showed an amorphous feature. The scale morphology of the cold sprayed coatings showed a unique behaviour. Without the KCl deposit, the

oxidised splats in a porous structure appeared. With the KCl deposit, faceted $MnCr_2O_4$ oxides in a well-defined geometry covered the entire surface.

- The catalytic effect of Cl on the activate oxidation of the Ni50Cr coatings promoted the thickening of the oxide scale. However, the poor microstructure of the oxide scale was the inevitable side effect of Cl. The incomplete coverage of the oxide scale on the coating surface undermined the effectiveness of the protection by the oxide scale.

- Further acceleration of the corrosion on the oxide scale by KCl was confirmed by the SEM cross-section observations and could be determined easily from the evolution of the peak intensities in the XRD patterns. These effects of KCl might be attributed to its interference in the entire activation oxidation process of the Ni50Cr alloys.

- Indicators showing the depth and the breadth of corrosive ions in the coatings, such as cracks in the HVOLF and HVOGF coatings, intensely oxidising splats in the cold sprayed coatings and grain boundary grooving in the laser cladded coatings appeared at the cross-sections. They were used for evaluating the corrosion performance of the coatings.

- The severity of degree of the corrosion attack is differed for the different coatings according to the penetration indicators. In the absence of the KCl deposit on the surface, the cold sprayed coating exhibited the poorest performance, as the intense oxidation of the splats could be observed up to 600 µm under the top surface of the coating. The HVOLF and HVOGF coatings had similar and acceptable performance. The laser cladded coating provided the

best corrosion resistance although the oxide scale on its surface cracked from the coating.

- In the presence of the KCl deposit, the cold sprayed coating and the HVOGF coating exhibited the poorest performance as the corrosive ions penetrated deep within the coatings (600 μm and 450 μm, respectively). The HVOLF coatings performed better than the HVOGF coatings, but the extent was limited. Large circular chromium chloride dots demonstrated failure destiny of the HVOLF coating in further exposure. Laser cladded coatings showed the best performance among the four coatings considered in this study because of its densest and defect-free microstructure. The corrosion rate was around 0.3 μm h^{-1}.

- The HVOLF thermal spray and the post-laser remelting process are recommended to simultaneously utilise the merits and eliminate drawbacks of the two techniques. The Ni50Cr coatings deposited using this two-step routine may have considerably better chlorine-induced corrosion resistance.

Chapter 6 Conclusions and future work

The research work in this study primarily focused on: 1. Identify the knowledge gap that existing in the area of high temperature application of NiCr-based coatings; 2. Optimisation of liquid fuelled HVOF (HVOLF), gas fuelled HVOF (HVOGF) and laser cladding processes parameters at the University of Nottingham to deposit coatings of better oxidation resistance; 2. Investigation of air, steam oxidation and fireside chlorine-containing corrosion resistance of coatings deposited with the most suitable parameters that were optimised (HVOLF, HVOGF and laser cladding) or defined (cold spray) in the stage of deposition; 3. Determination of best oxidation/corrosion-resistant coating deposition routine, according to the rank of oxidation/corrosion performance of deposited coatings, and the specific oxidation/corrosion mechanism of each coating. General conclusions of the research work presented in this thesis are summarised as follows.

According to the literature review, previous researches about the high temperature oxidation/corrosion of NiCr-based material most focused on the bulk alloys, rather than coating deposited with powder and using various techniques. Experience and knowledge that were obtained from the bulk alloys are abundant and may be useful when investigating the high temperature behaviour of NiCr-based coatings. Yet, recent studies on the high temperature oxidation/corrosion behaviours of NiCr-based coatings revealed that there are several obvious oxidation/corrosion related features that are different from those in the case of NiCr-based bulk alloys. For instance, the oxide scale on the surface of coatings are not as thick as the one on the surface of bulk alloys. In the oxidation of bulk alloys, preferable transport paths for oxidising ions

are grain boundaries while additional preferable transport paths such as porosity, oxides are added in the case of the oxidation of coatings. Moreover, dilute element that comes from the melting of substrate during the high-energy deposition process may be detrimental to the oxidation/resistance of deposited coatings. Hence, traditional principles and knowledge that can be used to describe and explain the high temperature oxidation/corrosion behaviour of NiCr-based bulk alloys may not be applied to NiCr-based coatings without modification. The knowledge gap between the high temperature oxidation/corrosion of NiCr-based alloys and coatings needs to be filled to some extent.

To optimise the process parameter sets of HVOLF and HVOGF thermal spray which mainly included fuel-oxygen ratio and total mass flow, three HVOLF coatings and two HVOGF coatings were deposited. After deposition, constituent properties of as-deposited coatings such as oxygen content, porosity and microstructure were examined and recorded. TGA test provided valuable information about the air oxidation performance of these five coatings and results were used to shortlist coatings with the best oxidation resistance. Three as-sprayed HVOLF coatings retained the phase of Ni50Cr powder (γ−(Ni, Cr) and α−Cr). Minor oxide phases were not detected by XRD scanning. While two as-sprayed HVOGF coatings were composed of NiO, Cr_2O_3 and $NiCr_2O_4$ oxides and elemental Ni along with γ−(Ni, Cr) solid solution. HVOLF coatings sprayed using lower oxygen stoichiometry had lower porosity. Effect of total mass flow rate on the porosity of as-sprayed HVOLF coatings is not as obvious as that of oxygen stoichiometry; yet, its effect on the oxygen content of coatings is apparent. HVOGF coatings sprayed using lower oxygen stoichiometry had less porosity and less oxygen content. Oxidation kinetics obtained using TGA

results showed that HVOLF 2 coating (medium level of oxygen content and porosity) had better oxidation performance than other two HVOLF coatings and for HVOGF coatings, HVOGF 2 had better oxidation performance than HVOGF 1 due to its lower oxidation and porosity. Moreover, HVOLF 2 coating had better oxidation resistance than HVOGF 2 coating.

Long-term air and steam oxidation exposure of HVOLF, HVOGF, cold sprayed and laser cladded coatings helped us obtained following conclusions. The main oxidation products on the surface of four coatings were all Cr_2O_3. Other oxide phases such as $MnCr_2O_4$ and $NiCr_2O_4$ were identified on the surface of cold sprayed coating and HVOGF coating respectively. The morphology and growth direction of oxides were determined by the strain status of splats, and they had significant influence on the properties of the oxide scale including integrity, thickness and microstructure. In air, the thickness of coatings was small due to the relatively low oxidation of NiCr alloys at 700 °C. When the oxidising atmosphere changed to steam, the oxidation rate increased but the oxide scale was still thin, owing to the consumption effect of OH^- on the Cr_2O_3 scale. HVOLF and HVOGF coatings had better steam oxidation resistance than cold sprayed and laser cladded coatings and are robust with the presence of steam during oxidation. Yet, whether a thick oxide scale can develop on the surface of HVOLF and HVOGF coatings need future longer-term steam oxidation test. Potential of HVOF thermal sprayed NiCr-based coatings in the high temperature steam oxidation application depends on the longer-time test results.

Fireside corrosion test in chlorine-rich environment of four coatings indicated different corrosion behaviour of four coatings. The main corrosion product developed on the top surface of HOVLF, HVOGF and laser cladded coatings was Cr_2O_3. While oxides

containing Mn is the main corrosion product for cold sprayed coatings. For scale morphology, HVOLF and HVOGF coatings shared similar features regardless of the presence of KCl deposit. Without KCl deposit, chromium oxides piled up to form a thin scale and on the surface of scale, individual oxides can still be distinguished. With KCl deposit, a cracked scale of oxide like parched earth appeared. Faceted $MnCr_2O_4$ spinel in well-defined geometry covered the entire surface of cold sprayed coatings with the presence of KCl. Without KCl, oxide scale of laser cladded coating was a mixture of oxides flakes and residual oxidized grain boundaries. With KCl, it changed to features like parched earth. There were no continuous oxide scales identified on the top surface of all four coatings due to the detrimental effect of Cl on oxide scales. Yet, the thickness of scale was enhanced due to the acceleration effect of Cl on the corrosion rate. Cross-section images of oxide scales and coatings underneath it showed the clear indication of Cl attack such as cracks in the HVOLF, HVOGF and cold sprayed splats and gain boundary grooving in the laser cladded coatings microstructure. The degree of attack of Cl varied in different coatings. HOVGF and cold sprayed coatings had the poorest performance since penetration of corrosive ions such as O^{-2} and Cl^- was most deep in them. HVOLF coating was not satisfactory either, but not so poor compared with HVOGF and laser cladded coatings. Laser cladding has the best corrosion performance due to its microstructure and thickness. Yet, whether the laser cladded coating could provide protection to the substrate for a quite long time needs subsequent long-term experiments.

Based on the abovementioned discussion and conclusions, two directions for the future work were summarised: 1. Increase the steam oxidation and chlorine-containing exposure dwell so that the long-term oxidation/corrosion resistance of coatings can be

investigated and these coatings' potential in practical high temperature application can be verified; 2. The HVOLF and the laser cladding technique have respective merits and drawbacks when depositing high temperature oxidation/corrosion resistance coatings. For instance, HVOLF coatings are cheap, no dilution contamination but less dense microstructure, and laser cladded coatings have a quiet dense microstructure but inevitable dilution contamination. Thereby, it is a promising solution to combine these two techniques together to deposit a coating of excellent microstructure and no detrimental elemental constituent. Developing this combination deposition routine and investigating the corrosion performance of coatings that are deposited using it is a good direction in the further work.

References

1. Franco, A. and N. Giannini, *Perspectives for the use of biomass as fuel in combined cycle power plants.* International journal of thermal sciences, 2005. **44**(2): p. 163-177.

2. Harb, J. and E. Smith, *Fireside corrosion in PC-fired boilers.* Progress in energy and combustion science, 1990. **16**(3): p. 169-190.

3. Davidsson, K.O., et al., *Potassium, chlorine, and sulfur in ash, particles, deposits, and corrosion during wood combustion in a circulating fluidized-bed boiler.* Energy & fuels, 2007. **21**(1): p. 71-81.

4. Kassman, H., et al., *Measures to reduce chlorine in deposits: Application in a large-scale circulating fluidised bed boiler firing biomass.* Fuel, 2011. **90**(4): p. 1325-1334.

5. Aho, M., *Reduction of chlorine deposition in FB boilers with aluminium-containing additives.* Fuel, 2001. **80**(13): p. 1943-1951.

6. Lith, S.C.v., et al., *Lab-scale investigation of deposit-induced chlorine corrosion of superheater materials under simulated biomass-firing conditions. Part 1: Exposure at 560 C.* Energy & Fuels, 2009. **23**(7): p. 3457-3468.

7. Michelsen, H.P., et al., *Deposition and high temperature corrosion in a 10 MW straw fired boiler.* Fuel Processing Technology, 1998. **54**(1): p. 95-108.

8. Hansen, L.A., H.P. Michelsen, and K. Dam-Johansen, *Alkali metals in a coal- and biomass-fired CFBC--measurements and thermodynamic modeling*. 1995, American Society of Mechanical Engineers, New York, NY (United States).

9. Nielsen, H., et al., *The implications of chlorine-associated corrosion on the operation of biomass-fired boilers.* Progress in energy and combustion science, 2000. **26**(3): p. 283-298.

10. Koppejan, J. and S. Van Loo, *The handbook of biomass combustion and co-firing*. 2012: Routledge.

11. Hoffmann, B.S., A. Szklo, and R. Schaeffer, *An evaluation of the techno-economic potential of co-firing coal with woody biomass in thermal power plants in the south of Brazil.* Biomass and bioenergy, 2012. **45**: p. 295-302.

12. Al-Mansour, F. and J. Zuwala, *An evaluation of biomass co-firing in Europe.* Biomass and Bioenergy, 2010. **34**(5): p. 620-629.

13. Basu, P., J. Butler, and M.A. Leon, *Biomass co-firing options on the emission reduction and electricity generation costs in coal-fired power plants.* Renewable energy, 2011. **36**(1): p. 282-288.

14. Young, D.J., *High temperature oxidation and corrosion of metals*. Vol. 1. 2008: Elsevier.

15. Manning, M., *Geometrical effects on oxide scale integrity.* Corrosion Science, 1981. **21**(4): p. 301-316.

16. Lipkin, D.a. and D. Clarke, *Measurement of the stress in oxide scales formed by oxidation of alumina-forming alloys.* Oxidation of Metals, 1996. **45**(3-4): p. 267-280.

17. Quadakkers, W., et al., *Differences in growth mechanisms of oxide scales formed on ODS and conventional wrought alloys.* Oxidation of Metals, 1989. **32**(1-2): p. 67-88.

18. Hou, P. and J. Stringer, *The effect of reactive element additions on the selective oxidation, growth and adhesion of chromia scales.* Materials Science and Engineering: A, 1995. **202**(1-2): p. 1-10.

19. Sarin, P., et al., *Iron corrosion scales: model for scale growth, iron release, and colored water formation.* Journal of environmental engineering, 2004. **130**(4): p. 364-373.

20. Birks, N., G.H. Meier, and F.S. Pettit, *Introduction to the high temperature oxidation of metals*. 2006: Cambridge University Press.

21. Poirier, J.-P., *Creep of crystals: high-temperature deformation processes in metals, ceramics and minerals*. 1985: Cambridge University Press.

22. Kofstad, P., *High temperature oxidation of metals.* 1966, 340 P. JOHN WILEY & SONS, INC., NEW YORK, N. Y, 1966.

23. Fromhold Jr, A., *Theory of Metal Oxidation. Vol. I. Fundamentals.* North Holland Publishing Co., Amsterdam, New York and Oxford. 1976, 547 p, 1976.

24. Okamoto, H., L. Kacprzak, and P. Subramanian, *Binary alloy phase diagrams*. 1996: ASM international.

25. Zhang, X., et al., *Effect of NiCr and NiCrAl coatings on the creep resistance of a Ni alloy.* Materials Science and Engineering: A, 2011. **528**(6): p. 2282-2287.

26. Oksa, M., et al., *Nickel-based HVOF coatings promoting high temperature corrosion resistance of biomass-fired power plant boilers.* Fuel Processing Technology, 2014. **125**: p. 236-245.

27. Oksa, M., J. Metsäjoki, and J. Kärki, *Thermal spray coatings for high-temperature corrosion protection in biomass co-fired boilers.* Journal of Thermal Spray Technology, 2015. **24**(1-2): p. 194-205.

28. Bhaduri, A., et al., *Selection of hardfacing material for components of the Indian Prototype Fast Breeder Reactor.* Journal of Nuclear materials, 2004. **334**(2-3): p. 109-114.

29. Kim, H.-J., et al., *Assessment of wear performance of flame sprayed and fused Ni-based coatings.* Surface and Coatings Technology, 2003. **172**(2-3): p. 262-269.

30. Sidhu, H.S., B.S. Sidhu, and S. Prakash, *Mechanical and microstructural properties of HVOF sprayed WC–Co and Cr3C2–NiCr coatings on the boiler tube steels using LPG as the fuel gas.* Journal of Materials Processing Technology, 2006. **171**(1): p. 77-82.

31. Al-Fadhli, H., et al., *The erosion–corrosion behaviour of high velocity oxy-fuel (HVOF) thermally sprayed inconel-625 coatings on different metallic surfaces.* Surface and Coatings Technology, 2006. **200**(20): p. 5782-5788.

32. Bala, N., et al., *Cold spray coating process for corrosion protection: a review.* Surface Engineering, 2014. **30**(6): p. 414-421.

33. Li, C.-J. and W.-Y. Li, *Deposition characteristics of titanium coating in cold spraying.* Surface and Coatings Technology, 2003. **167**(2): p. 278-283.

34. Champagne, V.K., *The cold spray materials deposition process: fundamentals and applications*. 2007: Elsevier.

35. Pawlowski, L., *The science and engineering of thermal spray coatings*. 2008: John Wiley & Sons.

36. Davis, J.R., *Handbook of thermal spray technology*. 2004: ASM international.

37. Bluni, S. and A. Marder, *Effects of thermal spray coating composition and microstructure on coating response and substrate protection at high temperatures.* Corrosion, 1996. **52**(3): p. 213-218.

38. Vilar, R., *Laser cladding.* Journal of laser applications, 1999. **11**(2): p. 64-79.

39. Toyserkani, E., A. Khajepour, and S.F. Corbin, *Laser cladding*. 2004: CRC press.

40. Hemmati, I., V. Ocelík, and J.T.M. De Hosson, *Dilution effects in laser cladding of Ni–Cr–B–Si–C hardfacing alloys.* Materials Letters, 2012. **84**: p. 69-72.

41. Kathuria, Y., *Some aspects of laser surface cladding in the turbine industry.* Surface and Coatings Technology, 2000. **132**(2-3): p. 262-269.

42. Kim, J.-D. and Y. Peng, *Melt pool shape and dilution of laser cladding with wire feeding.* Journal of Materials Processing Technology, 2000. **104**(3): p. 284-293.

43. Steen, W.M. and J. Mazumder, *Laser material processing*. 2010: Springer Science & Business Media.

44. Henderson, R. and K. Schulmeister, *Laser safety*. 2003: CRC Press.

45. Uusitalo, M., P. Vuoristo, and T. Mäntylä, *High temperature corrosion of coatings and boiler steels in reducing chlorine-containing atmosphere.* Surface and Coatings Technology, 2002. **161**(2): p. 275-285.

46. Uusitalo, M., P. Vuoristo, and T. Mäntylä, *High temperature corrosion of coatings and boiler steels in oxidizing chlorine-containing atmosphere.* Materials Science and Engineering: A, 2003. **346**(1): p. 168-177.

47. Uusitalo, M.A., P.M.J. Vuoristo, and T.A. Mäntylä, *High temperature corrosion of coatings and boiler steels below chlorine-containing salt deposits.* Corrosion Science, 2004. **46**(6): p. 1311-1331.

48. Ming, Q., L. Lim, and Z. Chen, *Laser cladding of nickel-based hardfacing alloys.* Surface and Coatings Technology, 1998. **106**(2): p. 174-182.

49. Song, B., T. Hussain, and K. Voisey, *Laser cladding of Ni50Cr: a parametric and dilution study.* Physics Procedia, 2016. **83**: p. 706-715.

50. Zahs, A., M. Spiegel, and H. Grabke, *The influence of alloying elements on the chlorine‐induced high temperature corrosion of Fe‐Cr alloys in oxidizing atmospheres.* Materials and Corrosion, 1999. **50**(10): p. 561-578.

51. Mohanty, B.P. and D.A. Shores, *Role of chlorides in hot corrosion of a cast Fe–Cr–Ni alloy. Part I: experimental studies.* Corrosion science, 2004. **46**(12): p. 2893-2907.

52. Chang, Y.-N. and F.-I. Wei, *High-temperature chlorine corrosion of metals and alloys.* Journal of materials science, 1991. **26**(14): p. 3693-3698.

53. Douglass, D. and J. Armijo, *The effect of silicon and manganese on the oxidation mechanism of Ni-20 Cr.* Oxidation of Metals, 1970. **2**(2): p. 207-231.

54. Wright, I.G. and R. Dooley, *A review of the oxidation behaviour of structural alloys in steam.* International Materials Reviews, 2010. **55**(3): p. 129-167.

55. Widmer, R. and N.J. Grant, *The role of atmosphere in the creep-rupture behavior of 80 Ni-20 Cr alloys.* Journal of Basic Engineering, 1960. **82**(4): p. 882-886.

56. Aalamialeagha, M., S. Harris, and M. Emamighomi, *Influence of the HVOF spraying process on the microstructure and corrosion behaviour of Ni-20% Cr coatings.* Journal of materials science, 2003. **38**(22): p. 4587-4596.

57. Ross, E.W. and C.T. Sims, *Nickel-base alloys.* Wiley-Interscience, John Wiley and Sons, Superalloys II--High Temperature Materials for Aerospace and Industrial Power, 1987: p. 97-133.

58. Kakac, S., H. Liu, and A. Pramuanjaroenkij, *Heat exchangers: selection, rating, and thermal design*. 2012: CRC press.

59. Shah, R.K. and D.P. Sekulic, *Fundamentals of heat exchanger design*. 2003: John Wiley & Sons.

60. Hu, Z.-F., *Heat-resistant steels, microstructure evolution and life assessment in power plants*, in *Thermal Power Plants*. 2012, InTech.

61. Fu, Y., *The welding of new heat-resisting steels used for boiler of 1000 MW class ultra-supercritical fossil-fired units [J].* Electric Power, 2005. **8**: p. 016.

62. Siddhartha, S. and R. Kumar, *Coal characterisation and design for fossil fuel fired boiler in thermal power plants.* 2014.

63. Holcomb, G., et al., *US-UK Collaboration on Fossil Energy Advanced Materials: Task 2—Materials for Advanced Boiler and Oxy-combustion Systems (NETL-US)*. 2014, National Energy Technology Laboratory-In-house Research.

64. Liu, Y., et al., *High-Temperature Corrosion Properties of Boiler Steels under a Simulated High-Chlorine Coal-Firing Atmosphere.* Energy & Fuels, 2017. **31**(4): p. 4391-4399.

65. Chongbin, W., et al., *Research on the Superheater Material Properties for USC Boiler with 700° C Steam Parameter*, in *Energy Materials 2014*. 2014, Springer. p. 151-159.

66. Saidur, R., et al., *A review on biomass as a fuel for boilers.* Renewable and sustainable energy reviews, 2011. **15**(5): p. 2262-2289.

67. Huber, G.W., S. Iborra, and A. Corma, *Synthesis of transportation fuels from biomass: chemistry, catalysts, and engineering.* Chemical reviews, 2006. **106**(9): p. 4044-4098.

68. Klass, D.L., *Biomass for renewable energy, fuels, and chemicals*. 1998: Elsevier.

69. McKendry, P., *Energy production from biomass (part 1): overview of biomass.* Bioresource technology, 2002. **83**(1): p. 37-46.

70. Pronobis, M. and W. Wojnar, *The rate of corrosive wear in superheaters of boilers for supercritical parameters of steam.* Engineering Failure Analysis, 2012. **19**: p. 1-12.

71. James, P. and L. Pinder, *Effect of coal chlorine on the fireside corrosion of boiler furnace wall and superheater/reheater tubing.* Materials at High Temperatures, 1997. **14**(3): p. 187-196.

72. Baxter, L.L., et al., *The behavior of inorganic material in biomass-fired power boilers: field and laboratory experiences.* Fuel processing technology, 1998. **54**(1): p. 47-78.

73. Grabke, H. and R. Bryers, *Incinerating municipal and industrial waste.* Hemisphere, New York, 1989. **161**.

74. Wulfinghoff, D.R., *Energy efficiency manual*. Vol. 3936. 1999: Energy Institute Press Maryland.

75. Cao, X., R. Vassen, and D. Stoever, *Ceramic materials for thermal barrier coatings.* Journal of the European Ceramic Society, 2004. **24**(1): p. 1-10.

76. DeMasi-Marcin, J.T. and D.K. Gupta, *Protective coatings in the gas turbine engine.* Surface and Coatings Technology, 1994. **68**: p. 1-9.

77. Li, X.-z., et al., *Investigations on the behavior of laser cladding Ni–Cr–Mo alloy coating on TP347H stainless steel tube in HCl rich environment.* Surface and Coatings Technology, 2013. **232**: p. 627-639.

78. Wang, D. and G.P. Bierwagen, *Sol–gel coatings on metals for corrosion protection.* Progress in organic coatings, 2009. **64**(4): p. 327-338.

79. Hussain, T., et al., *Fireside corrosion behavior of HVOF and plasma-sprayed coatings in advanced coal/biomass co-fired power plants.* Journal of thermal spray technology, 2013. **22**(5): p. 797-807.

80. Davis, J.R., *Nickel, cobalt, and their alloys*. 2000: ASM international.

81. Pollock, T.M. and S. Tin, *Nickel-based superalloys for advanced turbine engines: chemistry, microstructure and properties.* Journal of propulsion and power, 2006. **22**(2): p. 361-374.

82. Handbook, A., *Vol. 3: Alloy Phase Diagrams.* ASM International, Materials Park, OH, USA, 1992: p. 2.48.

83. Armanet, F., A. Vejux, and G. Beranger. *High Temperature Corrosion of Pure Nickel, and Ni--Cr, Fe--Ni--Cr or Co--Cr--W--Ni Alloys: Influence of Water Vapour Contents[of Environment]*. in *Behaviour of High Temperature Alloys in Aggressive Environments[Proc. Conf.], Petten, The Netherlands, Oct. 1979*. 1980.

84. Agarwal, D., W. Herda, and U. Brill, *Nickel alloys combat high-temperature corrosion.* Advanced Materials and Processes, 1995. **148**(4).

85. Hearley, J., J. Little, and A. Sturgeon, *The effect of spray parameters on the properties of high velocity oxy-fuel NiAl intermetallic coatings.* Surface and coatings technology, 2000. **123**(2): p. 210-218.

86. Herman, H., S. Sampath, and R. McCune, *Thermal spray: current status and future trends.* MRS bulletin, 2000. **25**(7): p. 17-25.

87. Sturgeon, A., *High velocity oxyfuel spraying promises better coatings.* Metals and materials, 1992. **8**(10): p. 547-548.

88. Harvey, D., *The tough truth–wear-resistant coatings using high velocity oxyfuel.* Industrial Lubrication and Tribology, 1996. **48**(2): p. 11-16.

89. Rusch, W., *Comparison of operating characteristics for gas and liquid fuel HVOF torches.* Thermal Spray 2007: Global Coating Solutions, 2007: p. 14-16.

90. Sudaprasert, T., P. Shipway, and D. McCartney, *Sliding wear behaviour of HVOF sprayed WC–Co coatings deposited with both gas-fuelled and liquid-fuelled systems.* Wear, 2003. **255**(7-12): p. 943-949.

91. Sharma, A., R.J. Gambino, and S. Sampath, *Anisotropic electrical properties in thermal spray metallic coatings.* Acta materialia, 2006. **54**(1): p. 59-65.

92. Brandt, O., *Mechanical properties of HVOF coatings.* Journal of Thermal Spray Technology, 1995. **4**(2): p. 147-152.

93. Dykhuizen, R.C. and M.F. Smith, *Gas dynamic principles of cold spray.* Journal of Thermal Spray Technology, 1998. **7**(2): p. 205-212.

94. Clarke, C. and B. Carswell, *Principles of astrophysical fluid dynamics*. 2007: Cambridge University Press.

95. Dykhuizen, R., et al., *Impact of high velocity cold spray particles.* Journal of Thermal Spray Technology, 1999. **8**(4): p. 559-564.

96. Papyrin, A., et al., *Cold spray technology*. 2006: Elsevier.

97. Moridi, A., et al., *Cold spray coating: review of material systems and future perspectives.* Surface Engineering, 2014. **30**(6): p. 369-395.

98. Li, C.-J., W.-Y. Li, and H. Liao, *Examination of the critical velocity for deposition of particles in cold spraying.* Journal of Thermal Spray Technology, 2006. **15**(2): p. 212-222.

99. Schmidt, T., et al., *Development of a generalized parameter window for cold spray deposition.* Acta materialia, 2006. **54**(3): p. 729-742.

100. Van Steenkiste, T. and J. Smith, *Evaluation of coatings produced via kinetic and cold spray processes.* Journal of Thermal Spray Technology, 2004. **13**(2): p. 274-282.

101. Kreye, H., S. Zimmermann, and P. Heinrich, *The role of the fuel gas in the HVOF process.* Thermal Spraying--Current Status and Future Trends., 1995. **1**: p. 393-398.

102. Schawlow, A.L. and C.H. Townes, *Infrared and optical masers.* Physical Review, 1958. **112**(6): p. 1940.

103. Gould, R.G. *The LASER, light amplification by stimulated emission of radiation*. in *The Ann Arbor conference on optical pumping, the University of Michigan*. 1959.

104. Ion, J., *Laser processing of engineering materials: principles, procedure and industrial application*. 2005: Butterworth-Heinemann.

105. Ready, J., *Effects of high-power laser radiation*. 2012: Elsevier.

106. Ready, J.F., D.F. Farson, and T. Feeley, *LIA handbook of laser materials processing*. 2001: Laser Institute of America Orlando.

107. Kou, S., *Welding metallurgy*. 2003: John Wiley & Sons.

108. Duley, W.W., *Laser welding*. 1999: Wiley.

109. Zhong, M., W. Liu, and H. Zhang, *Corrosion and wear resistance characteristics of NiCr coating by laser alloying with powder feeding on grey iron liner.* Wear, 2006. **260**(11): p. 1349-1355.

110. Khanna, A.S., *Introduction to high temperature oxidation and corrosion*. 2002: ASM international.

111. Atkins, P., *Physical Chemistry: Thermodynamics, structure, and change*. 2014: Macmillan Higher Education.

112. Wagner, C., *Theoretical analysis of the diffusion processes determining the oxidation rate of alloys.* Journal of the Electrochemical Society, 1952. **99**(10): p. 369-380.

113. Cheng, T.-L., Y.-H. Wen, and J.A. Hawk, *Diffuse-Interface Modeling and Multiscale-Relay Simulation of Metal Oxidation Kinetics With Revisit on Wagner ′ s Theory.* The Journal of Physical Chemistry C, 2014. **118**(2): p. 1269-1284.

114. Talbot, D.E. and J.D. Talbot, *Corrosion science and technology*. 2018: CRC press.

115. Mott, N., *A theory of the formation of protective oxide films on metals.* Transactions of the faraday society, 1939. **35**: p. 1175-1177.

116. Hasegawa, M., *Ellingham Diagram*, in *Treatise on Process Metallurgy: Process Fundamentals*. 2014, Elsevier. p. 507-516.

117. Selinger, B., *Science for fun: Ellingham and the iconic reactions of iron.* Chemistry in Australia, 2018(Feb 2018): p. 38.

118. *Ellingham Richardson-diagram*. March 30 2016 [cited August 07 2017; Availabefrom: https://commons.wikimedia.org/wiki/File:Ellingham_Richardson-diagram_english.svg.

119. Jung, J., B. Shollock, and K.-b. Yoo, *Transient oxidation of a nickel-base superalloy with varying oxygen partial pressure.* Oxidation of Metals, 2016. **85**(3-4): p. 221-229.

120. Yoneda, S., et al., *Investigation of Initial Transient Oxidation of Fe–xCr–6at.% Al Alloys Using Synchrotron Radiation During Heating to 1000° C in Air.* Oxidation of Metals, 2016. **86**(3-4): p. 357-370.

121. Chattopadhyay, B. and G. Wood, *The transient oxidation of alloys.* Oxidation of Metals, 1970. **2**(4): p. 373-399.

122. Ul-Hamid, A., *Diverse scaling behavior of the Ni–20Cr alloy.* Materials chemistry and physics, 2003. **80**(1): p. 135-142.

123. Ul-Hamid, A., *A TEM study of the oxide scale development in Ni-Cr alloys.* Anti-Corrosion Methods and Materials, 2004. **51**(3): p. 216-222.

124. Atkinson, H., *A review of the role of short-circuit diffusion in the oxidation of nickel, chromium, and nickel-chromium alloys.* Oxidation of metals, 1985. **24**(3-4): p. 177-197.

125. Stott, F., *The protective action of oxide scales in gaseous environments at high temperature.* Reports on progress in physics, 1987. **50**(7): p. 861.

126. Rhines, F. and J. Wolf, *The role of oxide microstructure and growth stresses in the high-temperature scaling of nickel.* Metallurgical Transactions, 1970. **1**(6): p. 1701-1710.

127. Hindam, H. and D. Whittle, *Microstructure, adhesion and growth kinetics of protective scales on metals and alloys.* Oxidation of metals, 1982. **18**(5-6): p. 245-284.

128. Calvarin, G., R. Molins, and A.M. Huntz, *Oxidation Mechanism of Ni—20Cr Foils and Its Relation to the Oxide-Scale Microstructure.* Oxidation of Metals, 2000. **53**(1): p. 25-48.

129. Kear, B., et al., *On the transient oxidation of a Ni-15Cr-6Al alloy.* Oxidation of Metals, 1971. **3**(6): p. 557-569.

130. Doychak, J., J. Smialek, and T. Mitchell, *Transient oxidation of single-crystal β-NiAl.* Metallurgical transactions a, 1989. **20**(3): p. 499-518.

131. Fujii, C. and R. Meussner, *The Mechanism of the High‐Temperature Oxidation of Iron‐Chromium Alloys in Water Vapor.* Journal of the Electrochemical Society, 1964. **111**(11): p. 1215-1221.

132. Wood, G., et al., *A Comparison of the Oxidation of Fe&&bond; Cr, Ni Cr and Co Cr alloys in oxygen and water vapour.* Materials and Corrosion, 1970. **21**(11): p. 900-910.

133. Polman, E.A., T. Fransen, and P.J. Gellings, *Oxidation kinetics of chromium and morphological phenomena.* Oxidation of Metals, 1989. **32**(5): p. 433-447.

134. Fry, A., S. Osgerby, and M. Wright, *Oxidation of Alloys in Steam Environments: A Review.* 2002.

135. Ikeda, Y. and K. Nii, *Microcrack generation and its healing in the oxide scale formed on Fe-Cr alloys.* Oxidation of Metals, 1978. **12**(6): p. 487-502.

136. Honda, K., et al., *Oxidation behavior of sus430 stainless steel in moist atmospheres at 873 k.* Oxidation of metals, 1992. **38**(5-6): p. 347-363.

137. Saunders, S., M. Monteiro, and F. Rizzo, *The oxidation behaviour of metals and alloys at high temperatures in atmospheres containing water vapour: A review.* Progress in Materials Science, 2008. **53**(5): p. 775-837.

138. Rahmel, A. and J. Tobolski, *Einfluss von wasserdampf und kohlendioxyd auf die oxydation von eisen in sauerstoff bei hohen temperaturen.* Corrosion Science, 1965. **5**(5): p. 333-346.

139. Saunders, S.R. and N.L. McCartney. *Current understanding of steam oxidation-power plant and laboratory experience*. in *Materials science forum*. 2006. Trans Tech Publ.

140. England, D.M. and A.V. Virkar, *Oxidation kinetics of some nickel-based superalloy foils in humidified hydrogen and electronic resistance of the oxide*

scale formed part II. Journal of the Electrochemical Society, 2001. **148**(4): p. A330-A338.

141. Hussain, N., et al., *High-temperature oxidation behavior of HASTELLOY C-4 in steam.* Oxidation of metals, 2004. **61**(5-6): p. 355-364.

142. Holcomb, G.R., *Steam oxidation and chromia evaporation in ultrasupercritical steam boilers and turbines.* Journal of the Electrochemical Society, 2009. **156**(9): p. C292-C297.

143. Agüero, A., R. Muelas, and V. Gonzalez, *HVOF coatings for steam oxidation protection.* Materials and corrosion, 2008. **59**(5): p. 393-401.

144. Sundararajan, T., et al., *Steam oxidation resistance of Ni-Cr thermal spray coatings on 9Cr-1Mo steel. Part 1: 80Ni-20Cr.* ISIJ international, 2003. **43**(1): p. 95-103.

145. Sundararajan, T., et al., *Steam oxidation resistance of Ni-Cr thermal spray coatings on 9Cr-1Mo steel. Part 2: 50Ni-50Cr.* ISIJ international, 2003. **43**(1): p. 104-111.

146. Stringer, J., B. Wilcox, and R. Jaffee, *The high-temperature oxidation of nickel-20 wt.% chromium alloys containing dispersed oxide phases.* Oxidation of metals, 1972. **5**(1): p. 11-47.

147. Kofstad, P. and K. Lillerud, *On high temperature oxidation of chromium II. Properties of and the oxidation mechanism of chromium.* Journal of the electrochemical society, 1980. **127**(11): p. 2410-2419.

148. Lang, E., *The role of active elements in the oxidation behaviour of high temperature metals and alloys*. 2012: Springer Science & Business Media.

149. Grabke, H.J., M. Spiegel, and A. Zahs, *Role of alloying elements and carbides in the chlorine-induced corrosion of steels and alloys.* Materials Research, 2004. **7**: p. 89-95.

150. Grabke, H., E. Reese, and M. Spiegel, *The effects of chlorides, hydrogen chloride, and sulfur dioxide in the oxidation of steels below deposits.* Corrosion science, 1995. **37**(7): p. 1023-1043.

151. McNallan, M.J., et al., *Morphology of corrosion products formed on cobalt and nickel in argon-oxygen-chlorine mixtures at 1000 K.* Oxidation of Metals, 1982. **17**(5-6): p. 371-389.

152. Hernas, A., et al., *High-temperature chlorine–sulfur corrosion of heat-resisting steels.* Journal of materials processing technology, 2004. **157**: p. 348-353.

153. Oksa, M., S. Tuurna, and T. Varis, *Increased lifetime for biomass and waste to energy power plant boilers with HVOF coatings: high temperature corrosion testing under chlorine-containing molten salt.* Journal of thermal spray technology, 2013. **22**(5): p. 783-796.

154. Oksa, M. and J. Metsäjoki, *Optimizing NiCr and FeCr HVOF coating structures for high temperature corrosion protection applications.* Journal of Thermal Spray Technology, 2015. **24**(3): p. 436-453.

155. Varis, T., et al., *High temperature corrosion of thermally sprayed NiCr and FeCr coatings covered with a KCl–K2SO4 salt mixture.* Surface and Coatings Technology, 2015. **265**: p. 235-243.

156. Martin, P., *Introduction to surface engineering and functionally engineered materials*. Vol. 74. 2011: John Wiley & Sons.

157. Gil, L. and M.H. Staia, *Microstructure and properties of HVOF thermal sprayed NiWCrBSi coatings.* Surface and Coatings Technology, 1999. **120**: p. 423-429.

158. Zhang, D., S. Harris, and D. McCartney, *Microstructure formation and corrosion behaviour in HVOF-sprayed Inconel 625 coatings.* Materials Science and Engineering: A, 2003. **344**(1): p. 45-56.

159. Abioye, T., D. McCartney, and A. Clare, *Laser cladding of Inconel 625 wire for corrosion protection.* Journal of Materials Processing Technology, 2015. **217**: p. 232-240.

160. Pieraggi, B., *Calculations of parabolic reaction rate constants.* Oxidation of metals, 1987. **27**(3-4): p. 177-185.

161. Monceau, D. and B. Pieraggi, *Determination of Parabolic Rate Constants from a Local Analysis of Mass-Gain Curves.* Oxidation of Metals, 1998. **50**(5): p. 477-493.

162. Wang, D. and D.W. Anderson, *Direct measurement of organic carbon content in soils by the Leco CR‐12 carbon analyzer.* Communications in Soil Science and Plant Analysis, 1998. **29**(1-2): p. 15-21.

163. Sorbie, K., Y. Wu, and S. McDougall, *The extended Washburn equation and its application to the oil/water pore doublet problem.* Journal of Colloid and Interface Science, 1995. **174**(2): p. 289-301.

164. *Microscope-optical path*. November 05 2007 [cited August 07 2017;from: https://upload.wikimedia.org/wikipedia/commons/e/e0/Microscope-optical_path.svg.

165. *Bragg Diffraction Planes*. March 06 2005 [cited August 07 2017; Available from: https://en.wikipedia.org/wiki/File:Bragg_Diffraction_Planes.png.

166. Goldstein, J., et al., *Scanning electron microscopy and X-ray microanalysis: a text for biologists, materials scientists, and geologists*. 2012: Springer Science & Business Media.

167. *Diagram of a scanning electron microscope*. March 03 2010 [cited August 07 2017; from: https://commons.wikimedia.org/wiki/File:Schema_MEB(en).svg.

168. *An electron from the primary beam dislodges an electron from the K shell of a Si atom in the sample*. June 12 2014 [cited August 07 2017; Available from: http://www.ammrf.org.au/myscope/analysis/eds/xraygeneration/characteristic/.

169. Song, B., et al., *Role of Oxides and Porosity on High-Temperature Oxidation of Liquid-Fueled HVOF Thermal-Sprayed Ni50Cr Coatings.* Journal of Thermal Spray Technology, 2017. **26**(3): p. 554-568.

170. Cullity, B.D., *Elements of X-ray Diffraction.* 2001.

171. Huang, P.K., et al., *Multi‐principal‐element alloys with improved oxidation and wear resistance for thermal spray coating.* Advanced Engineering Materials, 2004. **6**(1‐2): p. 74-78.

172. Saaedi, J., et al., *Phase formation in a Ni–50Cr HVOF coating.* Surface and Coatings Technology, 2008. **202**(24): p. 5804-5811.

173. Xie, D.-b., X. Xiong, and F.-h. Wang, *Effect of an enamel coating on the oxidation and hot corrosion behavior of an HVOF-sprayed Co–Ni–Cr–Al–Y coating.* Oxidation of metals, 2003. **59**(5-6): p. 503-516.

174. Yuan, F., et al., *Oxidation behavior of thermal barrier coatings with HVOF and detonation-sprayed NiCrAlY bondcoats.* Corrosion science, 2008. **50**(6): p. 1608-1617.

175. Edris, H., D. McCartney, and A. Sturgeon, *Microstructural characterization of high velocity oxy-fuel sprayed coatings of Inconel 625.* Journal of Materials Science, 1997. **32**(4): p. 863-872.

176. Hewitt, A., *Technology of Oxy-Fuel Gas Processes. Pt. 3. Choice of Suitable Fuel Gases.* Welding, 1972. **40**(12): p. 416-422.

177. Wanphut, S., *Optimisation of HVOF sprayed MCrAlY coatings for gas turbines*. 2014, University of Nottingham.

178. Samsonov, G.V., *The oxide handbook*. 2013: Springer Science & Business Media.

179. Kamali, R. and A. Binesh, *The importance of sensitive parameters effect on the combustion in a high velocity oxygen-fuel spray system.* International Communications in Heat and Mass Transfer, 2009. **36**(9): p. 978-983.

180. Paladino, A.E. and W. Kingery, *Aluminum ion diffusion in aluminum oxide.* The Journal of Chemical Physics, 1962. **37**(5): p. 957-962.

181. Turnbull, D. and R. Hoffman, *The effect of relative crystal and boundary orientations on grain boundary diffusion rates.* Acta Metallurgica, 1954. **2**(3): p. 419-426.

182. Song, B., et al., *Gas and liquid-fuelled HVOF spraying of Ni50Cr coating: Microstructure and high temperature oxidation.* Surface and Coatings Technology, 2017. **318**(Supplement C): p. 224-232.

183. Essuman, E., et al., *Protective and non-protective scale formation of NiCr alloys in water vapour containing high-and low-pO2 gases.* Corrosion Science, 2008. **50**(6): p. 1753-1760.

184. Wright, I.G. and R. Barry Dooley, *Morphologies of oxide growth and exfoliation in superheater and reheater tubing of steam boiler.* Materials at High Temperatures, 2011. **28**(1): p. 40-57.

185. Ericsson, T., *A study of the Cr-depleted surface layers formed on four Cr-Ni steels during oxidation in steam at 600° C and 800° C.* Oxidation of Metals, 1970. **2**(4): p. 401-417.

186. Sanchez, L., M. Hierro, and F. Perez, *Effect of chromium content on the oxidation behaviour of ferritic steels for applications in steam atmospheres at high temperatures.* Oxidation of metals, 2009. **71**(3-4): p. 173.

187. Bueno, P., et al., *Role of oxygen at the grain boundary of metal oxide varistors: A potential barrier formation mechanism.* Applied Physics Letters, 2001. **79**(1): p. 48-50.

188. Caplan, D. and G. Sproule, *Effect of oxide grain structure on the high-temperature oxidation of Cr.* Oxidation of Metals, 1975. **9**(5): p. 459-472.

189. Atkinson, A., R. Taylor, and A. Hughes, *A quantitative demonstration of the grain boundary diffusion mechanism for the oxidation of metals.* Philosophical Magazine A, 1982. **45**(5): p. 823-833.

190. Bollmann, W., *Crystal defects and crystalline interfaces*. 2012: Springer Science & Business Media.

191. Kelly, A. and K.M. Knowles, *Crystallography and crystal defects*. 2012: John Wiley & Sons.

192. Gottstein, G. and L.S. Shvindlerman, *Grain boundary migration in metals: thermodynamics, kinetics, applications*. 2009: CRC press.

193. Lemaitre, J. and J.-L. Chaboche, *Mechanics of solid materials*. 1994: Cambridge university press.

194. Prchlik, L., J. Pisacka, and S. Sampath, *Deformation and strain distribution in plasma sprayed nickel–aluminum coating loaded by a spherical indenter.* Materials Science and Engineering: A, 2003. **360**(1-2): p. 264-274.

195. Ueda, Y. and T. Yamakawa, *Analysis of thermal elastic-plastic stress and strain during welding by finite element method.* Transactions of the Japan Welding Society, 1971. **2**(2): p. 186-196.

196. Ueda, Y., K. Fukuda, and M. Tanigawa, *New measuring method of three dimensional residual stresses based on theory of inherent strain (welding mechanics, strength & design).* Transactions of JWRI, 1979. **8**(2): p. 249-256.

197. Bergman, H. *Modification of metal surface by excimer laser treatment*. in *The Proceedings of 2nd IFHT Seminar*. 1989. Lisbon, Portugal, Sept.

198. Pantelis, D., *Excimer laser surface modification of engineering metallic materials: case studies.* ASM International, Member/Customer Service Center, Materials Park, OH 44073-0002, USA, 1998., 1998: p. 179-203.

199. Stott, F.H., F.I. Wei, and C.A. Enahoro, *The influence of manganese on the High-temperature oxidation of iron-chromium alloys.* Materials and Corrosion, 1989. **40**(4): p. 198-205.

200. Guinier, A., *X-ray diffraction in crystals, imperfect crystals, and amorphous bodies*. 1994: Courier Corporation.

201. Mullins, W., *Grain boundary grooving by volume diffusion.* Transactions of the American Institute of Mining and Metallurgical Engineers, 1960. **218**(2): p. 354-361.

202. Song, B., et al., *Gas and liquid-fuelled HVOF spraying of Ni50Cr coating: microstructure and high temperature oxidation.* Surface and Coatings Technology, 2016.

203. Wright, I., B. Wilcox, and R. Jaffee, *The high-temperature oxidation of Ni-20% Cr alloys containing various oxide dispersions.* Oxidation of Metals, 1975. **9**(3): p. 275-305.

204. Weast, R.C., M.J. Astle, and W.H. Beyer, *CRC handbook of chemistry and physics*. Vol. 69. 1988: CRC press Boca Raton, FL.

205. Liu, Z., et al., *Oxidation behaviour of sputter-depositedNi–Cr–Al micro-crystalline coatings.* Acta Materialia, 1998. **46**(5): p. 1691-1700.

206. Gellings, P. and M. De Jongh, *Grain boundary oxidation and the chromium-depletion theory of intercrystalline corrosion of austenitic stainless steels.* Corrosion science, 1967. **7**(7): p. 413IN5417-416IN7421.

207. Wild, R., *High temperature oxidation of austenitic stainless steel in low oxygen pressure.* Corrosion Science, 1977. **17**(2): p. 8795-93104.